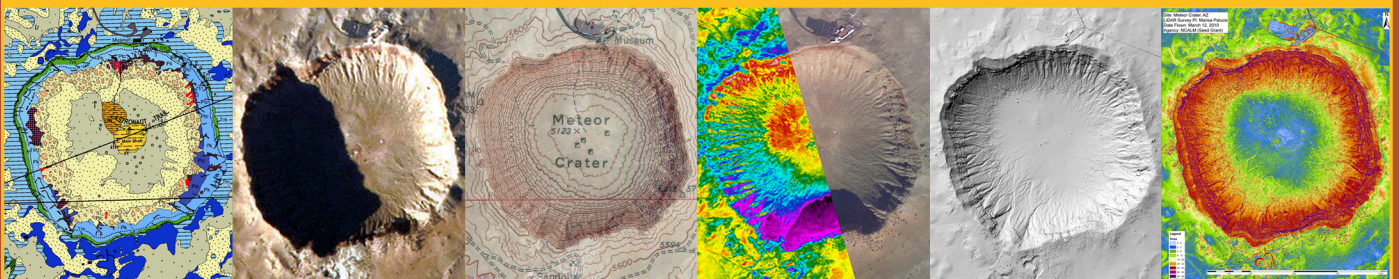


Guidebook to The Geology of Barringer Meteorite Crater, Arizona

a.k.a. Meteor Crater

2nd edition



Guidebook to the Geology of Barringer

Meteorite Crater, Arizona

(*a k a* Meteor Crater)

Second Edition

Prepared by

David A. Kring

for the

80th Annual Meeting

of the

Meteoritical Society

July 2017

Copyright © 2017

Single copy academic use of this material can be made as long as appropriate acknowledgment of the source is maintained. Republication of any portion of the guidebook or any commercial use requires written permission from the author (David A. Kring) or the Lunar and Planetary Institute, in addition to appropriate acknowledgment of the source.

Note about the Cover Art

The cover is designed to illuminate the world's best preserved impact crater, our efforts to use this world-class geologic site for training and research programs, and data relevant to the analysis of the crater. The background image was taken by the author. The picture of students in the Field Training and Research Program at Meteor Crater was taken by teaching assistant Josh Garber. The series of images showing different perspectives of the crater are, from left to right,

LPI's colorized version of Gene Shoemaker's geologic map
(http://www.lpi.usra.edu/publications/books/barringer_crater_guidebook/craterMap/)

an image of the crater taken by astronauts on International Space Station Expedition 38 for a training exercise (http://www.lpi.usra.edu/exploration/training/resources/measuring_meteor_crater/),

the topography of the crater as seen on a USGS 7.5' Meteor Crater Quadrangle,

an overlay of thermal imaging of the crater produced by Oleg Abramov,

a hillshade digital elevation map of the crater, and a slope map produced by Marisa Palucis from 25 cm resolution LiDAR data

(http://www.lpi.usra.edu/publications/books/barringer_crater_guidebook/LiDAR/).

These and other Barringer Meteorite Crater resources are available at

http://www.lpi.usra.edu/publications/books/barringer_crater_guidebook/

Impact cratering resources for students and educators are available at

<http://www.lpi.usra.edu/exploration/training/resources/>

LPI Contribution Number 2040



Frontispiece

Barringer Meteorite Crater (a.k.a Meteor Crater) is located in the southwestern United States, North America; 35.026° N, 111.024 °W.

Table of Contents

Title Page	i
Frontispiece	iv
Table of Contents	v
Preface and Acknowledgments	vii
Chapter 1 Introduction	1
Chapter 2 Target Stratigraphy	7
Chapter 3 Pre-impact Structure	27
Chapter 4 Barringer Meteorite Impact Crater	35
Chapter 5 Shock Metamorphism and Impact Melting	53
Chapter 6 Crater Rim Uplift and Crater Wall Collapse	69
Chapter 7 Overturned Rim Sequence	79
Chapter 8 Distribution of Ejecta	85
Chapter 9 Projectile	103
Chapter 10 Trajectory	115
Chapter 11 Energy of Impact	119
Chapter 12 Age of the Crater	121
Chapter 13 Environmental Effects of the Impact	125
Chapter 14 Post-Impact Lake and Volcanic Ash Deposits	131
Chapter 15 Post-Impact Erosion and Sedimentation	151
Chapter 16 Modern Atmospheric Conditions at the Crater	165
Trail Guides	171
Chapter 17 Crater Rim East Trail Guide	175
Chapter 18 Crater Rim West Trail Guide	201
Chapter 19 Crater Floor Trail Guide	223
Bibliography	251

❖ Preface and Acknowledgments

The geological guidebook that follows has been prepared for the occasion of the 80th Annual Meeting of The Meteoritical Society in Santa Fe, New Mexico, and a Society field trip to the crater. The guidebook is an expanded version of the first edition, which was prepared for the 70th Annual Meeting of The Meteoritical Society in Tucson, Arizona. While both guidebooks provide a trail-oriented geological tour of the crater, they are also designed to introduce readers to the geological processes that shaped the crater.

The geological processes involved in the formation of the crater have been broken down into a series of discrete topics. The goal is to illustrate how our understanding of those topics has evolved over the past 100+ years of study at the crater and how observations at the crater have influenced them. While our understanding of the processes involved in the crater's formation have grown, there are also a great number of topics that still need further research. In each section of the guidebook, I try to identify those unresolved issues with the hope that those comments will spawn new studies.

It is important to use this incredible impact crater to learn about the planet-shaping processes associated with asteroid and comet collisions. It is also important to use such a perfectly preserved site to train planetary scientists, many of whom are no longer emerging from the ranks of field-based geology programs and, thus, lack any other field experience. For that reason, we were very fortunate to receive funds from the NASA Lunar Science Institute and the NASA Solar System Exploration Research Virtual Institute for a Field Training and Research Program at Meteor Crater. We have, since the Society's last field trip to the crater, trained ~70 graduate students at the crater through that program. Those young investigators and the institutions they represented are responsible for a tremendous amount of new research reported in this edition of the guidebook and I thank them: Corwin Atwood-Stone (*University of Arizona*), Jeffrey Balcerski (*Case Western Reserve University*), David Blair (*Purdue University*), Samuele Boschi (*Lund University*), Aaron Boyd (*Arizona State University*), Jessie Brown (*University of New Brunswick*), Christy Caudill (*University of Western Ontario*), Mitali Chandnani (*University of Alaska Fairbanks*), Matthew Chojnacki (*University of Tennessee*), Shoshanna Cole (*Cornell University*), Laura Corley (*University of Hawaii at Manoa*), Kathleen Craft (*Virginia Tech University*), Sarah Crites (*University of Hawaii*), Natalie Curran (*University of Manchester*), Connor Davis (*Western University*), Patrick Donohue (*University of Notre Dame*), Sarah Drummond (*University of Tennessee-Knoxville*), Nicholas DiFrancesco (*Stony Brook University*), Joshua Garber (*University of California-Davis*), Tienielle Gaither (*Northern Arizona University*), Shannon Hibbard (*Temple University*), Michelle Hopkins (*University of Colorado-Boulder*), Matthew Huber (*University of Vienna*), Kynan Hughson (*University of California Los Angeles*), Steven Jaret (*Harvard University*), Christine Jilly (*University of Hawaii*), Mallory Kinczyk (*North Carolina State University*), Katrina Korman (*Temple University*), Myriam Lemelin (*Université de Sherbrooke*), Anna Losiak (*University of Vienna*), Analisa Maier (*University of Colorado*), Aviva Maine (*Northern Arizona University*), Audrey Martin (*University of Tennessee*), Ellinor Martin (*Lund University*), Mélissa Martinot (*Vrije Universiteit Amsterdam*), Cameron McCarty (*University of Tennessee*), Francesca McDonald (*University of Manchester*), Julie Mitchell (*University of Houston-Clear Lake*), Stephanie Montalvo Delgado (*University of Puerto Rico at Mayaguez*), Raquel Nuno (*Arizona State University*), Lissa Ong (*University of Arizona*), Lillian Ostrach (*Arizona State University*), Katie O'Sullivan (*University of Notre Dame*), Seda Oezdemir (*University of Vienna*), Ross Potter (*Imperial College London*), Kathryn Powell (*Washington University*), Kathryn Rathbun (*University of Iowa*), Nisa Rhodes (*University of Texas at El Paso*), Stuart Robbins (*University of Colorado-Boulder*), Margaret Rosenburg (*California Institute of Technology*), Adam Sarafian (*Massachusetts Institute of Technology*), Douglas Schaub (*Stony Brook University*), Laura Seward

(*University of Central Florida*), Bhairavi Shankar (*University of Western Ontario*), Erin Shea (*Massachusetts Institute of Technology*), Katherine Shirley (*Stony Brook University*), Kelsi Singer (*Washington University*), Eugenie Song (*University of Washington*), Michael Sori (*Massachusetts Institute of Technology*), Joshua Snape (*University College London*), Sebastian Sturm (*Westfälische Wilhelms-Universität Münster*), Hannah Susorney (*Johns Hopkins University*), Matthieu Talpe (*Massachusetts Institute of Technology*), Kevin Thaisen (*University of Tennessee*), Michael Veto (*Arizona State University*), David Weiss (*Brown University*), Matthew Wielicki (*University of California Los Angeles*), Felicity Williams (*Open University*), Malte Willmes (*Westfälische Wilhelms-Universität Münster*), Emily Worsham (*University of Maryland*), and Michael Zanetti (*Washington University*). The teaching assistants for the classes were Axel Wittmann, Mike Zanetti, Josh Garber, and Martin Schmieder.

We supplemented that formal program with additional training and/or research opportunities for nearly two dozen students and postdoctoral researchers at the crater: Oleg Abramov (*LPI*), Denise Anders (*LPI*), Katherine Bermingham (*University of Maryland*), Ana Cernok (*LPI*), Adeene Denton (*LPI*), Amy Fagan (*LPI*), Miriam Galenas (*University of Maryland*), Justine Grabiec (*LPI*), Connor Hilton (*University of Maryland*), Debra Hurwitz (*LPI*), Katherine Joy (*LPI*), Georgiana Kramer (*LPI*), Celestine Mercer (*LPI*), Amanda Nahm (*LPI*), Takafumi Niihara (*LPI*), Teemu Öhman (*LPI*), Jennifer Rapp (*JSC*), Martin Schmieder (*LPI*), Barry Shaulis (*LPI*), Samuel Simmons (*University of Houston*), Matt Weller (*Rice University*), Oliver White (*LPI*), and Emily Worsham (*University of Maryland*).

Finally, with additional support from the Barringer Family Fund for Meteorite Impact Research, students Marisa Palucis (*University of California Berkeley*) and Ankit Verma (*Trinity College*) have been able to conduct detailed research at the crater. Their efforts and the insights they are providing are gratefully acknowledged.

Because members of The Meteoritical Society formed the core of the principal investigators in the original Apollo sample program, the Society might also appreciate the important role geologic sites like Barringer Meteorite Crater can have in training astronauts who may, at some future point in time, be asked to collect samples from the Moon, an asteroid, or even Mars. Fortunately, since the Society last met at the crater, I have had an opportunity to use the wonderfully exposed geology at the crater to train three groups of NASA astronauts, along with astronauts from the Canadian Space Agency (CSA) and Japan Aerospace Exploration Agency (JAXA). It has been a thoroughly rewarding experience to work with such gifted people who absorb the lessons to be learned at the crater with considerable zeal.

In parallel with those training and research programs, several independent research projects were initiated to study structural elements of the crater, the distribution of ejecta both on the surface and in the subsurface, gully formation in the crater walls, the general breakdown of rock exposed by the impact, and modern meteorological attributes. That work produced several new insights about the crater that will be described in the chapters that follow. I thank each of those teams for their research and am happy to report that several additional projects are in development, so credible research at the crater will continue.

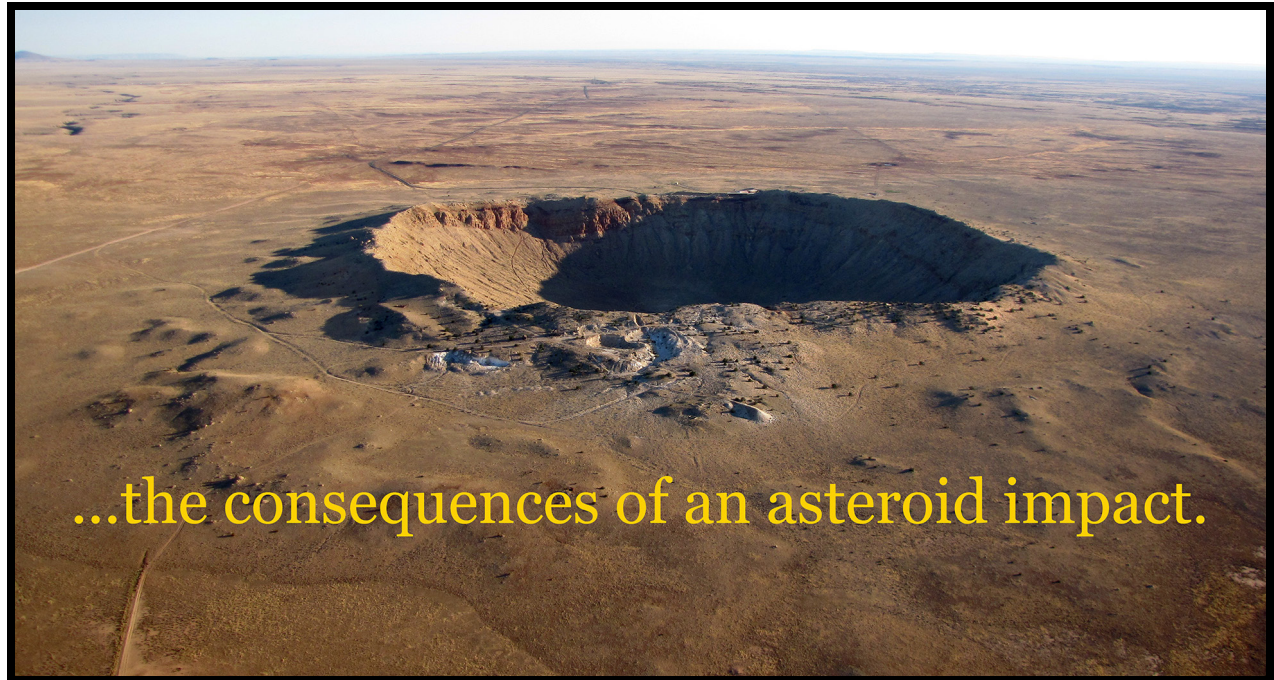
The goal of those activities is to bring the crater and the processes that shaped it alive for our community, affiliated scientific disciplines, and the general public. That endeavor is only possible because of the tremendous support of Drew Barringer, President of the Barringer Crater Company, and Brad Andes, President of Meteor Crater Enterprises. I thank the entire Barringer family for its stewardship of the crater and its interest in preserving the site for education and scientific research. The field training and research activities at the crater have also been facilitated by Lanah Butterfield, Vice President of Meteor Crater Enterprises, and the incredibly helpful MCE staff. Some of our recent research was conducted on the surrounding Bar T Bar Ranch, which was made possible with the gracious

support of Judy Chilson Prosser, an owner and operator of the ranch. I thank Carleton Moore for his insights about the crater and Canyon Diablo meteorites. I might add that he repeatedly provided presentations about Canyon Diablo meteorites to students in our Field Training and Research Program at Meteor Crater, which greatly enriched the students' experiences. I also thank Martin Schmieder for kindly assisting this field trip by providing a tour of the crater rim while I lead a tour of the crater walls and crater floor.

For the production of this guidebook, I thank Linda Chappell, Sandra Cherry, and David Bigwood at the Lunar and Planetary Institute (LPI) for helping me obtain copies of some of the older publications about the crater; Jennifer Steil for converting first edition files into a more modern format; John Blackwell and Ronna Hurd for their assistance with some of the illustrations in the guidebook; and Delia Enriquez for printing and binding the document you now hold in your hands. I thank Linda Garcia in the LPI Meeting Planning Services department and Beth Ha and Shannon Clark at the University of New Mexico for their help organizing the field trip. Likewise, I thank Karen Ziegler and the organizing committee of the 80th Annual Meeting of The Meteoritical Society for promoting the field trip.

To all who participate in the field trip, I thank you for your interest.

David A. Kring
Houston



1. Introduction



Science does not always move forward in a straight line and rarely at a constant cadence. The study of Barringer Meteorite Crater (*a k a* Meteor Crater) is a classic example. Although an immense collection of meteorites of undisputable extraterrestrial origin was gathered at northern Arizona's crater (Foote, 1891), the association was considered coincidental by many (*e.g.*, Gilbert, 1896) and nearly fifteen years passed before a serious case linking the meteorites to the impact origin of the crater was presented (Barringer 1905; Tilghman 1905). That latter effort was part of an intense mining operation at the crater to recover the suspected projectile. The works were extensive, including a reservoir in the distant Canyon Diablo, a pipeline to the crater, and camps on both the crater rim and crater floor. Sadly for investors, economically viable deposits of metal were never recovered. Sadly for science, decades passed before the implications of Barringer's work were appreciated.

There are many ways to trace the path of this story, but perhaps the best place to begin is with the mineralogist A. E. Foote, who published the first scientific report about the crater and meteorites found there. Foote's interest was piqued by a railroad executive who sent him a sample of native iron and requested an analysis. Foote deduced the sample was a fragment of a meteorite and, having been told more material existed in northern Arizona ("185 miles due north from Tucson"), promptly traveled to the site from Philadelphia. Foote and his team collected several large masses (201, 154, and 40 lbs), 131 smaller masses (ranging from 1/16 oz to 6 lbs 10 oz), and 200 lbs of oxidized meteorite fragments. After returning to Philadelphia, he received three additional large masses (632, 506, and 145 lbs). Several of the larger samples were perforated with cavities similar to the one in the spectacular Tucson ring meteorite ("Signet Iron"). The iron meteorites also contained troilite, daubréelite, carbon, and diamonds (up to 1/8 inch diameter), the latter of which were described as being mostly black and of little commercial value.

The purpose of Foote's paper was to describe the diamond-bearing iron meteorites, but he was clearly impressed with the "Crater Mountain," where the samples were found and provided the scientific community with its first geologic description. He noted an uplifted rim of sandstone and limestone dipping 35 to 40° that stood 432 ft above the surrounding plain. The crater floor appeared to be 50 to 100 ft below the surrounding plain. He further noted that he could not locate any "lava, obsidian or other volcanic products," and, thus, concluded that he was "unable to explain the cause of this remarkable geological phenomenon." He did not recognize any genetic association between the crater and meteorite irons. Nor did he add any remarks about the unusual quantity of iron meteorites. With regard to the iron oxide fragments, however, he concluded that a large iron meteorite of 500 to 600 pounds "had become oxidized while passing through the atmosphere and was so weakened in its internal structure that it had burst into pieces not long before reaching the earth."

Foote presented his paper at a meeting of the American Association for the Advancement of Science (AAAS) in Washington DC. Sitting in the audience was the chief geologist of the United States Geological Survey, Grove Karl Gilbert. Gilbert developed an immediate interest in the crater and its association with meteoritic iron. Having also recently heard T. C. Chamberlin's (1890) proposal for a new scientific method of "multiple working hypotheses," Gilbert decided to apply the principle to the origin of the crater. He posited two origins: (1) that the crater was produced by the impact of a large iron mass from space and (2) that the crater was produced by a volcanically-driven steam explosion, in which case the fall of meteoritic irons at that locality was coincidental and had nothing to do with the formation of the crater. He reasoned that if the impact of a "stellar body" occurred, it must still lay beneath the crater floor, but would be absent if the crater was produced by a volcanic steam explosion. To determine if a meteoritic mass lay beneath the crater floor and, thus, test the hypotheses, he devised several measurements that were conducted during a two week stay at the crater in November, 1891. He measured the volume of the crater

and ejected material contained in the rim: if the volumes are equal, he reasoned, then a mass did not lie buried beneath the crater floor. He also measured the magnetic field in the vicinity of the crater, assuming that a buried mass of iron would deflect magnetic instruments. While making those measurements, he also made notes about uplifted strata in the upper crater walls and the distribution of ejected sedimentary blocks and iron masses around the crater.

To compare the volume of the crater cavity and crater rim, Gilbert's team generated a topographic map with a contour interval of 10 feet, which is a remarkable achievement. It is a higher resolution topographical result than that currently available on the USGS Meteor Crater 7.5 minute quadrangle, which has a 20 ft contour interval. Unfortunately, Gilbert's map has not resurfaced and is only available in a small reproduction in his 1896 paper. (About 100 years later, David Roddy developed another 10 ft contour map of the crater that he informally distributed to some investigators. The map is available from the present author.) Using the 1891 map, Gilbert calculated that the crater cavity and the ejected rim material had the same volume, from which he concluded a buried mass could not be partially filling the crater volume. Interestingly, Gilbert did not recognize the lake sediments that partially filled the crater or discuss the change in density between the original target strata and the rim deposits, both of which affect this type of calculation. Nor does he describe the red Moenkopi Formation in the walls of the crater. His team's measurements of magnetism at the crater were negative: they did not reveal any variations in direction or intensity inside or outside the crater, leading Gilbert to conclude that a mass did not exist beneath the crater floor.

Thus, the tests of the meteoritic impact theory as envisioned by Gilbert failed. Consequently, he turned to the other hypothesis and observed that Arizona's crater "is in the midst of a great volcanic district." (See Fig. 1.1 for a modern view of the volcanic district.) He then drew comparisons between Arizona's crater and several volcanic vents around the world, including the maars in Germany that would again draw attention during the Apollo era. Interestingly, he also referred to Lonar Crater of India, which, because it occurs within the Deccan Traps, he concluded also had a volcanic origin. As we now know, Lonar Crater has an impact origin. Based on these comparisons, Gilbert erroneously concluded that of the two hypotheses the steam explosion origin for northern Arizona's crater was the correct solution. Having applied Chamberlin's principle of multiple working hypotheses, Gilbert concluded his report with a principle of his own, one that remains a benchmark of comparative planetology today (although it has an echo of uniformitarianism): "tentative explanations are always founded on accepted explanations of similar phenomena," in this case referring to the similarities he believed existed between Arizona's crater and the volcanic ones to which he alluded.

Gilbert's (1896) conclusion that the crater was produced by a steam explosion greatly influenced the geologic community, because he was one of the nation's most eminent geologists. He had already been the chief geologist at the USGS for eight years and would continue in that post for many more years. At the time of his report, he was also President of the Geological Society of Washington. Indeed, he presented his report in the form of the annual presidential address to the society, which was then published in *Science*.

Quite unaware of Gilbert's work (at least initially), Daniel Moreau Barringer independently heard about the crater and its meteoritic irons from S. J. Holsinger on the veranda of the San Xavier Hotel in Tucson (Fig. 1.2). Barringer was entranced, particularly with the potential wealth associated with a source of metallic iron and nickel. He was well-schooled in the mining industry, having already made a fortune with silver. He quickly obtained the crater property and began a series of investigations of the structure with his business partner, Benjamin Chew Tilghman. Barringer was soon in a position to challenge the conclusions of Gilbert and he produced a series of reports over a 25 year period, beginning with his first report to The Academy of Natural Sciences of Philadelphia in 1905.

Barringer obtained the property in 1903, formed the Standard Iron Company to extract the metal, and immediately began a survey and drilling operation (Fig. 1.3 and 1.4). By the time Barringer prepared his 1905 report, he had made more than ten trips to the crater.

In comparison to Gilbert's report, Barringer's paper provides a much better description of the stratigraphic units and their regional context. He also provides a series of observations that are relevant to the structure's formation. He points out that meteoritic irons are concentrically distributed around the crater, suggesting the occurrence is not coincidental, but rather tied directly to the formation of the crater. (In a later paper (1910), he also observes that the concentration of irons increases towards the rim of the crater.) He describes uplifted strata in the crater walls, which he argues were "turned out bodily by the force which produced this enormous hole." He describes a mix of underlying strata in a breccia at the crater surface and, in one location, correctly notes the inverted stratigraphy of ejected material. Barringer found that some of the meteoritic irons are buried within the ejecta and, thus, both must have formed at the same time. He notes that the largest ejected blocks are distributed east and west, indicating a plane of symmetry that he would later map to the trajectory of an impacting object. Barringer focused a lot of attention on pulverized silica that he found beneath lake sediments and in ejected material. He noted that individual grains are sharply fractured, which is inconsistent with a sedimentary origin, and inferred the silica is crushed target sandstone. In some cases, he wrote, the silica was powdered so completely that no silt or sand grittiness was detectable with one's teeth. In a companion paper, his partner, Tilghman (1905), makes similar arguments. Importantly, Tilghman also describes three boreholes that encountered iron masses buried 300, 400, and 480 ft below the crater floor, which, like irons buried within the ejecta blanket, illustrated the simultaneous fall of the irons and production of the crater.

In counterpoint to Gilbert's findings, Barringer also wrote that he was unable to find any eruptive rock or any other evidence of volcanic-related activity. He organized eight arguments against a volcanic steam explosion hypothesis and three additional arguments against any other type of volcanic action. Barringer bluntly criticized Gilbert and his conclusion of a volcanic steam explosion, writing that if Gilbert "examined the surface carefully, it does not seem possible to me that any experienced geologist could have arrived at such a conclusion." Barringer's geologic and petrologic methods trumped Gilbert's geophysical techniques and he wanted it well known. Tilghman (1905), in his companion paper, emphasized that the drilling did not encounter any volcanic material beneath the crater to a depth of 1400 ft relative to the surrounding plane, thus demonstrating there is no magmatic conduit that could have fed a volcanic steam explosion.

For Barringer and his heirs, the issue was settled: Arizona's crater was produced by a meteoritic impact. The geologic community was less receptive. In general, processes that could be described as catastrophic were ignored or abandoned in favor of uniformitarian concepts. The problem continues to plague geology, although progress is being made (Marvin, 1990).

One of the most significant series of events to affect the scientific community's perception of Barringer's thesis was a re-examination of the problem by Gene Shoemaker (1960) and the Apollo exploration of the heavily cratered lunar surface. Shoemaker drew upon new observations of crater excavation associated with nuclear explosions and developed an analytical model for the penetration mechanics of hypervelocity impact events. One of the strengths of his work was the superb geologic description he provided of diagnostic features at Meteor Crater and nearly identical features that he found at the nuclear Teapot Ess Crater: crater rims overturned in synclinal folds, upper fold limbs composed of debris that preserves an inverted stratigraphic sequence, glass in the uppermost components of the debris, and crater floors covered with breccia lenses. With Ed Chao, he later discovered evidence of the shock-metamorphic transformation of quartz in target sediments to coesite and stishovite (Chao *et al.*, 1960, 1962).

Collectively, the work of Barringer, Tilghman, Shoemaker, and Chao demonstrated the impact origin of Barringer's crater and also provided the diagnostic geologic and petrologic tools needed to recognize structures formed by similar processes elsewhere on Earth and in the Solar System. We now understand that impact cratering is one of (if not the) dominant geologic process affecting planetary surfaces.

For students interested in additional details about the early exploration of the crater, I recommend the following primary references: Barringer (1910, 1914, 1924), Fairchild (1907), and Merrill (1908). I also recommend a very nice and pleasantly concise review written by Brandon Barringer (1964) and a longer, book-length review written by William Hoyt (1987). Both of the latter reviews include details of the mining operations associated with studies of the crater's origin. For an intimate portrait of Barringer and his enterprise, the best source is a small book written by Nancy Southgate and Felicity Barringer (2002).



Fig. 1.1. Three views of the volcanic terrains in the vicinity of Barringer Meteorite Crater (a.k.a. Meteor Crater) that influenced G. K. Gilbert when interpreting the origin of the crater. The eastern portion of the San Francisco Volcanic Field is visible northwest of the crater (top panel). The stratovolcano in the midst of the field, near Flagstaff, is visible from the crater rim (lower left). Also visible from the crater rim are the basalts of East and West Sunset Mountains south of the crater (lower right).



Fig. 1.2. View of the San Xavier Hotel, Tucson, where S. J. Holsinger told D. M. Barringer about northern Arizona's crater and its meteoritic irons. This photograph (c. 1893) was taken approximately a decade before that conversation in 1902. Arizona was a territory at the time, not receiving statehood until 1912. The photograph appears courtesy of the George Mason University and should not be reproduced further without permission.

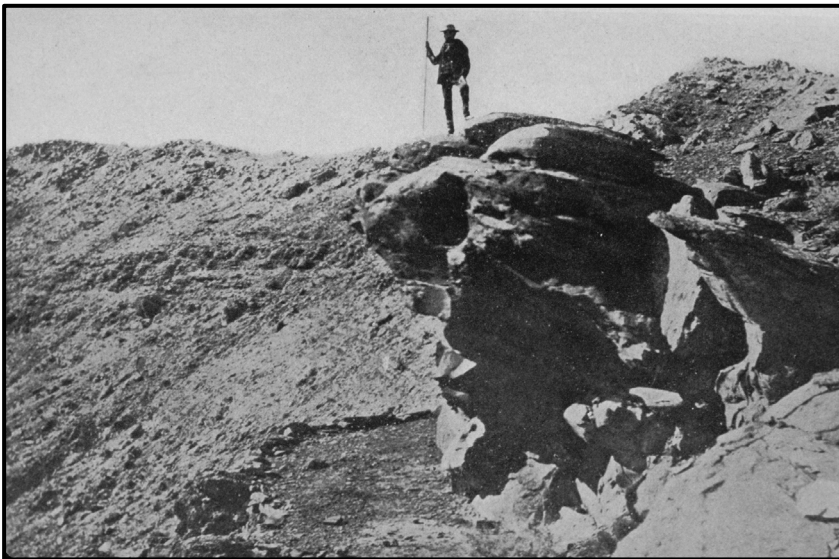


Fig. 1.3. View of the upper crater wall and crater rim, with uplifted (tilted) red Moenkopi in foreground. (Bottom panel of Plate VIII in Barringer, 1910.)

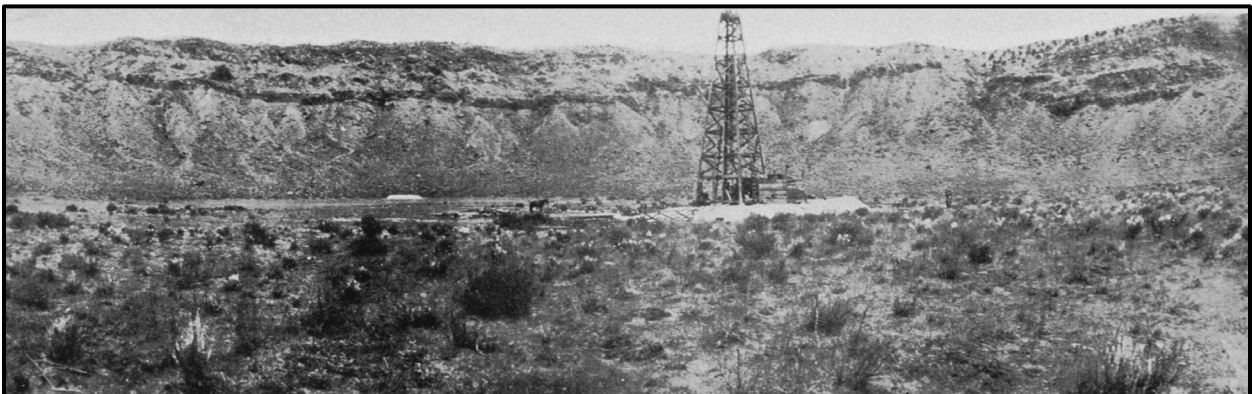


Fig. 1.4. (below) View of crater floor and a drilling unit near crater center. (Bottom panel of Plate IV in Barringer, 1910.)

2. Target Stratigraphy



The impact event excavated material from the Colorado Plateau, which is a broad region in the Four Corners area that is composed of relatively flat lying sedimentary rocks. A flat-lying, multi-layered sedimentary target has made Barringer Meteorite Crater a particularly important impact site, because the structural deformation created by the impact is relatively easy to observe.

Plateau sediments in the vicinity of the crater are ~1,070 m (~3,510 ft) thick and overlie a crystalline basement of continental crust (Fig. 2.1). The Devonian Martin Formation unconformably overlies the basement, which is, in turn, unconformably covered by the Mississippian Redwall Formation. These units are covered by a Permian section that is poorly sampled in the immediate vicinity of the crater. A small amount of the Molas Formation may occur at the base of the Permian section, followed by the Naco Formation. The thickness of the latter is not well-known and is inferred on the basis of a seismic refraction horizon (Ackerman *et al.*, 1975) believed to occur between the Naco and the overlying Supai Formation (Roddy, 1978). The Supai is the thickest sedimentary unit in the section. It is covered by the Coconino Sandstone, Toroweap Formation, Kaibab Formation, and Moenkopi Formation, all of which are exposed in the crater walls. These units represent the upper portion of the well-known Grand Canyon sequence and are the critical units involved in the impact event (Fig. 2.1). Detailed descriptions of these latter units follow.

Coconino Sandstone. The Coconino Sandstone is white, fine-grained, and saccharoidal (*i.e.*, a granular texture similar to loaf sugar) quartzose sandstone that occurs in massive beds with cross-stratification. The unit was defined in the plateau province by Darton (1910) and subsequently described in greater detail by Noble (1914) in the Grand Canyon, where outcrops of the sandstone are particularly spectacular. Sets of cross-stratified units are sometimes 30 m (100 ft) thick. The sedimentary environment was controversial for several decades, but an eolian environment was the eventual consensus (McKee, 1934, and Reiche, 1938; *cf.*, Schuchert, 1918, and Read, 1950). Thus, the Coconino's high-angle cross-bedded laminae are fossilized sand dune slopes produced when northern Arizona was covered by a huge sand dune field similar to the modern Sahara. The Coconino thickens to the south, where it has a maximum thickness of 330 m (1000 ft; Kieffer, 1974). In the vicinity of the impact, the Coconino is 210 to 240 m (700 to 800 ft) thick (Shoemaker, 1974). It is the basal unit excavated by the impact event. Only the upper portions of the Coconino Sandstone, however, are exposed in the crater walls.

The sandstone is >95% quartz. Grains are well-rounded (Fig. 2.2) and have dimensions that are 0.1 to nearly 4 mm, with an average length of 0.1 to 0.2 mm (Table 2.1). The sandstone is porous, but the porosity is heterogeneously distributed. Samples may have <10% porosity, but can also have 25% porosity, a variation that can influence the propagation of a shock wave and shock-metamorphic effects.

Chemical analyses of Coconino Sandstone exposed in the crater walls reflect the high concentration of quartz (See *et al.*, 2002). Silica (SiO₂) totals range from 96.99 to 97.54%, with an average value of 97.03 wt% (Table 2.2). The dominant impurity is Al₂O₃.

Because the Coconino Sandstone is such an important target component (representing ~70% of the stratigraphic depth of the excavation cavity; calculated from reconstruction by Roddy (1978)), its physical properties have been investigated experimentally (Table 2.1). Microscopic radial fracturing of Coconino occurs at tensile stresses of 30 MPa, which is a factor of 10 less than that of crystalline rocks (Ai and Ahrens, 2004) and approximately a factor of 10 higher than that measured in Kaibab samples that were recovered from the uplifted rim of the crater (Watkins and Walters, 1966).

Toroweap Formation. The Toroweap is a thin (up to 10 ft or 3 m) layer of sandstone and dolomite at the crater. Elsewhere in northern Arizona the unit can be thicker and composed of limestone with substantial amounts of yellow sandstone and reddish mudstone. The Toroweap formed on the floor of a shallow sea that migrated into the area from the west. The sandy portions represent a fluctuating ancient shoreline of western North America during the Permian.

Much more is known about the Toroweap (*e.g.*, McKee, 1938) than will be summarized here, because the formation is such a thin unit at the crater. In other areas of northern Arizona, the limited stratigraphic extent of the Toroweap is partly the result of erosion, because the contact between the Toroweap and overlying Kaibab is normally unconformable (McKee, 1938). At the crater, however, the limited stratigraphic thickness appears to reflect limited sedimentation, because Shoemaker (1974) describes the contact between the Toroweap and Kaibab as conformable.

The Toroweap is not quite as pure a quartz sandstone as the Coconino (Table 2.2). It contains additional Al_2O_3 and probably carbonate (reflected by enhanced Mg, Ca, and LOI abundances). The average silica abundance is 93.34 wt%.

Kaibab Formation. The Kaibab Formation at the crater is 260 to 265 ft (79 to 81 m) thick and composed of dolomite, dolomitic limestone, and thin calcareous sandstone horizons. Fossil shells are apparent (Fig. 2.3), although preservation is often poor because of diagenesis. One also finds preserved burrows of marine organisms that lived and fed in the sea-floor sediments. The Kaibab was deposited in a low-energy marine environment during the Permian over 250 million years ago.

The first report of a thick magnesian limestone (dolomite) was provided by Jules Marcou in a report from the 1853-54 expedition across northern Arizona that was led by Lieutenant Whipple (and, hence, popularly known as the Whipple Survey). Once called the Aubrey limestone, the unit was renamed the Kaibab limestone in 1910 when the USGS assigned the term Aubrey to a larger group of rocks that contained the magnesian limestone. A formal description of the Kaibab Formation was produced by McKee (1938), who measured sections throughout the region, including several sections in the vicinity of Meteor Crater. These sections occur in Walnut Canyon, in Padre Canyon at Hwy 66, at an outcrop ~10 miles southwest of Winslow, and at several locations along Clear Creek. McKee (1938, p. 8) briefly describes 150 ft of Kaibab at Meteor Crater, although Shoemaker (1960) measured 260 to 265 ft (79 to 81 m). In general, the Kaibab thins regionally from the north to south or northwest to southeast.

The Kaibab has three members that are designated alpha (α), beta (β), and gamma (γ) from the top to the bottom of the sequence (Fig. 2.1). The oldest member (γ) represents a time of advancing seas, the middle member (β) the time with the most extensive seas, and the youngest member (α) a time of receding seas. Sand units mixed with the uppermost (α) dolomite beds have been interpreted as a shoreline facies. They also erode in different fashions, as illustrated in the crater walls. The α and γ members form cliffs, whereas the β member often erodes to form a slope. In outcrop, one finds that diagenesis and weathering have conspired to produce a distinctive vuggy texture (Fig. 2.3) that is commonly called tear-pants for obvious reasons.

The Kaibab varies horizontally (geographically), which McKee (1938) divided into several facies. Facies 3 of the α member, facies 4 of the β member, and facies 3 of the γ member of the Kaibab occur at Barringer Crater (Fig. 2.4). Facies 3 of the α member contains trilobites (*Ditomopyge*), brachiopods (*Chonetes*, *Marginifera*, and *Productus bassi*), cephalopods (*Orthoceras* and *Plagioglypta*), gastropods (*Pleurotomaria*, *Euphemus*, *Bellerophon*, *Euomphalus*, *Bucanopsis*, and *Naticopsis*), and pelecypods (*Allorisma*, *Leda*, *Astartella*, *Pleurophorus*, *Nucula*, and *Schizodus*). Facies 4 of the β member contains brachiopods (*Pugnoides* and *Hustedia*), pelecypods (*Schizodus*, *Leda*, *Pleurophorus*, *Deltopecten*, and *Myalina*), and a long-stem echinoid (*Archaeocidaris*).

Because the Kaibab Formation is an important target unit at the crater, a NASA-sponsored drilling project recovered several cores from the rim of the crater and one core from a distant site unaffected by the impact event (Watkins, 1966). The latter was analyzed to provide pre-impact properties of the Kaibab (Watkins and Walters, 1966), which are summarized in Table 2.3 (drill core hole KC-2). These samples were recovered from Kaibab that was buried by a basalt lava flow associated with the SP cinder cone north of Flagstaff. This hole penetrated the same Kaibab α and β facies as those exposed at the impact site (Fig. 2.4). Measurements of recovered samples include porosity, permeability, compressive strength, tensile strength, Poisson's ratio, Young's modulus, the shear modulus, bulk modulus, and compressional and shear velocities.

Five diamond drill holes (DDH) were drilled along the southern crater rim (Fig. 2.5) to produce core samples. Two of the holes (DDH-3 and DDH-4) provide most of the data. The DDH-3 hole is located about 150 m south of the modern topographic rim of the crater. Drill hole DDH-4 is located 10 m south of the modern topographic rim of the crater. These holes penetrated impact ejecta, Moenkopi, and Kaibab, producing Meteor Crater Cores (MCC), although physical measurements were not always tied to these lithologies. Physical properties from a depth of 21 to 31 m (69 to 102 ft) in MCC-3 are listed in Table 2.4. Abrupt changes in Young's, shear, and bulk moduli suggest a lithologic change at a depth of ~29 m. Samples in the 29 to 31 m interval may be tied to Kaibab, because those values in the MCC-3 data (Table 2.4) are similar to those of Kaibab in the KC-2 data (Table 2.3).

Lithological control in core MCC-4 is better than that in MCC-3, as shown in Tables 2.5 and 2.6. In this core, the Kaibab begins at a depth of 21 m and continues to the bottom of the hole at 106 m. The thickness of the Kaibab in the core (~85 m) is similar to that measured in outcrop (79 to 81 m). The porosity in core samples ranges from ~2% (in dolomite) to ~30% (in some sandstone horizons). The permeability is equally variable. The MCC cores are curated in the USGS facility in Flagstaff.

Because Kaibab is composed of both dolomite and sandstone, carbonate fractions range from 20 to 97 vol% with quartz being responsible for most of the remaining material (Table 2.6; Haines, 1966). The carbonate fractions generally increase with stratigraphic height. Petrographically (*e.g.*, Fig. 2.2), dolomite occurs as (i) a microcrystalline matrix with smaller fraction of subangular to subrounded quartz grains, the latter of which are well sorted in size with an average diameter of 0.1 mm; (ii) microcrystalline clasts, in which grain diameters are ~0.01 mm and clast diameters range from 0.5 to 7 mm, with an average of 2.5 mm diameter; (iii) as anastomosing stringers, and (iv) coarse anhedral grains with diameters of 0.5 to 4 mm (Haines, 1966). The unit also contains minor plagioclase, microcline, and opaque minerals. Sericite occurs at one specific stratigraphic interval.

The composition of the Kaibab varies with stratigraphic position as the beds vary between different mixtures of sand and dolomite. Silica in 12 stratigraphic subdivisions of the Kaibab ranges from 16.36 to 57.43 wt%, with an average of 38.32 wt% (Table 2.2; See *et al.*, 2002). Dolomite (MgO, CaO, and CO₂) dominate the remainder of the material in the samples, but ~2 wt% Al₂O₃ and Fe₂O₃ also occur in the unit.

Moenkopi Formation. The strikingly red Moenkopi is the lower of two Triassic sedimentary sequences that dominate the Painted Desert province. Interestingly, the Moenkopi and the underlying yellowish Kaibab span the Permian-Triassic boundary, which represents the largest mass extinction event in the marine record during the Phanerozoic. The contact between these two formations is unconformable, however, so sediments deposited precisely at the P-T boundary do not exist and the sequence cannot be used to determine the cause of the P-T mass extinction event. One hypothesis being explored elsewhere in the world is that the P-T mass extinction, like the Cretaceous-Tertiary (K-T) event that claimed dinosaurs and 75% of the species on Earth, was caused by an impact event far larger in scale than that represented by Barringer Crater.

In the vicinity of the crater, the Moenkopi Formation is composed of two members: Wupatki and Moqui (McKee, 1954). An uppermost Holbrook Member and the overlying Chinle Formation do not occur in the vicinity of the crater, although the latter is abundant to the east, northeast, and north. Where covered by the Chinle (and, thus, not eroded), the Moenkopi can reach a thickness of 600 to 700 ft (183 to 213 m). In the walls of the crater, however, the Moenkopi ranges from only 7 to 30 ft (2 to 10 m).

Some of the beds of Moenkopi are a calcareous siltstone with an iron-rich matrix (Fig. 2.2). Within the MCC-4 core, quartz content of the siltstone varied from 55 to 80%, the remainder being composed of carbonate (Table 2.6). Porosity ranged from 7.5 to 18.2% and the permeability is low. Quartz is subrounded, equant, and well-sorted, with an average diameter of 0.1 mm (Haines, 1966). Some of the quartz recovered in the MCC-4 core has wavy extinction. Calcite is typically coarser (0.2 mm average) than the quartz. It also envelopes quartz and has anhedral margins, indicating a secondary origin. Diagenetic growth of calcite nodules, up to 6 mm, with embedded quartz occurs in some intervals (Haines, 1966). Other detrital grains include feldspar and unidentified opaque material in trace amounts. The matrix is very fine-grained and not well-characterized, but is stained by iron. The Moenkopi also contains fissile intervals that contain abundant sericite and muscovite (Haines, 1966).

Those mineral assemblages produce strata with compositions that are moderately silicious (averaging 65.30 wt% SiO₂) and also contain significant quantities of CaO (and presumably CO₂), Al₂O₃, Fe₂O₃, FeO, and K₂O (Table 2.2).

Moenkopi sediments were deposited on a coastal floodplain at the edge of a sea, similar to modern Louisiana. Many of the beds were deposited on intertidal mud flats, where several sedimentary features were produced (Fig. 2.6): desiccation (mud) cracks, longitudinal and interference ripple marks (the latter indicating conflicting current directions), sole marks, worm and shrimp burrows that wander across slabs, raindrop impressions, reptile and amphibian trackways, and abundant fossils. One of the most important fossil quarries in the Moenkopi is located at the crater (Camp *et al.*, 1947; Peabody, 1948; Welles and Cosgriff, 1965).

A University of California excavation team worked the site in the 1930's. The finds include tetrapod tracks with beaded skin surfaces and over 20 skulls. Trackways produced by multiple species of amphibians and reptiles were recovered (Fig. 2.7). Some of the skulls represented a new species of capitosaurid amphibian (Fig. 2.8). The type specimen from the quarry is called *Parotosaurus peabodyi* (Welles and Cosgriff, 1965).

The basal Wupatki Member begins with a red, thin (~1 ft thick), fissile shale, although this shale does not outcrop in all locations around the crater. The Wupatki Member is dominated by a cross-bedded, but relatively massive siltstone unit that outcrops as a rounded pink ledge-forming unit that often erodes into a series of orbicular knobs. The unit is 2 to 6 m (7 to 20 ft) thick. Outcrops of the Wupatki Member form a veneer on the landscape in the immediate vicinity of the crater.

Stratigraphically above the Wupatki Member is a dark red siltstone and sandstone unit about 8 m (25 ft) thick that is called the Moqui Member of the Moenkopi (Shoemaker and Kieffer, 1974). This unit is very fissile compared to the Wupatki member. The overturned sequence usually occurs in this unit, which, because of its fissile nature, makes it difficult to put one's finger on the contact between upright and overturned Moenkopi in the rim sequence. (See discussion in Chapter 7).

The Moenkopi is a well-known building stone at the crater and elsewhere in the region. The first museum at the crater (on northwest crater rim) and another building (on southwest ejecta blanket) were built of the stone, as was Harvey Nininger's American Meteorite Museum that existed along Highway or Route 66 from 1946 through 1953. In Flagstaff, the Babbitt Brothers Building (built between 1888 and

1891), Atlantic and Pacific Railroad Depot (1889), Old Main at Northern Arizona University (1894), and the Coconino County Courthouse (1894-95) are built with blocks of Moenkopi, which is often called Arizona Red Sandstone.

Topography at the time of impact

Pre-impact topography can be inferred from the existing topography, because the crater is so young and erosion may have been small. (See Chapters 8 and 15 for discussion of post-impact erosion.) A better measure of the topography at the time of impact, however, can be made using the topography visible in the crater walls and buried beneath impact ejecta. As discussed above, the Moenkopi in the crater walls varies in thickness from 2 to 10 m, implying topography up to 8 m. A drilling campaign through the ejecta blanket revealed buried topography with an average relief of 5 to 10 m and a maximum of 23 m (Roddy *et al.*, 1975). Grant and Schultz (1993) used ground-penetrating radar to image the subsurface on the west side of the crater. They found Moenkopi ridges beneath the ejecta blanket that were approximately 200 m wide and 5 m high. Gilbert (1896) also tried to reconstruct the topography before the crater formed. He extended existing topographic contours beyond the crater ejecta blanket towards crater center. His method assumes there has been little erosion since the crater formed. His restored topographic map suggests variation of about 3 m and the possibility of a small SW-NE stream channel at the point of impact.

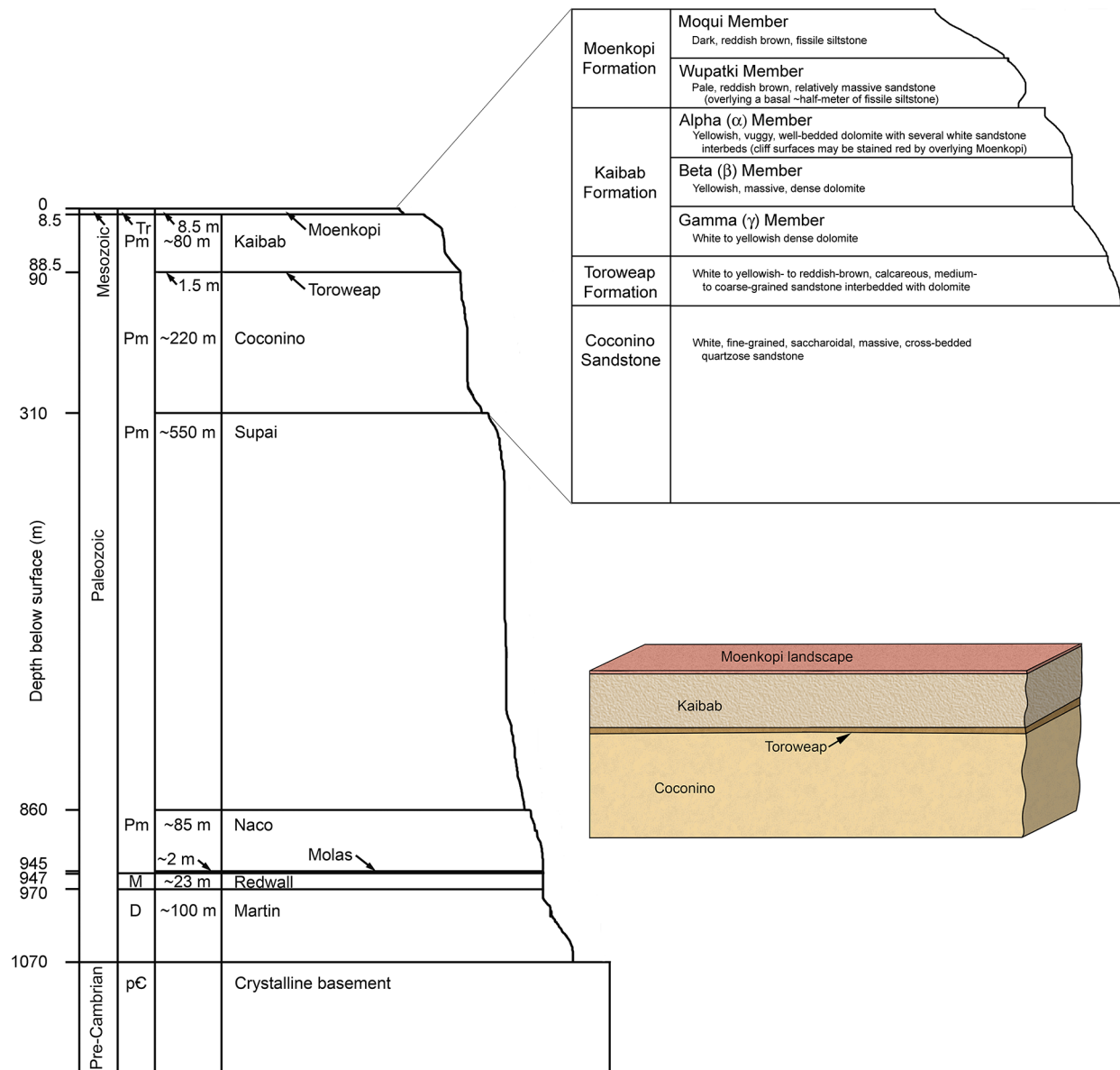


Fig. 2.1. Stratigraphy (left) of plateau sediments and the underlying crystalline basement in the vicinity of Barringer Crater, as a properly scaled function of depth below the surface. An unscaled blow-up of the four formations excavated to form the crater is also shown (upper right), with additional details of the members within those formations. Those strata will be represented with a color scheme (lower right) used in schematic diagrams throughout the guidebook.

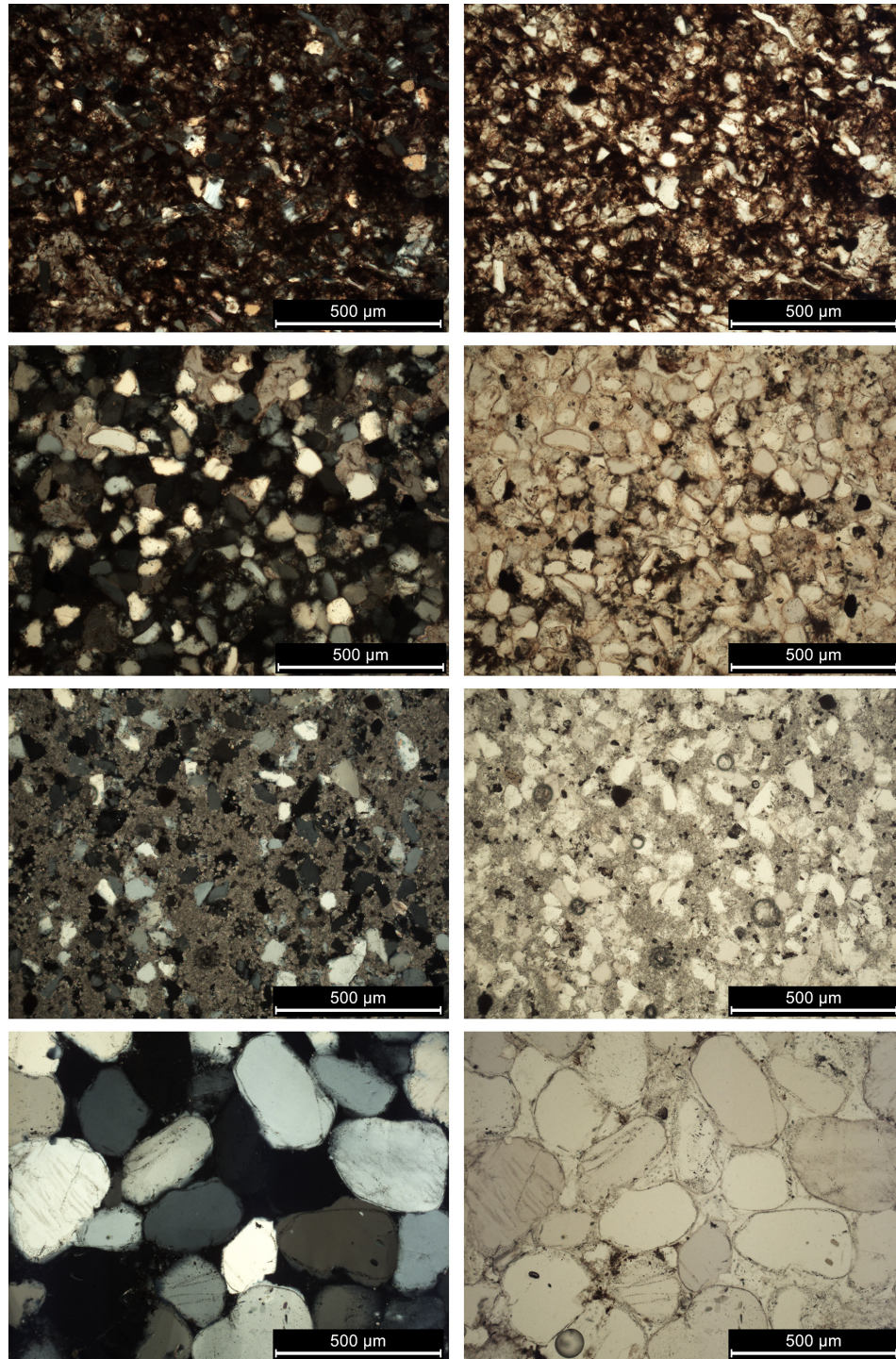


Fig. 2.2. Thin-section views of target lithologies in cross-polarized (left) and plane (right) light. The lithologies are in stratigraphic order. The Coconino is a coarse-grained quartz sandstone (bottom row). The Kaibab is a sandy carbonate. The Wupatki Member of the Moenkopi is a quartz siltstone with minor hematite and carbonate. The Moqui Member of the Moenkopi (top row) is a quartz-rich fissile siltstone with abundant hematite. Note that the quartz in the Moqui Members is more angular (less mature) than that in the Wupatki Member. The Toroweap (not shown), which occurs stratigraphically between the Coconino and Kaibab, has thin beds that alternate between sandstone and sandy carbonate. The scale bar in each image is 500 μm . Sample numbers are (bottom to top): MC52315-2, MC21205-17, MC101510-1, and MC101510-2.

Table 2.1. Physical properties of the Coconino Sandstone

Bulk density (g/cm ³)	Grain density (g/cm ³)	Quartz (vol%)	Feldspar (vol%)	Other minerals	Average grain size (mm)	Modal grain size (mm)	Porosity (%)	Crushing strength dry (dynes/cm ²) (10 ⁸)	Crushing strength H ₂ O sat. (dynes/cm ²) (10 ⁸)	Tensile strength (MPa)	Cp (km/s)	Cs (km/s)	Reference
2.26	2.67	-	-	-	-	-	15.2	3.20	3.71	-	-	-	1
1.99	-	97	3	-	0.12-0.15	-	24-25	-	-	-	-	-	2
1.98	2.67	97	3	tr	0.117	0.149	25	3.14	3.64	-	-	-	3
-	-	>95	<1	<4	0.19	-	9-18*	-	-	-	-	-	4
-	-	>95	<1	<4	0.19	-	<10**	-	-	-	-	-	4
2.08	-	-	-	-	-	-	-	-	-	17***	2.81	1.82	5
2.08	-	-	-	-	-	-	-	-	-	20****	2.81	1.82	5

* for massive Coconino sandstone beds

** for laminated Coconino sandstone beds

*** for strain rate of 1/2.4 x 10⁶/s**** for strain rate of 1/1.4 x 10⁶/sData tabulated as published. To compare the crushing and tensile strengths, 3.14 and 3.64 x 10⁸ dynes/cm² = 31.4 and 36.4 MPa

References: (1) Shoemaker et al., 1963; (2) Ahrens and Gregson, 1964; (3) Shipman et al., 1971; (4) Kieffer, 1971; (5) Ai and Ahrens, 2004

Table 2.2. Compositions of target lithologies at Barringer Meteorite Crater*

Formation	Stratigraphic thickness (m)	Cumulative target rock thickness (m)	SiO ₂	TiO ₂	Al ₂ O ₃	Fe ₂ O ₃	FeO	MnO	MgO	CaO	Na ₂ O	K ₂ O	P ₂ O ₅	LOI	Total
Moenkopi	12.3	12.3	65.30	0.43	7.67	2.63	1.88	0.06	0.99	10.17	0.02	1.42	0.11	11.05	99.10
Kaibab	73	85.3	38.32	0.12	2.02	2.05	0.16	0.03	11.57	19.31	0.03	0.51	0.19	27.29	99.57
Toroweap	1.4	86.7	93.34	0.08	2.02	0.73	0.17	0.01	0.88	1.07	0.00	0.38	0.06	2.14	100.16
Coconino	34.4	121.1	97.03	0.07	1.49	0.67	0.05	0.00	0.06	0.12	0.00	0.19	0.03	0.51	99.55

* See *et al.* (2002); analyses of individual stratigraphic intervals can also be found in that source.



Fig. 2.3. Fossils (a-c) and diagenetic features (d) in the Kaibab Formation. Fossils are apparent in the unit, but are often poorly preserved because of diagenetic alteration (a). Better examples can be found, albeit rarely, as illustrated by the two specimens (b-c) recovered by Meteor Crater Enterprises staff. Tear-pants weathering of Kaibab surfaces (d) reflects the mix of carbonate, sulphate, and silica fluids involved in the formation of the dolomite. In the alpha member of the Kaibab, a prominent diagenetically-altered bed is often described as the yellow vuggy unit or yellow vuggy dolomite. It is a useful marker bed. (e) Despite the diagenesis that has affected the Kaibab, rare fossils with better preservation exist, illustrating the heterogeneous nature of diagenesis. Southwest quadrant of the crater. A 33-cm-long hammer for scale.

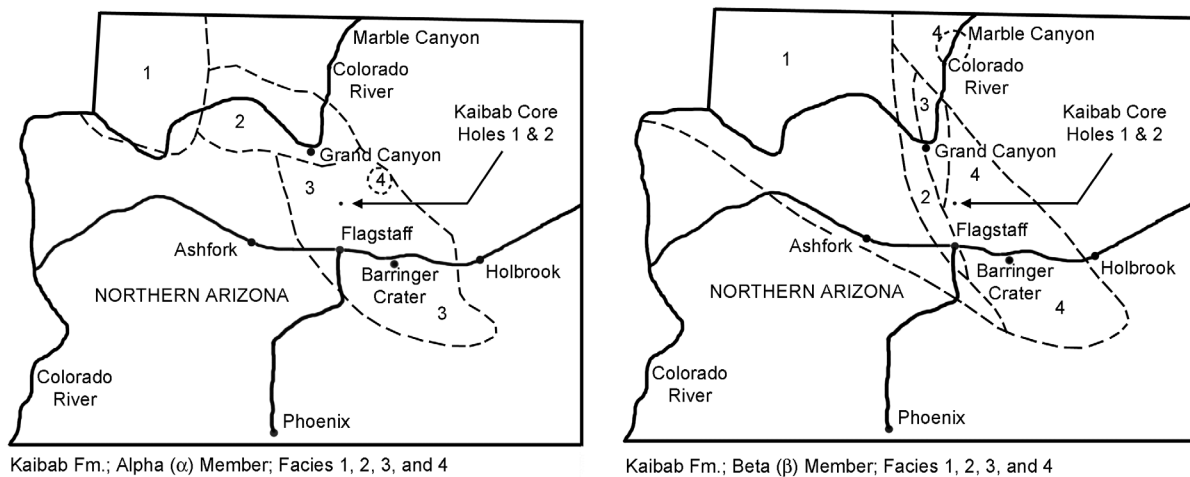


Fig. 2.4. The geographic distribution of facies within the Kaibab Formation of northern Arizona. Barringer Meteorite Crater occurs in Facies 3 of the Alpha Member (left panel) and Facies 4 of the Beta Member (right panel) of the Kaibab Formation. Drill core samples of Kaibab dolomite unaffected by the impact event were recovered in the vicinity of SP cinder cone, northwest of the crater. The Kaibab at that location represents the same facies as that at the impact crater. (Map modified from McKee, 1938.)

Table 2.3. Physical properties of the Kaibab Formation recovered from a site unaffected by impact event*

Drill core hole KC-2 (to represent unshocked Kaibab)
Located ~1 km west of the SP Crater Lava Flow

Depth (m)	Dry Bulk Density (g/cm ³)	Grain Density (g/cm ³)	Porosity (%)	Permeability (millidarcies)	Unconfined Compressive Strength (dynes/cm ²) (10 ⁸)	Tensile Strength (dynes/cm ²) (10 ⁷)	Poisson's Ratio	Young's Modulus (dynes/cm ²) (10 ¹¹)	Shear Modulus (dynes/cm ²) (10 ¹¹)	Bulk Modulus (dynes/cm ²) (10 ¹¹)	V _p (mps)	V _s (mps)
Static Measurements												
2.5	2.49	2.88	13.5	-	-	6.21	0.316	7.16	2.83	6.28	-	-
5	2.18	2.87	24	-	8.54	-	0.264	4.45	1.76	3.14	-	-
7.2	2.29	2.66	13.9	-	-	1.57	0.192	1.65	0.70	1.00	-	-
8.3	2.08	2.85	27	-	6.6	-	0.249	4.12	1.65	2.74	-	-
11.2	2.49	2.85	12.6	-	9.89	-	0.326	6.33	2.39	6.07	-	-
15.2	2.18	2.72	19.9	-	-	3.03	0.125	2.42	1.08	1.08	-	-
17.9	2.23	2.85	21.8	-	4.08	-	0.157	3.32	1.44	1.62	-	-
18.7	2.16	2.69	19.7	-	-	1.2	0.088	1.28	0.59	0.87	-	-
22.3	2.09	2.78	24.8	-	8.54	-	0.155	2.60	1.12	1.25	-	-
Avg	2.24	2.79	19.69	-	7.53	3.00	0.21	3.70	1.51	2.67	-	-
Std Dev	0.15	0.08	5.30	-	2.26	2.28	0.08	2.02	0.75	2.14	-	-
#	9	9	9	-	5	4	9	9	9	9	-	-
Pulse Measurements												
2.5	2.49	2.88	13.5	-	-	-	0.254	7.03	2.80	4.77	5800	3400
5	2.18	2.87	24	-	-	-	0.198	4.42	1.85	2.44	4800	2900
7.2	2.29	2.66	13.9	-	-	-	0.131	1.61	0.71	0.72	2700	1700
8.3	2.08	2.85	27	-	-	-	0.205	3.82	1.58	2.16	4500	2800
11.2	2.49	2.85	12.6	-	-	-	0.237	6.63	2.68	4.20	5600	3300
15.2	2.18	2.72	19.9	-	-	-	0.147	2.85	1.24	1.34	3700	2400
17.9	2.23	2.85	21.8	-	-	-	0.245	2.91	1.16	1.90	3900	2300
18.7	2.16	2.69	19.7	-	-	-	0.06	1.45	0.69	0.55	2600	1800
22.3	2.09	2.78	24.8	-	-	-	0.209	2.78	1.15	1.60	3900	2300
Avg	2.24	2.79	19.69	-	-	-	0.187	3.72	1.54	2.19	4167	2544
Std Dev	0.15	0.08	5.30	-	-	-	0.063	1.99	0.77	1.45	1129	602
#	9	9	9	-	-	-	9	9	9	9	9	9
Avg	2.24	2.79	19.69	-	7.53	3.00	0.198	3.71	1.52	2.43	4167	2544
Std Dev	0.15	0.08	5.30	-	2.26	2.28	0.073	1.95	0.74	1.79	1129	602
#	9	9	9	-	5	4	18	18	18	18	9	9

* Watkins and Walters (1966); Core type NX, which produces a 75 mm diameter hole and a 54.8 mm diameter core
Data is tabulated as originally published. However, to convert to modern units: 1 dyne/cm² = 0.1 pascals;
thus, a tensile strength of 3.00×10⁷ dyne/cm² = 3.00×10⁶ pascals = 3.00 MPa

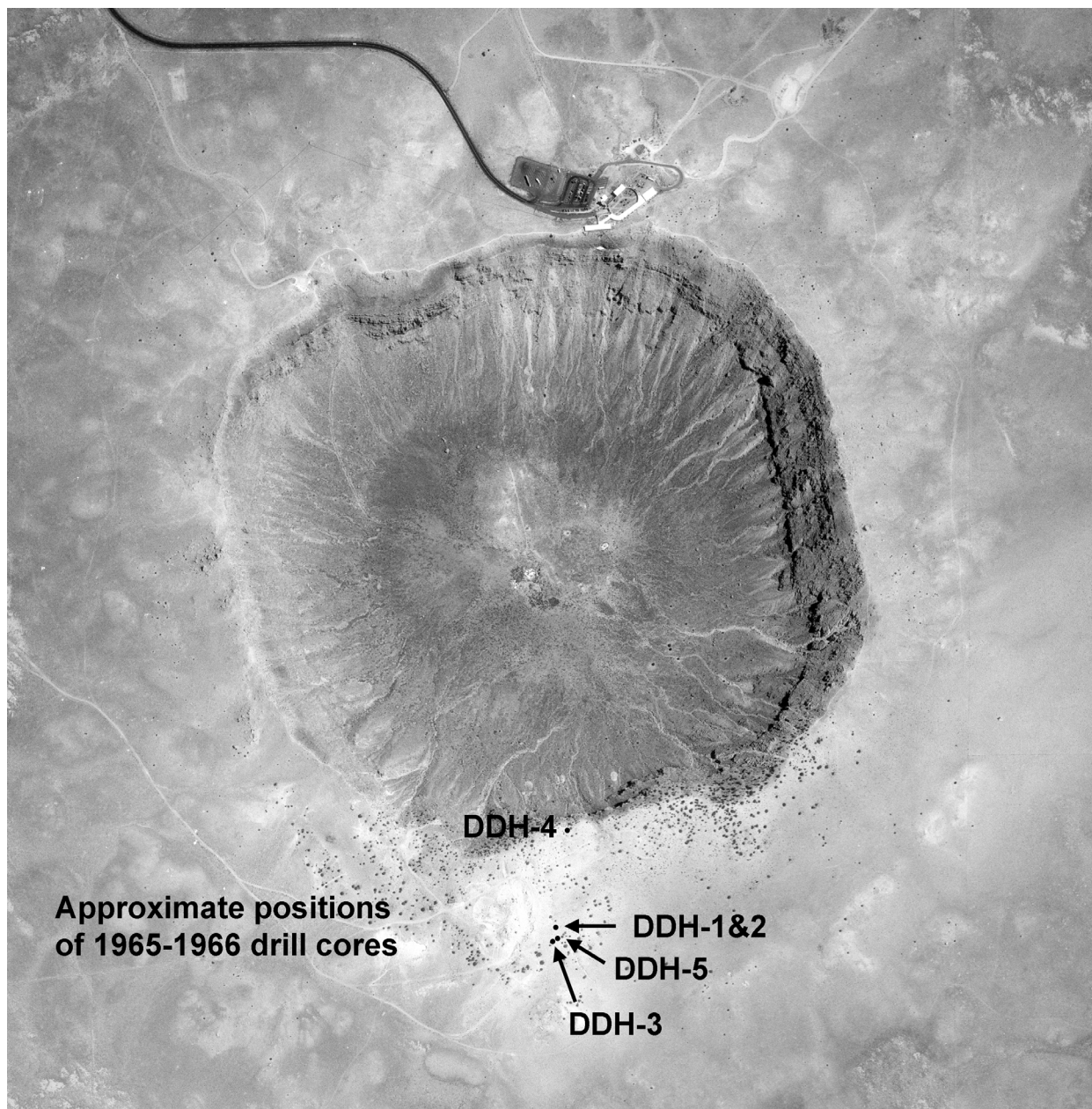


Fig. 2.5 The approximate locations of five boreholes drilled in 1965-1966. These boreholes were recorded as Diamond Drill Holes (DDH) 1 to 5 and produced Meteor Crater Cores (MCC) 1 to 5 that are currently curated by the USGS in Flagstaff. The DDH-4 borehole on the crater rim was drilled from January 26 to March 7, 1966 and the final DDH-5 borehole was drilled from March 18 to March 30, 1966. The cores were used to assess physical properties of rock around the crater (*e.g.*, Tables 2.4 – 2.6).

Table 2.4. Physical properties of crater lithologies

Meteor Crater Core MCC-3*

South side of crater, 150 meters from topographical crater rim

Depth (m)	Dry Bulk Density (g/cm ³)	Grain Density (g/cm ³)	Porosity (%)	Permeability (millidarcies)	Unconfined Compressive Strength (dynes/cm ²) (10 ⁶)	Tensile Strength (dynes/cm ²) (10 ⁷)	Poisson's Ratio	Young's Modulus (dynes/cm ²) (10 ¹¹)	Shear Modulus (dynes/cm ²) (10 ¹¹)	Bulk Modulus (dynes/cm ²) (10 ¹¹)	Vp (mps)	Vs (mps)
Static Measurements												
21.1	1.98	2.70	26.8	-	Sample too soft for testing	-	-	-	-	-	-	-
23.4	2.30	2.69	14.5	-	6.37	-	0.118	0.98	0.43	0.44	-	-
24.1	2.28	2.71	15.8	-	5.55	-	0.195	0.48	0.26	0.20	-	-
28.1	2.22	2.65	16.3	-	-	0.47	0.165	0.60	0.30	0.33	-	-
29.0	2.49	2.81	12.1	-	Sample too small for testing	-	-	-	-	-	-	-
29.8	2.30	2.81	18.1	-	8.68	-	0.172	3.83	1.95	1.63	-	-
30.0	2.14	2.90	26.3	-	-	2.16	0.220	1.88	1.12	0.77	-	-
30.3	2.41	2.82	14.6	-	6.44	-	0.197	4.55	2.50	1.90	-	-
30.4	2.44	2.80	12.9	-	-	2.94	0.135	6.23	2.84	2.74	-	-
Pulse Measurements												
Avg	2.28	2.77	17.5	-	6.76	1.86	0.172	2.65	1.34	1.14	-	-
Std Dev	0.16	0.08	5.4	-	1.34	1.26	0.036	2.24	1.09	0.96	-	-
#	9	9	9	-	4	3	7	7	7	7	-	-
21.1	1.98	2.70	26.8	-	-	-	0.239	0.37	0.14	0.23	1470	860
23.4	2.30	2.69	14.5	-	-	-	0.235	1.01	0.41	0.64	2260	1330
24.1	2.28	2.71	15.8	-	-	-	0.194	1.98	0.83	1.07	2180	1340
28.1	2.22	2.65	16.3	-	-	-	0.052	1.28	0.61	0.47	2410	1660
29.0	2.49	2.81	12.1	-	-	-	-	-	-	-	3850	-
29.8	2.30	2.81	18.1	-	-	-	0.179	3.75	1.59	2.98	4210	2630
30.0	2.14	2.90	26.3	-	-	-	0.304	3.06	1.17	2.59	4940	2620
30.3	2.41	2.82	14.6	-	-	-	0.222	0.71	0.29	0.43	1840	1100
30.4	2.44	2.80	12.9	-	-	-	0.143	5.23	2.28	2.45	4750	3060
Avg	2.28	2.77	17.5	-	-	-	0.196	2.17	0.92	1.36	3101	1825
Std Dev	0.16	0.08	5.4	-	-	-	0.075	1.70	0.73	1.13	1331.132	825
#	9	9	9	-	4	3	8	8	8	8	9	9
Avg	2.28	2.77	17.5	-	6.8	1.86	0.185	2.40	1.11	1.26	3101	1825
Std Dev	0.16	0.08	5.4	-	1.3	1.26	0.059	1.91	0.91	1.02	1331	825
#	9	9	9	-	4	3	15	15	15	15	9	9

* Watkins and Walters (1966): Core type NX, which produces a 75 mm diameter hole and a 54.8 mm diameter core Data is tabulated as originally published. However, to convert to modern units: 1 dyne/cm² = 0.1 pascals; thus, a tensile strength of 1.86×10⁷ dyne/cm² = 1.86×10⁶ pascals = 1.86 MPa

Table 2.5. Physical properties of crater lithologies and a lithologic assessment

Meteor Crater Core MCC-4*

South side of crater, 10 meters from topographical crater rim

Depth (m)	Sub- surface elevation (m)	Dry Bulk Density (g/cm ³)	Grain Density (g/cm ³)	Porosity (%)	Permeability (millidarcies)	Lithologic Assessment**
8.2	1731.8	2.18	2.85	23.5	17.3	Ejecta - Sandstone
9.3	1730.7	2.17	2.93	25.9	2.5	Ejecta - Sandstone
10.7	1729.3	2.19	3.63	18.2	1.3	Moenkopi - Sandstone
16.0	1724.0	2.44	2.89	15.6	<0.4	Moenkopi - Sandstone
20.0	1720.0	2.48	2.68	7.5	<0.4	Moenkopi - Shaly Sandstone
21.0	1719.0	2.68	2.73	1.8	<0.4	Kaibab - Dolomite
21.4	1718.6	2.63	2.74	4.0	<0.4	Kaibab - Calc-dolomite
22.0	1718.0	2.61	2.68	2.6	<0.4	Kaibab - Dolomite
29.5	1710.5	2.44	3.04	20.0	<0.4	Kaibab - Dolomite
34.0	1706.0	2.18	2.81	23.2	26.8	Kaibab - Dolomite
37.5	1702.5	2.22	3.03	26.7	4.7	Kaibab - Dolomite
47.6	1692.4	2.39	2.99	20.1	3.8	Kaibab - Sandstone and Dolomite
54.4	1685.6	2.15	3.05	29.5	25.1	Kaibab - Sandstone and Dolomite
61.0	1679.0	2.33	2.74	15.0	1.5	Kaibab - Sandstone and Dolomite
68.0	1672.0	2.17	2.89	24.9	16.8	Kaibab - Sandstone and Dolomite
75.8	1664.2	2.14	2.72	21.3	16.7	Kaibab - Sandstone and Dolomite
81.7	1658.3	2.12	2.82	24.8	30.6	Kaibab - Sandstone and Dolomite
87.5	1652.5	2.15	3.02	28.8	37.6	Kaibab - Sandstone and Dolomite
91.5	1648.5	2.24	2.68	16.7	4.2	Kaibab - Sandstone and Dolomite
94.8	1645.2	2.35	2.91	19.2	1.7	Kaibab - Dolomite
98.3	1641.7	2.13	2.87	25.8	33.3	Kaibab - Sandstone
101.9	1638.1	2.12	2.65	22.0	80.7	Kaibab - Sandstone
105.9	1634.1	2.18	2.65	18.3	15.5	Kaibab - Sandstone
Avg		2.29	2.87	18.9	~13.9	
Std Dev		0.18	0.21	8.1	~19.1	

* Watkins and Walters (1966); core type NX, which produces a 75 mm diameter hole and a 54.8 mm diameter core

** Haines (1966); the elevation data for these lithologies are also calculated from a 1,740 m collar height provided by this author

Table 2.6. Physical and mineralogical properties of the Moenkopi and Kaibab formations.

Moenkopi Properties

Meteor Crater Core MCC-4*,**

South side of crater, 10 meters from topographical crater rim

Depth	Sub-surface elevation	Carbonate	Quartz	Cavities	Insoluble residue (mostly qtz)	Dry Bulk Density	Grain Density	Porosity	Permeability
(m)	(m)	(vol%)	(vol%)	(vol%)	(wt%)	(g/cm ³)	(g/cm ³)	(%)	(millidarcies)
10.7	1729.3	-	-	-	-	2.19	3.63	18.2	1.3
11.4	1728.6	25	75	-	71.7	-	-	-	-
16.0	1724.0	-	-	-	-	2.44	2.89	15.6	<0.4
16.1	1723.9	45	55	-	-	-	-	-	-
20.0	1720.0	-	-	-	-	2.48	2.68	7.5	<0.4
20.1	1719.9	20	80	-	-	-	-	-	-

* Haines (1966); vol% determined visually in thin-section; wt% insoluble residue after acid dissolution of carbonate

** Watkins and Walters (1966)

Kaibab Properties

Meteor Crater Core MCC-4*,**,***

South side of crater, 10 meters from topographical crater rim

Depth	Sub-surface elevation	Carbonate	Quartz	Cavities	Insoluble residue (mostly qtz)	Dry Bulk Density	Grain Density	Porosity	Permeability
(m)	(m)	(vol%)	(vol%)	(vol%)	(wt%)	(g/cm ³)	(g/cm ³)	(%)	(millidarcies)
21.0	1719.0	97	3	Tr	-	2.68	2.73	1.8	<0.4
21.4	1718.6	95	2	3	-	2.63	2.74	4.0	<0.4
22.0	1718.0	95	5	-	-	2.61	2.68	2.6	<0.4
22.6	1717.4	-	-	-	24.6	-	-	-	-
22.7	1717.3	65	35	-	-	-	-	-	-
23.3	1716.7	40	60	-	-	-	-	-	-
29.5	1710.5	-	-	-	-	2.44	3.04	20.0	<0.4
29.9	1710.1	75	10	15	-	-	-	-	-
30.2	1709.8	-	-	-	5.1	-	-	-	-
32.6	1707.4	70	10	20	-	-	-	-	-
34.0	1706.0	-	-	-	-	2.18	2.81	23.2	26.8
37.5	1702.5	75	25	-	-	2.22	3.03	26.7	4.7
45.5	1694.5	75	20	5	-	-	-	-	-
45.5	1694.5	-	-	-	41.4	-	-	-	-
47.6	1692.4	-	-	-	-	2.39	2.99	20.1	3.8
53.4	1686.6	75	10	15	-	-	-	-	-
54.4	1685.6	-	-	-	-	2.15	3.05	29.5	25.1
61.0	1679.0	35	65	-	-	2.33	2.74	15.0	1.5
61.0	1679.0	-	-	-	73.7	-	-	-	-
67.5	1672.5	75	10	15	-	-	-	-	-
68.0	1672.0	-	-	-	-	2.17	2.89	24.9	16.8
69.8	1670.2	55	45	-	-	-	-	-	-
75.6	1664.4	-	-	-	69.6	-	-	-	-
75.7	1664.3	44	55	1	-	-	-	-	-
75.8	1664.2	-	-	-	-	2.14	2.72	21.3	16.7
81.7	1658.3	-	-	-	-	2.12	2.82	24.8	30.6
81.8	1658.2	55	43	2	-	-	-	-	-
87.4	1652.6	60	40	-	-	-	-	-	-
87.5	1652.5	-	-	-	-	2.15	3.02	28.8	37.6
91.5	1648.5	-	-	-	-	2.24	2.68	16.7	4.2
91.5	1648.5	-	-	-	48.5	-	-	-	-
91.6	1648.4	60	35	5	-	-	-	-	-
94.8	1645.2	-	-	-	-	2.35	2.91	19.2	1.7
95.0	1645.0	25	75	-	-	-	-	-	-
95.0	1645.0	-	-	-	76.4	-	-	-	-
98.3	1641.7	-	-	-	-	2.13	2.87	25.8	33.3
98.5	1641.5	40	60	-	-	-	-	-	-
98.5	1641.5	-	-	-	66	-	-	-	-
101.5	1638.5	-	-	-	71.5	-	-	-	-
101.9	1638.1	-	-	-	-	2.12	2.65	22.0	80.7
103.0	1637.0	20	75	5	-	-	-	-	-
105.9	1634.1	-	-	-	-	2.18	2.65	18.3	15.5
106.0	1634.0	40	60	-	-	-	-	-	-
106.0	1634.0	-	-	-	56.5	-	-	-	-

* Haines (1966); vol% determined visually in thin-section; wt% insoluble residue after acid dissolution of carbonate

** Watkins and Walters (1966)

*** Kaibab is logged from 21 to 106 m for a total of 85 m, which is comparable to Shoemaker's measured thickness of 79-81 m.

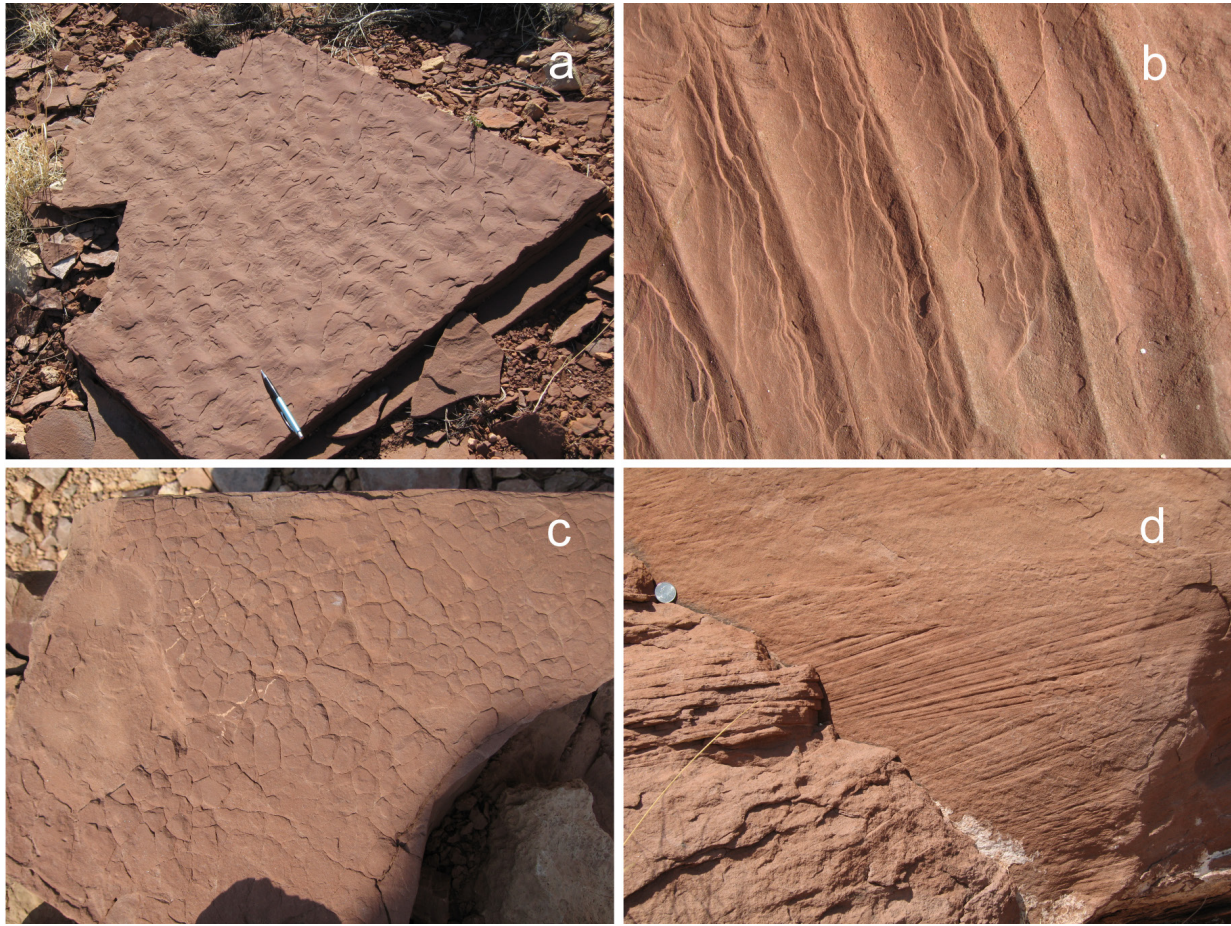
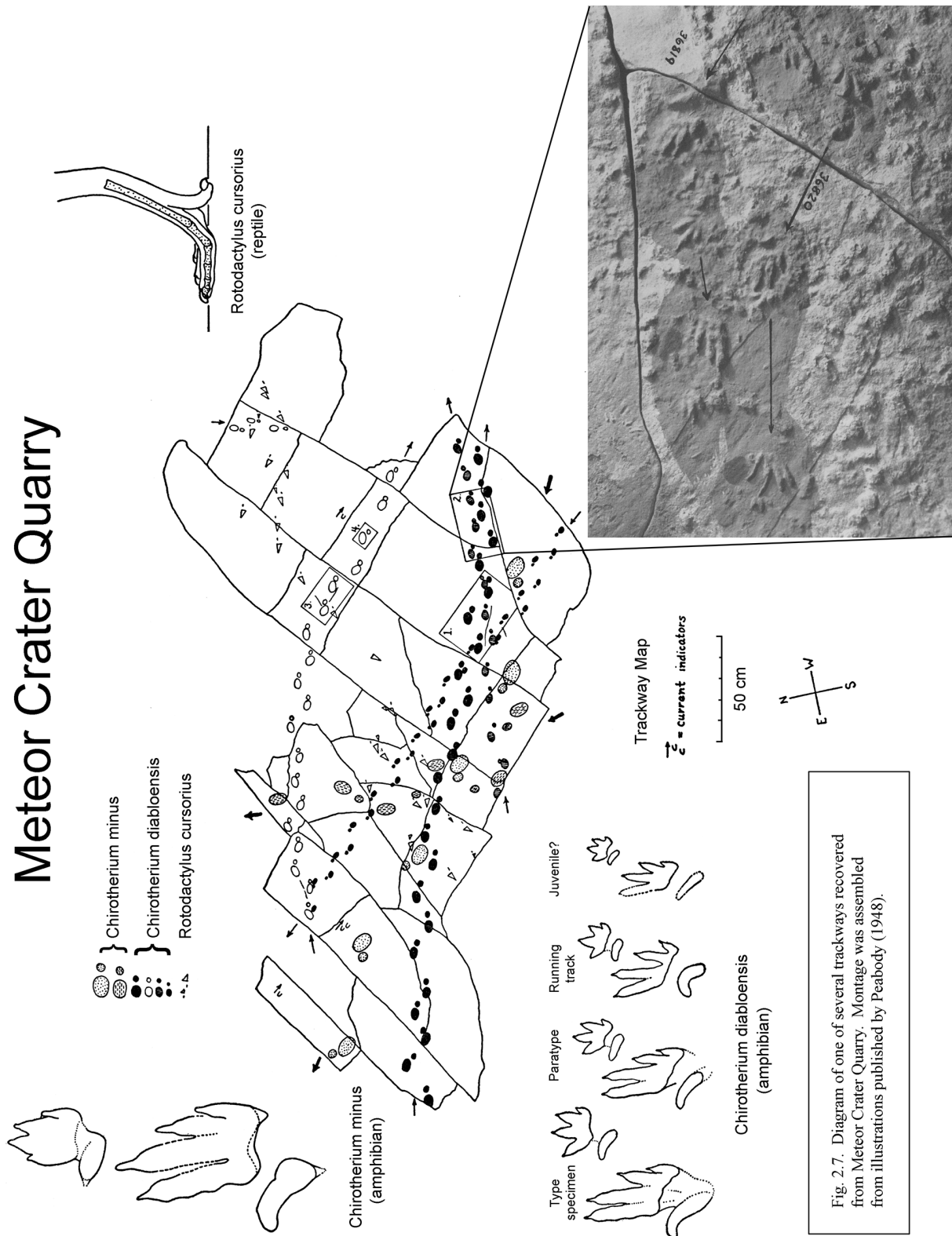


Fig. 2.6. Moenkopi sediments were deposited in a shallow-water coastal environment that was above wave base. A variety of wave-driven ripple marks, representing several types of current velocities, occur in the Moenkopi as illustrated in an oblique view of a slab (a) and an overhead view of another slab (b). Water often receded, producing dessication or mud cracks (c). Particularly important for the interpretation of the crater rim structure is the geopetal nature of cross-bedding exposed in the Moenkopi (d). This particular block is oriented normally, although the cross-beds in other blocks in the crater rim may be overturned.

Meteor Crater Quarry



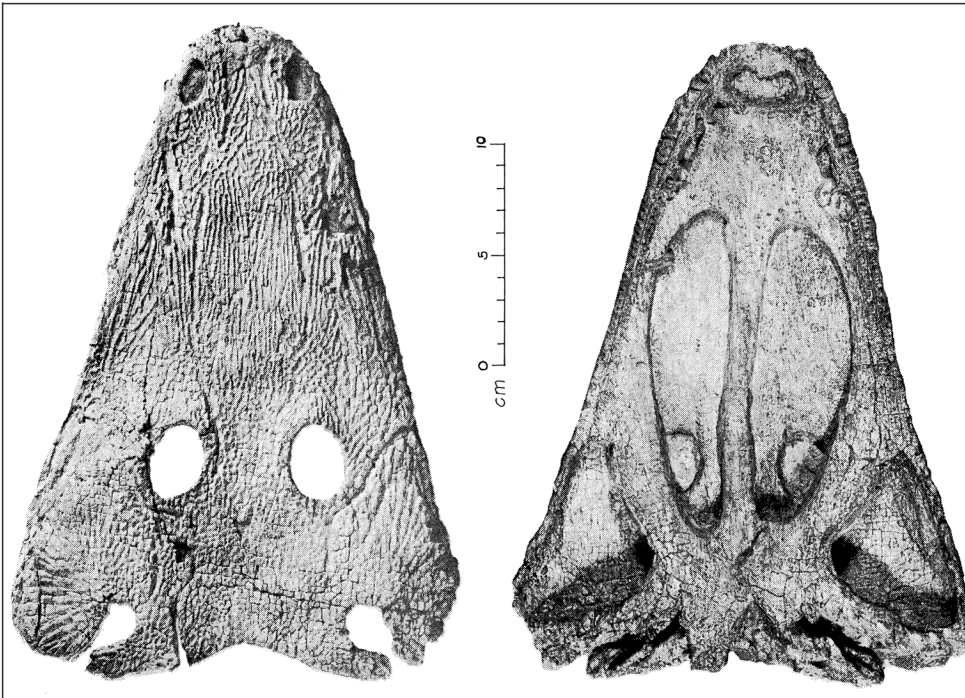
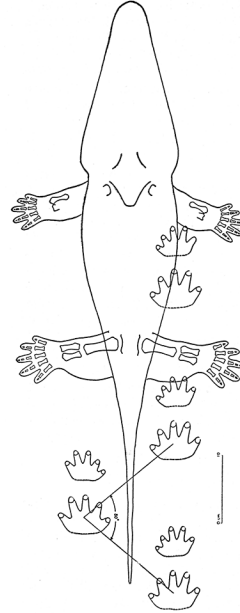
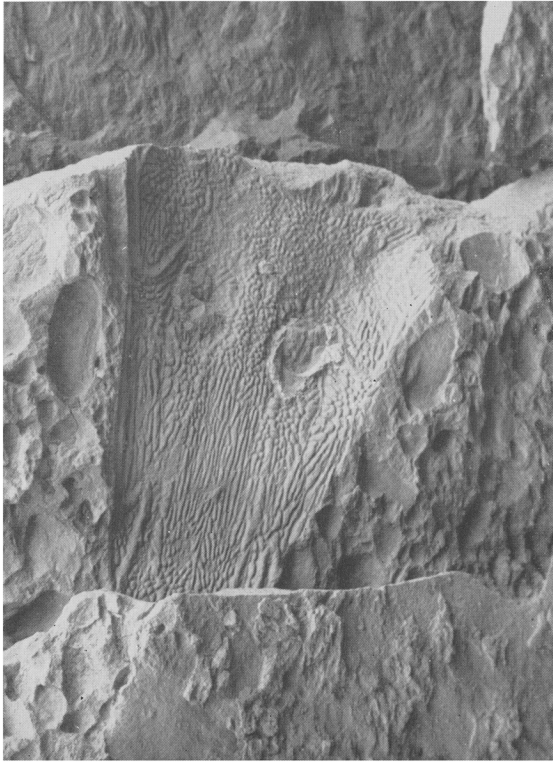


Fig. 2.8. A nearly complete skull of a new species of Labyrinthodont Family Capitosauridae that was recovered from the Moenkopi Formation in the Meteor Crater Quarry. This new species, *Parotosaurus peabodyi*, was described by Welles and Cosgriff (1965). The midline length of the skull is 28.3 cm (11.1 in). Teeth are 6 mm long. There is room for 80 teeth in the peripheral row on each side of the maxillary, although Welles and Cosgriff suggest only half these were functional on the living animal. This is the type specimen for the species, but more than 20 skulls were recovered from the quarry, the largest of which had a midline length of 43.8 cm (17.2 in).



Impression of capitosaurid skulls were also recovered from a nearby quarry in Moqui Wash, including an example that occurs with shale pebbles in a fluvial fore-set bed (top photograph from Peabody, 1948). A sketch of a capitosaurid and the tracks it produced at Moqui Wash is also shown (bottom illustration, also from Peabody, 1948).

Meteor Crater Quarry

3. Pre-impact Structure



The impact occurred in a relatively flat lying ($4 \pm 1^\circ$; Kumar and Kring, 2008) sequence of Permian and Triassic sediments. There are two structural interpretations of the region. One is the classic interpretation of Shoemaker (1960) and another is a more recent rendering produced by a USGS mapping project (Ulrich *et al.*, 1984; Bills *et al.*, 2004).

Folds in the region are evident, but subtle. According to Shoemaker (1960), synclines and anticlines occur within a few kilometers of the crater and the impact occurred on a gentle anticlinal bend or monoclinical fold that runs approximately NNW-SSE (Fig. 3.1). Although a thin-veneer of Moenkopi occurs at the crater, it is absent around Canyon Diablo and over a vast region to the west of the crater. The presence of Moenkopi at the impact site is fortuitous, however, because it greatly assists in interpretation of crater formation (as discussed in Chapter 7). In contrast, others (Ulrich *et al.*, 1984; Bills *et al.*, 2004) mapped a series of small anticlinal ridges (Fig. 3.2) that run nearly perpendicular to the anticlinal bend of Shoemaker (1960). These structural features were measured using plane table and alidade techniques (George Ulrich and Richard Hereford, personal communication, 2015) and are considered robust.

Target sediments are cross-cut by NW-SE trending normal faults (Fig. 3.1) that may be many kilometers long, but only have offsets of a few to about 30 m (Shoemaker, 1987). The region is also cross-cut by a strong set of joints that can extend for hundreds of meters (Kelley and Clinton, 1960), with pre-impact orientations of that seem to have formed a conjugate NW-SE and weaker SW-NE. Roddy (1978) measured the joints within a few kilometers of the crater and found the most prominent orientations in Moenkopi are 293° (with a range of 290 to 297°) and in Kaibab are 304° (with a range of 301 to 308°). A secondary set is oriented 23° (with a range of 10 to 32°) in the Moenkopi and 30° (with a range of 17 to 36°) in the Kaibab. As Roddy (1978) describes, these joints remain vertical in canyon walls down to depths of 100 m in the region and have been implicated in the unusually square shape of the impact crater (Shoemaker, 1960, 1987), as discussed further in the next chapter. Indeed, based on that finding, polygonally-shaped craters on other planetary surfaces (*e.g.*, on the Moon (Eppler *et al.*, 1983) and Mars (Öhman *et al.*, 2008)) have been used to study target structural histories.

Meteor Crater is the best terrestrial example of pre-impact tectonic structures affecting impact crater processes. Those joints are visible in the crater walls (Kumar and Kring, 2008), but in orientations that may have been affected by impact. It can be difficult to see the pre-impact joints in the surrounding bedrock unaffected by the impact, because access to the land is closed. Fortunately, some of those features are illuminated with indicator plants that form long lines of vegetation (*e.g.*, sagebrush, snakeweed, rabbitbrush, groundsel, cliffrose, grama) along joints, providing an easy-to-observe method to study their orientations and spatial properties (Kring, 2015). These vegetation lines are adjacent to the paved road from the interstate highway to the crater visitor center and can even be seen from a moving vehicle.

Aerial and ground-level views of the vegetation lines are shown in Fig. 3.3. The joints capture water in the arid environment, providing the necessary sustenance for plant growth. These lineations occur beyond the edge of the ejecta blanket. Where vegetation lines are present, bedrock is either exposed or covered with only a thin shaly scree or organic-poor soil.

The bearings of 80 vegetation lines were measured (Kring, 2015). Thirty-eight bearings were measured adjacent to Meteor Crater Road on the north side of the crater, which is on the west limb of the monocline that Meteor Crater may penetrate (per Shoemaker's mapping, Fig. 3.1). Forty-two bearings were measured on the south side of the crater on the east limb of the monocline. The monocline, which affects dips by only a degree or less in the immediate vicinity of the crater (Roddy, 1978), had little effect on the bearings. The measurements confirm the dominant joint set runs NW-SE (Shoemaker, 1960;

Roddy, 1978). A smaller number of minor cross-joints exist, which are generally oriented NE-SW. These weaker cross-sets have short lengths (≤ 5 m) and are bounded by the longer NW-SE-trending joints.

On the south side of the crater the spacing of the dominant joints ranges from 2.00 to 6.40 m and the spacing of minor cross-joints ranges from 1.55 to 3.42 m (or far greater where they were virtually non-existent). On the north side of the crater the spacing of dominant joints ranges from 1.35 to 7.20 m.

The bearings are illustrated in a rose diagram (Fig. 3.3). The 61 measurements of the dominant joint set produce a mean bearing of $114 (294) \pm 1.1^\circ$ (corrected for a magnetic declination of 10.6° E at the time of the measurements). The bearings of the joints in the weaker set are between 25 and 30° . These values are consistent with Roddy (1978), which included 24 rock surface measurements and 158 stereophotographic measurements on both Moenkopi and Kaibab surfaces. In the subset of Moenkopi data, Roddy (1978) reported an average bearing for $293^\circ (=113^\circ)$ with a range from 290 to 297° . A small fraction of the joints has other orientations.

An additional set of measurements were made in the first Moenkopi ridge beyond the continuous ejecta blanket on the NNW side of the crater (Kring *et al.*, 2015). There, 206 measurements indicate a dominant joint bearing of $117 (297) \pm 2.1^\circ$ (Fig. 3.4). It is important to note that the joints highlighted by surficial vegetation lines and atop this ridge are in the Moenkopi, which forms a thin veneer over the thicker Kaibab Formation and Coconino-Toroweap sandstones. To evaluate the consistency of the joint orientations, a small number (37) of measurements were made in Kaibab along Canyon Diablo at Two Guns, NNW of the crater. The dominant orientation in that Kaibab is $125 (305) \pm 7.6^\circ$ (Fig. 3.4).

The bearing of the dominant joint set measured with vegetation lines corresponds to high points on the crater rim (Fig. 3.3) that are bounded by radial corner faults (Kring, 2015). In the SE quadrant, the orientations of the joints correspond to a high topographical point (elev. 5,706 ft) on the rim on a block that is bounded by two major faults along which the block rose far higher than the adjacent crater walls (see Fig. 18.18 and 19.13 for more details of block movement). In the NW quadrant, the orientations of the joints correspond to Barringer Point (elev. 5,723 ft), beneath which an extra section of Kaibab was thrust into the crater wall (see Fig. 6.3 and 6.4 elsewhere in the guidebook). A cross-section of the crater along the bearing that connects those two points is illustrated in Chapter 4 (Fig. 4.2). As nicely shown in Fig. 2a of Kumar and Kring (2008) and Fig. 8b of Poelchau *et al.* (2009), both the NW and SE blocks are structurally higher than the adjacent blocks in the crater wall.

The orientation of the weaker joint set corresponds (albeit less precisely) with the two highest topographic points in the NE and SW quadrants. In the NE quadrant, the joint bearing corresponds roughly to Moon Mountain, adjacent to the museum, and beneath which lay an extra section of Kaibab that was thrust into the crater wall. In the SW quadrant, the joint bearing corresponds with a major fault in that quadrant, but is directly adjacent to the highest point (elev. $\sim 5,740$ ft) along the entire crater rim. Another thrust wedge of Kaibab exists beneath that topographically high point.

Thus, the joints appear to have had two effects on crater formation. They made it easier for material to be excavated parallel to joints (*e.g.*, Gault *et al.*, 1968; Poelchau *et al.*, 2009; Eppler *et al.*, 1983), enlarging the radial dimensions of the crater in those directions. As illustrated previously (Fig. 12 of Poelchau *et al.*, 2009), the joint sets also made it easier for the crater walls to be uplifted parallel to the joints and allowed thrust wedges to be added in the crater walls, both of which contributed to topographically high blocks along the crater rim. Relatively higher erosion rates along the faults that bounded those uplifted blocks (Kumar and Kring, 2008; Kumar *et al.*, 2010) further accentuated the non-radial symmetry of the crater rim. A preliminary numerical model of the process was reported by Plesko (2013).

The west and east boulder fields of ejecta, originally noted by Barringer (1905), bisect the major and minor joint orientations. Although this distribution could reflect the trajectory of the impactor, it is also possible that excavation flow, oblique to both sets of joints, created Kaibab blocks with dimensions of the joint spacing and deposited them relatively close to the crater rim, because excavation flow was not as effective in that direction.

Before departing this topic, two other observations should be noted. First, the joint spacing can vary between the units. In Walnut Canyon National Monument, where a section of Kaibab and Coconino is exposed 47 km from bedrock effects of impact, the joint spacing in Kaibab is generally 1 to 3 m and in Coconino generally 5 to 10 m.

Second, measurements by Kumar detected a different orientation in the target Kaibab (Kumar and Kring, 2008), posing a problem for the interpretation of excavation flow described above. While that work reported fracture orientations in Moenkopi similar (*e.g.*, a mean of $\sim 110^\circ$, albeit with a spread from 80 to 140°) to those inferred from the vegetation lines (see their Fig. 3f), the orientation in Kaibab appears to be $\sim 74^\circ$ and, thus, perpendicular to the east and west crater walls and parallel to the north and south crater walls. Kumar seems to have detected a pre-impact structural orientation coincident with the axes of anticlines mapped (Fig. 3.2) across the target area.

Other features in the area can have slightly different orientations. For example, a ~ 15 m-wide and >25 m deep fissure in Kaibab northwest of the crater (Kring and Andes, 2015) has a bearing of 165° . It is possible, perhaps even likely, that fissures and related cavernous openings occurred in the target rocks, potentially affecting local transmission of shock and rarefaction waves and, consequently, heterogeneities in excavation flow. Other nearby slots in the Kaibab, enhanced by dissolution of the dolomite, have orientations of 145° , 132° , and 130° , although the latter then swings to a bearing of 112° .

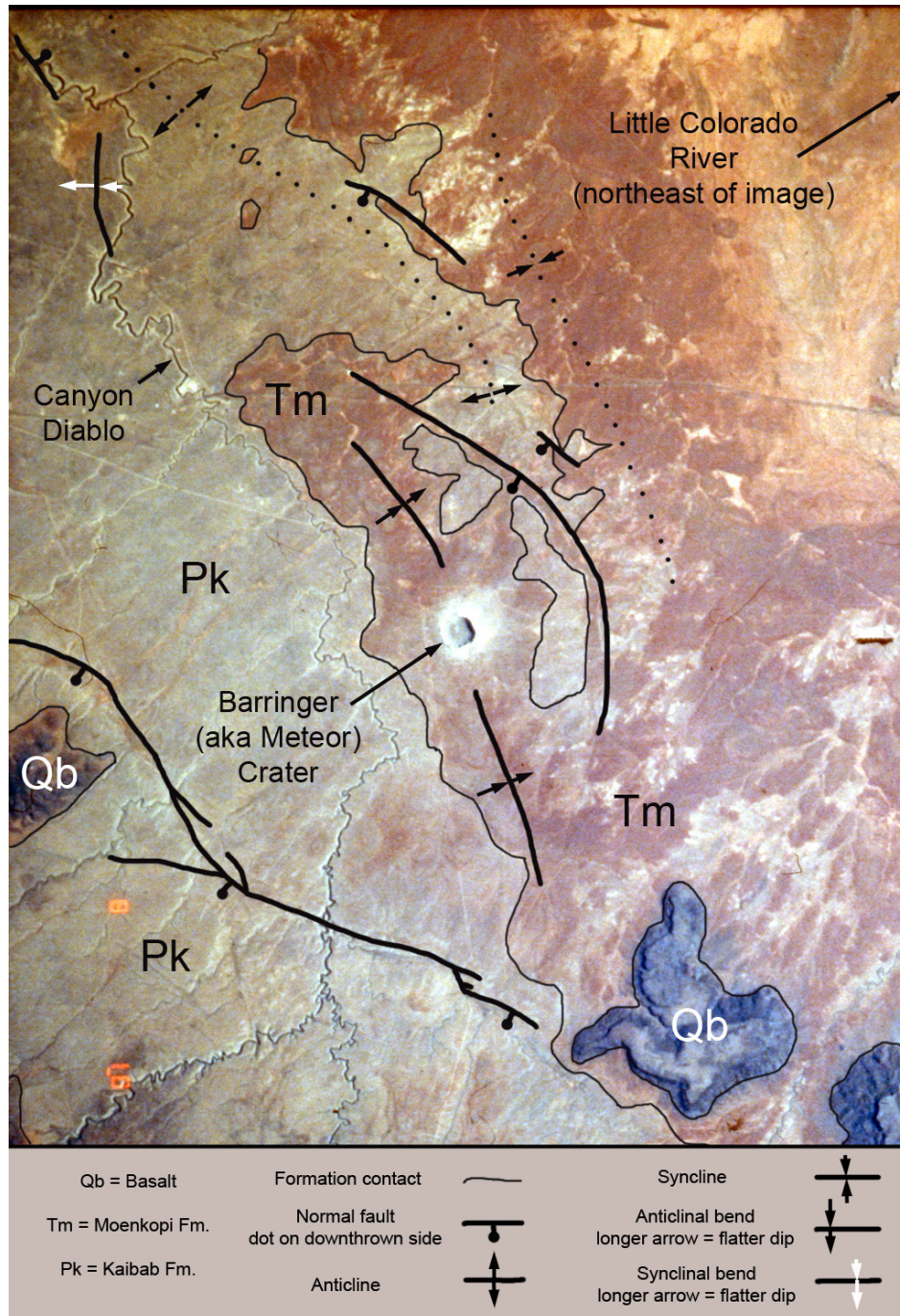


Fig. 3.1. Bedrock geologic map for the region around Barringer Meteorite Crater (a. k. a. Meteor Crater) imprinted on an image taken from Space Shuttle Columbia (a cropped version of image #STS040-614-058). The formation contacts of Moenkopi (Tm) and Kaibab (Pk) are approximate, because Moenkopi is thin and becomes patchy in the vicinity of the crater. No effort was made to represent Pleistocene and Holocene alluvium or to distinguish Quaternary basalt (Qb) from talus derived from the basalt. Pleistocene impact ejecta and older subsurface lithologies exposed in the crater walls are also not mapped at this scale. Solid-line normal faults are mapped as seen in the image. Solid-line anticlines are inferred from geologic exposure and are consistent with the geologic map of Shoemaker (1957-1958, as published in 1960). Anticlinal and synclinal bends are taken from Shoemaker (1960); solid lines represent more precise location of axes than do dotted lines.

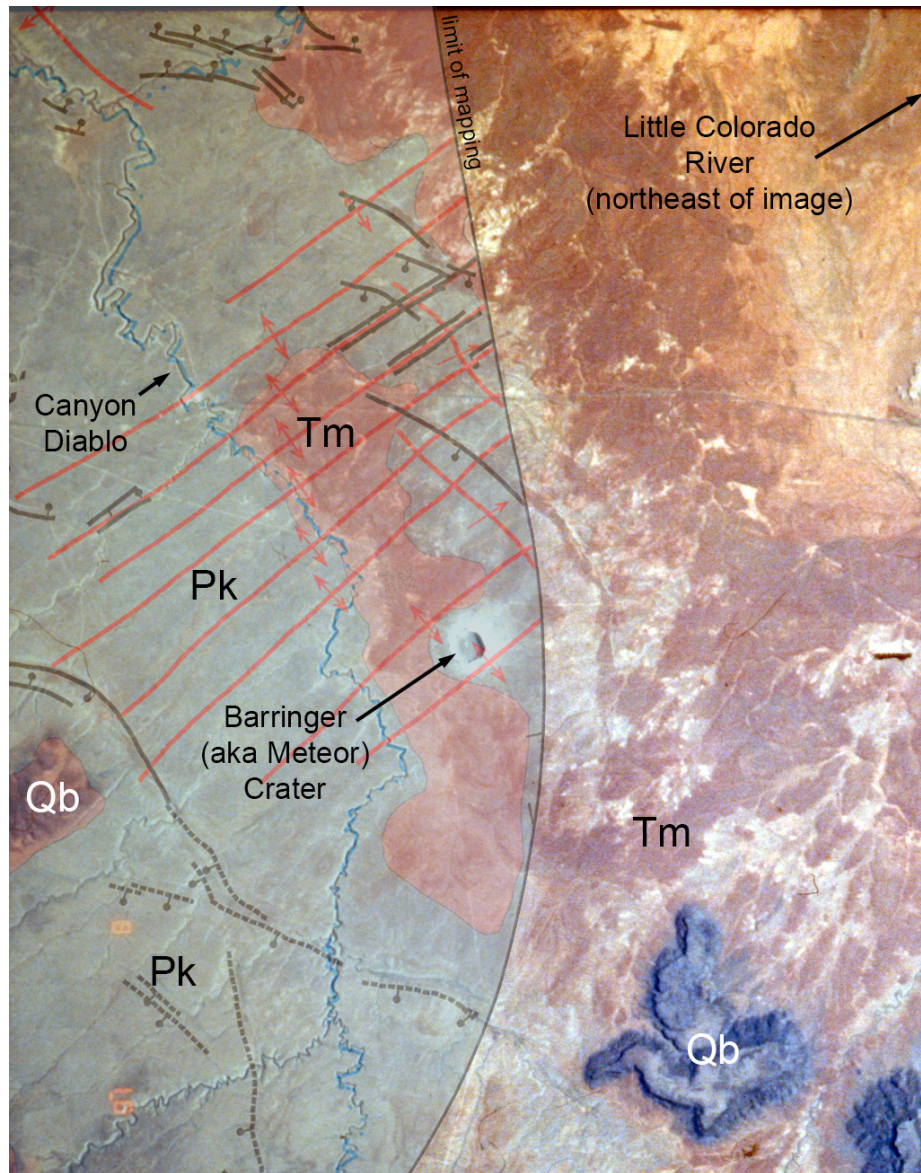


Fig. 3.2. Structural map for the region around Barringer Meteorite Crater (a. k. a. Meteor Crater) imprinted on an image taken from Space Shuttle Columbia (a cropped version of image #STS040-614-058). The structural details here are derived from Bills *et al.* (2004) and Ulrich *et al.* (1984). In contrast to the structure shown in Fig. 3.1, a set of southwest-northeast trending anticlines (shown in red) cross the impact site. The drainage system that feeds from the southwest to the Little Colorado River in the northeast roughly parallels the anticlinal structures. George Ulrich and Richard Hereford (personal communication, 2015) say the structures were measured with plane table and alidade techniques. Symbols in the figure are the same as those in Fig. 3.1. A slight mis-match in the overlay of the structural map and the Space Shuttle Columbia image is likely do to oblique nature of the shuttle photograph. The map was not distorted to fit the image (or vice versa).

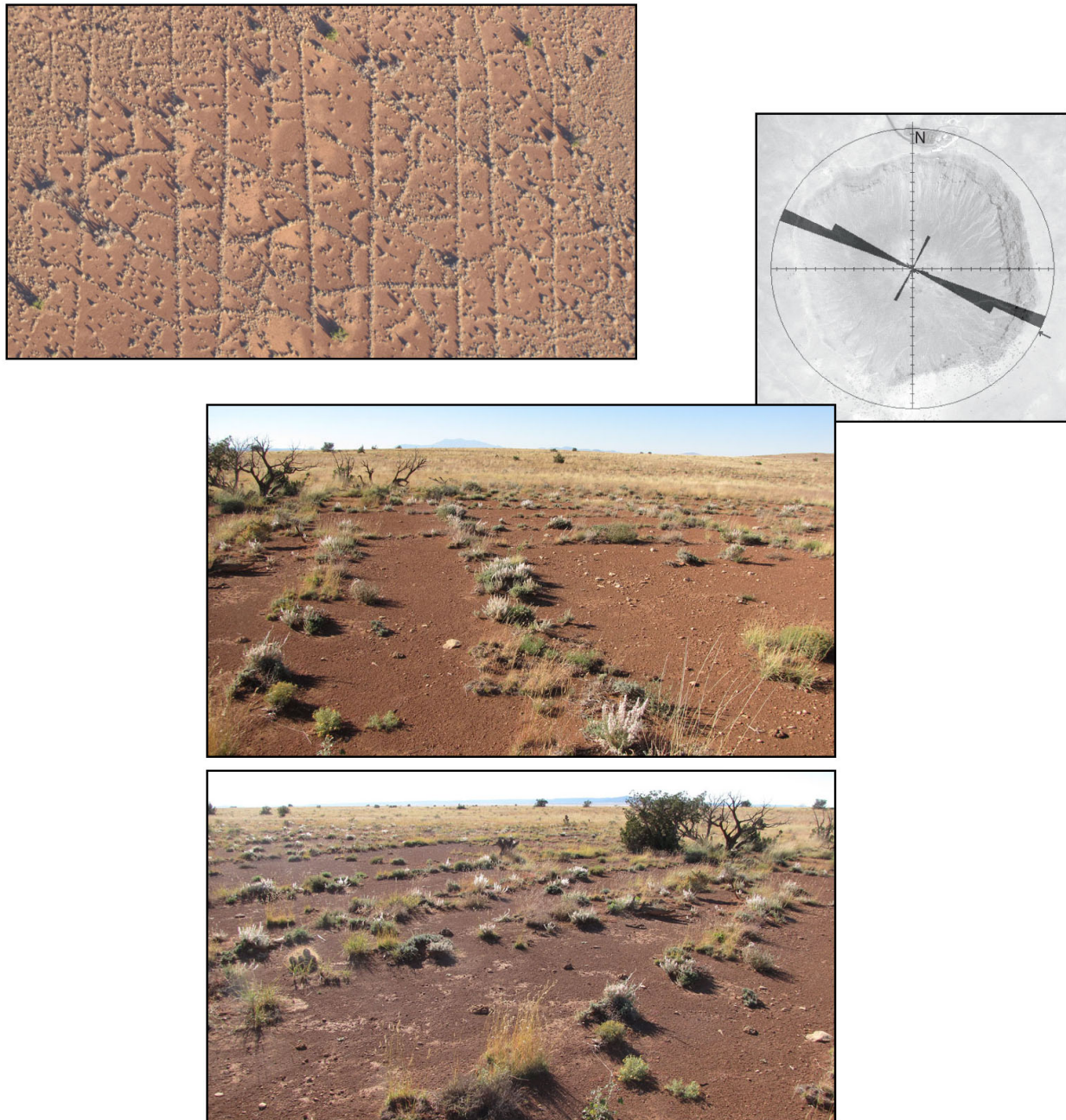


Fig. 3.3. (upper left) Aerial view of vegetation lines in bedrock Moenkopi that surrounds Barringer Meteorite Crater. Spacing between the lines is typically a few meters. The dominant NW-SE joint set is oriented vertically in this photograph. (center) Roadside views of several vegetation lines on shaly Moenkopi that trend away from viewer (center top) and lie oblique to the viewer (center bottom). (upper right) Rose diagram with the bearings of vegetation lines, which are the same as the bearings of joints in outcrops of Moenkopi. Eighty measurements with a dominant set at $114\ (294) \pm 1.1^\circ$ and a weaker set at 25 to 30° . The rose diagram is shown on top of a picture of the crater to illustrate the relative orientation of the joints and the crater.

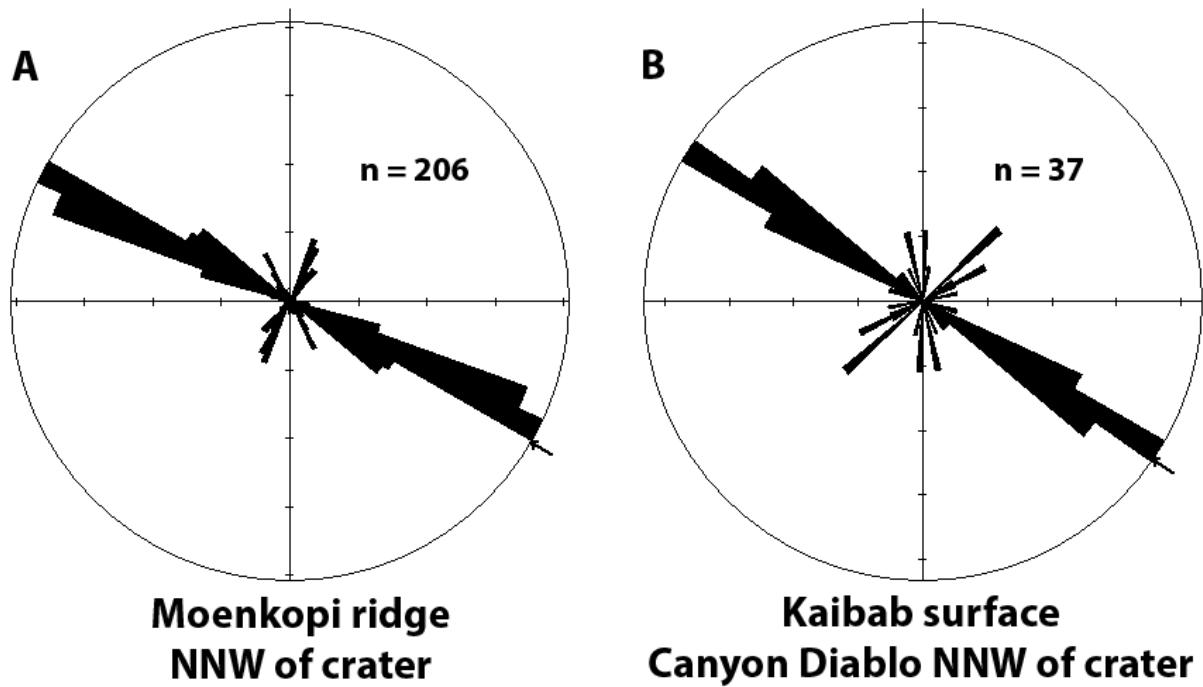


Fig. 3.4. In addition to the bearings of joints in Moenkopi inferred from vegetation lines (Fig. 3.3), 206 measurements were made on a 6-m-high ridge of Moenkopi NNW of the crater (Kring *et al.*, 2015). The measurements of the bearings of those joints indicate a dominant set at $117 \pm 2.1^\circ$ and two minor sets at 20 to 40° and 150 to 155° . That orientation is similar to the $114 \pm 1.1^\circ$ inferred from vegetation lines (Fig. 3.3). Another set of joints was measured on a Kaibab surface along the Canyon Diablo at Two Guns NNW of the crater. Although there are fewer measurements ($n = 37$ rather than 206), the dominant orientation is also similar, $125 \pm 7.6^\circ$. All measurements were corrected for the magnetic declination at the time the measurements were made.

4. Barringer Meteorite Impact Crater



Barringer Meteorite Crater has a diameter of ~1.2 km (Fig. 4.1 and 4.2). It is topographically defined by a rim that rises 30 to 60 m above the surrounding plain and a bowl-shaped depression that is ~180 m deep. The upper crater walls have average slopes of ~40 to ~50°, although they also include vertical to near-vertical cliffs (Fig. 4.2 and 4.3). The crater floor is below the surrounding plain, which is a feature that distinguishes Barringer Crater from most volcanic structures where craters are perched on volcanic summits (*e.g.*, cinder cones, shield volcanoes, and stratovolcanoes). Volcanic maars are the principal exception.

The crater has a simple bowl-shaped morphology, which is the classic “simple” crater morphology that characterizes impact craters that are $\lesssim 2$ km diameter in sedimentary targets and $\lesssim 4$ km diameter in crystalline targets (under Earth’s gravity). In contrast, larger “complex” craters may have central peaks, central peak rings, modification zones where the crater walls extensively collapse, and possibly external structural deformational rings.

Tear faults cross-cut the crater in four areas, producing “corners” that give the crater a squared shape in plan view, rather than a circular one. The region was cross-cut by a strong set of SE-NW joints and a weaker set of SW-NE joints prior to impact (Shoemaker, 1960; Roddy, 1978), which are generally thought to have been activated into tear faults during the excavation phase of the crater forming event.

Shoemaker (1960) produced the definitive geologic map of the crater (Fig. 4.4), which illustrates the target lithologies in the crater walls and the redistribution of target lithologies in a surrounding ejecta blanket. It also shows that the upper crater walls and uplifted crater rim are composed of Coconino, Toroweap, Kaibab, Moenkopi, and debris from those units. Debris also occurs within the crater in the form of complex breccia deposits that Shoemaker (1960) mapped as three units: authigenic breccia, allogenic breccia, and mixed debris.

Authigenic breccias are monomict, intraformational breccias that are caused by disruptive shear within formations (*e.g.*, Kaibab). This type of breccia is present along faults that cross-cut the crater walls and crater rim.

Allogenic breccias are sometimes dominated by components from a single formation, but in other cases are composed of fragments from multiple formations. These breccia deposits are displaced, however, having flowed down crater walls. They also contain shock-melted Coconino (lechatelierite) and meteoritic debris. Remnants of these breccias occur on upper crater walls, but they also flowed downward to form a thick breccia lens at the bottom of the crater (Fig. 4.5). Shoemaker (1974) suggested that downward flows of allogenic breccia converged on the crater floor to form a “central peak” beneath Silica Hill. Where exposed in crater walls, the allogenic breccia is dominated by debris from the Kaibab Formation. In the breccia lens on the crater floor, however, the breccia is dominated by fragments from the Coconino Formation. As illustrated in the W-E cross-section of Fig 4.5, the lens of allogenic breccia on the crater floor is generally believed to conform to a hemispherical transient crater. As discussed below, however, the subsurface extent of the breccia is still uncertain.

Stratigraphically above and resting on the allogenic breccia is a unit Shoemaker (1960) called “mixed debris.” This unit contains material from all four formations, including all five stages of shocked Coconino sandstone (as defined by Kieffer, 1971), plus meteoritic debris. In one of the deposits that outcrops along the east crater wall, Shoemaker (1974) also described lapilli of shock-melted Kaibab

dolomite. Although not described by Shoemaker, I have also found fragments of vesicular mixed melts in that breccia. Shoemaker interpreted this mixed debris unit to be fall-out material. That is, material blasted into the atmosphere above the crater and then re-deposited on top of the crater after it was excavated. Shoemaker (1960) only found this material within the crater. Exposed patches are found along the upper crater walls and a 10.5 m (35 ft) thick layer sits on top of the allogenic breccia on the crater floor. This latter unit appears to be normally size-sorted (*i.e.*, coarse fragments on the bottom of unit and finer fragments at top of unit; Shoemaker, 1974). Mixed debris was probably deposited beyond the crater rim on top of the ejecta blanket, although it has since been stripped away by erosion, except in a small number of locations (Chapter 18; Kring *et al.*, 2012). Fragments of the type of material found in the mixed debris unit are found in younger (post-impact) alluvium terraces that surround the crater.

Post-impact erosion and sedimentation has modified the crater interior, which is evident in both the aerial image of the crater (Fig. 4.1) and the geologic map (Fig. 4.4). Talus and finer debris components have collected at the base of the crater walls, reducing the steepness of the crater walls. Although the topography of the crater is still dramatic, erosional reduction of the rim height, shallowing of the crater wall slope, and sediment filling of the crater floor has reduced the observable size of the crater.

A ~30 m (100 ft) section of lake sediments covers the allogenic breccia in the center of the crater. Moving radially outward from crater center, these lake sediments are interfingered with alluvium being shed from the crater walls. After the impact event the climatic conditions became increasingly arid and the lake evaporated, producing a ~1.6 m (10 ft) thick sequence of playa beds (Shoemaker, 1974).

The erosional processes that produced the talus and alluvium deposits continue today, as evident from the large Kaibab boulders strewn about the crater floor and continuous loss of the fragile allogenic and mixed breccia deposits that cling to the crater walls. Multiple cubic yards of these scientifically valuable breccias are sometimes lost each year.

To help readers correlate the surface geologic units described above with the observable landscape, I have produced an overlay (Fig. 4.6) of Shoemaker's geologic map and an aerial photograph.

Our ability to extend this surface geology downward into the subsurface is greatly enhanced by extensive drilling and deep shafts that were excavated during mining operations at the crater, augmented by later subsurface imaging using several geophysical techniques.

Between 1903 and 1908, the Standard Iron Company drilled 28 holes in the crater floor (maximum depth 1,085 ft or 323 m), excavated 7 shafts on the crater floor (maximum depth of 222 ft or 68 m), excavated 6 shafts on the southern ejecta blanket, excavated 1 shaft on the northern ejecta blanket, excavated 1 shaft just beyond the northern ejecta blanket, and excavated several trenches in the ejecta blanket at sites distributed around the entire crater (Barringer, 1910). Fairchild (1907) reports there were more than 50 pits and trenches on the external slopes of the crater.

Many of the boreholes were reamed with a toothed, hardened steel bit that produced a 2½ inch core, if the rock had sufficient structural integrity (Fairchild, 1907). Because of its inherent weakness, most material in the breccia lens was washed upward by flowing water in the form of disaggregated chips and sand. Only large boulders in the breccia lens and bedrock below the breccia lens were recovered in core form (*e.g.*, in holes 4, 6, 7, and 8). Unfortunately, none of that core material survives.

The boreholes drilled in the crater floor indicate the breccia lens bottoms at a depth of 600 to 700 ft (180 to 210 m) (Table 4.1), which corresponds to the base of the Coconino (Shoemaker, 1960; Roddy, 1978). These boreholes provided the data used to estimate the depth of the breccia lens in Shoemaker's

cross-section of the crater (Fig. 4.5). According to Shoemaker (1974), the Supai Formation was recovered at depths exceeding 700 ft (210 m), whereas Fairchild (1907) reports red beds of the Supai were encountered at depths of 830, 860, and 870 ft (253, 262, and 265 m) beneath the crater floor. Seismic refraction data (Ackermann *et al.*, 1975) is consistent with a breccia lens that bottoms ~190 m beneath the crater floor. The seismic refraction data also suggest the target rocks are fractured beneath the ejecta blanket to distances of 900 m beyond the crater rim and to a depth of at least 800 m below the crater floor and possibly to the crystalline basement.

Holsinger wrote in a letter (as reported by Fairchild, 1907) that a large slab of Coconino slumped down the crater wall during the formation of the breccia lens. Several boreholes northeast of the main shaft encountered a block of the sandstone at depths ranging from 160 to 200 ft before punching through it. The slab is 250 to 400 ft (76 to 122 m) thick, dips at an angle of 40°, and covers 4 to 5 acres (1.6 to 2.0×10^4 m²). Approximately 100 ft of breccia is above the slab and more than 100 ft is below it. Meteoritic material occurs in the breccia beneath the slab.

The United States Refining, Smelting, and Mining Company drilled the deepest exploration hole at the crater on the south rim in 1920-1922 and drove a nearly 400-ft long adit or drift into the wall of the crater when the drill stem broke and drill tools were lost at a depth of 311 ft. After the drilling tools were recovered at the end of the adit, drilling continued until a final depth of 1,376 ft (419 m) was reached, which is approximately 827 ft (252 m) (per Hager, 1953) beneath the level of the crater floor. Not only did the adit solve the drilling problem, it also penetrated meteorite-bearing mixed debris between the talus and crater wall, suggesting additional mixed breccia may survive beneath a protective sheath of talus if needed for future research.

Interestingly, the deep borehole encountered several hundred feet of breccia with Ni traces and an apparent concentration of meteoritic debris in the final 30 feet of the hole (Barringer, 1924; see also Table 4.2, which is a log of this borehole). If the borehole was plumbed vertically, then this breccia lies far outside the transient crater. Thus, there is a discrepancy between the symmetrical view of the breccia lens represented by Fig. 4.5 and the borehole data of Barringer. Shoemaker was aware of the drill hole data and the discrepancy it represented, but was unable to resolve the conundrum.

Some possible solutions: (a) breccias and the transient cavity extend beneath the south rim, which, as interpreted by Barringer, might imply something about the trajectory of the impacting asteroid; (b) the drill hole may have curved towards the crater center while descending and essentially intersected a crater cavity with a geometry similar to that inferred by Shoemaker in Fig. 4.5; or (c) a vein, network of veins, or some other horizon of meteoritic debris and/or breccia was injected into the wall of the transient crater cavity and into the surrounding Coconino bedrock. The first solution defies our current understanding of transient crater cavities, unless strong asymmetry was caused by an oblique impact. The second solution is uncomfortable, because the adit that intersects the drill hole at a depth of 311 feet suggests the hole is vertical. The hole would have had to curve tremendously at greater depths to pierce the breccia lens depicted in Shoemaker's cross-section. The third option is also uncomfortable, because the breccia beneath the rim is several hundred feet thick, which, if taken at face value, implies an injection of material far larger than that considered feasible in the past. I suspect (c) is the correct solution.

Seismic refraction (Ackermann *et al.*, 1975) and gravity (Regan and Hinze, 1975) data paint an independent image of the breccia zone. A model derived from the seismic refraction data suggests the breccia lens is symmetrical, concentrated in the center of the crater, and does not, at depth, extend to the diameter of the crater (Fig. 4.7). A model of the gravity at the crater also suggests the breccia lens is concentrated in the center of the crater and does not, at depth, extend to points beneath the crater rim (Fig. 4.7). An asymmetric feature is recognized on the south side of the crater, but it suggests the breccia

lens is less wide (not wider) towards the south. Thus, these geophysical models are generally consistent with Shoemaker's cross-section through the breccia lens.

The seismic refraction data, however, also suggests a possible explanation for the breccia and meteoritic components in the 1,376 ft borehole. It is clear that the walls of the transient crater (that is, the bedrock beyond the breccia lens) was highly fractured by the impact event. The seismic model includes fractured bedrock to within ~150 m of the bottom of the 1,376 ft borehole. It is possible that the breccia encountered in the borehole represented fractured wall rock, rather than the breccia lens. It is also possible that the traces of meteoritic material represent veins of material injected into that crater wall, producing the Ni-traces seen several times while the drill passed through the fractured wall rock. This requires, however, the injection of meteoritic material nearly 300 m beyond the walls of the transient crater with a radius of ~500 m and depth of ~300 m. The magnitude of brecciation may have been greater than that depicted in Fig. 4.7, if either the zone of fracturing was wider than in the model or if the drill curved towards the crater center. Thus, one might be able to explain the occurrence of breccia and meteoritic material in the hole and still be consistent with estimated dimensions of the breccia lens. The remaining problem is the rather thick (Barringer estimated 30 ft thick) zone of oxidized asteroid at the bottom of the hole. This would seem to require an unusually large vein of injected material in the crater wall. A completely satisfying explanation will probably escape us, unless a series of new boreholes, with coring capabilities, are drilled on the crater floor and crater rim. I hypothesize shatter cones exist along the path from the crater wall to the bottom of the 1,376 ft borehole. Interestingly, traces of impactor material have been found on the surfaces of shatter cones in other impact craters (*e.g.*, Schmieder *et al.*, 2015).

Additional drilling occurred after the 1,376 ft hole was completed, but it did not resolve the origin of the Ni traces beyond the transient crater wall. In 1928, the Meteor Crater Exploration and Mining Company began the final phase of mining operations with three more drill holes (maximum depth 721 feet) in the same area as the 1,376 ft hole. The company then sank a final shaft at the crater from June 1928 through mid-July 1929, when the shaft reached a final depth of 713 ft. Operations stopped there because of flooding. Further exploration of the meteoritic debris beneath the south rim was never pursued further.

Drilling operations were renewed several decades later, but in this case for scientific purposes in support of the Apollo program. The USGS, under contract to NASA, drilled 5 holes on the south rim in 1965-1966 (maximum depth of 366 ft) and excavated a single trench to provide physical information for lunar analogue studies. The USGS also drilled 116 holes through the ejecta blanket and 45 holes beyond the ejecta blanket in the early 1970's. Some of this latter material survives and is available for credible research projects from the USGS.

Roddy (1978) collated the above drilling and geophysical data and converted the structural depths to values relative to the pre-impact surface. He determined that the average pre-impact surface elevation was $1,683 \pm 2$ m. He estimated the distances from that surface to the top of the fallout, top of breccia lens, base of breccia lens, and base of fractured rock are ~150, ~160, ~310, and 990 m, respectively. He also estimated the average height of the structural uplift in the rim is ~47 m above the pre-impact surface and that the pre-erosion thickness of ejecta on the rim was $\sim 20 \pm 5$ m, with the caveat that the latter was variable.

Beginning with Shoemaker's (1960) comparison of Meteor Crater with nuclear explosion craters (see also Short, 1964) a picture of the processes involved in the crater's formation has matured. Details about the trajectory, energy, and several other parameters are still being debated in the community, but several general attributes of the processes that created the crater can be summarized with two generic

graphics (Fig. 4.8 and 4.9). The impacting asteroid penetrated the Moenkopi surface to a depth approximately equal to its diameter and, in an explosive release of its kinetic energy, generated a downward and laterally radiating shock wave. As that shock wave radiated through an increasingly larger volume of rock in the Earth's crust, peak shock pressures declined. Thus, the highest, vapor- and melt-producing shock pressures occurred near the point of impact.

A shock wave simultaneously radiated upward through the projectile, producing a reflected rarefaction wave that then radiated downward into the target. After the shock wave and rarefaction wave passed through a section of the Earth's crust, a residual particle velocity was imparted on the material. The effect of that velocity was to establish a flow of rock that initially moved downward and radially outward, before moving upward and outward. This is the flow of material that excavated the crater cavity and ejected debris onto the surrounding landscape. Material remaining along the crater walls slumped inward, forming a breccia lens. Depending on the energy of an event, that breccia lens may incorporate impact melt fragments. In the case of Barringer Crater, which is one of the smallest hypervelocity impact craters, very little melt appears to have been incorporated into that breccia lens. The total time involved in this dramatic re-organization of rock, melt, and vapor was only a few seconds.

Morphological and geophysical data were recently used to constrain numerical models of the impact processes that produced the final structure of the crater and its associated gravity anomaly (Collins *et al.*, 2016). Impact speeds, impactor physical states (*e.g.*, one coherent dense mass or a ruptured lower-density cloud of iron fragments), and target properties were investigated. The best fit to the final crater diameter, rim height, and depth to the top and bottom of the breccia lens was generated by an impact speed of 15 km/s, impactor mass of 3.2×10^8 kg, and damaged target cohesion of 50 kPa. For a discussion of the important role of dilatency and other details of the impact process, I refer readers to Collins *et al.* (2016) and the subsequent final report (in preparation). For our purposes here, Gareth Collins (personal communication, 2017) kindly replotted output parameters to illustrate the distribution of shock pressures as mapped onto pre-impact target locations and in the final crater (Fig. 4.10).

A discussion of the details involved in this generalized impact cratering scenario, like the trajectory and energy of impact, are discussed in later chapters.

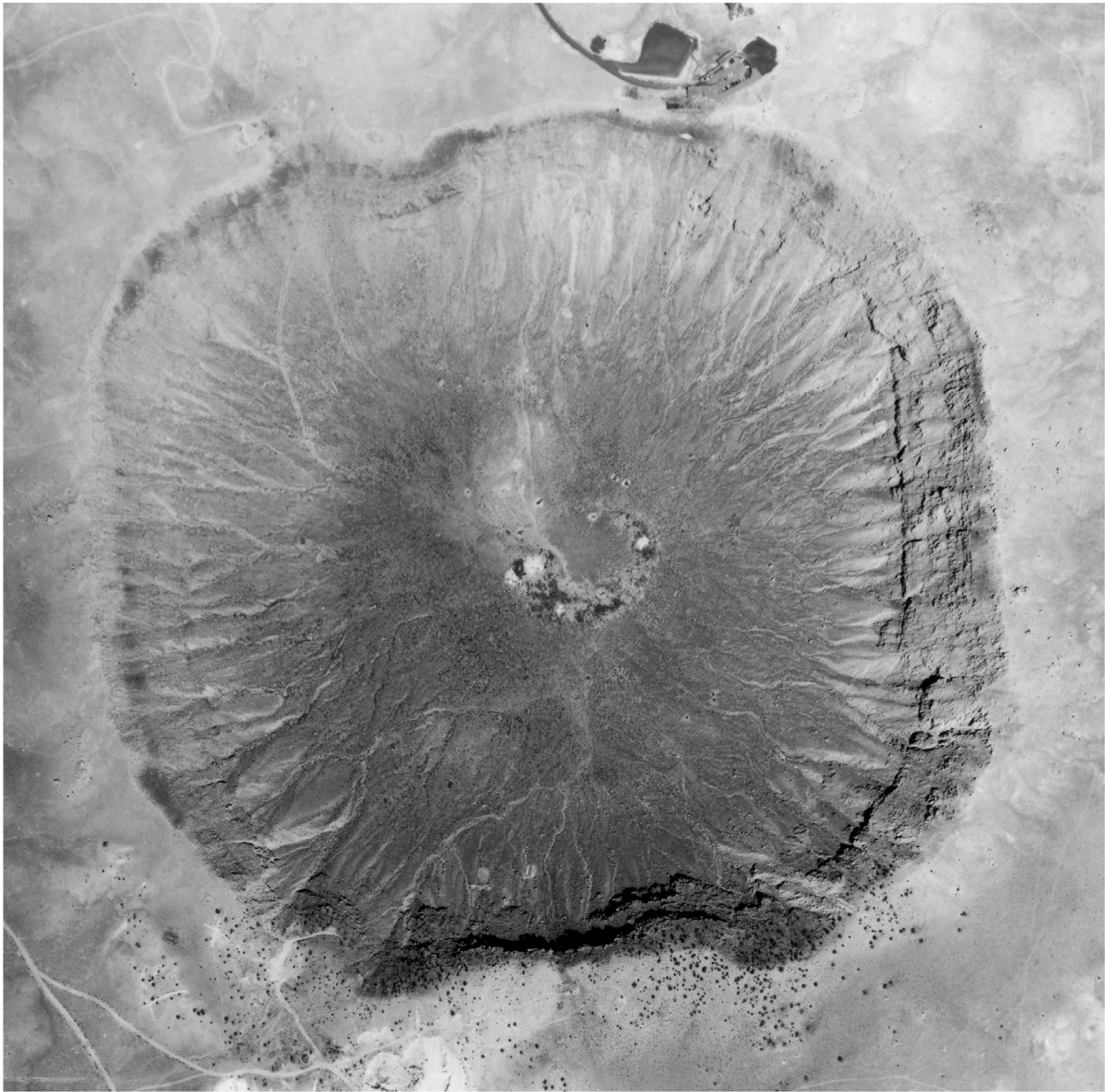


Fig. 4.1. Overhead aerial view of Barringer Meteorite Crater. The crater is ~1.2 km in diameter. The central depression is ~180 m deep and the crater rim rises 30 to 60 m above the surrounding plain. North is at the top of the image and the sun is illuminating the crater from the SSE, creating shadows beneath the cliffs in the southern crater wall and, to a lesser extent, beneath the cliffs in the eastern crater wall. The current museum complex is located on the NNE crater rim. Remnants of mining operations are visible on the crater floor, the south crater wall, and on the SW flank of the crater. Two-needle pinyon pine and juniper dot the southern flank of the crater and the uppermost southern crater wall. Several faults cut through the crater wall and rim sequence. The crater is a modified circle, with slightly squared corners that are associated with those tear faults. The faults may have been activated along pre-existing joints in this portion of the Colorado Plateau (*e.g.*, Shoemaker, 1960).

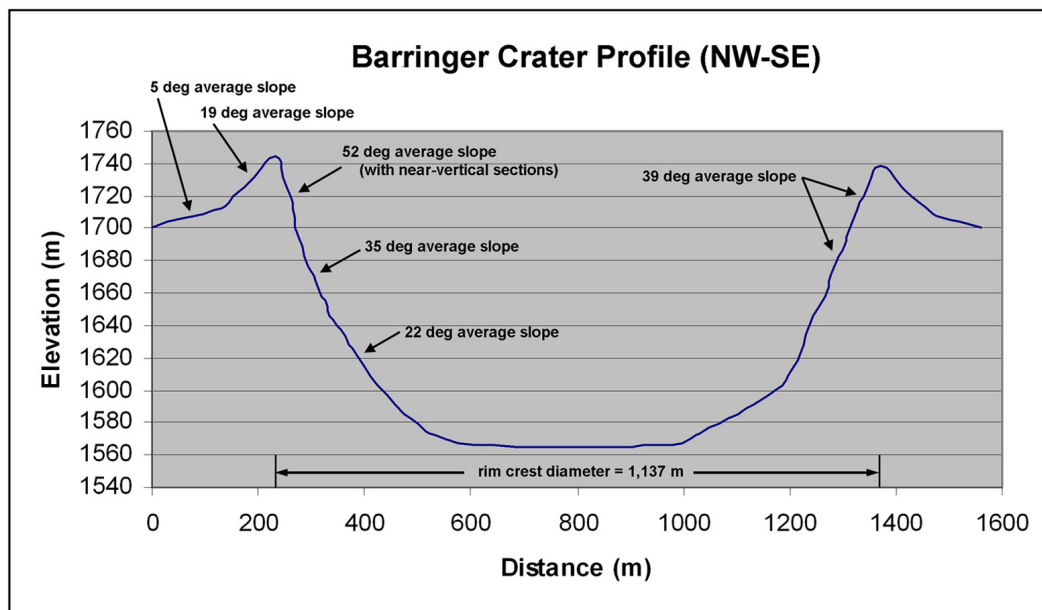
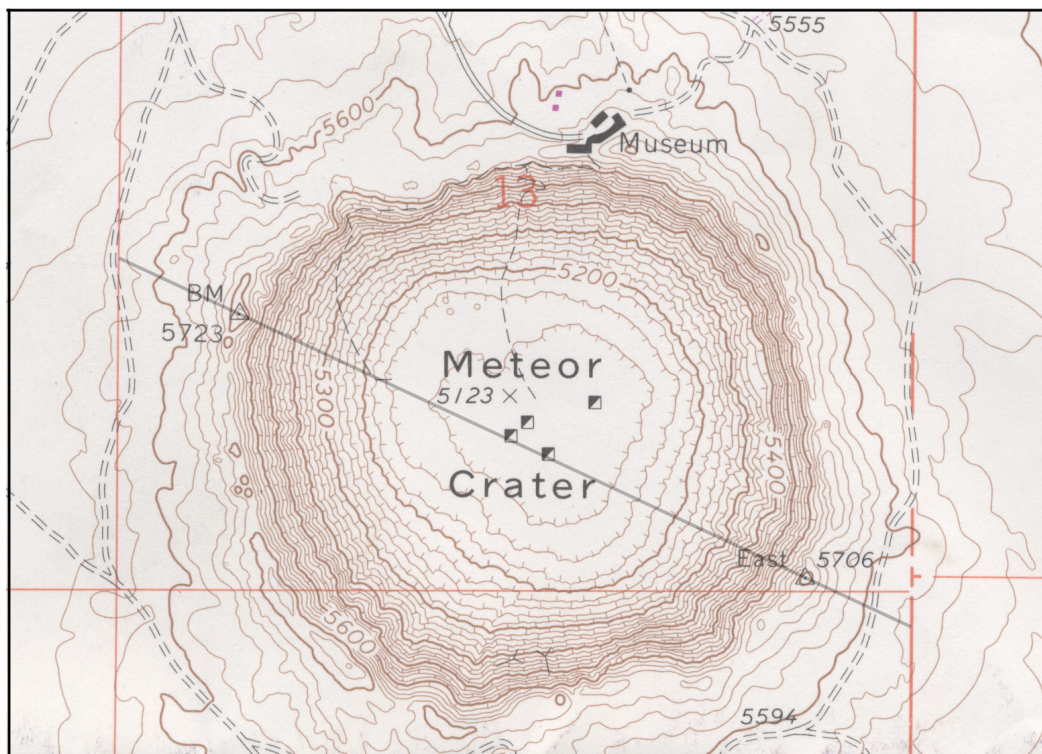


Fig. 4.2. Topographic map of the crater (top panel) as presented on the current USGS 7.5 minute quadrangle for Meteor Crater. The map is contoured in 20 ft intervals. Barringer Point (5,723 ft) is one of the highest locations on the crater rim. A line drawn across the map from NW to SE indicates the location of a cross-section through the crater (bottom panel). The cross-section is calibrated in meters and is vertically exaggerated. Slopes in the upper crater wall average ~50 degrees and include near vertical cliffs.

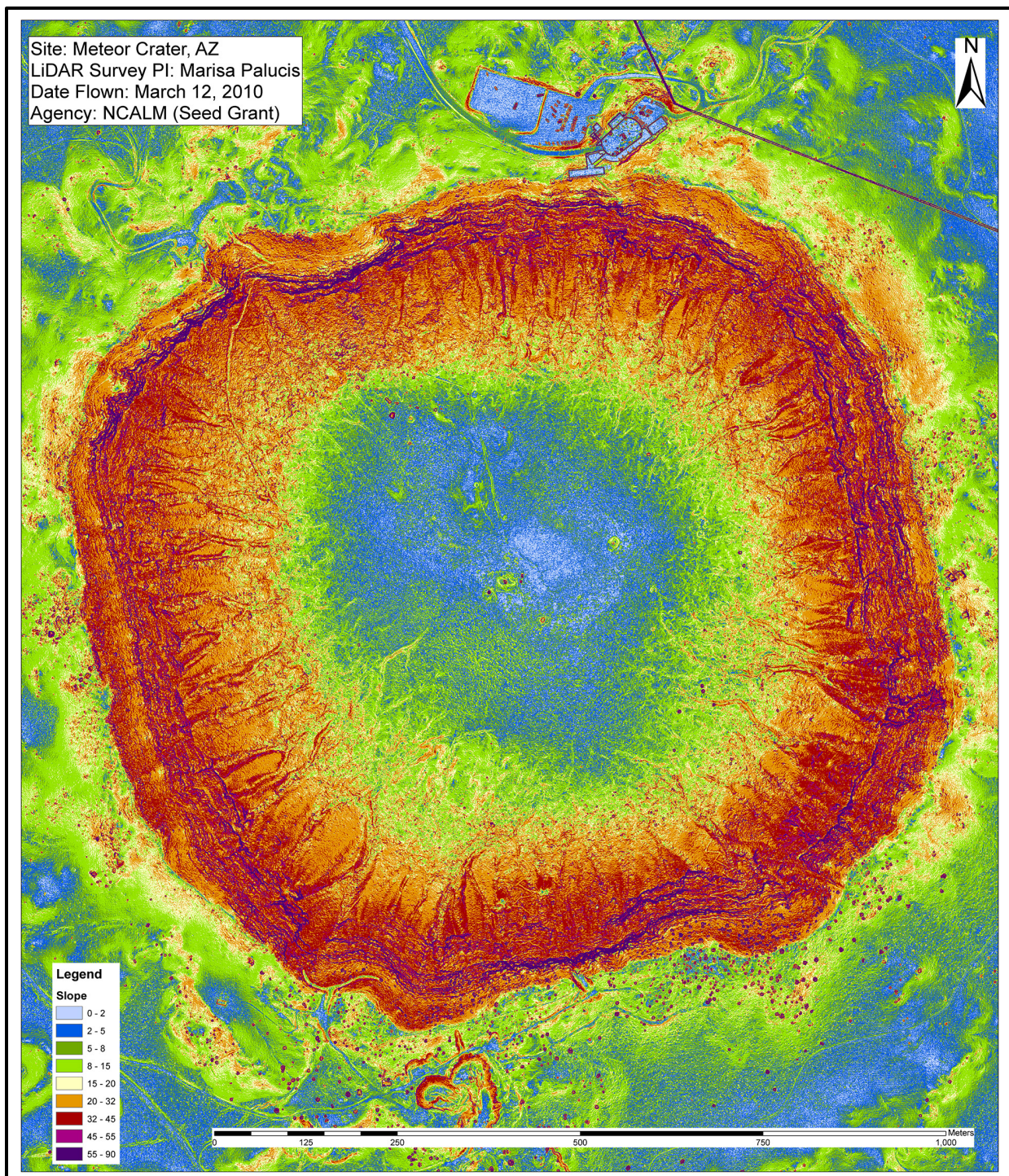


Fig. 4.3. New LiDAR techniques are enhancing the resolution available for studies of the crater. Here, for example, is a slope map that Palucis produced from a new aerial LiDAR survey conducted in 2010. This slope map and the source digital elevation map (DEM) with 25 cm resolution highlight many features not easily discerned any other way. The data were initially applied to a study of gullies on the crater wall (Palucis *et al.*, 2012a,b). These and other electronic data are curated at the Lunar and Planetary Institute (LPI) along with an electronic copy of this guidebook. The url is http://www.lpi.usra.edu/publications/books/barringer_crater_guidebook/.

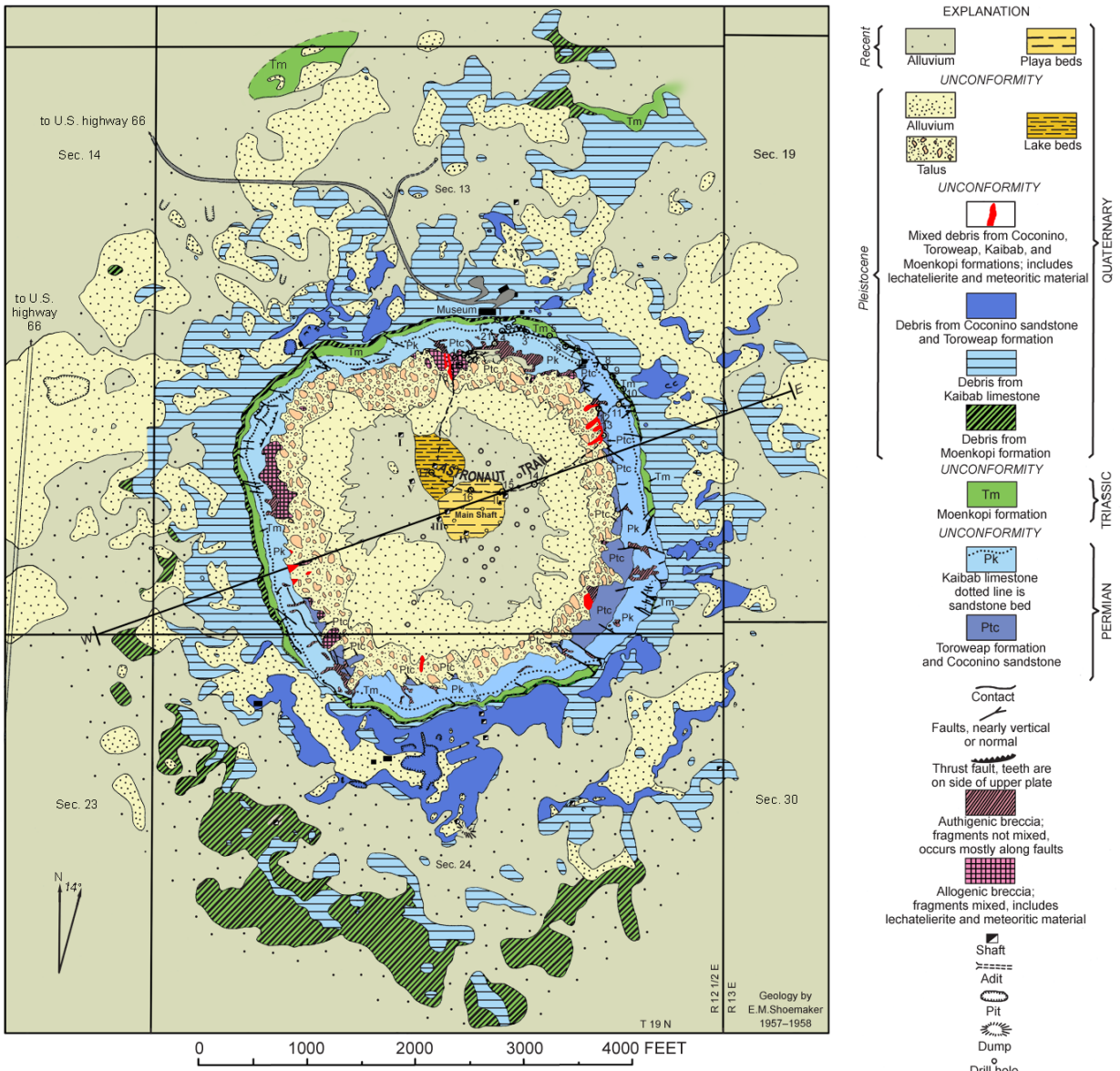


Fig. 4.4. Geologic map of Meteor Crater, Arizona, produced by Eugene M. Shoemaker (1960). In addition to locating the bedrock lithologies (Coconino-Toroweap, Kaibab, and Moenkopi), he also mapped the interior breccia deposits, exterior debris deposits, and faults that cross-cut the crater walls. Many of the features represented by this map had previously been identified by Barringer (*e.g.*, 1905), but Shoemaker mapped them in exquisite detail and provided useful comparisons to geologic features produced in a nuclear explosion crater. This figure is a colored version of Shoemaker's original map. Target lithologies visible in the crater walls are the Permian Toroweap and Coconino sandstones (undivided, Ptc), Permian Kaibab Formation (Pk), and Triassic Moenkopi Formation (Tm). Over-turned and ejected Quaternary debris from those units are identified with diagonal hatching (Moenkopi ejecta), horizontal hatching (Kaibab ejecta), and a different shade of color (Coconino ejecta). Impact-generated breccias are identified with different shades of red and pink. A west-east cross-section across the structure is shown in Fig. 4.5. Color added by Kring (2007).

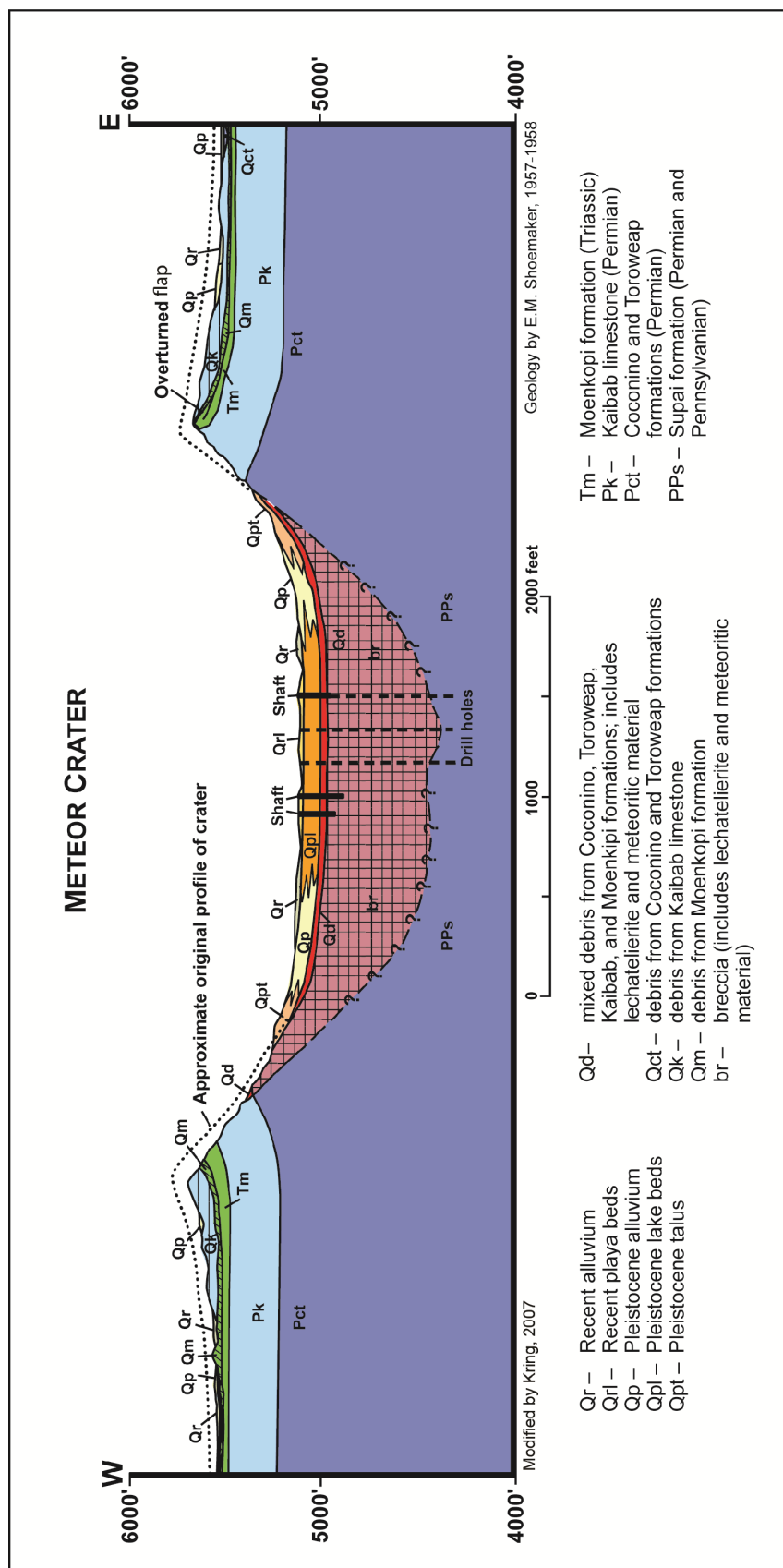


Fig. 4.5. Structural and lithological cross-section through Meteor Crater along a W-E axis. See Fig. 4.4 for the location of the W-E axis and Shoemaker (1960) for the original presentation of this cross-section. The breccia (Br) refers to the allogenic breccia described in the text. The mixed debris unit (Qd) refers to the mixed debris unit or fall-back breccia described in the text. Although not precisely defined in drill core and, thus not marked in the cross-section, the boundary between the Coconino Formation (Pct) and underlying Supai Formation (PPs) is near the bottom of the breccia lens. The cross-section has been redrawn from Shoemaker (1974) and keyed in color.

Table 4.1. Partial summary of exploration boreholes and shafts produced by Standard Iron Company on the crater floor

Hole No. or Shaft No.	Radial distance from Main Shaft	Approx. bearing of hole or shaft from crater center	Approx. elevation at top of hole	Total depth of hole	Depth of hole normalized to 5135 ft datum	Thickness of lake sediments	Depth to Variety A sandstone	Range of Ni-bearing material	Depth to solid rock
	(ft)	(ft)	(ft)	(ft)	(ft)	(ft)	(ft)	(ft)	(ft)
Main Shaft	0	-	5135	222	222	-	-	-	-
2	80	230	-	-	-	-	-	-	-
8	90	125	5135	1085	1085	-	-	-	1030
Shaft III	100	230	5135	-	-	-	-	-	-
1	110	235	-	-	-	-	-	-	-
4	120	180	-	-	-	-	-	-	-
3	130	185	-	-	-	-	-	-	-
23	160	65	-	800	-	-	40	520-620	660
6	200	0	5135	1059	1059	-	-	-	1030
5	250	230	5140	1003	998	-	-	-	-
Shaft IV	250	135	5135	>15	-	-	-	-	-
22	300	45	-	860	-	-	30	600-620	650
7	320	135	5135	960	960	-	-	450-550	-
Shaft VI	320	345	5140	36	31	35	-	-	-
20	330	75	5135	780	780	-	40	640-680	720
12	380	110	5135	881	881	60	60	595-640	700
11	440	165	5135	830	830	-	-	-	640
14	460	125	5135	780	780	-	50	540-620	670
13	480	100	5135	740	740	-	20	598-660	640
21	500	75	-	760	-	-	20	620-640	660
Shaft II	510	70	5135	145	145	100	-	-	-
16	570	110	-	750	-	-	20	540-620	640
9	590	140	5140	670	665	-	-	-	-
Shaft V	600	310	5140	>15	-	-	-	-	-
15	620	125	5140	750	745	-	50	590-600	650
10	650	155	5150	745	730	-	-	-	640
17	650	100	5140	720	715	61	40	520-580	600
19	730	85	5140	680	675	-	-	-	620
Shaft I	740	330	5155	>15	-	-	-	-	-
18	800	100	5150	660	645	-	-	-	630
24	-	-	5140	-	-	-	-	550-650	-
1**	1750	-	5684	1376	827	-	-	? - 1376	-

Sources: Merrill (1908) and Hager (1953) for borehole data; elevations at top of holes determined by correlating numbered hole positions on Barringer's (1910) map with un-numbered hole positions on a current USGS 7.5 min quadrangle topographic map

* Merrill provides a range from 450 to 584 ft, whereas Hager provides range of 550 to 584 ft; Merrill's value of 450 ft is consistent with Barringer (1910)

** Hole drilled by U. S. Smelting, Refining, and Mining Company on south crater rim

Table 4.2. Log of 1,376 foot deep churn drill hole on south rim of Meteor Crater*

Drilling by U. S. Smelting, Refining, and Mining Company
 L. F. I. Holland, drilling superintendent to 326 ft; C. W. Plumb, drilling superintendent to 1,376 ft
 Drilling began November 1920; drilling completed November 1922

Depth from (ft)	to (ft)	Description
0	174	Limestone. Many crevices in limestone
174	195	{Interval not logged}
195	200	Sandstone. Lighted center goes out of sight. White, loose
200	250	Limestone. Drilling past broken cores
250	257	Limestone. Particles of shale ball
257	283	Limestone
282	288	Limestone. Sand commenced to show in bailings
288	290	Brown and yellow stained saccharoidal sand. Much iron and steel, no nickel
290	311	Sand
311	312	Lost hole. Underreamer at bottom
312	326	In tunnel 71-vesicular sandstone
326	380	White sandstone, very quick. 375' hard material dropped in hole
380	384	Drill twisted off
390	425	White sandstone
425	460	White sandstone
460	464	Red cong. Or coarse red sandstone. Small shells, 1/8" long
464	468	Red clay-streaks of white calcite
468	480	Red or cong. or coarse red sandstone
480	500	Red sandstone or conglomerate. Steel
500	520	White sandstone
600	603	White sandstone
603	605	Hard conglomerate
605	607	Hard conglomerate
607	615	Possibly white sandstone with reddish streaks
615	620	Hard conglomerate
620	627	Whitish sandstone
627	669	White sandstone
669	684	White sandstone (?), red sandstone at bottom
684	725	Red sandstone. Hard to get samples
725	750	Crevice. Coarse grains of limestone, sandstone, and silica
750	801	Red mud or clay, white streaks
801	820	Red clay with calcite streaks
820	876	Large crevice. Rounded pebbles of limestone, silica, and sandstone. Iron nodules, all cemented
876	930	Same conglomeratic material
930	940	Conglomerate as above
940	942	Red clay
942	953	Red clay
953	957	Iron nodule. No nickel
957	1096	Alternating layers of white and gray sandstone. Drilled easily
1096	1100	Hard drilling, iron nodule, no nickel
1100	1130	Hard nodules, similar to 958. Segregations from sandstone, filled with small black particles-silicon, effervesces readily
1130	1287	Hard boulders in siliceous white sandstone. 1" to 6". Some nodules show nickel reaction-perhaps shale balls. Some greenish material, looks like clay
1130	1134	4' very hard, like rest of boulders
1134	1145	Soft sandstone. Small greenish pieces of metal or slag in sample. Slight show of nickel
1145	1168	Hard and soft material, slight nickel, layers 6 inches to one-foot layers
1168	1187	Very soft, white silica sand. Then hard and white like silica sand found in crater
1187	1188	Five hours, sample very black, heavy, greenish pieces of metal, very strong nickel
1188	1190	Same as above
1190	1208	First foot hard. Then alternate hard and soft in 6 inches to one foot
1208	1228	Very soft for 15', then hard and rough. Good test of nickel. Silica sand almost transparent
1228	1251	2' hard, rough. Five hours on last foot, stray nickel
1231	1235	4' hard, rough
1235	1249	Silica sand, medium soft. Slight nickel
1249	1271	Soft, white sandstone. Hard nodules at 1,255', 1,260', 1,270'. No nickel
1271	1276	Hard and rough. Like nest of hard boulders. Fine nickel test
1276	1287	Easier for 5 feet. Then harder and rough, fine nickel test
1287	1293	Drilled very hard 4', hard to get samples. Then easier, good nickel
1293	1311	Hard few inches. Then very soft. Fair nickel test
1311	1323	Easy drilling 10', then very rough. Samples quite black. White sandstone and black material about 50 per cent each. Few pieces red sandstone showing. Shells. White sandstone getting harder. Samples show good nickel test
1323	1335	Drilling rough for 7 feet. Then smooth and very hard. Many pieces of <i>hard red sanstone</i> . Also many shells 1/8" long. Fine nickel test
1335	1339	Reamed very hard, like in boulders size of baseball. Drillings looked very black. Samples all gave fine nickel test, about 75 per cent mineral
1339	1350	Drilling hard but smooth. Some red sandstone but mostly black or brownish pieces of material, very magnetic. Best nickel test yet
1350	1352	Hard for 2 feet. Lost sludge at once. Lost circulation. From 1,095' to 1,352' black mineral particles, plentiful
1352	1360	Formation about as last 250 feet. Nickel about same
1360	1370	Formation hard and rough. Shale ball appearance. Last 2500 feet
1370	1376	Extremely hard and rough. Strong nickel test. Samples look as if we are passing through a recemented mass of conglomerate as we find shells, rounded pebbles of red sandstone and of limestone, and also a great many small brown pieces resembling shale balls. Stuck and had to abandon at 1,376 feet. Bit appears to have wedged under boulders

* Hager (1953), who obtained access to drilling record from R. N. Hunt, chief geologist for the U. S. Smelting, Refining, and Mining Company in Salt Lake City, Utah

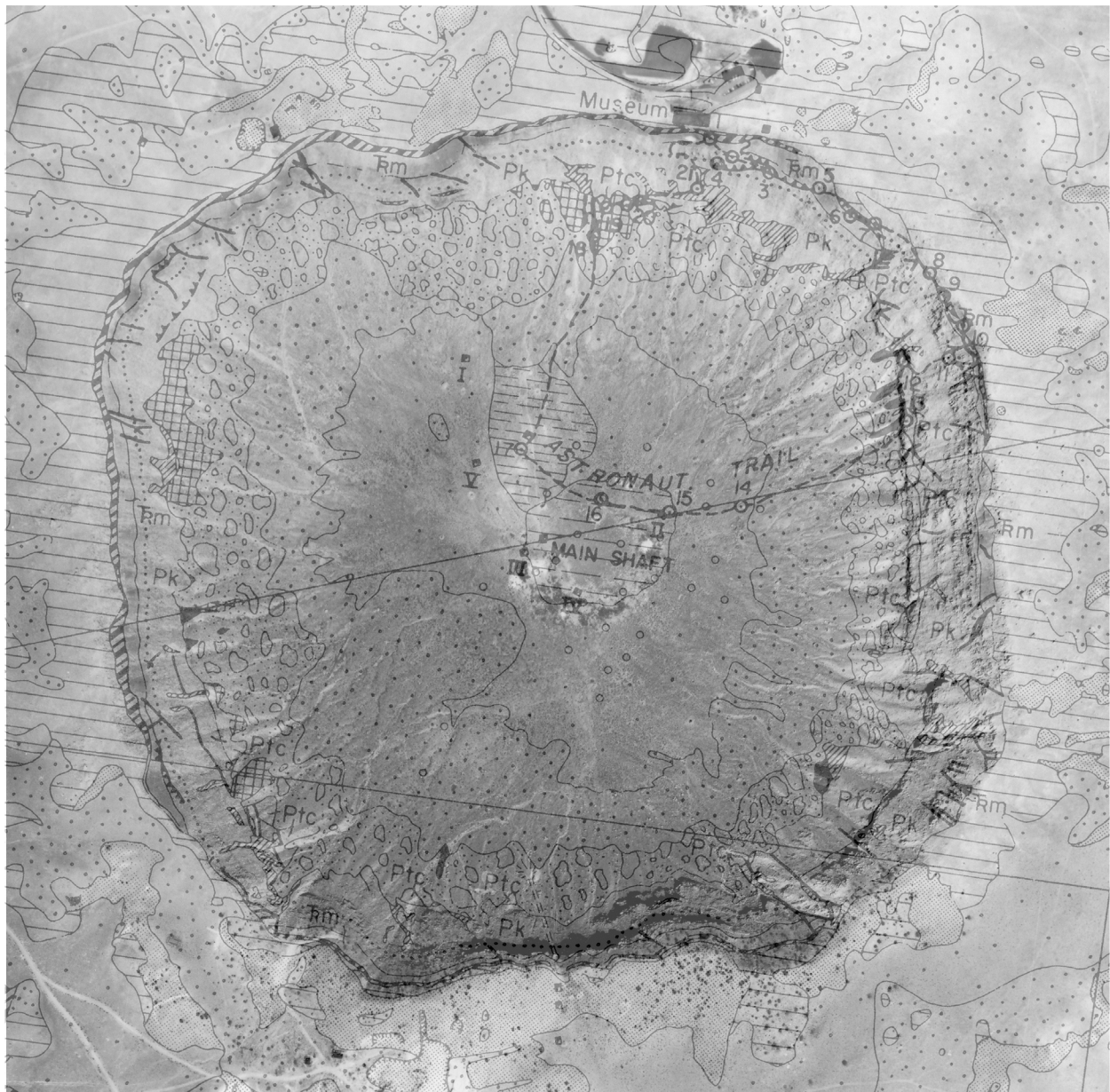


Fig. 4.6. An overlay of Shoemaker's 1960 map with an overhead aerial photograph of the crater. The Astronaut Trail is the route featured during the 1974 Meteoritical Society field trip to the crater, but is severely degraded and no longer functional. The approximate locations of some of the mining features (e.g., main shaft, several smaller shafts, and borehole locations) are marked on the crater floor. See Fig. 4.4 for key to map symbols.

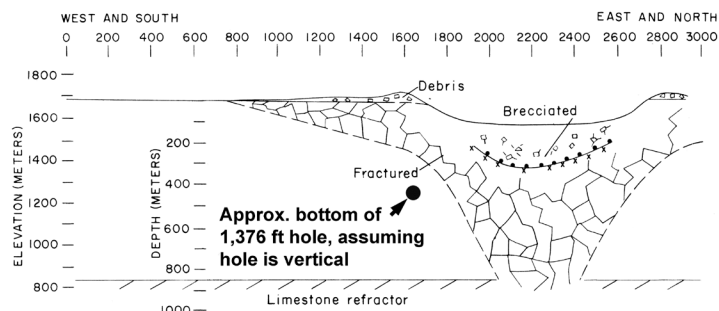
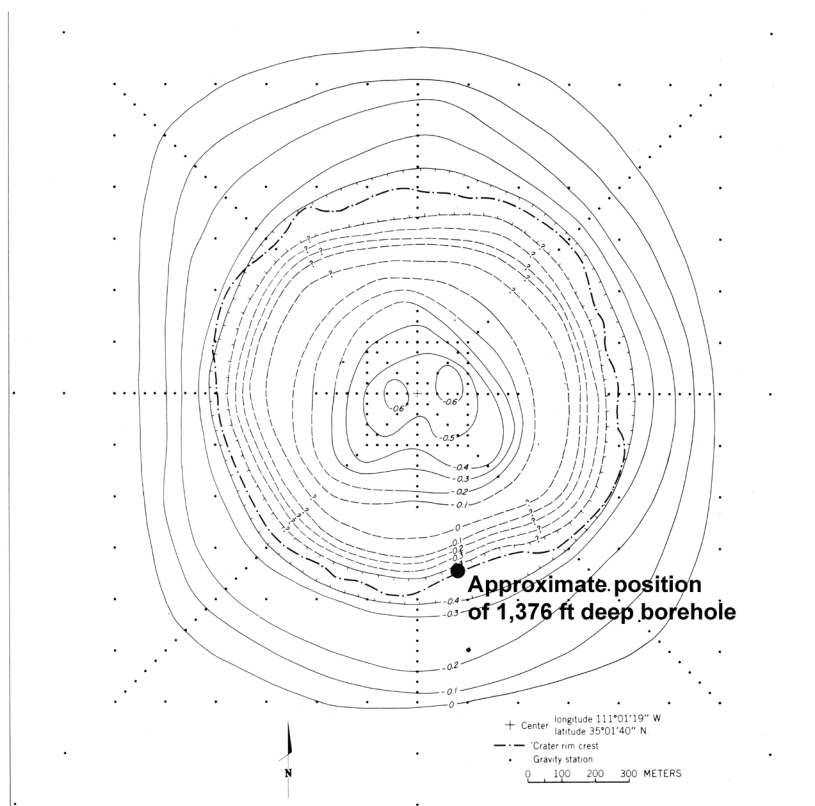
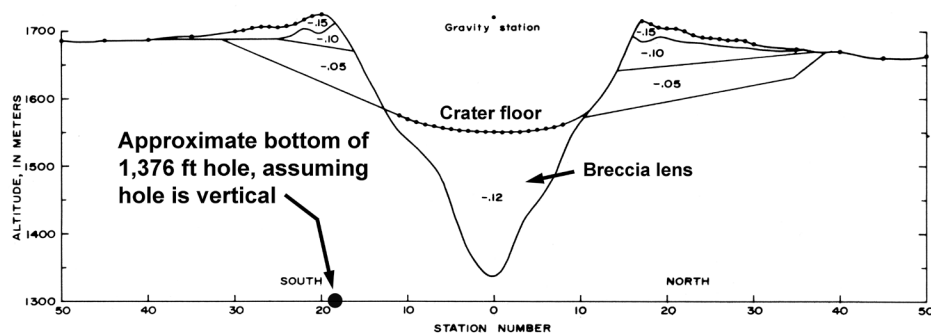


Fig. 4.7. Models of the subsurface structure of Barringer Crater. Model based on seismic refraction data illustrates the extent of ejected debris, the breccia lens, and fractured walls of the crater (top panel). Model based on gravity anomalies illustrates the floor of the breccia lens in a south-north cross-section (middle panel) and in plan view (bottom panel). (Composite illustration based on Ackermann *et al.*, 1975, and Regan & Hinze, 1975.)



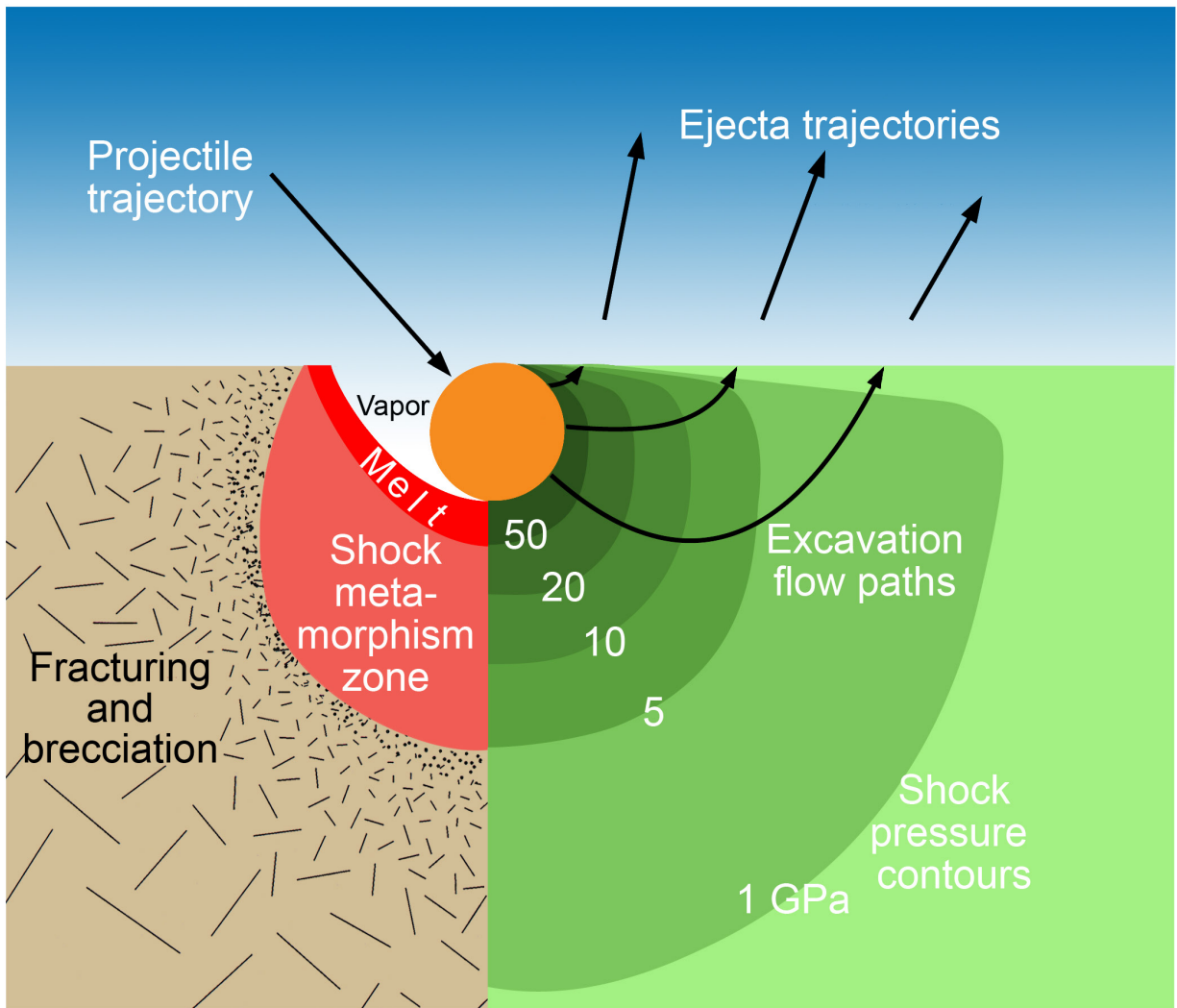


Fig. 4.8. Schematic diagram of the peak shock pressure contours generated during an impact event (right side of diagram) and the type of deformation generated by those shock conditions (left side of diagram). The projectile penetrates to a depth approximately equivalent to its diameter or slightly deeper. The projectile is largely transformed to melt and vapor (the relative proportions of which depend on the energy of the impact event), although a small (<10%) fraction of it may survive as solid fragments. Some of the melted projectile will be mixed with a zone of molten target material (shocked to pressures >50 GPa), but a fraction of it will also be ejected with the vaporized components of the projectile. Shock pressures in the target decrease with distance. Beyond the regions where the target is vaporized and melted, target material will undergo a series of solid state transformations (between shock pressures of ~5 to ~50 GPa), including the production of planar fractures, planar deformation features (or shock lamellae), higher-pressure polymorphs, and diaplectic glasses. At the greatest distances (and lowest shock pressures), the bedrock may be sculpted into shatter cones and fractured. The vaporized, melted, and otherwise shock-metamorphosed material within the transient cavity will flow downward and outward and then upward and outward on paths perpendicular to the shock isobars and ejected into the atmosphere before falling back to the surface on ballistic trajectories. The flow and ejection processes mix material of several different shock levels (including completely unshocked material) and produce complex breccias. (Illustration from an educational poster, Geological Effects of Impact Cratering, David A. Kring, NASA Univ. Arizona Space Imagery Center, 2006. Modified from a figure in *Traces of Catastrophe*, Bevan M. French, 1998.)

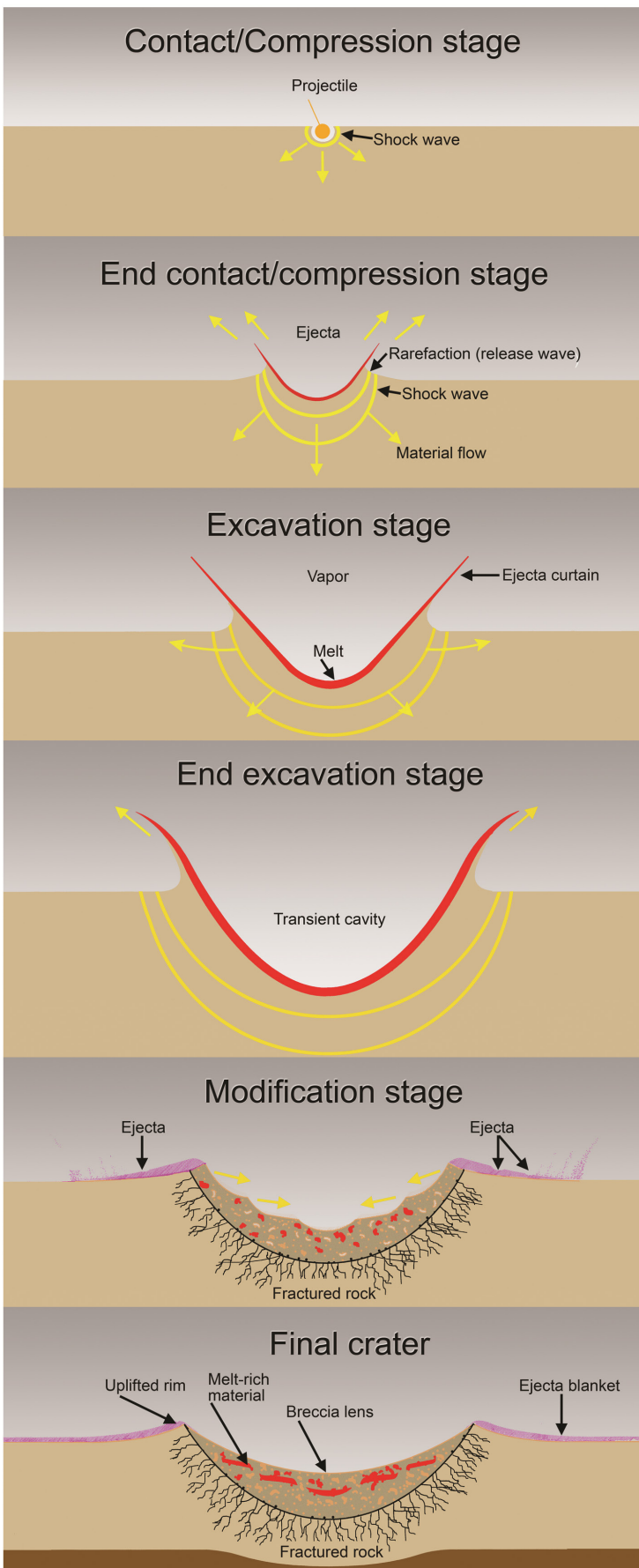


Fig. 4.9. Six views of simple crater formation (generic and schematic). Projectile penetrates the surface and generates a shock wave. A transient crater begins to grow as excavation begins. The transient crater reaches its maximum depth before reaching its maximum radius. When excavation is complete, any remaining debris on the crater walls slump inward to form a breccia lens. Melt will be distributed in the ejecta and any material that falls back on top of the breccia lens. If the crater-forming event is energetic enough, then melt will also be incorporated into the breccia lens. (Illustration from an educational poster, Geological Effects of Impact Cratering, David A. Kring, NASA Univ. Arizona Space Imagery Center, 2006. Modified from a figure in *Traces of Catastrophe*, Bevan M. French, 1998.)

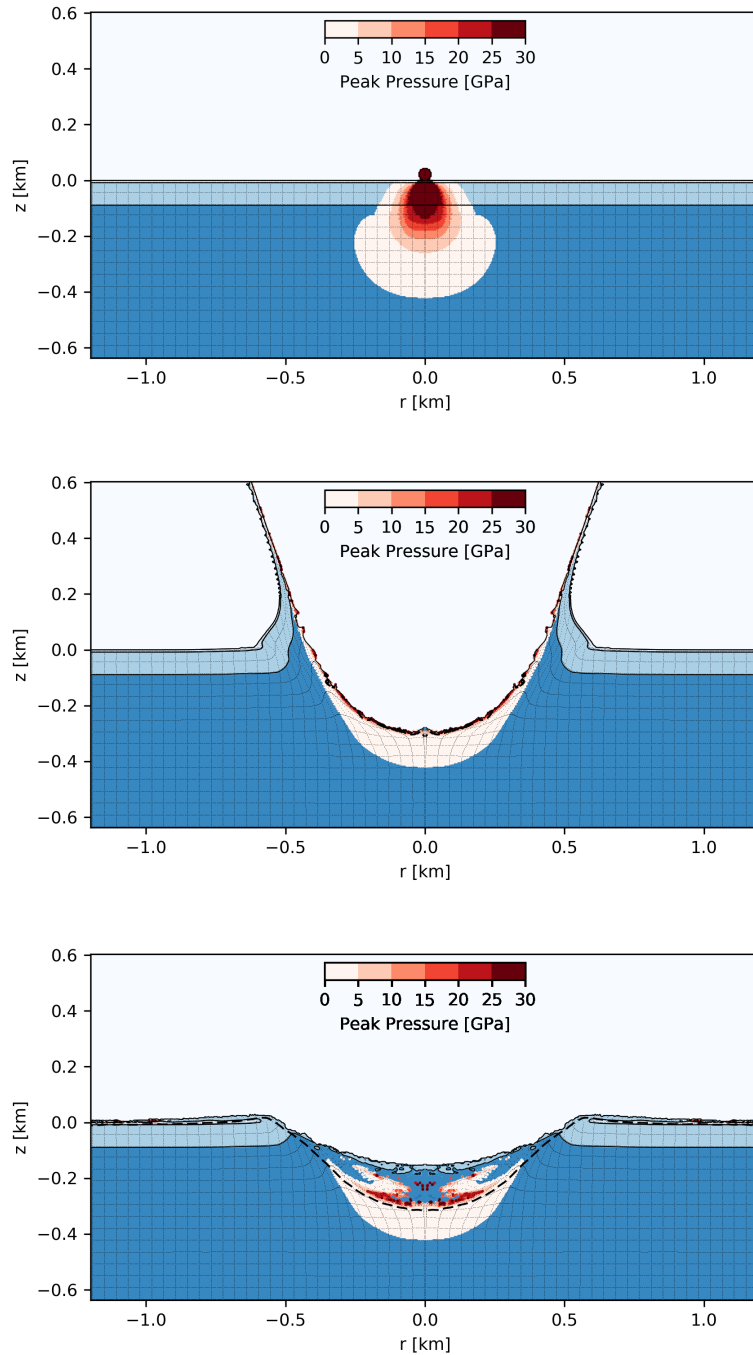


Fig. 4.10 As described in a preliminary report (Collins *et al.*, 2016), computer models of the impact have been made to better understand the formation of simple craters in layered sedimentary targets. The target was modeled with 8.5 m porous (18%) dry sandstone (Moenkopi); 80 m porous (19%) dry limestone (Kaibab); 37.5 m porous (22%) dry sandstone (Toroweap and upper Coconino); and wet sandstone (deeper, water-saturated Coconino). Shock pressures are color coded from 1 GPa to 30 GPa. Melting of these lithologies may begin at ~30 GPa (Wünnemann *et al.*, 2008), but potentially as low as 20 GPa (Kowitz *et al.*, 2016). The top panel illustrates shock pressure distribution within that target. The middle panel shows the transient crater forming. The bottom panel illustrates the final crater with a dashed line along a strain contrast representing the base of the breccia lens. The distribution of shock pressures seen in material along the base of the breccia lens is accurate, because tracer density in the models is good in that location. The tracer density is poor in the middle to the top of the breccia lens, so the absence of highly shocked material there may not be real. These panels are kindly provided by Gareth Collins for this guidebook ahead of his own publication of the final model results.

5. Shock Metamorphism and Impact Melting



Shock-metamorphic products have become one of the diagnostic tools of impact cratering studies. They have become the main criteria used to identify structures of impact origin. They have also been used to map the distribution of shock-pressures throughout an impact target. The diverse styles of shock metamorphism include fracturing of crystals, formation of microcrystalline planes of glass through crystals, conversion of crystals to high-pressure polymorphs, conversion of crystals to glass without loss of textural integrity, conversion of crystals to melts that may or may not mix with melts from other crystals.

Shock-metamorphism of target lithologies at the crater was first described by Barringer (1905, 1910) and Tilghman (1905), who recognized three different products. The first altered material they identified is rock flour, which they concluded was pulverized Coconino sandstone. Barringer observed that rock flour was composed of fragmented quartz crystals that were far smaller in size than the unaffected quartz grains in normal Coconino sandstone. Most of the pulverized silica he examined passed through a 200 mesh screen, indicating grain sizes $<74\text{ }\mu\text{m}$ (0.074 mm), which is far smaller than the 0.2 mm average detrital grain size in normal Coconino (Table 2.1). Fairchild (1907) and Merrill (1908) also report a dramatic comminution of Coconino, although only 50% of Fairchild's sample of rock flour passed through a 100 mesh screen, indicating grain sizes $<149\text{ }\mu\text{m}$. Heterogeneity of the rock flour is evident in areas where sandstone clasts survive within the rock flour. The rock flour is pervasive and a major component of the debris at the crater. Barringer estimated that 15 to 20% of the ejecta is composed of rock flour.

He also noted that surviving rock fragments of Coconino in the debris deposits are altered, describing a Variety A sandstone (which is lightly to moderately shocked sandstone with a greater density than unaffected Coconino) and a Variety B sandstone (which was melted, is vesicular, and will float on water). Variety A sandstone is distributed within the rock flour. According to Tilghman (as recorded by Merrill, 1908), it constitutes ~2% of the sandstone debris and ranges in size from fractions of an inch to blocks 10 to 12 ft in diameter. One of the boreholes apparently penetrated a 50 ft block 500 ft below the crater floor. Barringer (1910) noted that Variety A shock-metamorphosed sandstone is far more abundant than the pumiceous Variety B sandstone, but also suggests that Variety B material may have decomposed over time and be partly responsible for rock flour. As far as I know, a quantitative microscopic study of the rock flour and the relative proportions of different types of silica components in it has not been done to evaluate this suggestion.

Based on a microscopic examination of crater lithologies in thin-section, Merrill (1908, after Diller) began to augment Barringer's shock-classification of the sandstone. The initial phase of shock crushed the sandstone, reduced porosity, and created fractures in quartz grains where they collided. In a second phase of shock-metamorphism, the interlocking of the quartz is so complete that the sandstone resembles a holocrystalline rock. The quartz also often has undulatory extinction. He suggests the quartz was altered under intense pressure and deformed "in an almost putty-like or plastic condition." Rocks shocked to this state also have interstitial pockets of a nearly isotropic, fibrous, and scaly material that has the composition of opal (silica with water). In the third stage of shock-metamorphism, the rocks become increasingly vesicular or pumiceous glass with relict grains of unaltered quartz. Merrill wrote that the damage was limited to samples of the Coconino. He could not find any deformation in cores of the underlying Supai sandstone, recovered beneath the breccia lens, that were available at the time. He wrote that "in no instance did they show any signs whatever of the shattering, fusion, or metamorphism so characteristic of the overlying white sandstone [Coconino]."

The next contribution to the study of shock metamorphism at the crater was provided by Rogers (1928) in his Presidential Address to The Mineralogical Society of America. He recognized that some of the silica glass (lechatelierite) in Variety B shock-metamorphosed sandstone has the same texture as quartz in unaffected sandstone, writing that “Lechateli  rite (silica glass) ... retains the granular texture from which it was derived” and that the lechateli  rite grains are “paramorphs ... after quartz.” This characteristic shock-metamorphic material is generically called thetamorphic or diaplectic glass today (e.g., Chao, 1967; St  ffler, 1972).

In some of the dominantly sheared, yet granular Coconino, it was eventually realized that some pockets of suspected glass or devitrified glass (the nearly isotropic pockets of Merrill) were instead coesite, a high-pressure polymorph of silica. Indeed, the first natural occurrence of coesite was found at Meteor Crater (Chao *et al.*, 1960) and has become another important criterion for identifying an impact crater. Soon thereafter, another high-pressure polymorph of silica, stishovite, was also found at the crater (Chao *et al.*, 1962). Chao and his colleagues reported that both phases occur in Variety A sandstones and survive as a minor constituent in the melted Variety B sandstone.

Kieffer (1971, 1976) continued the detailed examination of shocked Coconino in an effort to expand upon the shock-metamorphic sequence that occurs in the rocks and, where possible, interpret them in the context of the mechanics of the rock’s interaction with a passing shock wave. She divided shocked samples into the five classes recognized today:

Class 1. Initially, the porosity of the rocks was reduced, largely by grain rotation, but no fracturing of quartz grains occurs (Class 1a). At slightly higher shock conditions, the grains began to fracture and may have small amounts of plastic deformation (Class 1b). The fractures appear to have been produced by concussion when neighboring grains collide, because the fractures often radiate from the point of contact between grains. Class 1a rocks have remnant porosity, but Class 1b rocks do not. Class 1 rocks do not contain any higher pressure silica polymorphs.

Class 2. The porosity of the Coconino was completely consumed as grains deformed plastically, forming a puzzle-like fabric. Symplektic pockets occur between grains where pores once existed. Coesite formed in the symplektic regions. These rocks will be 80 to 95% quartz, 2 to 5% coesite, 3 to 10% glass, and have no detectable stishovite.

Class 3. Like class 2 rocks, plastic flow of quartz collapsed the pore space. Coesite is abundant in cryptocrystalline pockets and stishovite begins to appear in opaque regions that surround the coesite-bearing cryptocrystalline pockets. Estimates for the amount of coesite range from 18 to 32% in these rocks, in addition to 0 to 20% glass and traces of stishovite.

Class 4. Vesicular glass formed adjacent to coesite-rimmed quartz grains. Only 15 to 45% of the original quartz survives. These samples have abundant coesite (10 to 30%) and glass (20 to 75%). They do not have any detectable stishovite using optical microscope techniques.

Class 5. This is an extreme version of class 4, where the glass and vesicles dominate the rock and only a few quartz relicts survive. These samples are 80 to 100% glass, with 0 to 15% quartz and 0 to 5% coesite. Most samples that can still be recovered at the surface are only 1 to 5 centimeters thick, although I have seen blocks of this glass that are ~15 cm thick.

Examples of samples with silica glass and vesicular silica glass are illustrated in hand specimens (Fig. 5.1 and 5.2) and in thin-section (Fig. 5.3). The silica glass – or lechatelierite – samples come in all

sizes. While cm-scale examples are shown in Fig. 5.1 and 5.2, a block of lechatelierite with a visible diameter of 5 ft exists in the Science Shaft (number II) (Shoemaker, field notes, January 30, 1958).

Unlike quartz-bearing crystalline target rocks (*e.g.*, granites and gneisses), the quartz grains in shocked Coconino sandstone have very few planar shock features (either fractures or closer-space lamellae). Typically less than 5% of the grains in Class 2 or 3 rocks have planar features. This reflects one of the important differences between impact cratering events in crystalline targets and sedimentary targets. In the latter, a greater fraction of the impact energy is consumed closing pore space, so that there are fewer solid state transformations and higher post-shock temperatures than at similar impact sites in crystalline targets.

Increasing shock pressures also destroyed fluid inclusions that occurred in the Coconino sandstone (Elwood Madden *et al.*, 2006). Two-phase inclusions begin to disappear under Class 1 conditions and are completely gone in Class 3 samples. The number of inclusions in Class 1 and 2 samples, however, remains the same, as the two-phase inclusions are transformed into single-phase inclusions. The total number of inclusions in Class 3 and 4 rocks are lower, indicating that fluid inclusions are destroyed by the plastic deformation and phase changes that occur under those shock conditions. Very few one-phase inclusions survive in Class 4 and 5 samples. Thus, crystal components in the sandstone are dehydrated by shock-metamorphism.

In contrast to these extensive studies of Coconino sandstone, very little is known about the effects of solid phase shock transformation in the Moenkopi and Kaibab Formations. The Moenkopi shales and siltstones are so fine-grained that optical microscope identification of any shock transformation that may have occurred is difficult. The Moenkopi also represents the free surface of the impact site, which would have reduced the volume that saw peak shock pressures in excess of 5 GPa (Fig. 4.8). Shock-metamorphism in the carbonate fraction of the Kaibab is a challenge to study, because it is difficult to discriminate shock-induced deformation from other types of geologic deformation in that type of material. Carbonate is too easily deformed to be used routinely for shock-metamorphic studies. Nonetheless, samples from Barringer Crater probably offer one of the best opportunities to document the progression of deformation that occurs in dolomite; it may be worth further study. It might also be interesting to determine how the quartz fraction within the Kaibab has been affected by shock (both where it is embedded within carbonate and where it occurs in isolated beds of sandstone).

At higher shock levels, target rocks are melted. A rare example of incipient melting and melt flow in a cataclastic sandstone is shown in Fig. 5.4. As melting consumes a target lithology, melts from individual phases are mixed, producing “normal melts” or “mixed melt,” that are then distributed in deposits of mixed debris inside the crater and deposits of alluvium on the outermost flanks of the crater. Some of these mixed melts also entrain fractions of the impacting asteroid.

Impact-generated melts at the crater were first described by Nininger (1954, 1956, 1957). The melts range in morphology from melt splashes that encompass clasts of target rock (Fig. 5.5) to a variety of isolated aerodynamic forms, although most specimens are irregularly shaped with pitted (and often vesicular) surfaces. The largest clasts found with melt splashes were 5 to 6 cm in length and composed of Coconino sandstone. Molten particles collided with each other in flight, because some melt fragments have compound droplet morphologies. Impactite melt “bombs” were up to 2.25 cm wide (Nininger, 1957). Melt particle colors have many different colors, although they are usually shades of gray, brown, and red-stained brown in bulk form. Yellow and bright red colors are often evident in thin-section. The melt particles (or, at least those that are easily recoverable) range in size from a millimeter to a few centimeters. The volume of total melt produced is still debated and is hard to evaluate now because of the extensive effects of erosion (which stripped the fall-out unit around the crater) and previous

collections of melt. Ninninger (1956) reported that most melts were within 1,500 ft (~460 m) of the crater rim and that none were found beyond 1 ½ mi (2.4 km) from the crater rim.

While working on the Surveyor missions to the Moon, Shoemaker also collected melt specimens that appear to be composed wholly of vesicular melt and those that welded fragments of target rock together (Shoemaker *et al.*, 1967). These impactites were up to 4 cm in size (Fig. 3-27a of Shoemaker *et al.*, 1967). At least two of the specimens in Shoemaker's collection are curated by the Smithsonian Institution. I have collected impact melt specimens in several locations around the crater, which I curate in the Barringer Crater Reference Collection.

In addition, melt specimens and meteoritic material are being recovered from the drill cuttings from the ejecta blanket (Gaither *et al.*, 2012). That observation suggests that shock-melted material and particles of the disrupted asteroid may have penetrated the ejecta curtain (assuming bioturbation is not carrying the particles to depth). It would be interesting to quantify the amount of mixing. It would also be interesting to determine if that mixing occurred during the initial explosive and compressive phase of impact or during ejection and overturning of debris in the ejecta curtain. If meteoritic material and impact melt are only found in the distal portions of the ejecta blanket or on top of the ejecta blanket, then that suggests any mixing occurred during the explosive and compressive phase. If the material is found instead within the ejecta near the rim of the crater, then that suggests mixing occurred later in the crater-forming processes during the ejection and overturning of debris in the ejecta curtain. In the latter case (or any intermediate case), it would also be interesting to determine how far any meteoritic or impact melt penetrated the ejecta curtain; *i.e.*, how deep in the overturned sequence it is found.

Before describing the Barringer Crater melts further, it might be useful to make some general comments about impact melts. One of the oft-spoken attributes of impact melts is their homogeneity. In large complex craters with substantial impact melt sheets, the melt is often a homogenized mixture of the complex target lithologies that were melted. Only subtle compositional variations have been reported. There must always be an exception to prove the rule and that exception is Sudbury. In that case the melt sheet is heterogeneous, because of post-impact igneous differentiation.

In contrast, melts that are ejected from a crater are often incompletely mixed. For example, in the case of Chicxulub, which involved a diverse target assemblage of carbonates and silicates, a range of Ca-rich to Ca-poor melt droplets were deposited in moderately distal ejecta deposits.

In simple impact craters, like Barringer, there is not sufficient molten material to form a coherent melt sheet. Even in the larger (4 km diameter) Brent simple crater in Canada, only sufficient melt to form pods within a breccia lens was generated. In Barringer Crater, there is no detectable melt pods within the breccia lens. Nor are there any significant melt pools on the crater walls and in the ejecta blanket. There was either an insufficient volume of melt produced by the impact event and/or it was too finely disseminated (possibly because of a relative high volatile content in the target rocks; Kieffer and Simonds, 1980) to produce those types of deposits. Melts were locally produced within the transient cavity and not well mixed. In addition, a highly disparate proportion of projectile material was added to the melts. A relatively large range of melt compositions is the result.

A preliminary petrographic study of Barringer Crater melts was generated during the Apollo era by Greenwood and Morrison (1969), who reported that Fe,Ni-metal was entrained in the melt and that the silicate fraction of the melt precipitated olivine, actinolite, and magnetite. Much more detail, however, was revealed by Hörz *et al.* (2002) and See *et al.* (2002), who thoroughly studied the chemical compositions of target strata and 80 melt particles generated from them. They confirmed that the melts contain immiscible Fe-Ni metal alloys and sulfides from the projectile, although they also noted that the

metal and sulfide often have chemically fractionated compositions. Nickel is enhanced in the metal and sulfide. The abundance of FeO from target lithologies is on the order of 2 wt%, yet FeO contents of the silicate portions of the melts are often 25 to 30 wt%. The enhanced FeO is attributed to oxidation of meteoritic iron component from the projectile, which is consistent with the Ni/Fe fractionation in the metal and sulfide.

In principal, it is possible that some of the FeO in the silicate impact melts came from silicate inclusions within the type IAB iron asteroid. Inclusions in type IAB meteorites are generally about 70% mafic silicates (olivine and pyroxene), 10% sodic plagioclase, 10% metal, 10% sulfide. However, in the specific case of the Canyon Diablo meteoritic fragments, silicates are usually associated with troilite-graphite nodules, which represent about 8.5% of the meteorites (Buchwald, 1975). Silicates in Canyon Diablo specimens are much less common than in other type IAB meteorites, so they are not likely to be a significant source of FeO. Hörz *et al.* (2002) found that the projectile component is greater in melts that have a significant Kaibab component and less in those that have a larger Moenkopi component. This is consistent with models in which the projectile passes through the thin Moenkopi cover and penetrates the underlying Kaibab (Fig. 5.6 and 5.7).

A significant fraction of the projectile-derived FeO was incorporated into olivine and pyroxene that precipitated from the impact melt. Olivine and pyroxene compositions vary considerably between melt particles (and within some melt particles). These two phases are not in equilibrium with each other, nor with the surviving metal alloys entrained in the melts. The crystallization of olivine and pyroxene in a sedimentary province or, in this case, in melts generated from sedimentary siltstone, dolomite, and sandstone, is unusual. It appears that CO₂ in the target carbonate was driven off, forming refractory (Ca, Mg, and Fe-rich) residues that mixed with Si and meteoritic components. Most of the melts are highly vesicular, which is further testament to the thorough loss of target volatiles. A preliminary study of impact melts by another group (Kargel *et al.*, 1996) also reported 100% decarbonation of melted Kaibab.

Many of the melt particles have regions that produce low analytical totals (typically 70 to 90 wt%), implying a volatile component (*e.g.*, H₂O, OH, CO, or CO₂) exists within them. Hörz *et al.* (2002) and See *et al.* (2002) heated several representative samples to drive off any gases and analyze them. Only water vapor was detected, which is probably the result of post-impact oxidation and hydration rather than an inherent property of the melts. No CO or CO₂ was detected, indicating that component of the target carbonates was thoroughly excised during the formation of the large collection of melts studied.

Although almost all melts studied suggest strong degassing, small amounts of CO₂-charged impact melt appear to have also been produced. Thin-layers and veneers of melts with carbonate-like compositions have been recovered (Fig. 5.8 and 5.9; originally published by Kring, 2007; see also Gaither *et al.*, 2016). Although a direct detection of CO₂ has not yet been reported, analytical totals are consistent with a CO₂ rather than H₂O component. The presumed CO₂-charged melts are in direct contact with refractory olivine and pyroxene-bearing melts that are highly vesiculated and that were obviously degassed. Although the silicate-dominated melts were thoroughly degassed, the splashes of CO₂-charged melts imply there were small batches of melt that did not degas. Presumably, they were heated to temperatures needed for melting, but not hot enough to degas or were quenched before degassing could occur.

Interestingly, a quench zone of carbonate crystals along the boundary of the carbonate-dominated melt in Fig. 5.8 suggests an un-degassed molten sample collided with a previously degassed melt that had already solidified. This illustrates the complexity and speed with which material is affected by the impact event and mixed. It is important to note that not all carbonate rinds around melt particles are

quenched melt. Many melt particles are coated by caliche. Careful petrologic and isotopic analyses can separate the two occurrences (Cernok and Kring, 2009; Hörz *et al.*, 2015; Osinski *et al.*, 2015; Chapter 15).

Incomplete degassing and, thus, quenching of carbonate melt at Meteor Crater appears to be rare, although some seem to argue otherwise. Ca,Mg-rich (9 to 20 wt%) silicate glasses and crystalline calcite globules within silicate glass have been reported in an area Shoemaker mapped as alluvium, but reinterpreted to be an ejected impact breccia (Osinski *et al.*, 2015). These observations, like those of Hörz *et al.* (2002), indicate the Kaibab was melted, but true carbonate melts remain rare. The CO₂ was degassed, leaving melts enriched in the cations (Si, Mg, and Ca) of the sandy carbonate.

To test the possibility of additional carbonate melt hiding as disseminated particles, the ashy matrix of fall-back breccia from inside the crater was studied (Cernok and Kring, 2009). This is the unit (see Chapter 19) that contains all of the target lithologies, including shocked varieties like lechatelierite, and meteoritic debris. The matrix is dominantly <5 µm in size and composed of angular to sub-rounded quartz grains (Fig. 5.10) and minor K-feldspar and calcite. The matrix also contains rare shards of silicate that are either fractured quartz or glass.

Hörz *et al.* (2002) suggested different depths of melting for different melt compositions (Fig. 5.7), including two options for a silica-rich variety. In one of those options, melting occurred at depths <30 (*i.e.*, no deeper than the upper Kaibab), while the other option required melting to depths >90 m (*i.e.*, into the upper Coconino). A numerical model of target melting (Artemieva and Pierazzo, 2011) suggests melting can occur as deep as the Coconino, but that most ejected melt was produced from 30 to 40 m depth and should be dominated by Moenkopi and upper Kaibab. This is also the case in a more recent model calculation by Collins *et al.* (2016) and illustrated in Fig. 4.10.

Observations at Barringer Crater, in addition to those at craters with larger melt volumes, imply a two-step mixing process for crater melts: (1) mixing of projectile material with local (stratigraphically-limited) target melts and (2) mixing of those melts along the crater wall to produce a homogeneous melt composition. In the case of Barringer Crater, step (1) occurred, but (2) did not occur or only partially occurred, because there is tremendous heterogeneity among silicate melt compositions, in addition to the sharp contrast between silicate-dominated and carbonate-dominated melts. Either there was not sufficient melt volume along the crater wall to facilitate homogenizing melt mixing or the material was ejected before that mixing could occur. The high volatile content of the target lithologies (11 wt% for Moenkopi and 27 wt% for Kaibab; See *et al.*, 2002) may have triggered an early and/or particularly violent disruption of melt volumes (Kieffer and Simonds, 1980) and expansion out of the crater.



Fig. 5.1. Shocked Coconino sandstone can have several appearances. Here, three examples with increasing vesiculation (top to bottom) are shown with sawn surfaces. A 1-cm cube is shown for scale. Samples MC51817-12, MC51817-8, and MC51817-10.



Fig. 5.2. Shocked and vesiculated sample of Coconino sandstone shown with a natural, rough surface. A 1-cm cube is shown for scale. Sample MC51311-1.

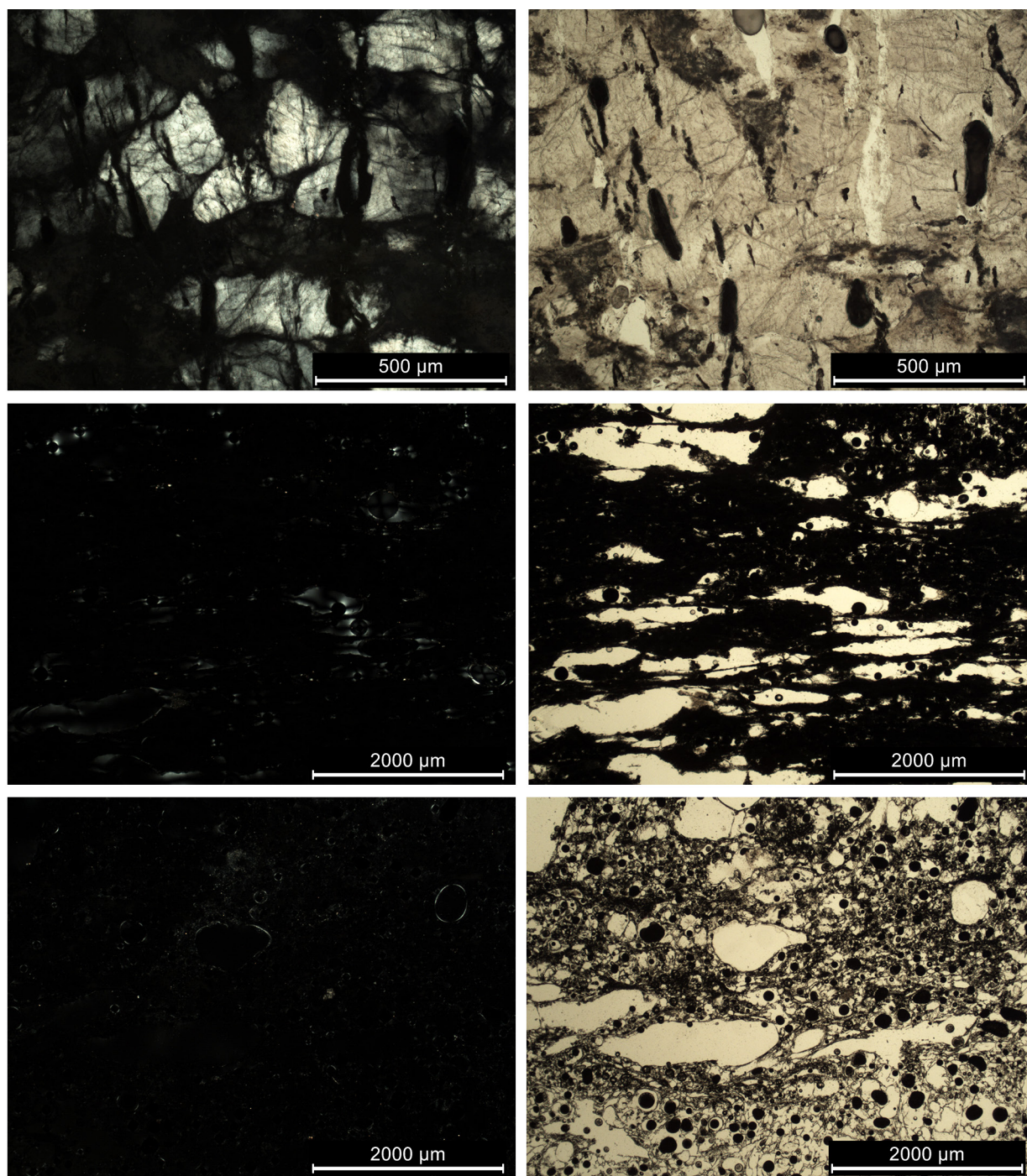


Fig. 5.3. Thin-section views of shocked Coconino sandstone in cross-polarized (left) and plane (right) light. All three samples contain abundant shock-produced glass, which is isotropic and, thus, appears black in all three left panels. The uppermost sample contains relict quartz grains that are crudely aligned horizontally across the field of view. Often in samples like that one, coesite and open (decompression) fractures occur in a near-perpendicular orientation (*e.g.*, the near-vertical features in the top right panel), which cut across both the relict quartz and the adjacent silica glass. The middle sample is composed of glass and flattened vesicles produced by shock vapor. The vesicles are off-white colored in the left panel. The bottom sample is composed of abundant gas vesicles of all sizes, ranging from about 100 microns in diameter along the lower edge of the field of view to nearly 2 mm in length in the middle of the field of view. The scale bars in the top row are 500 μm and those in the bottom two rows are 2 mm. Sample numbers are (top to bottom): MC21204-10B, MC21503-2, and MC21503-1.

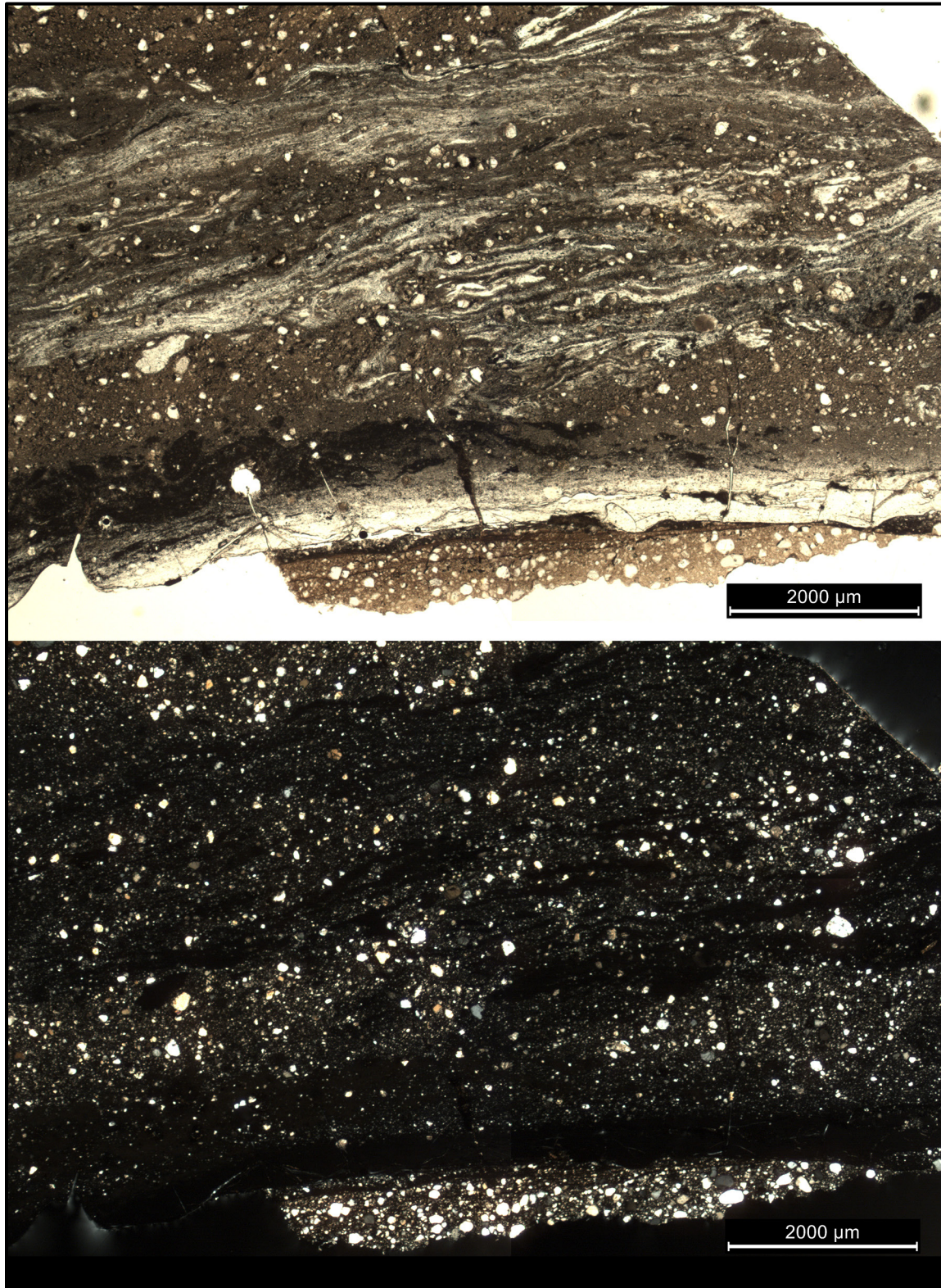


Fig. 5.4. Rare example of incipient shock melting and the production of schlieren in cataclastic sandstone, shown in plane-polarized light (top) and cross-polarized light (bottom). In addition to the flow-like features, there is also a zone of glass near the base of the thin-section, appearing pale green to colorless in plane-polarized light and isotropic in cross-polarized light. The surviving quartz grains have been reduced in size and are angular. Scale bar is 2 mm. Sample MC91704-1.

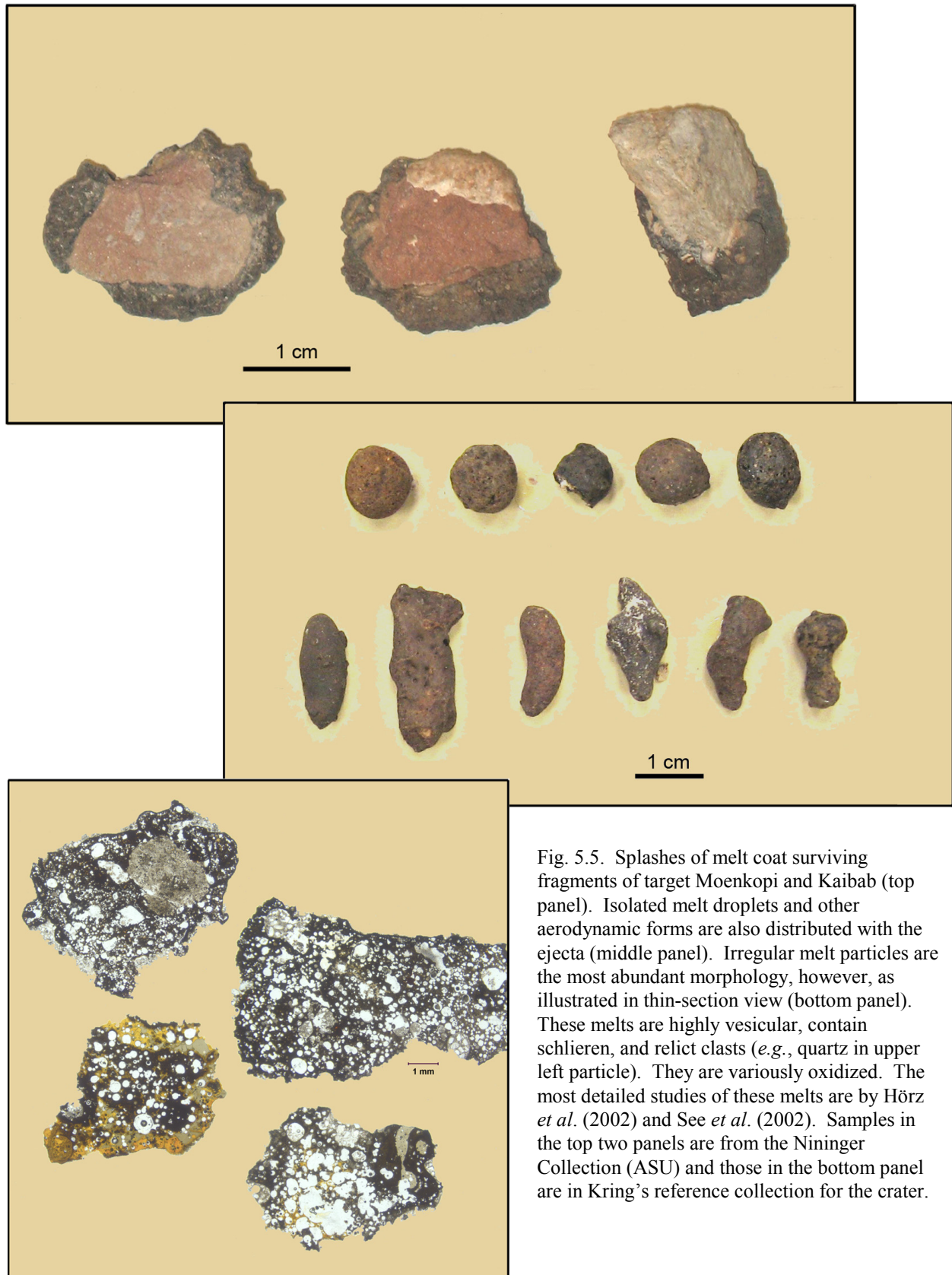


Fig. 5.5. Splashes of melt coat surviving fragments of target Moenkopi and Kaibab (top panel). Isolated melt droplets and other aerodynamic forms are also distributed with the ejecta (middle panel). Irregular melt particles are the most abundant morphology, however, as illustrated in thin-section view (bottom panel). These melts are highly vesicular, contain schlieren, and relict clasts (*e.g.*, quartz in upper left particle). They are variously oxidized. The most detailed studies of these melts are by Hörz *et al.* (2002) and See *et al.* (2002). Samples in the top two panels are from the Nininger Collection (ASU) and those in the bottom panel are in Kring's reference collection for the crater.

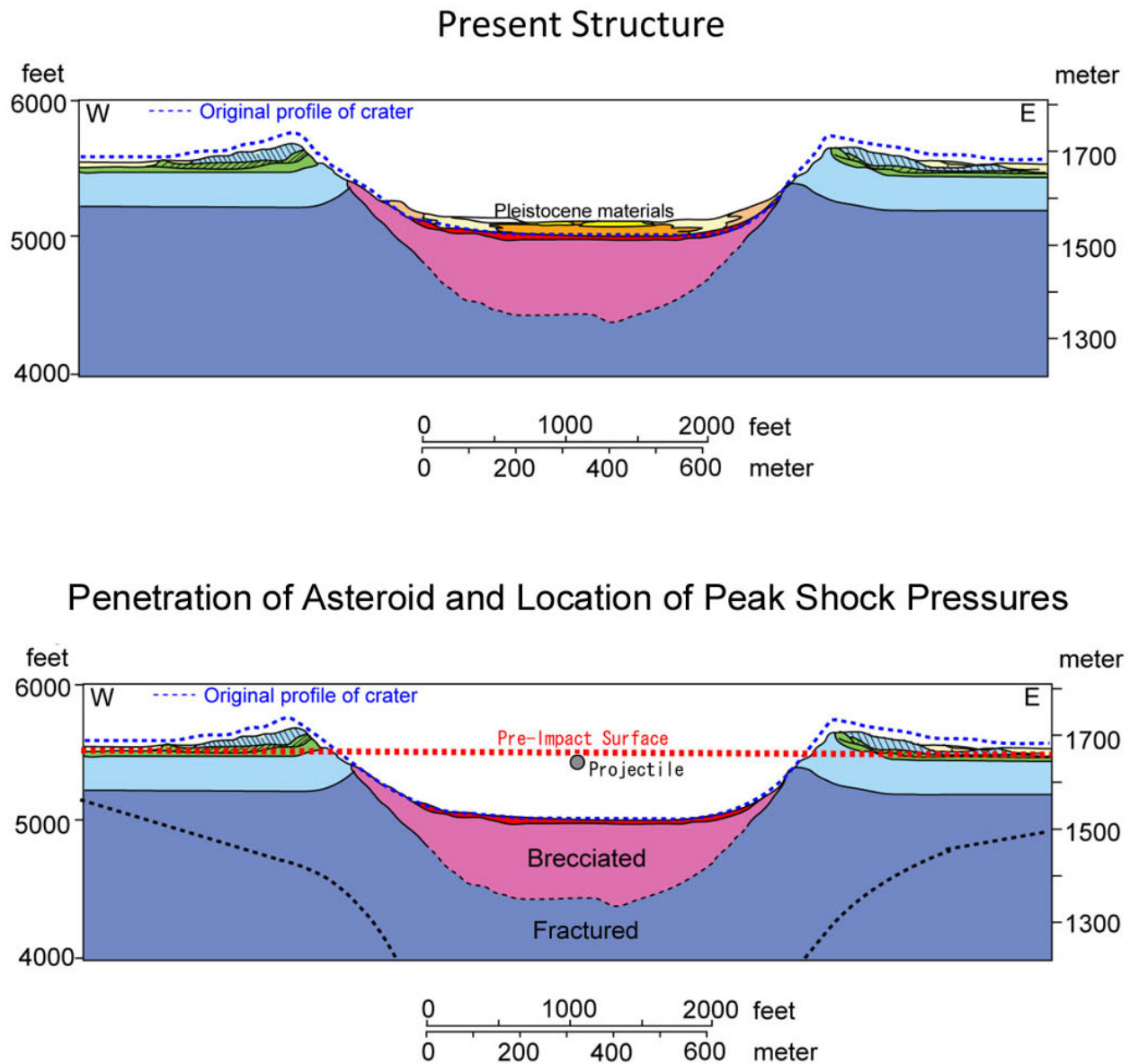


Fig. 5.6. These schematic cross-sections of the crater illustrate the current crater form (top) and the size of the impacting iron asteroid relative to that of the crater (bottom). The lower panel also illustrates the location of the impact explosion relative to locations on the crater rim and the crater floor. I thank Takafumi Niihara for pulling together this illustration for one of our training exercises for postdoctoral researchers.

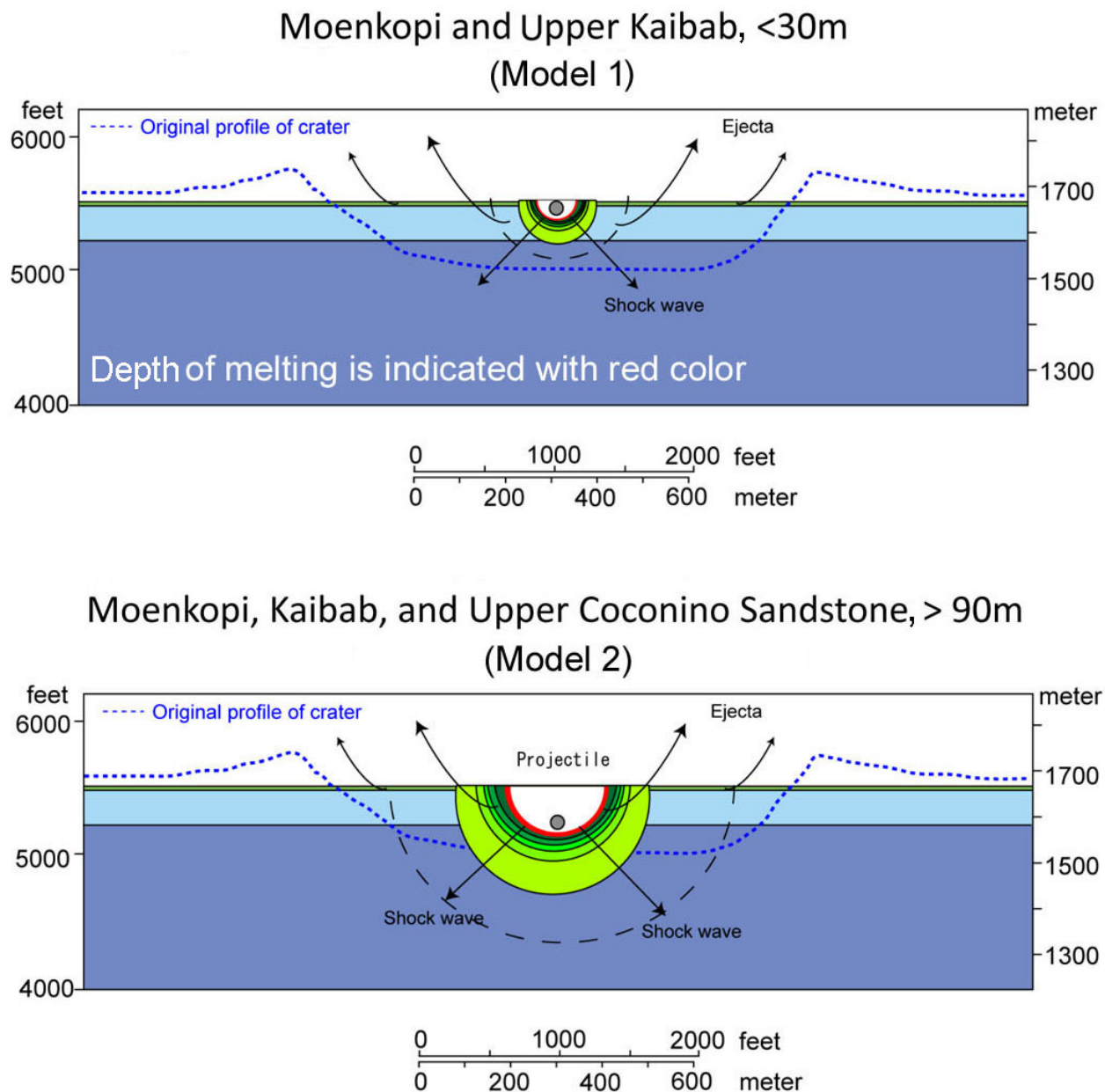


Fig. 5.7. Based on the compositions of impact melt particles, Hörz *et al.* (2002) suggested different depths of melting. One composition suggested a mixture of 55% Moenkopi, 40% quartz-rich upper Kaibab, and 5% meteorite. Two other compositions suggested different model depths of melting. In both cases, the dominant component (50 to 70%) of the melt particles is degassed sandy carbonate of the Kaibab formation, along with a greater proportion (15 to 20%) of meteoritic material. Those melts are also slightly more siliceous than average Kaibab, so Model 1 proposes a larger fraction of the quartz-rich upper Kaibab (top panel), whereas Model 2 proposes an additional silica-rich component from the underlying Coconino sandstone (bottom panel). In Model 1, the depth of melting is <30 m, while that in Model 2 is >90 m. As noted, the melts entrain abundant iron from the impacting asteroid, which is schematically represented by the projectile remaining adjacent to the melt. This schematic representation does not imply the asteroid is buried in the floor of the crater; indeed, large fractions of the asteroid were blown out of the crater and disseminated. I thank Takafumi Niihara for pulling together this illustration for one of our training exercises for postdoctoral researchers. Readers may want to compare these geochemistry-constrained melting depths with calculated shock pressures in a numerical model (Fig. 4.10), which favors Model 1.

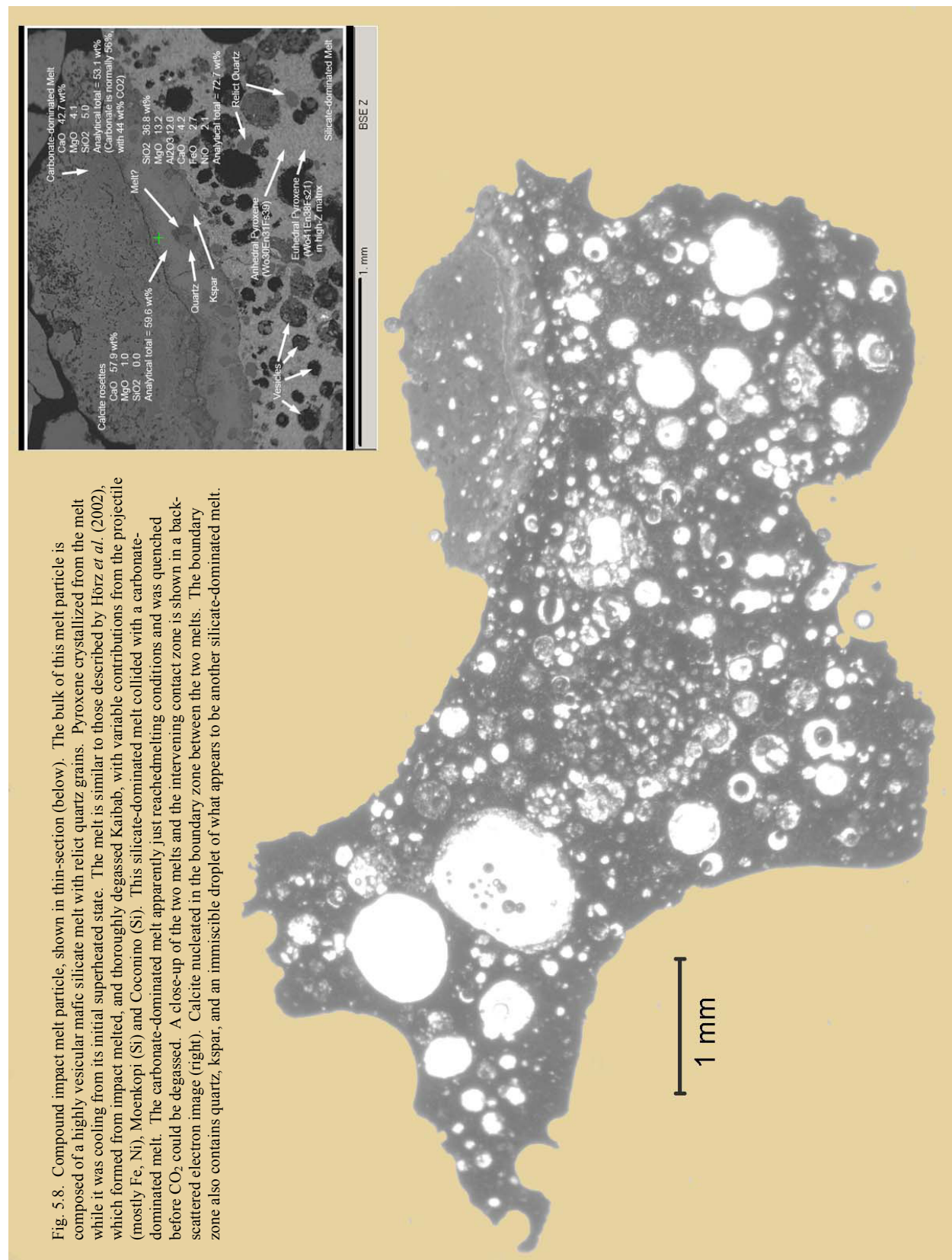


Fig. 5.8. Compound impact melt particle, shown in thin-section (below). The bulk of this melt particle is composed of a highly vesicular mafic silicate melt with relict quartz grains. Pyroxene crystallized from the melt while it was cooling from its initial superheated state. The melt is similar to those described by Horz *et al.* (2002), which formed from impact melted, and thoroughly degassed Kaibab, with variable contributions from the projectile (mostly Fe, Ni), Moenkopi (Si) and Coconino (Si). This silicate-dominated melt collided with a carbonate-dominated melt. The carbonate-dominated melt apparently just reached melting conditions and was quenched before CO₂ could be degassed. A close-up of the two melts and the intervening contact zone is shown in a back-scattered electron image (right). Calcite nucleated in the boundary zone between the two melts. The boundary zone also contains quartz, kspars, and an immiscible droplet of what appears to be another silicate-dominated melt.

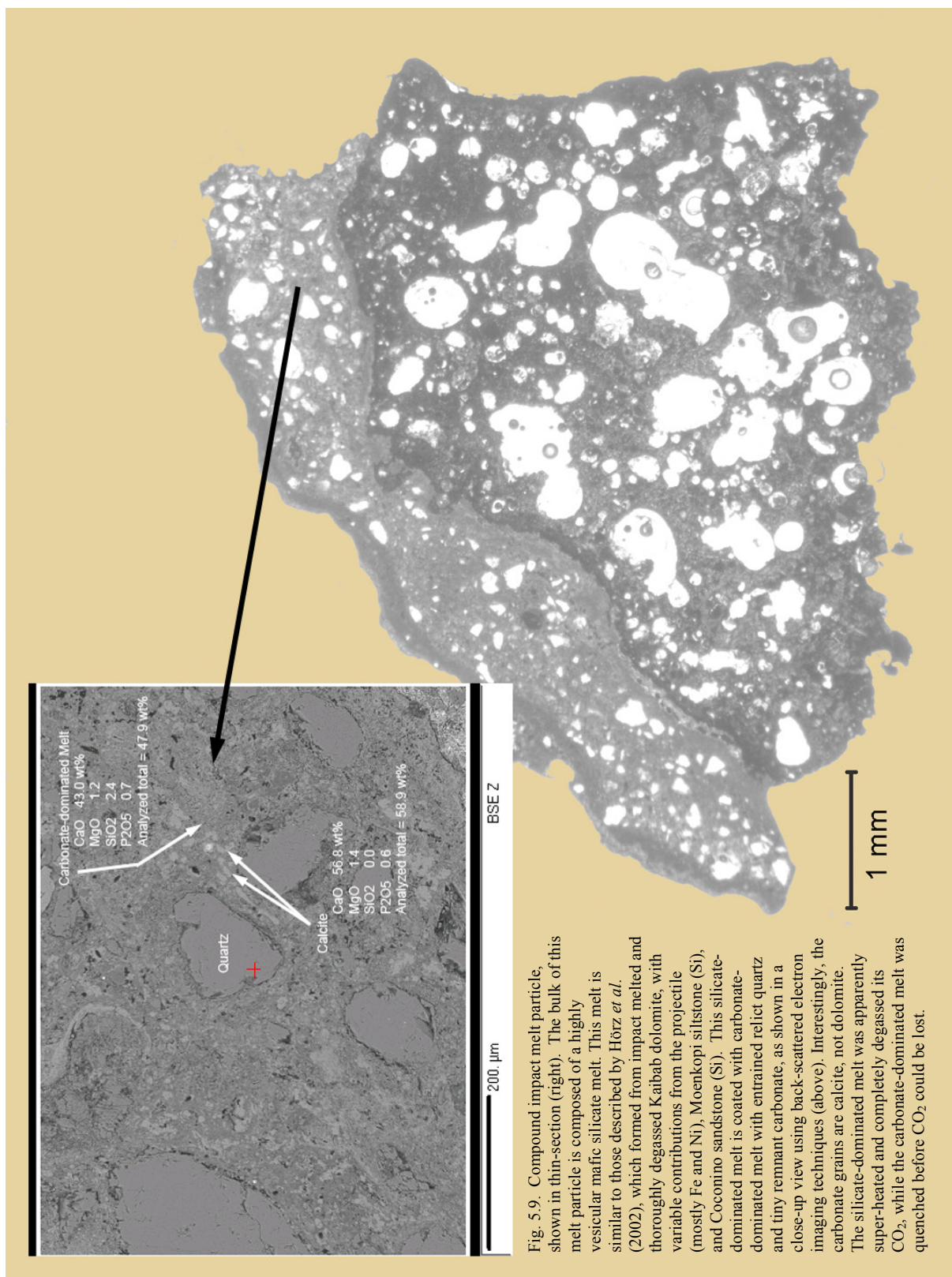


Fig. 5.9. Compound impact melt particle, shown in thin-section (right). The bulk of this melt particle is composed of a highly vesicular mafic silicate melt. This melt is similar to those described by Hörz *et al.* (2002), which formed from impact melted and thoroughly degassed Kaibab dolomite, with variable contributions from the projectile (mostly Fe and Ni), Moenkopi siltstone (Si), and Coconino sandstone (Si). This silicate-dominated melt is coated with carbonate-dominated melt with entrained relict quartz and tiny remnant carbonate, as shown in a close-up view using back-scattered electron imaging techniques (above). Interestingly, the carbonate grains are calcite, not dolomite. The silicate-dominated melt was apparently super-heated and completely degassed its CO₂, while the carbonate-dominated melt was quenched before CO₂ could be lost.

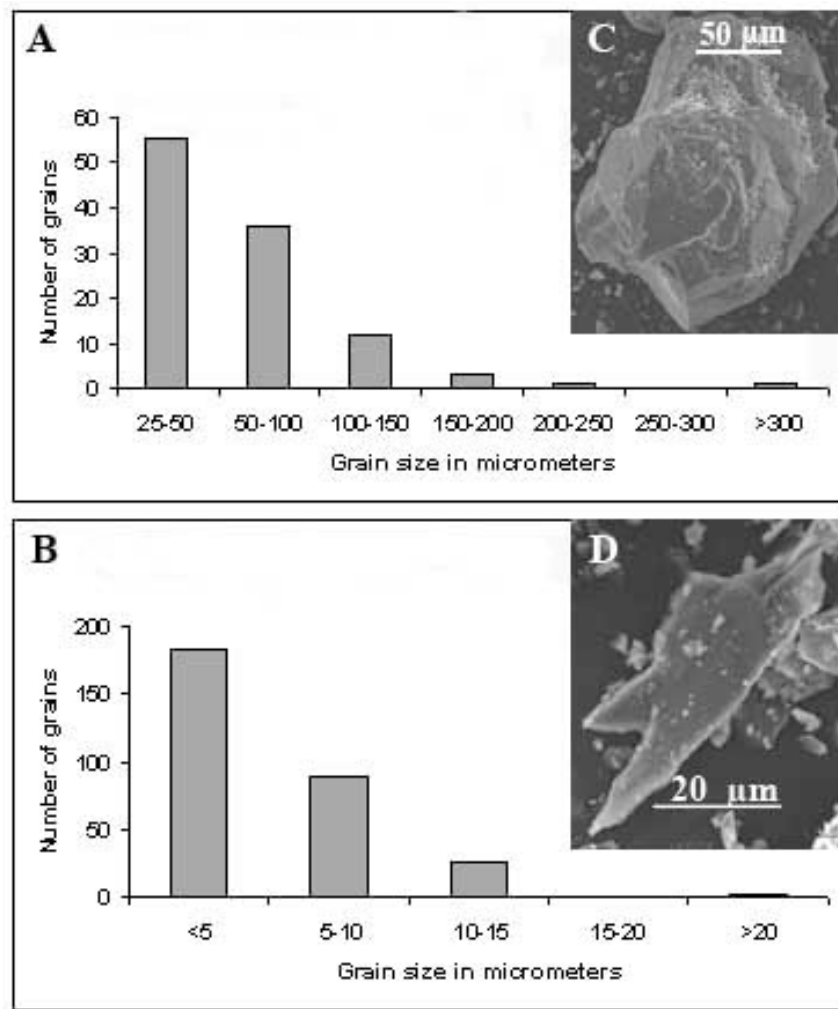


Fig. 5.10. To determine if a shock-melted, now glassy, carbonate component lies hidden in the matrix of the fallback breccia in the crater, the breccia matrix was examined by Cernok and Kring (2009). Here, the grain size distribution of that breccia matrix is shown; the number of small particles exceeds that of large particles on all scales. (A) Grain size distribution on a 500 μm scale. (B) Grain size distribution on a 20 μm scale. (C) Scanning Electron Microscope (SEM) image of a sub-rounded quartz crystal that represents the dominant component of the breccia matrix. (D) SEM image of an irregular silica shard. No carbonate glass fragments were detected.

6. Crater Rim Uplift and Crater Wall Collapse



The basic processes involved in crater rim uplift are understood, but there is a lot of evidence at the crater that has not been fully explored and may eventually paint a better picture of the processes that occur at the margins of transient impact craters.

It is clear from almost all vantage points that the horizontal strata in the pre-impact target were uplifted and now have outward dipping orientations. Pre-impact dips are estimated to have generally been <3 or 4° . The regional dip of the underlying Supai is 0.7° to the northeast (Roddy, 1978). Strata in the crater walls, however, typically dip 30 to 40° . The unusual outward dipping strata were noted by all of the early geologic explorers (*e.g.*, Foote, 1891; Gilbert, 1896; Barringer, 1905; Tilghman, 1905).

The uplift in the crater walls is a continuation of the processes that excavated the crater. Within the crater cavity, that flow was sufficient to uplift and launch material, producing the cavity that we now observe. The capacity to eject material decreased with radial distance. Immediately beyond the margins of the transient cavity, there was sufficient energy to generate flow and, hence, uplift of material, but not sufficient energy to eject it. Thus, we see uplift in the crater walls. Similar uplift occurs in the walls of chemical and nuclear explosion craters.

The uplifted walls did not collapse into their pre-impact horizontal positions after the excavation flow ceased. The uplift is preserved for several reasons, including intense fracturing in the crater walls that “bulk up” the rock, the injection of breccia into the crater walls from the crater cavity, and fault-facilitated stratigraphic thickening within the crater walls. The uplift is accentuated with ejecta, producing a rim that towers over the surrounding landscape.

Fracturing in the crater walls is evident (Fig. 6.1). A study of that fracturing (Kumar and Kring, 2008) found three organized sets of fracture orientations, in addition to irregularly-oriented fractures. Those orientations are conical, radial, and concentric relative to the center of the crater, which are similar to orientations produced experimentally in Coconino sandstone (Shoemaker *et al.*, 1963).

Estimates for the amount of bulking in the walls, however, are sketchy, but some insights are available from experimental explosion craters. For example, in the walls of a ~ 230 ft diameter crater produced by an 85-ton chemical explosion in volcanic rock (Pre-Schooner II; Frandsen, 1967), the bulk density declined by 27, 37, and 47% in three trenches cut through the crater wall. The average (37%) bulking factor measured in the crater walls is similar to the bulking factor measured in ejecta on the crater's flanks (38%) and in fallback ejecta within the crater (37%). These are generally higher values than those used by investigators at Barringer Crater. Regan and Hinze (1975) estimated a 5% density decrease (*e.g.*, 2.18 vs. 2.30 g/cm³) in the crater breccia lens relative to pre-impact rock, based on a gravity study. This 5% bulking factor has been applied by others (Roddy *et al.*, 1975). A similar bulking value (6 to 10%) was obtained with a single direct density measurement of crater rim ejecta (Walters, 1966). If these bulking values for the breccia lens and ejecta are approximately the same as that in the crater wall, then part of the uplift at Barringer Crater is due to bulking. However, bulking is apparently a smaller component of rim uplift at Barringer Crater than it is around some experimental explosion craters.

The only other data point we have thus far for the amount of brecciation in the crater walls is an observation made by Haines (1966). In core recovered from one of the NASA-sponsored boreholes (MCC-4; Chapter 2), he logged 1,059 fractures in 107.4 m. These were horizontal fractures with an

average spacing of 2 to 3 inches. Having examined material from other sites in that particular drilling campaign, he apparently believed the fractures were a property of the rock, rather than a drilling artifact.

In addition to this *in situ* brecciation and bulking of the crater walls, injected breccias from the crater cavity have also been proposed as a mechanism for maintaining crater rim uplift. Barringer (1905) was the first person to articulate the idea, suggesting that the crushed silica he observed beneath lake sediments and in ejecta was also propelled beneath the uplifted limestone and red sandstone walls. As discussed in Chapter 4, a deep borehole into the crater wall from the south crater rim encountered injected material, including fragments of the asteroid.

Structural uplift has also been attributed to a variety of faults (*e.g.*, Shoemaker, 1960; Shoemaker and Kieffer, 1974; Roddy, 1977). They are often called “thrust” faults, to capture the idea that material is thrust into the crater walls or up the crater walls. The faults are not, however, always technically thrust faults. The term overthrust has also been used to describe structural features at craters, particularly around experimental explosion craters, but this term is applied to an overturned sequence of debris on the crater rim, not structure within the crater wall. The overturned sequence on the crater rim will be discussed in the following chapter.

Interpreting structure in crater walls is complicated, because the crater wall has been rotated during uplift, in addition to being faulted. The relative timing of faulting and rotation still needs to be examined along many of the faults now exposed in the crater walls. Some options include (Fig. 6.2): (a) An apparent thrust fault, produced by a normal fault along which the foot-wall moved up and outward from the crater, which was then rotated during crater wall uplift. (b) Reverse or thrust fault along which lower strata were moved down and outward from the crater and then rotated during crater wall uplift, possibly forming an anticline with a radially-directed plunge line at the top of the crater wall. (c) Thrust fault produced after crater wall uplift and outward dipping rotation; in this case there should be a rupture of the Moenkopi beneath the ejecta blanket. (d-e) High-angle thrust fault or reverse fault that essentially moves material up the crater wall, possibly forming an anticline with a radially-directed plunge line at the top of the crater wall. This type of fault would be produced during crater flow uplift, although it is unclear whether it would occur early, late, or throughout the uplift process. We (Thomas Kenkmann, Michael Poelchau, and I) have observed a fault within one ejected block of debris near the museum complex. Assuming the block was excavated during crater formation (rather than museum construction), the block indicates that thrusting occurs during the compression and excavation phases, not during a modification phase of crater formation.

Good structural descriptions of most faults and their orientations relative to bedding do not yet exist. The best described fault occurs in the north-northeast wall of the crater, within the Kaibab-Alpha (Shoemaker and Kieffer, 1974). In this case, the fault dips about 45°, while the beds in the upper plate dip 30°. The sequence is thickened and forms a wedge that produces an anticline in the uppermost Kaibab, Moenkopi, and impact ejecta. This forms one of the highest uplifted points along the crater rim. (See Chapter 17 for locations with a good view of this structure.) These observations are consistent with Fig. 6.2b. Two other options (a and c) do not satisfy observations, because they thin the sequence and also have faults with shallower dips than bedding. For this particular location, options (d-e) are also not appropriate, because the fault dips away from crater center, not towards crater center. However, Roddy (1977) indicates that (d-e) occur elsewhere in the crater. It is also possible that complex (multi-)fault systems were activated. For example, a wedge shaped block might be thrust into the expanding wall of the crater (Fig. 6.3; Poelchau *et al.*, 2009), bounded by a thrust fault on top and a normal fault on the base, that then maintains crater wall uplift after excavation flow has ceased.

Thrust faulting is evident along the crater walls, with offsets of fractions of a meter to several meters. They cross-cut strata in both the Kaibab-Alpha and Kaibab-Beta. It is unknown if additional fault-bounded repetition of strata occurs in the lower crater walls of the covered Coconino. The faults, however, are poorly described and a much better structural description is needed. Qualitatively, a significant fraction of crater rim uplift is attributable to thrust faults. More work is needed to quantify this contribution.

One of the attributes of a fault-thickened section is an anticline in the overlying crater wall bedrock and overlying ejecta. These are particularly evident at Barringer Point and Moon Mountain, two of the highest topographic points around the rim of the crater. Both are illustrated in the trail guides for the crater (Chapters 17 and 19). The thrust wedges created a circumferentially-distributed series of alternating anticlines and synclines (Fig. 6.4). These structures were also cross-cut by tear faults in some portions of the crater walls. Drag folds along those tear faults accentuated the anticline-syncline structure (*e.g.*, in the northwest corner of the crater).

All of these structures were produced during the excavation phase of crater formation, which moved material upward along the crater wall. In contrast, the subsequent modification stage provided an opportunity for material to begin moving down along the crater wall. This is the source of the breccia lens on the crater floor. Large slabs of bedrock also slumped down the crater walls. Drilling revealed that at least one large slab of Coconino was incorporated into the breccia lens. Other fragments of slumped rock were left hanging on the crater walls (Fig. 6.5), bounded by authigenic breccias that were created by shear while they moved. Neither the blocks nor the authigenic breccias exposed in the crater walls are well-documented. (To be clear, some authigenic breccias were produced during the thrusting described above. Thus, there are two generations of authigenic breccias.)

Other types of shear within and between strata generated during crater excavation and modification are preserved in blocks that bound the crater wall. “Chatter” marks are found within blocks of Kaibab (Fig. 6.6). These chatter marks may be small drag folds that were created along a shear plane; they have been observed at other craters in sedimentary targets (Thomas Kenkmann, personal communication, 2007). Slippage lineations created when rock broke along shear planes have also been found (with Michael Poelchau and Thomas Kenkmann). The direction of shear is indicated by a sharp leading edge where the rock popped apart (Fig. 6.6). After further study, it is hoped that these newly identified structures will assist with an enhanced description of crater flow.

Collectively, there are four sources of a topographically-high crater rim: (i) uplift of crater wall strata; (ii) bulking of those strata; (iii) thrusting of units into the crater wall beneath the rim; and (iv) deposition of an overturned ejecta sequence, the latter of which is addressed in the next chapter.

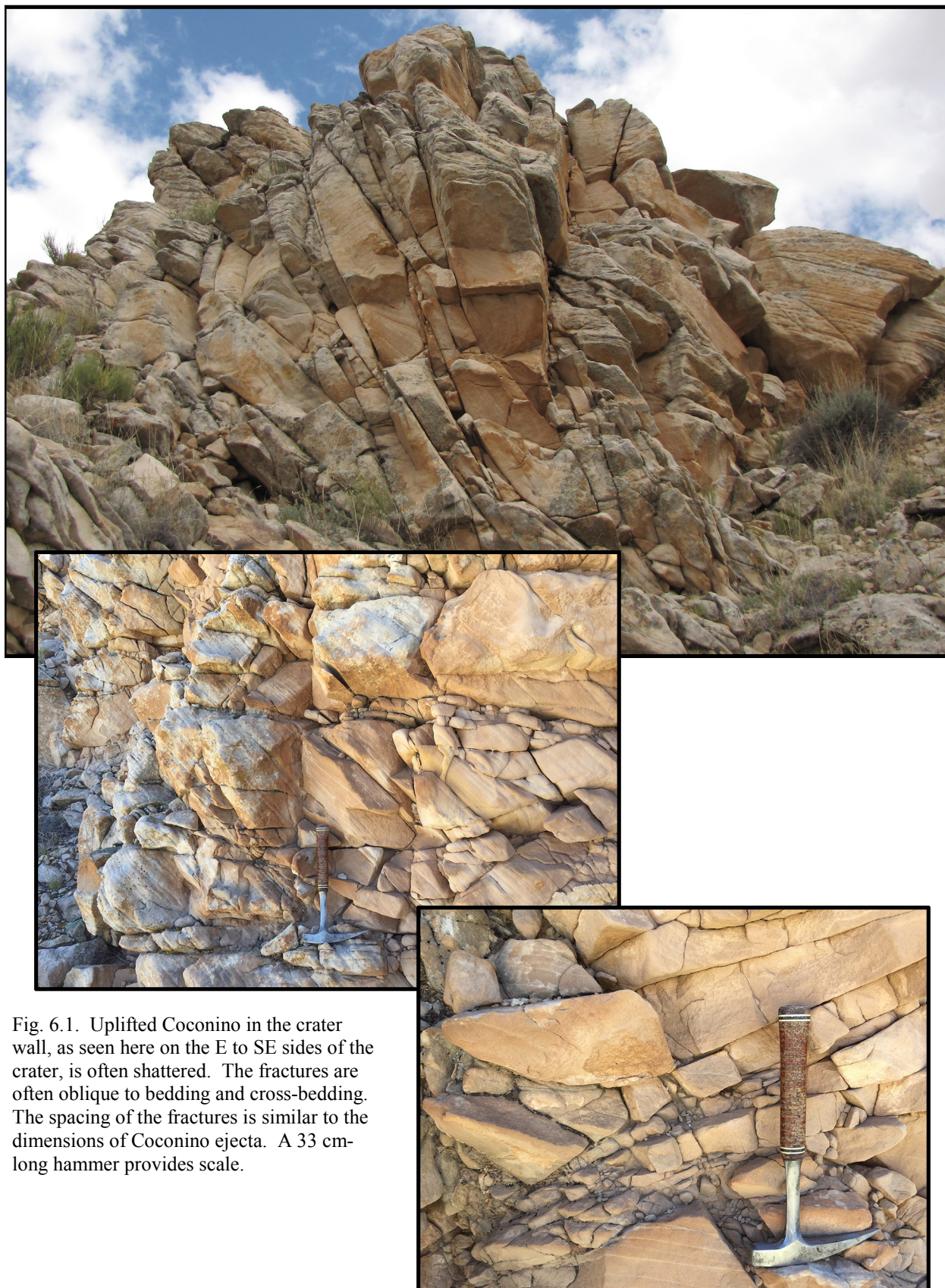
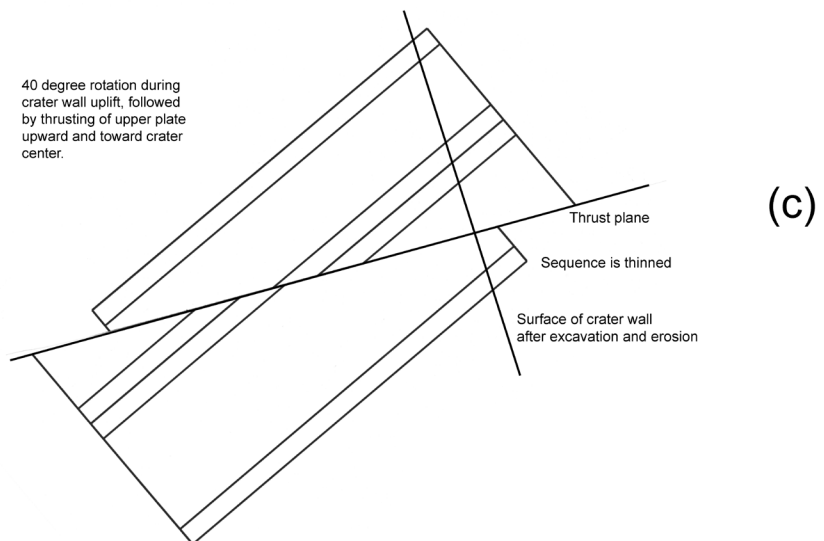
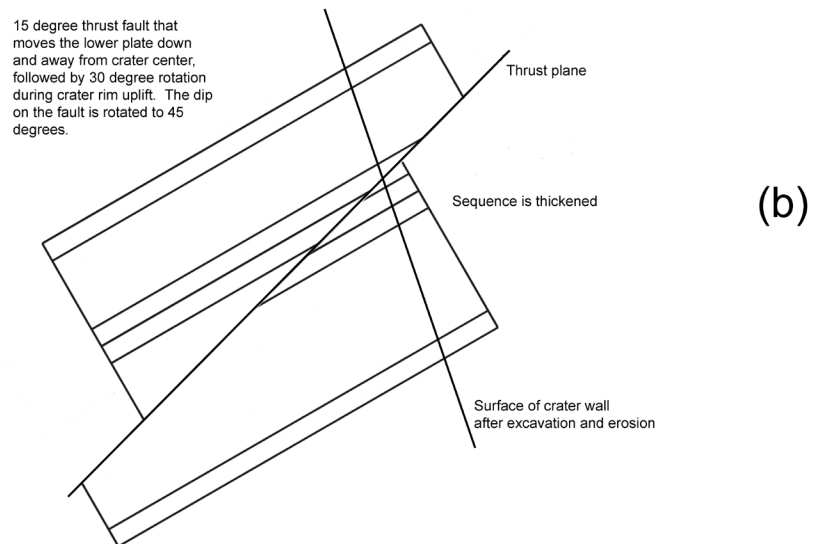
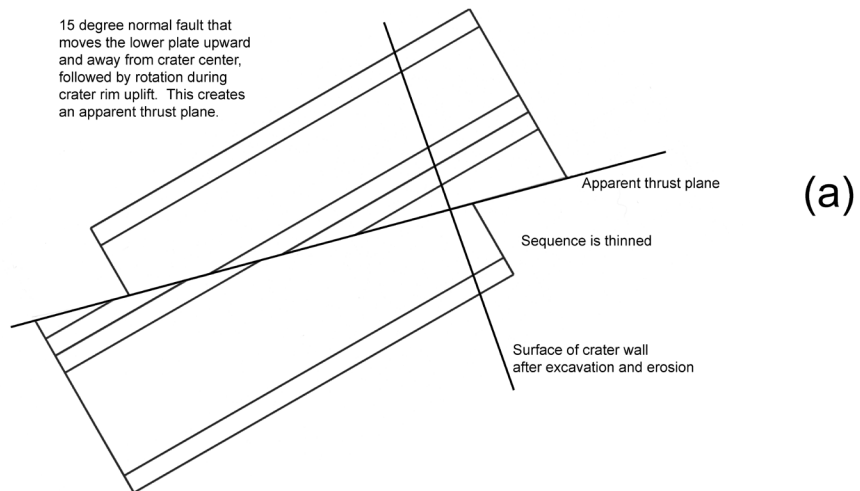


Fig. 6.1. Uplifted Coconino in the crater wall, as seen here on the E to SE sides of the crater, is often shattered. The fractures are often oblique to bedding and cross-bedding. The spacing of the fractures is similar to the dimensions of Coconino ejecta. A 33 cm-long hammer provides scale.



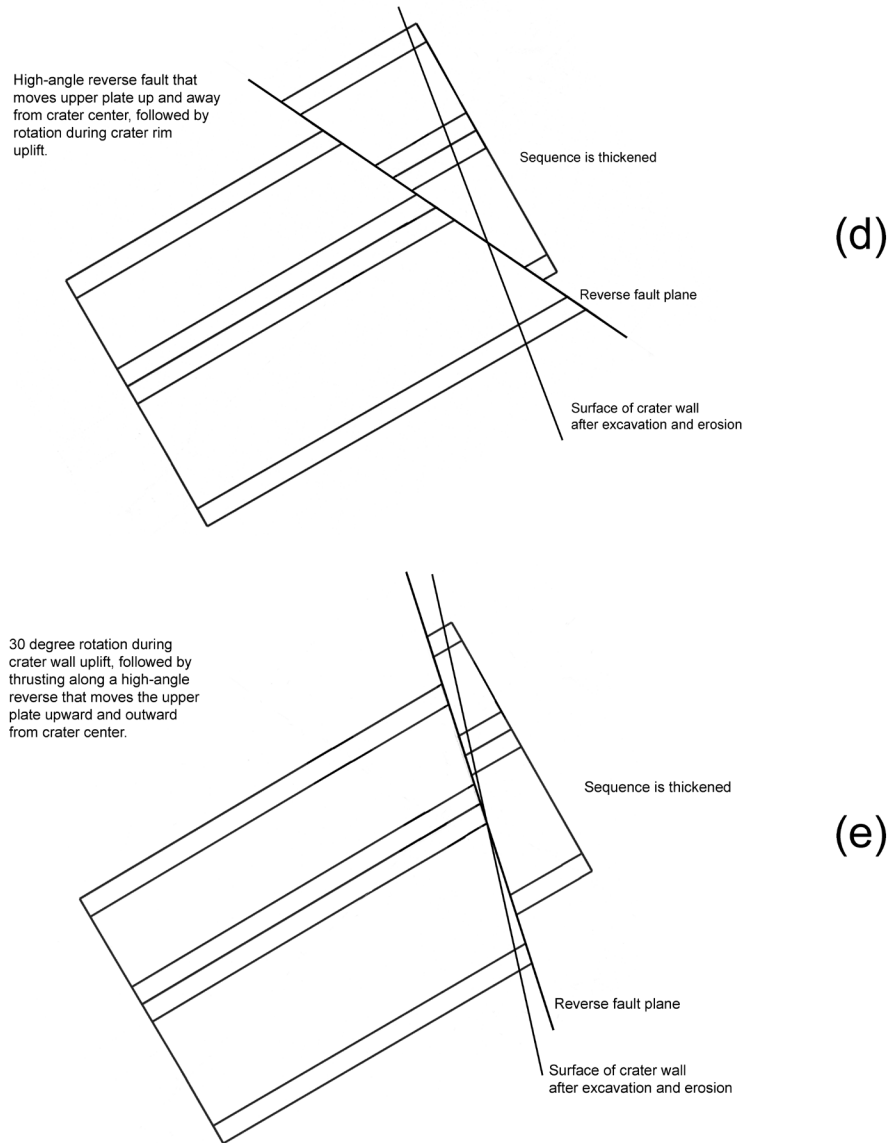


Fig. 6.2. Schematic block diagrams of possible fault movements and rotation during crater excavation and rim uplift (a-c, previous page; d-e, this page). A thrust fault (b) that moves the lower plate down and away from crater center, followed by rotation during rim uplift, is consistent with observations in the north-northeast crater wall. High-angle thrusts or reverse faults (d-e) that move the upper plate up and away from crater center have also been proposed for some of the features at the crater (Roddy, 1977).

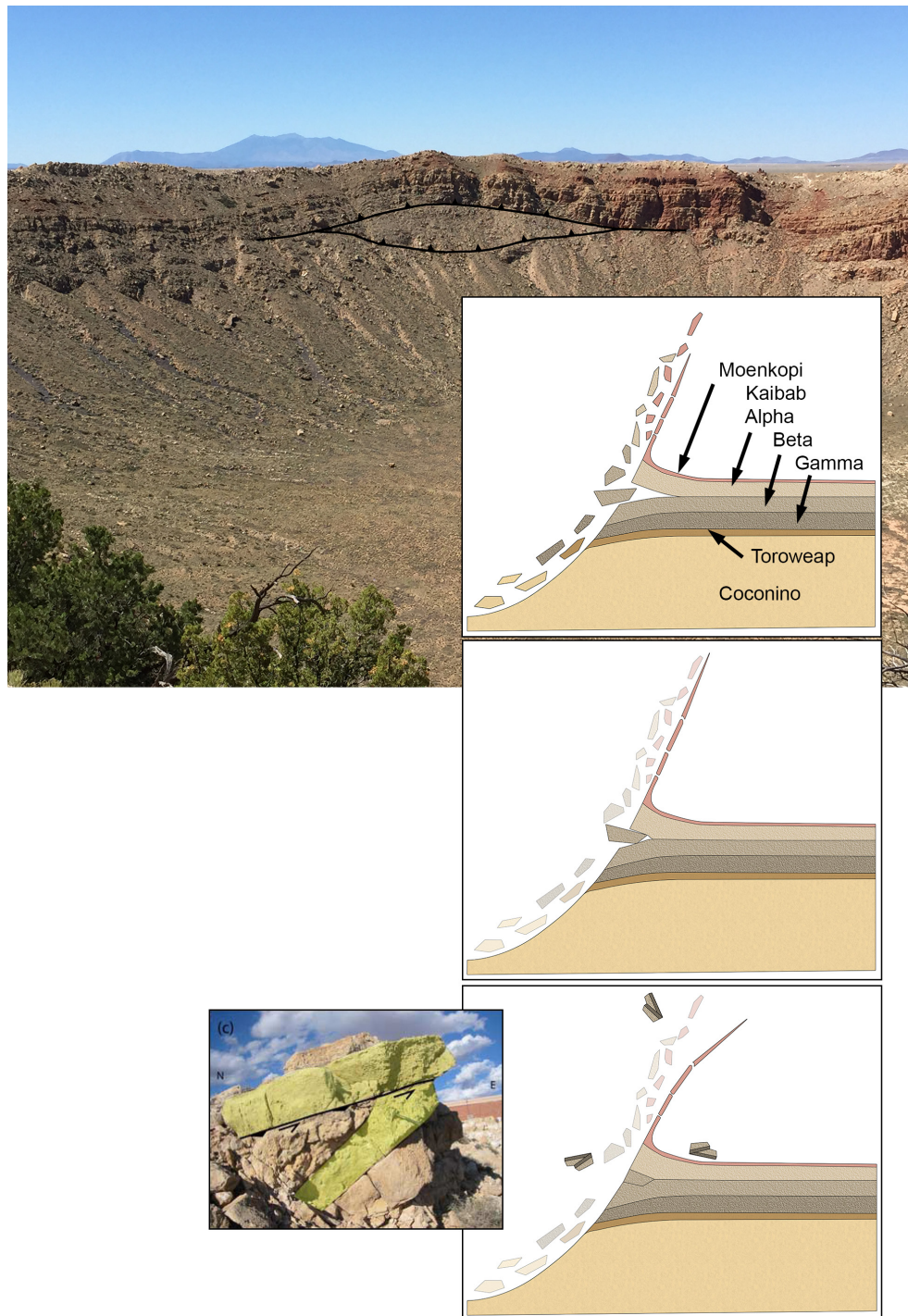


Fig. 6.3. Photograph of a thrust wedge beneath Barringer point (top), with schematic crater wall cross-sections illustrating how a block of Kaibab Beta was thrust into crater wall (top and middle insets), where it now resides (lower right inset). Wedges of rock are thrust into the crater wall in several locations, producing anticlinal structures (Fig. 6.4). As previously shown by Poelchau *et al.* (2009), one of those thrust ramps was ejected from the crater (lower right inset) and lies near the museum (lower left inset). The panels with the schematic diagrams use the same color scheme for Moenkopi, Toroweap, and Coconino used in other diagrams in the guidebook, while the Kaibab has been further subdivided to illustrate that Kaibab Beta is the unit thrust into the crater wall beneath Barringer Point.

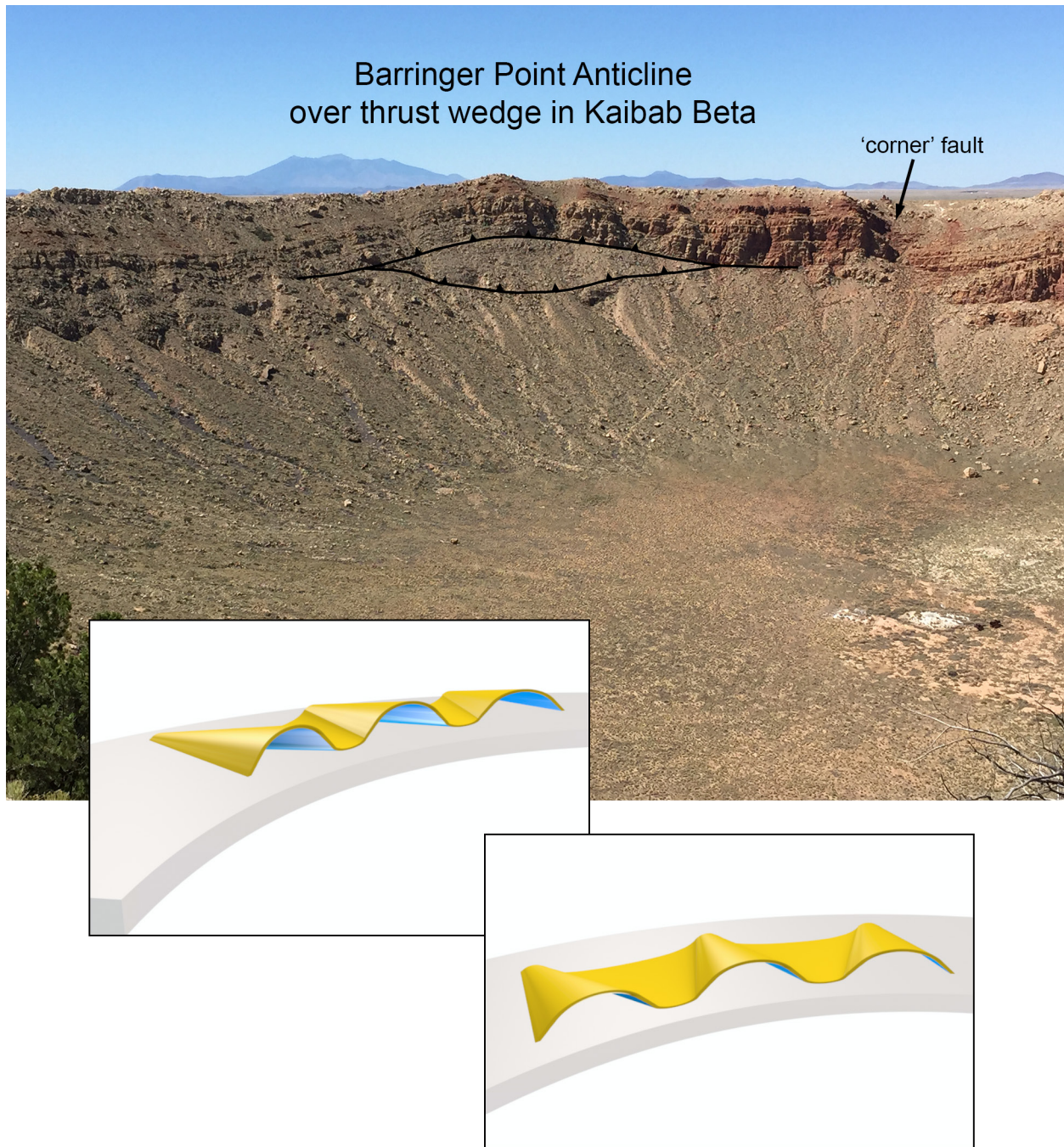


Fig. 6.4. (top) A wedge of thinly-bedded Kaibab Beta is thrust into the Kaibab sequence in the WNW crater wall, producing an anticline in the overlying Kaibab Alpha and Moenkopi. (left inset) Uplifted crater walls can have an alternating anticline and syncline structure, which at Barringer Meteorite Crater is ruptured by cross-cutting faults, such as the one in the NW corner of the crater. (lower right inset) That anticline-syncline structure produces an undulating upper surface. Ejecta can potentially fill troughs on the surface of the synclines, producing, for example, lobes of Coconino debris on top of the overturned Kaibab ejecta on the north and east sides of the crater. See Figs. 8.4 and 17.12.



Fig. 6.5. A portion of the crater wall beneath the museum platform. A sequence of Kaibab (upper right) and Coconino (center) sit on the crater wall and were later covered with colluvium (far left) deposited from the upper crater wall. Portions of the Coconino are shattered. A portion of the Kaibab also has a cataclastic texture. The entire block may sit on a fault surface along which it moved up and/or down the crater wall during the excavation and/or modification phases, respectively. This is one of those curious structural vignettes at the crater needing a little more attention.

Fig. 6.6. Elements of shear in blocks of Kaibab dolomite. “Chatter” marks are visible on some surfaces. In the upper right panel, the marks occur on top of an outcrop. They are located between and are oriented perpendicular to the arrows. In the middle panel (below), the marks are visible on a near-vertical block of dolomite along the crater wall; the chatter marks trend horizontally across the image. Slippage lineations also occur along shear planes (lower right panel), in this case indicating upward shear.



7. Overturned Rim Sequence



Shock pressures overwhelm the material strength of rock in the immediate vicinity of an impact event. Thus, rock under the influence of shock does not behave in the immovable, brittle fashion that we normally assign to it. The excavation flow (Fig. 4.8 and 4.9) that generated the crater produced a nearly instantaneous folding of the bedrock in the rim of the crater, which is partly responsible for the height of the rim above the surrounding plain. Structural overturning of the strata was noted by Barringer (1910) in the northwest corner of the crater: "... the strata exposed in the walls of the crater gradually increase from 5 degrees up to vertical and in one place they are slightly overturned." In that same paper, he also characterizes the stratigraphic consequences, writing that a deeper sandstone is on top of shallower sandstone, which is on top of even shallower limestone. Shoemaker (1960) pointed out that similar overturned sequences are produced in the rims of nuclear explosion craters (*e.g.*, the crater produced by the ~1 kt Ess or Teapot Ess explosion in 1955). An overturned rim sequence is now recognized as one of the hallmarks of an impact crater.

Traditionally, students are introduced to this overturning in a study of the Moenkopi in the northeast rim of the crater, where cross-bedded laminae within the siltstone can be used to identify the overturned sequence. Additional details of those outcrops are provided in the trail guide for the east crater rim (Chapter 17). The overturned sequence can, however, be seen around the entire crater. For example, on the south rim of the crater, one finds the Wupatki and Moqui members of the Moenkopi repeated and overturned (Fig. 7.1).

Before examining another example of the overturned sequence, it is perhaps useful to first examine a schematic diagram that illustrates the structural and stratigraphic context of the overturned rim sequence. In structural terms, the overturned rim is a syncline with a circumferential axial trace or compound syncline, because there are actually two folds involved. The first is associated with the uplift and outward tilting of the beds in the crater walls (as described in the last chapter) and the second is with the complete overturning of those strata. With regard to the latter, there are actually two types of overturning evident in the crater rim (Fig. 7.2). Structural overturning occurs when the dips of the beds pass a vertical plane (and, thus, have dips exceeding 90°). Stratigraphic overturning occurs when the dips of the beds are rotated 90° beyond the outward dip of the lower limb of the fold. Thus, if the outward dips of the rim strata are, say, 35°, stratigraphic overturning occurs when the beds exceed dips of 125° (90° + 35°). Indeed, some strata will dip 215° (180° + 35°) on the overturned upper limb of that fold, relative to their pre-impact orientation.

Several locations exist on the east side of the crater where erosion reveals the fold hinge in the Kaibab and Moenkopi units. An example of a fold hinge in Moenkopi is shown in Fig. 7.3. The axial plane is within the fissile Moqui Member of the Moenkopi. In overturned sequences where the hinge is not exposed, it is often difficult to identify the axial plane because of the fissile nature of the Moqui. One often has to rely on the geopetal characteristics of the Wupatki Member to demonstrate the overturned stratigraphic context. This and other fold hinges are included in the trail guide for the east crater rim.

The Moenkopi is not everywhere exposed along the upper crater walls, because it is buried within the overturned Kaibab and Coconino. Access to the Moenkopi is facilitated by rim erosion, as illustrated in a series of time-steps in Fig. 7.4. As erosion cuts back into the crater walls, it removes fold hinges in the deeper layers (*e.g.*, Kaibab) and reveals overturned sequences in the shallower layers (*i.e.*, Moenkopi). Folds in both the Kaibab and Moenkopi are evident along the east crater rim. As discussed

further in the next chapter, the amount of erosion is still being debated, but Shoemaker (1974) argued that 40 ft (12 m) occurred on the outer flank of the northeast corner of the crater, which suggests a cut back of the inner crater wall probably also occurred in that area.

The Moenkopi exposed in upper crater walls will not everywhere be the same thickness. This partly reflects pre-impact topographical relief that existed on the Moenkopi, because it was the eroding surface unit on the landscape. It also is partly the result of structural thinning that occurred during the overturning process, which is manifest in a series of small faults in the overturned rim sequence.

The views in Fig. 7.4 are idealized. Hummocky ejecta and crater rays will modify the distribution, which will be discussed further in the next chapter. The amount of erosion that occurs is also variable. Consequently, as one circumnavigates the crater rim, one might be walking on Coconino (as in top panel of Fig. 7.4) or on Kaibab (as in bottom panel of Fig. 7.4). The amount of overturned debris on the rim crest varies accordingly. Roddy (1978) estimated the original rim was covered with $\sim 20 \pm 5$ m of debris, which is a structurally-thinned remnant of an excavated stratigraphic thickness of at least 88 m (corresponding to Kaibab and Moenkopi, which dominate the exposed rim sequence) and also much less than a total excavated stratigraphic thickness of 300 to 310 m (corresponding to Coconino, Toroweap, Kaibab, and Moenkopi). Currently, 0 to ~ 20 m of ejected debris survives on the current rim crest, depending on location around the crater. A greater fraction of the uplifted rim is the result of the uplifted strata beneath the overturned debris sequence, which is responsible for ~ 47 m of the uplift (Roddy, 1978).

Deviations from the idealized view of Fig. 7.4 are evident in the south rim of the crater (Kring *et al.*, 2011a,b). A portion of the Kaibab has been sheared radially outward, so that it is mostly missing from a portion of the rim. Radially outward shearing also carried a hinge in the overturned Coconino towards the south. Key outcrops revealing that motion are discussed further in Chapter 18, one of the trail guides. That motion may also provide a clue about impact trajectory (Kring *et al.*, 2011b), as discussed further in Chapter 10.

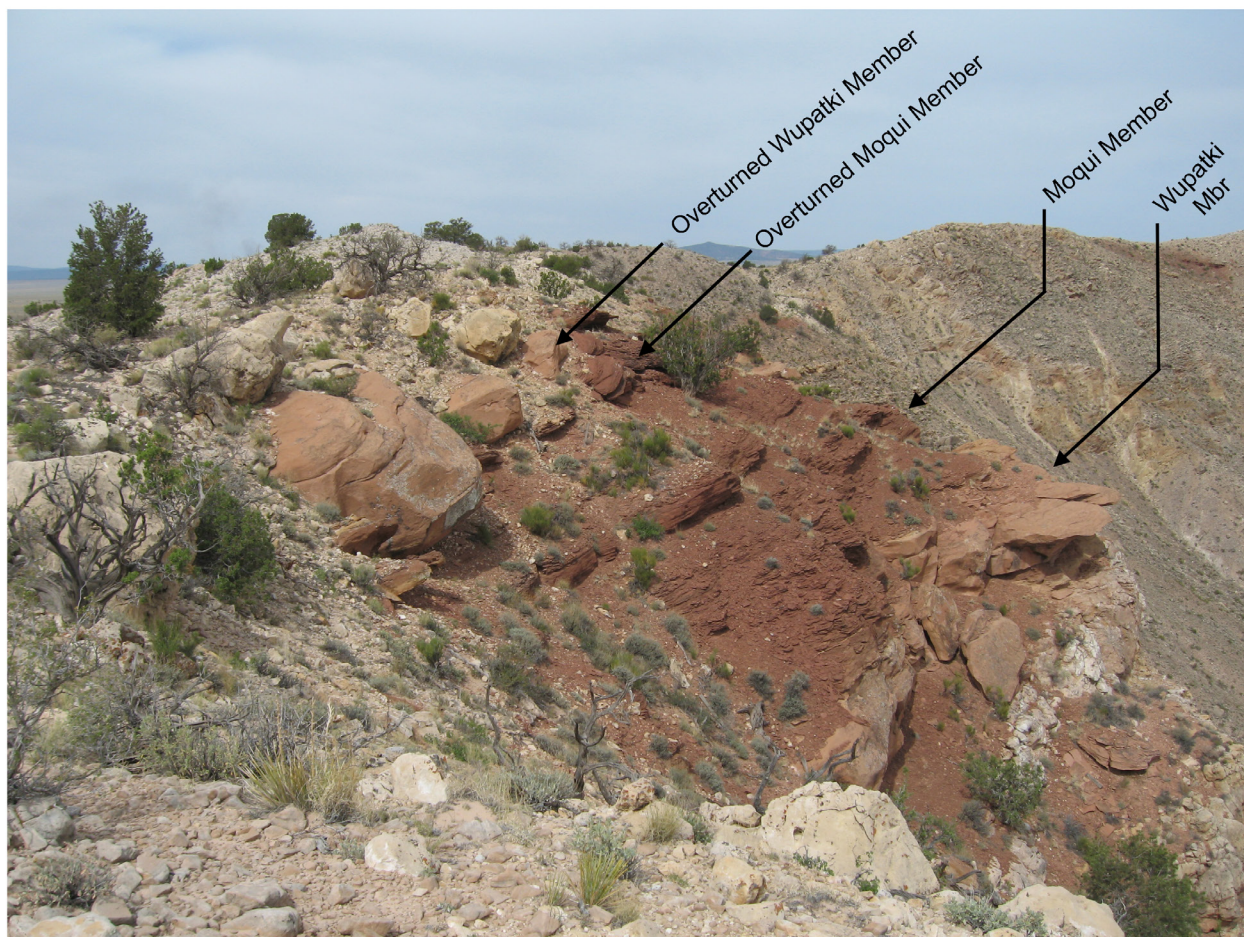


Fig. 7.1. Stratigraphic overturning of the Moenkopi Formation in the upper crater wall. The characteristic orbicular outcropping of the Wupatki Member sits on top of the Kaibab Formation (lower far right). Above the Wupatki is the fissile Moqui Member. The Wupatki-Moqui sequence is repeated, but overturned (center). Kaibab debris (upper far left) sits on top of the overturned Wupatki Member. Outcrop is on the south side of the crater. View is looking west.

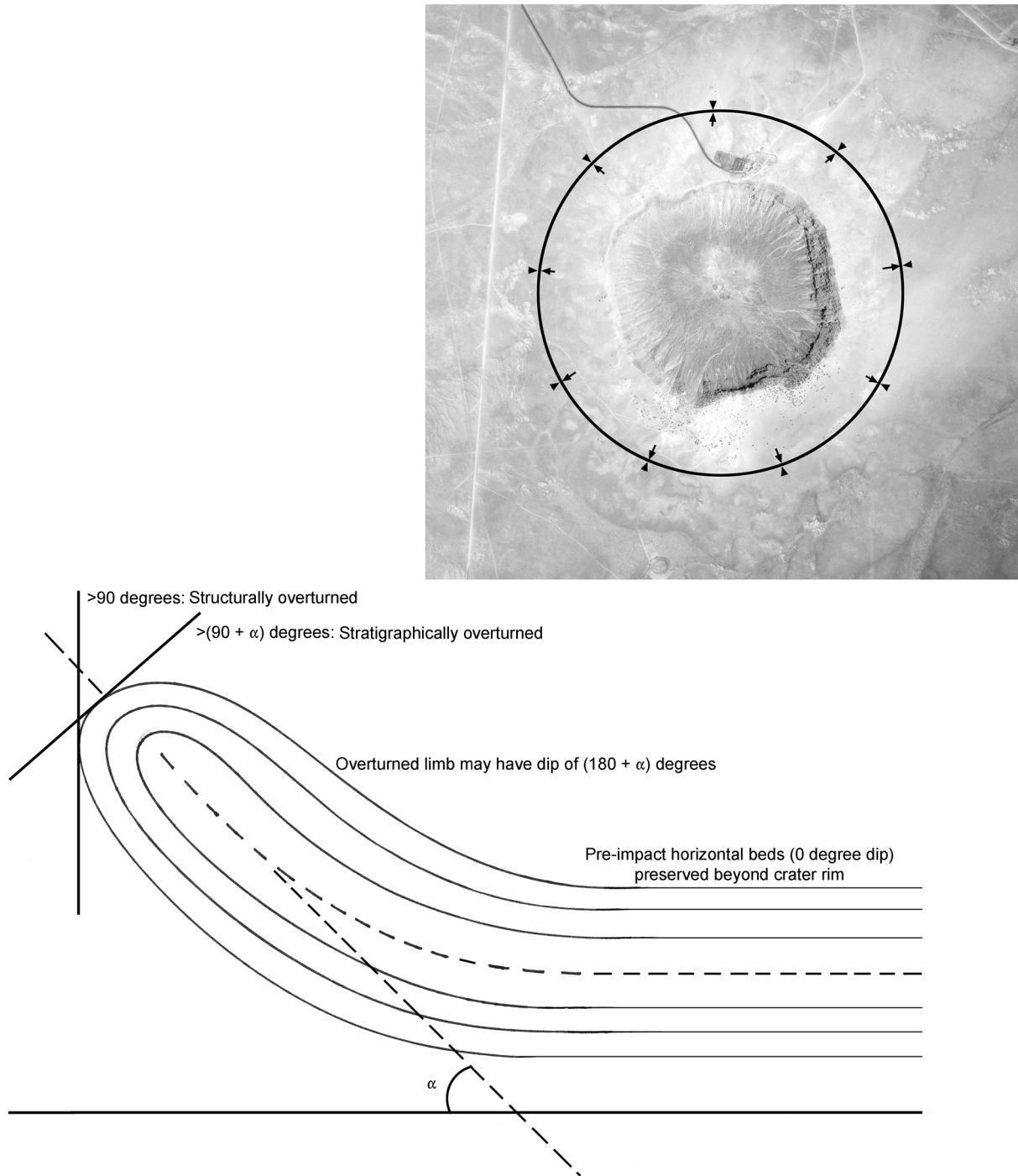


Fig. 7.2. Schematic diagram of the structural and stratigraphic overturning that occurs in the ring syncline of an impact crater rim (bottom). The axis of the ring syncline is not shown in the schematic diagram; it is perpendicular to the page and would trace a circle around the crater in a plan or map view. At Barringer Crater, the amount of uplift in the crater walls typically corresponds to an α of 35 to 40 degrees. The axial trace of the ring syncline at Barringer Crater is ~900 m from crater center or slightly more than 300 m beyond the crater rim (inset, upper right), based on the results of an intense drilling program (Roddy *et al.*, 1975) that penetrated the ejecta blanket and determined the elevation of subsurface bedrock. An independent measurement using ground-penetrating radar (Pilon *et al.*, 1991) suggests the axial trace may be slightly farther, ~400 m beyond the crater rim.

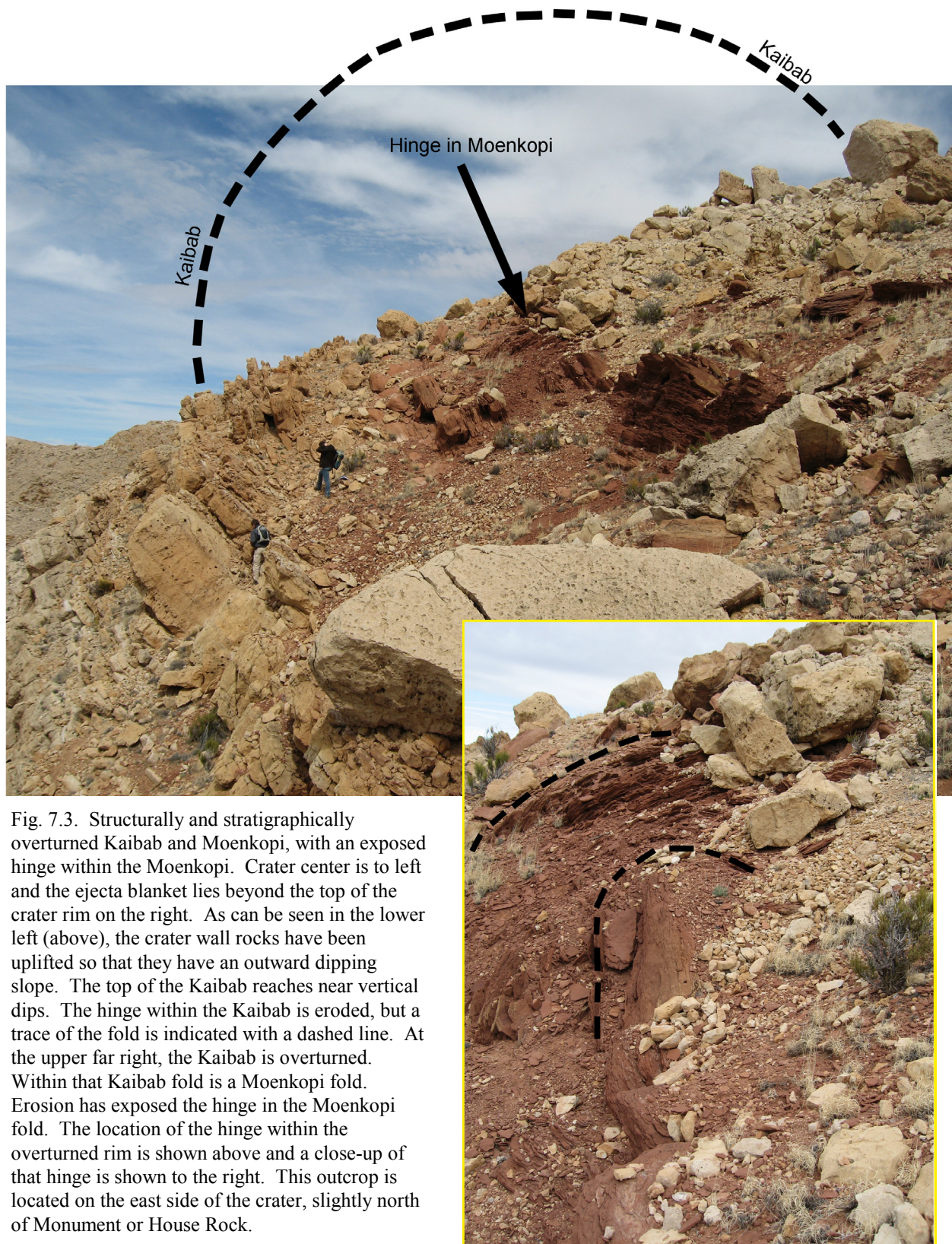


Fig. 7.3. Structurally and stratigraphically overturned Kaibab and Moenkopi, with an exposed hinge within the Moenkopi. Crater center is to left and the ejecta blanket lies beyond the top of the crater rim on the right. As can be seen in the lower left (above), the crater wall rocks have been uplifted so that they have an outward dipping slope. The top of the Kaibab reaches near vertical dips. The hinge within the Kaibab is eroded, but a trace of the fold is indicated with a dashed line. At the upper far right, the Kaibab is overturned. Within that Kaibab fold is a Moenkopi fold. Erosion has exposed the hinge in the Moenkopi fold. The location of the hinge within the overturned rim is shown above and a close-up of that hinge is shown to the right. This outcrop is located on the east side of the crater, slightly north of Monument or House Rock.

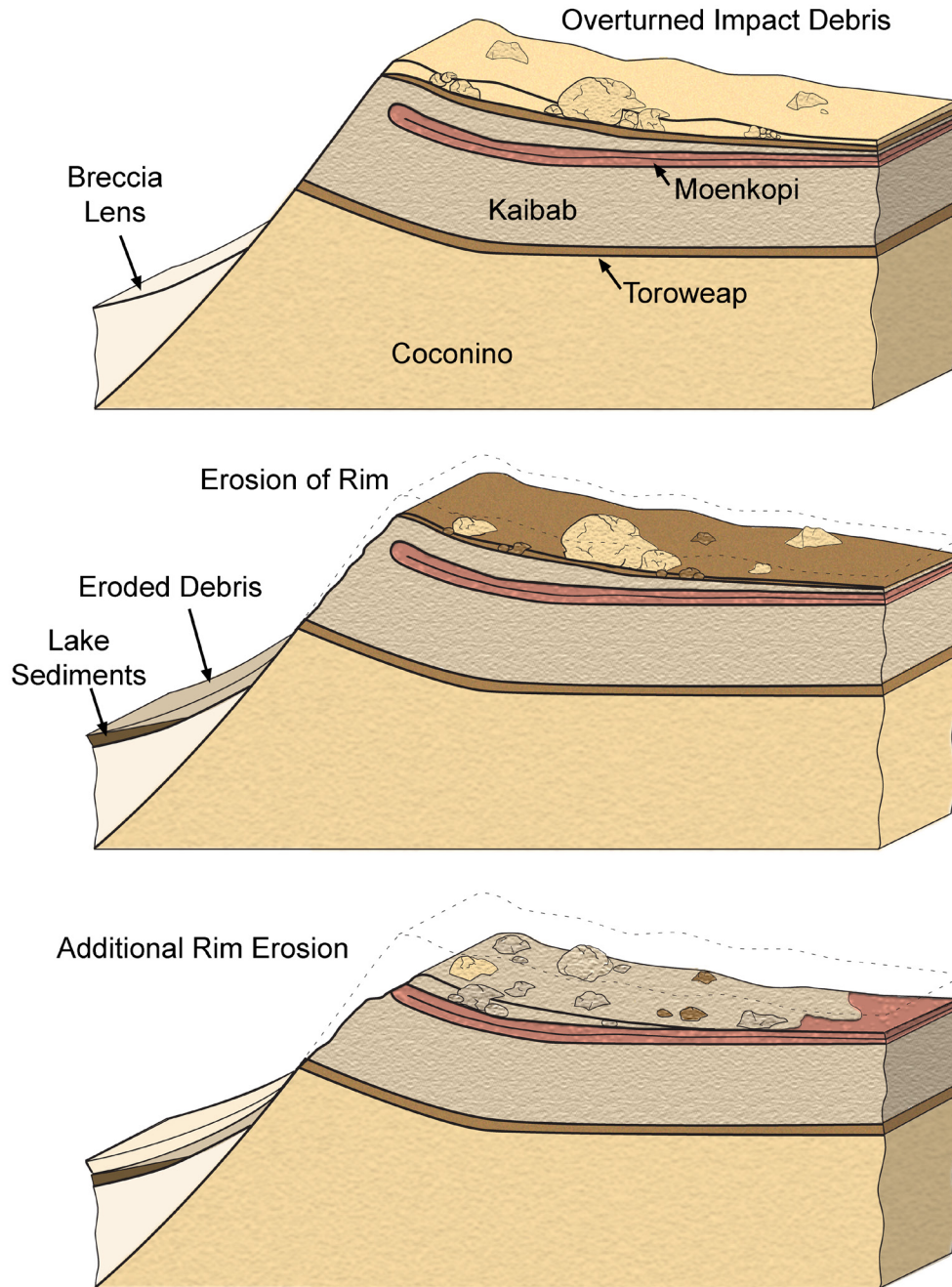


Fig. 7.4. Schematic illustration of the overturned rim sequence and its evolution during subsequent erosion. Immediately after impact, the rim is at its maximum height. The rim and ejecta blanket contain a complete overturned sequence of Moenkopi, Kaibab, Toroweap, and Coconino (top panel). This is an idealized view. Hummocky ejecta distribution and crater rays will modify this distribution. A breccia lens partially fills the crater. Over time, erosion of the rim exposes deeper levels in the upper crater wall and impact ejecta blanket (middle panel). Eroded debris falls to the crater floor. Coarse talus deposits interfinger with finer-grained lake sediments being deposited at the same time. Additional debris is washed down the flanks of the ejecta blanket towards the surrounding plain, where it collects in alluvium terraces (not shown). Additional erosion (bottom panel) exposes a Moenkopi fold hinge in the upper crater wall. It also creates an eroded pavement on the flank of the crater that is dominated by Kaibab. Erosion on the crater rim is not everywhere the same. Consequently, along the trail that circumnavigates the crater rim, one might be walking on Coconino (top panel) or on Kaibab that sits above an exposed Moenkopi hinge (bottom panel).

8. Distribution of Ejecta



The overturned rim sequence described in the previous chapter is part of a larger extended blanket of debris. A nearly continuous layer of rubble radiates outward over distances in excess of a kilometer beyond the crater rim. An extensive rotary drilling campaign helped map out the extent of this unit, its thickness, and internal structure (Roddy *et al.*, 1975). Along several transects across the ejecta blanket, debris extends from 1,341 to 1,860 m from crater center, with an average radial distance of 1,543 m (Fig. 8.1). Roddy (1978) estimates the original extent of the continuous ejecta blanket was ~2,500 to 3,000 m.

Previously, mapping by Barringer and Shoemaker (*e.g.*, Fig. 4.4) showed that Coconino debris is prevalent on the south side of the crater and forms patches around the east and north sides of the crater. It is absent on the west side of the crater. Drilling of the ejecta blanket showed further that the thickness of the ejecta blanket is greatest on the south side (see, for example, the lower panel of Fig. 8.1), with some blocks of Kaibab visible in the field at distances of 1.5 km from crater center.

Barringer (1910) argued that a deeper unit of the Coconino (a browner sandstone) is deposited on the southeast side of the crater and, thus, that the deepest units excavated were ejected to the southeast. I do not recall Shoemaker or Roddy reporting a similar distribution, but it is true that some of the Coconino on the southeast side is stained brown.

Roddy *et al.* (1975) examined the contact between the bedded Moenkopi and overlying debris to determine if there was any erosion, brecciation, and mixing when the ejected material landed, similar to the process that generated the Bunte Breccia around the Ries Crater. No significant effects were found. Above normally-bedded Moenkopi, drilling routinely encountered a well-defined overturned sequence of the target lithologies: Moenkopi, Kaibab, Toroweap, and Coconino.

The thickness of the debris, however, is substantially thinner than the pre-impact sequence (*e.g.*, ~20 m on the crater rim versus ~300 m in the walls of transient crater). It is also distributed laterally over greater distances. The existing ejecta blanket beyond the crater rim is 1.6 to 2.6 times wider than the crater radius (from data in Roddy *et al.*, 1975) and distributed over ~7.5 km² or ~1,850 acres. In other words, the debris now covers an area ~9 times larger than the crater. This thinning is also apparent in the rotary drill data of Roddy *et al.* (1975), who noted that the Moenkopi becomes thin to discontinuous with increasing distance from the crater. (See Chapter 18 for additional insights about ejecta thinning.) In addition, deeper lithologies (*e.g.*, Coconino) are concentrated on the crater rim, while shallower lithologies (*e.g.*, Moenkopi) occur at greater distances. Thus, the stratigraphy in the pre-impact target is preserved as one walks down slope from the crater rim.

The coarsest material within the ejecta blanket is concentrated near the crater rim. Gilbert (1896), for example, reported blocks of limestone up to 60 ft in diameter (probably Monument Rock) and sandstone up to 100 ft in diameter (the location of which is uncertain) near the crater rim. These are immense blocks of debris and typically scale with the size of the crater-forming event (Fig. 8.2). A carbonate boulder 60 ft in diameter, with a density of 2.24 g/cm³ (Table 2.3), has an approximate mass of 7.2×10^9 g or over 7,000 metric tons. Monument Rock also sits more than 50 m above its pre-impact position and several tens of meters beyond the crater rim. Barringer (1905) described ejected blocks of debris with masses up to 5,000 tons. These early explorers were particularly impressed with two boulder fields, dominated by Kaibab blocks, that were distributed roughly symmetrically, occurring on both the east and west sides of the crater (Fig. 8.3). As discussed further in Chapter 10, Barringer used these boulder fields in his assessment of the impacting projectile's trajectory.

Although we often idealize the continuous ejecta blanket as a well-ordered set of inverted target strata, local complexities exist within the debris blanket. For example, along the north rim of the crater, the surface of Kaibab ejecta was undulating or hummocky, forming a depression that was filled with Coconino debris (Fig. 8.4). This particular deposit was described by Barringer (1910) as one of the “spurts or jets” of sandstone that surround the crater, thinking they were akin to crater rays. The ejected strata have also been fragmented, so that the overturned units are better described as partially-disrupted, semi-coherent sheets. The degree of disruption increases towards the surface of the ejecta blanket. Overturned Moenkopi is very coherent, Kaibab less so, and Coconino sandstone on top of the debris blanket has been fractured much more severely (Fig. 8.5). A nearly 20 metric ton sample of overturned Coconino demonstrated that fragments had been reduced to $40 \times 40 \times 90$ cm and smaller (Walters, 1966), far smaller than many of the Kaibab boulders in the underling layer of ejected debris. The additional disruption may reflect the inherent structural integrity of the pre-impact lithologies. It may, however, also be a function of the material’s position in the overturned sequence. Moenkopi and Kaibab were contained within additional debris, whereas the ejected and overturned Coconino represented an unbounded free surface.

Not surprisingly, the density of material incorporated into the ejecta blanket is less than that of the original target rocks. In a NASA-sponsored study during the Apollo era, 19,320 kg or 10.31 m^3 of ejecta were excavated at the surface to a depth of 2 m. The ejecta was excavated on the overturned flap of the southern rim of the crater, where it is dominated by loose sand and platy blocks of Coconino-Toroweap sandstone. The bulk density of the ejecta was 1.87 g/cm^3 (Walters, 1966), which is 6 to 10% lower than that (1.98 to 2.08 g/cm^3 ; Table 2.1) of isolated Coconino sandstone fragments that have been used for shock experiments (Ahrens and Gregson, 1964; Shipman *et al.*, 1971; Ai and Ahrens, 2004). A decrease in density is a general property of impacts into consolidated lithologies like those at Barringer Crater. It may not apply, however, to unconsolidated sediments. Following a nuclear test explosion in alluvium (Sedan at the Nevada Test Site), an ejecta density identical to pre-shot target density (1.5 g/cm^3) was measured (Carlson and Roberts, 1963). In some cases, shock may even compress and cement unconsolidated target materials, effectively increasing density in both crater walls and ejecta.

The continuous ejecta blanket represents the bulk of excavated debris, but there are other ejecta components. Isolated blocks of debris were flung far beyond the continuous ejecta blanket. These are sometimes called missile debris and, around experimental explosion craters, have produced secondary craters. Barringer (1910) reported fragments of Kaibab that were ejected $2\frac{1}{2}$ to 3 miles (4 to 5 km) in blocks weighing 50 to several hundred pounds (Table 8.1). In addition, Gilbert (1896) found at least one Kaibab block $3\frac{1}{2}$ miles beyond the crater rim. Rocks landing 3, 4, and 5 km beyond the crater rim were hitting at speeds of about 650 to 850 km/hr, which is about half the sound speed in air (1224 km/hr) and about an order of magnitude less than seismic velocities in the sedimentary rocks around the crater. As far as I know, no secondary craters associated with those blocks have been described. Smaller pebble- to cobble-size components also blanket the surrounding landscape (Figs. 8.6 and 8.7), a feature not evident in any geologic map of the crater.

Also not reliably mapped are denser patches of discontinuous Kaibab ejecta deposits. Grant and Schultz (1993) briefly pointed to a candidate deposit in one of their figures (their Fig. 12). More detailed mapping of that and other nearby deposits (Kring *et al.*, 2015) confirmed they are discontinuous lobes of Kaibab ejecta that landed with horizontal velocities of ~ 250 to 300 km/s and then skated or flowed radially outward, in one case flowing up a ridge of Moenkopi (Fig. 8.8). Similar patches of Moenkopi might also exist, but they would be difficult to recognize on top of the bedrock Moenkopi or the shale-rich soil that often sits on top of Moenkopi bedrock.

The transition from continuous to discontinuous ejecta around the crater is an issue needing more attention and a mapping project is underway to clarify that distribution (Kring *et al.*, 2015; Durda and Kring, 2015; Schmieder *et al.*, 2017). Shoemaker mapped the surface geology, producing map views of the continuous ejecta. Later, Roddy conducted a drilling campaign to determine a subsurface measure of the continuous ejecta and proposed a more extensive unit (Fig. 8.9). The region between those two limits is currently being remapped (*e.g.*, Schmieder *et al.*, 2017) and is revealing additional surficial deposits of Kaibab ejecta and other interesting deposits. For example, a knoll in the southeast quadrant contains both Kaibab and Moenkopi ejecta. The Kaibab is concentrated on the face towards the crater, while Moenkopi debris is concentrated on the far side of the knoll. Thus, as in Fig. 8.8, a lobe of Kaibab debris mantles the crater-facing side of a knoll.

The material in the ejecta curtain that fell to produce the continuous ejecta blanket was traveling on ballistic trajectories. The time required for that material to be emplaced increased with radial distance. Material near the rim landing within a few seconds at relatively low speeds, while material at the edge of the continuous ejecta blanket had times of flight several tens of seconds and would land with speeds in excess of a 100 km/hr (Fig. 8.10),.

There were probably two other debris components beyond the rim of the crater: a fall-out or fallback unit and a base-surge unit. Neither of these units was mapped by Shoemaker, but they are inferred from observations within Barringer Crater and around experimental (particularly nuclear) explosion craters. A fallback debris deposit on top of the overturned ejecta blanket is inferred from fallback debris that is observed within the crater (Chapter 4). It is likely to have covered the crater rim, but its radial extent is unknown. Did it, for example, cover all the overturned ejecta blanket? Or could it have extended even farther? An important component of the fallback unit within the crater walls is meteoritic material and may have also been an important component of the fallback unit beyond the crater rim. Barringer (1910) reported fragments of meteoritic material out to distances of $\sim 5\frac{1}{2}$ mi (Chapter 9). Gilbert (1896) reported a meteoritic mass 8 mi (nearly 12.8 km) east of the crater, which is more than twice the distance of the farthest Kaibab block he observed. In addition, Nininger (1956) reported impact-melted spherules of projectile material out to a distance of 5 mi (8 km) from the crater rim, although erosional transport may have modified their distribution.

Impact melt fragments are another component of fallback debris (Fig. 8.11). Unfortunately, a good survey of its distribution has not been published. Nininger (1956) reported that melt fragments were abundant within 1,500 ft (~ 0.46 km) of the crater rim, but decreased rapidly at greater radii to a maximum extent of $1\frac{1}{2}$ miles (2.4 km). Taken at face value, this suggests the impact melt in a fallback debris unit extended to greater radii than the continuous overturned ejecta blanket. This is consistent with observations around the Sedan nuclear test explosion in alluvium, which distributed fused material beyond the continuous overturned ejecta blanket, but not as far as some missile ejecta. Unfortunately, erosional transport may have modified the distribution of melt fragments around Barringer Crater, so it is difficult to make an independent assessment of the distribution.

While Shoemaker did not map a fallback unit beyond the crater rim, it is clear that his alluvium deposits were composed of fallback debris. Indeed, recent studies suggest that some of those alluvium deposits may be primary fallback debris deposits, not just reworked, secondary deposits of debris (Kring *et al.*, 2012; see also Chapter 18). Those deposits can be up to (and possibly greater than) 7 m thick.

A base-surge deposit likely formed on top of the fallback unit. A base-surge unit is produced from a collapsing column of the finest components in up-thrown ejecta. It has been observed around several experimental nuclear explosion craters. Unfortunately, no remnant of this unit survives at Barringer Crater, so we can only crudely estimate its distribution. In the case of the Sedan nuclear explosion crater

in alluvium, isolated blocks of debris (missiles) landed up to 3 times farther than the continuous ejecta blanket and the base surge deposit extended more than 5 times farther than the continuous ejecta blanket (Carlson and Roberts, 1963). Thus, using Roddy's measurements of the existing continuous ejecta blanket around Barringer Crater, a base-surge deposit may have radiated outward for distances of 7.5 to 15 km (and possibly farther). Fine-grained base surge deposits are susceptible to wind and can be redistributed within days of crater formation. This unit was probably stripped from the region around the crater very quickly.

Estimates of the total mass of ejected material have varied. Barringer (1910) estimated more than 300 million tons of rock was ejected from the crater. A modern value derived by Roddy *et al.* (1975) is 175 million metric tons, which includes 60, 113.8, and 1.2 million metric tons from the Coconino-Toroweap, Kaibab, and Moenkopi, respectively. Not all of this mass, however, can be accounted for in existing debris deposits. They estimate 100 million metric tons survive in the overturned rim sequence and continuous ejecta blanket; 22.2 million metric tons were redeposited inside the crater; and 5.6 million metric tons were deposited as fallback ejecta. Thus, 27% of the ejected mass is missing. These mass estimates utilized a volume bulking factor of 5% in ejected units, which is based on geophysical estimates of 2.30 g/cm³ for an average density of undisturbed bedrock and 2.18 g/cm³ for the density of the breccia lens. This may be a slightly low correction, given that analyses of the ejected material suggest a 6 to 10% density decrease (1.87 vs. 1.98 to 2.08 g/cm³) measured on the south crater rim (above). Roddy *et al.* (1975) also suggested that the missing mass can be accounted for as (a) material ejected beyond the continuous ejecta blanket, (b) material distributed in fine particles that were lofted high by the impact and carried away by wind, and (c) erosion that has stripped material from the ejecta blanket. They estimate that (a) and (b) explain 5 to 10% of the mass deficit and that the remainder is an erosional loss.

Shoemaker and Kieffer (1974) measured 40 ft (12 m) of erosion on the northeast crater flank. They argue that this is a minimum number and estimate that total rim erosion is 50 to 75 ft (15 to 20 m). They also suggest that erosion may be as much as 100 ft (30 m), assuming Coconino debris was deposited and subsequently eroded where Kaibab ejecta is currently exposed. This result also implies that the outer flank of the crater rim was originally steeper than now observed, because the alluvium and colluvium that covers the Coconino sandstone ejecta pediment softened the slope. It is worth noting that erosion has been more severe in some areas around the crater than in others. Barringer (1910) reported that the silica pits on the southwest side of the crater were a natural arroyo when he arrived, having an expanse of 200 to 300 yds and a depth of 10 to 12 feet. Thus, some sections of the ejecta blanket were severely dissected before any mining operations disturbed them.

While analyzing samples to determine the age of the impact event, Nishiizumi *et al.* (1991) also measured the exposure ages at different levels along an ~10 m-tall Kaibab boulder (Whale Rock; Fig. 8.3 and 18.16) on the west side of the crater. Their analyses suggest the uppermost 8 m of the boulder were uncovered in ~27,000 yrs at an average rate of 30 cm/1000 yrs, and 1.2 m were uncovered in the last 23,000 yrs at an average rate of 5 cm/1000 yrs. Thus, at least where Whale Rock is located, 9 m of finer-grained ejecta has apparently been eroded.

In contrast, Grant and Schultz (1993) reported smaller amounts of erosion around the crater, although they focused their studies on debris farther from the rim crest and on shallower slopes. They based their estimate on the production of coarse erosional lag deposits and the sediment budgets of multiple drainage systems on the flank of the crater. They estimated <1 m of erosion beyond 1/4-1/2 crater radii from the crater rim, although loss of 2 to 3 m of material occurred in small areas. These estimates of erosion are smaller than those in previous studies, but Grant and Schultz (1993) suggest that there are true variations with radial distance from the crater rim: Higher erosional rates determined by

Shoemaker and Kieffer (1974), Roddy *et al.* (1975), and Nishiizumi *et al.* (1991) reflect erosional conditions on or near the steep rim crest, whereas their results reflect erosional conditions on the shallower flanks of the ejecta blanket.

Sitting on, and emerging from, the eroding ejecta blanket are boulders ejected from the crater. An assessment of their size distribution is underway (Durda and Kring, 2015). The work began in the northeast quadrant, where all boulders with diameters >25 cm are being mapped. Thus far, 40,955 boulders have been recorded in that quadrant. Although that is a preliminary study, it is already clear that clusters and rays of boulders were deposited in that quadrant of the crater. Because the type of ejecta varies significantly in different directions around the crater, a proposal to map the boulders in all quadrants has been submitted. Once complete, it will be possible to evaluate how pre-impact target properties (*e.g.*, lithology, stratigraphic thickness, joint spacing) affect the size distribution of ejected boulders. That will, in turn, provide a baseline for assessing ejected boulder size distributions around craters on the Moon and Mars.

A feature of the ejecta blanket often overlooked is its hummocky topography (Fig. 8.12). That topography is unlikely to be a product of post-impact erosion, in part because it would require a circumferential erosion pattern, rather than a downslope-directed and/or radial erosional pattern. The hummocky topography appears to be a primary feature of ejecta emplacement. Part of the hummocky nature of the ejecta blanket may reflect the inverted topography of the pre-impact Moenkopi landscape. However, another important cause of the hummocky topography appears to be shearing of Kaibab away from the crater rim during the emplacement of the ejecta blanket, which was, in some places, further accentuated by normal faults that separated the unit into more discrete blocks (Kring *et al.*, 2011a,b). Evidence for that type of shear and extension of the ejecta blanket is seen along the Crater Rim West trail (Chapter 18).

That shear of Kaibab away from the crater rim is also likely responsible for the surviving distribution of Coconino ejecta around the crater. As can be seen in Shoemaker's geologic map (Fig. 4.4), Coconino ejecta is concentrated on the south side of the crater. Excavated sandstone initially covered the entire ejecta blanket, but most of it has been eroded from the north, west, and east sides of the crater, exposing Kaibab. On the south rim of the crater, however, the base of the overturned Coconino and Toroweap sandstone was lower than anywhere else around the crater, because Kaibab was sheared from the rim sequence. In addition, the dips of the uplifted (and underlying) target units are subdued in the south crater wall. In the measured section, dips are only 15 to 20°, whereas they are typically twice those values elsewhere around the crater. Thus, fault-modification of the normal ejecta process created lower topography and shallower slopes on the south side of the crater, which reduced erosion rates and allowed the Coconino ejecta to survive there.

Table 8.1. Radial extent of impact components

Ejecta Component	Distance from Crater Rim (km) (crater radii)		Distance from Crater Center (km) (crater radii)		References
Continuous Overturned Ejecta Blanket					
Observed Range	0.748-1.267	1.46-2.48	1.341-1.860	2.62-3.64	1
Average of Observed Range	0.95	1.86	1.543	3.02	1
Estimate of Average Pre-erosional Extent	1.9-2.4	3.7-4.7	2.5-3.0	4.89-5.87	2
Isolated Blocks of Kaibab					
Observed Maximum	5.6	11	6.2	12	3
Impact Melt Fragments					
Observed Maximum	2.4	4.7	3.0	5.9	4
Meteoritic Fragments of Asteroid					
Observed Maximum	8.8	12	9.3	12	5
	13	25	13.5	26	3
Melted Meteoritic Spherules					
Observed Maximum	8.0-9.6	16-19	8.6-10	17-20	4,6

(1) Roddy *et al.*, 1975; (2) Roddy, 1978; (3) Gilbert, 1896; (4) Ninninger, 1956; (5) Barringer, 1910; (6) Rinehart, 1958

Value for crater radii is based on a 1,022 m estimate of a pre-erosional crater diameter measured at the pre-impact elevation (Roddy, 1978). The current average crater rim diameter is taken to be 1,186 m (Roddy, 1978).

I emphasize that the values above are observed distances. Erosion may have affected the distribution of ejecta components.

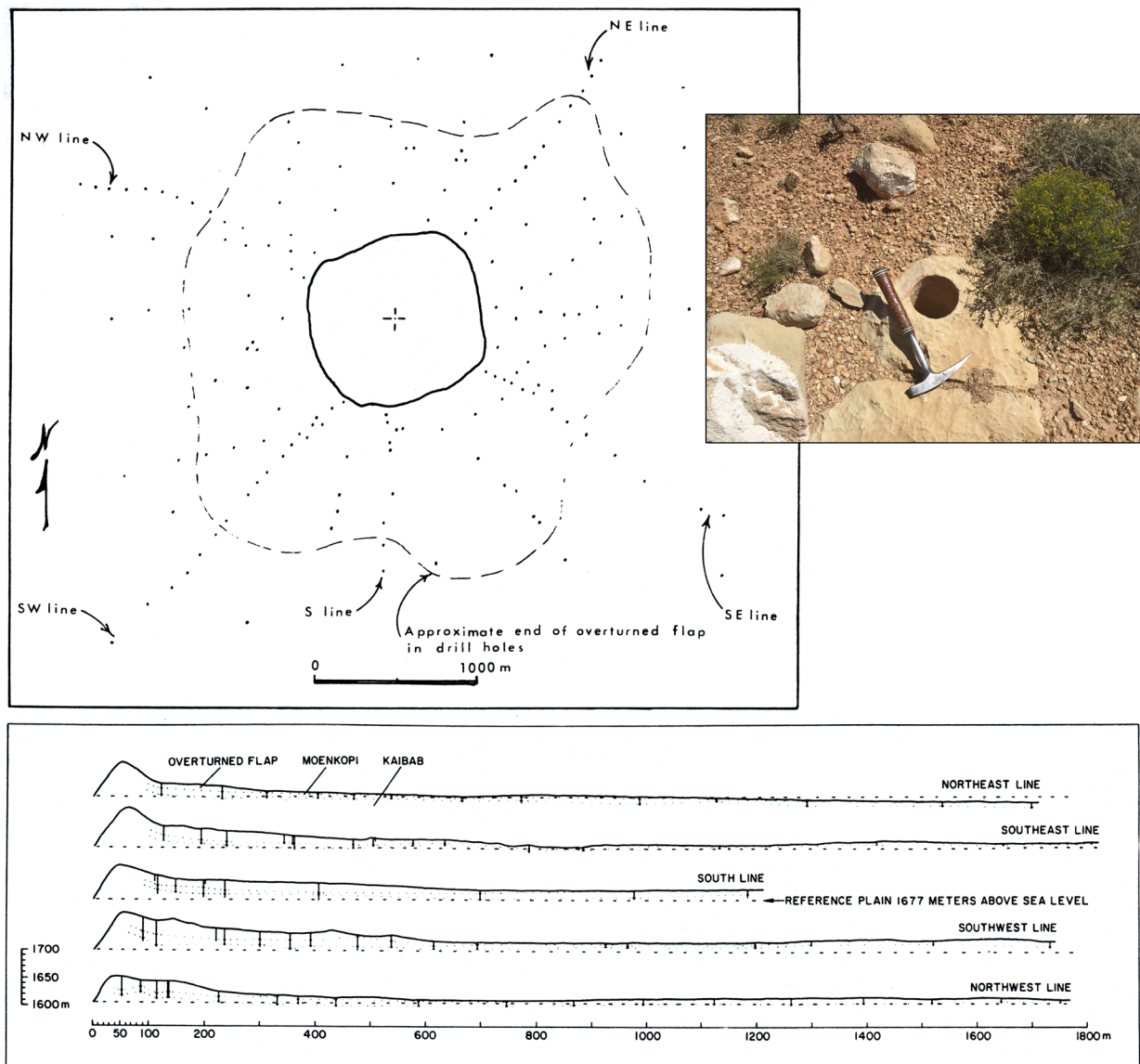


Fig. 8.1. Locations of rotary drill holes around Meteor Crater (top left panel) and generalized geologic cross-sections along five transects (bottom panel). Both panels are from Roddy *et al.* (1975). The lateral extent of the ejecta blanket is mapped in the plan view and illustrates slight asymmetry. The average radial extent of the ejecta blanket around the crater is 1,543 m from crater center. In the cross-sections, the locations of the drill holes are indicated by vertical lines. Subtle dotted lines within each profile also indicate the top and bottom of Moenkopi encountered in the drill holes. These symbols are poorly expressed in the original figure and have not (yet) been redrawn. An example of one of the drill holes is shown in the top right panel with a 33-cm-long hammer for scale.

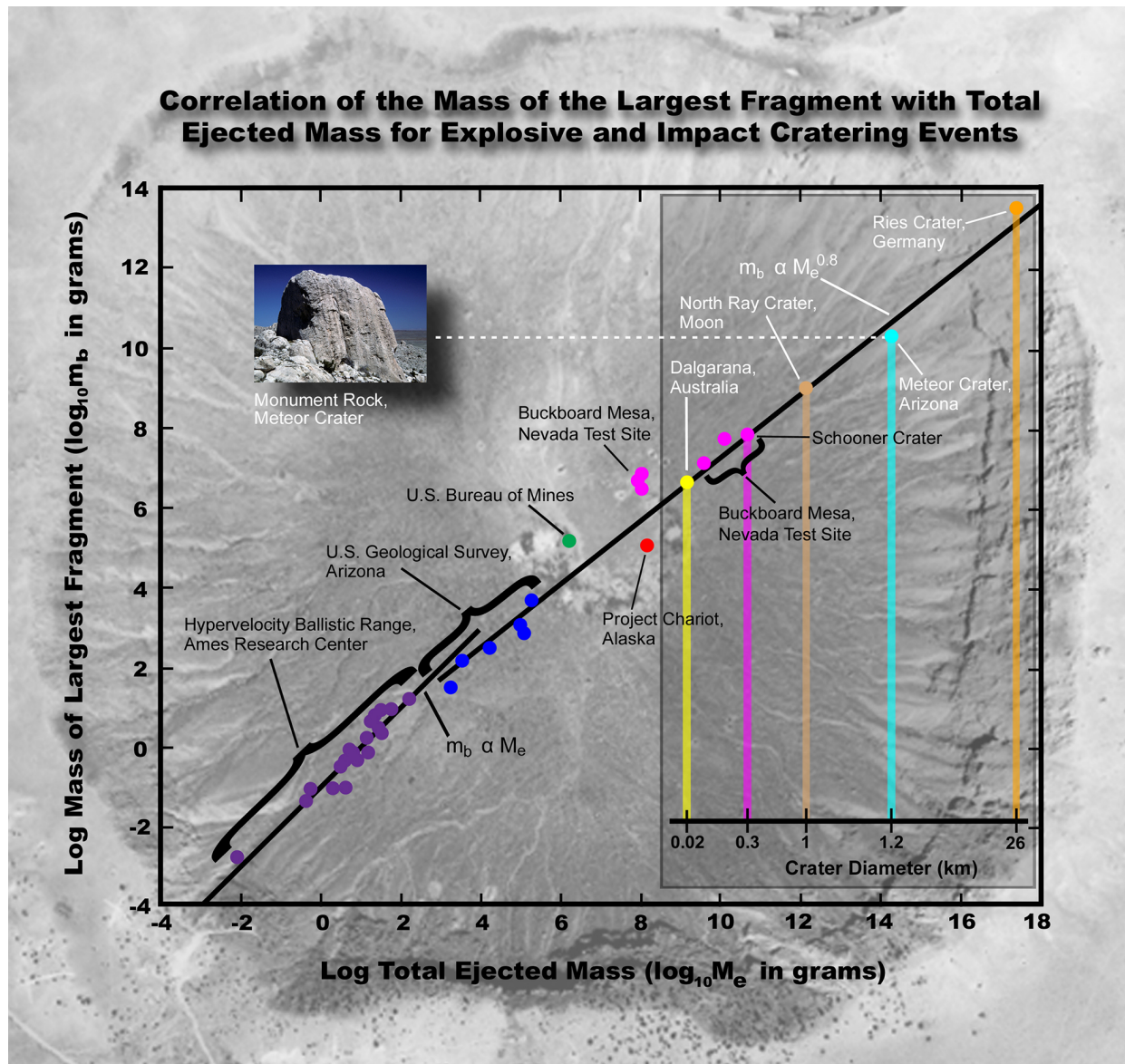


Fig. 8.2. Data from multiple explosion cratering experiments (black labels) and four impact craters (white labels) indicate that the mass of the largest ejected block (m_b) scales with the total mass of ejected material (M_e). The inset illustrates that the mass of the largest ejected block also scales with crater diameter. Blocks of rock ejected from the 1.25 km diameter Meteor Crater approach the size of a garage, while those ejected from the 26 km diameter Ries Crater are the sizes of hills. This diagram is modified from a figure produced by Gault *et al.* (1963). The diagram also includes data from the North Ray Crater on the Moon (Apollo 16 Preliminary Science Report, NASA SP-315, 1972). Image Credit: Andrew Shaner & David A. Kring; and can be downloaded from the LPI Classroom Illustration library at <http://www.lpi.usra.edu/exploration/training/resources/>

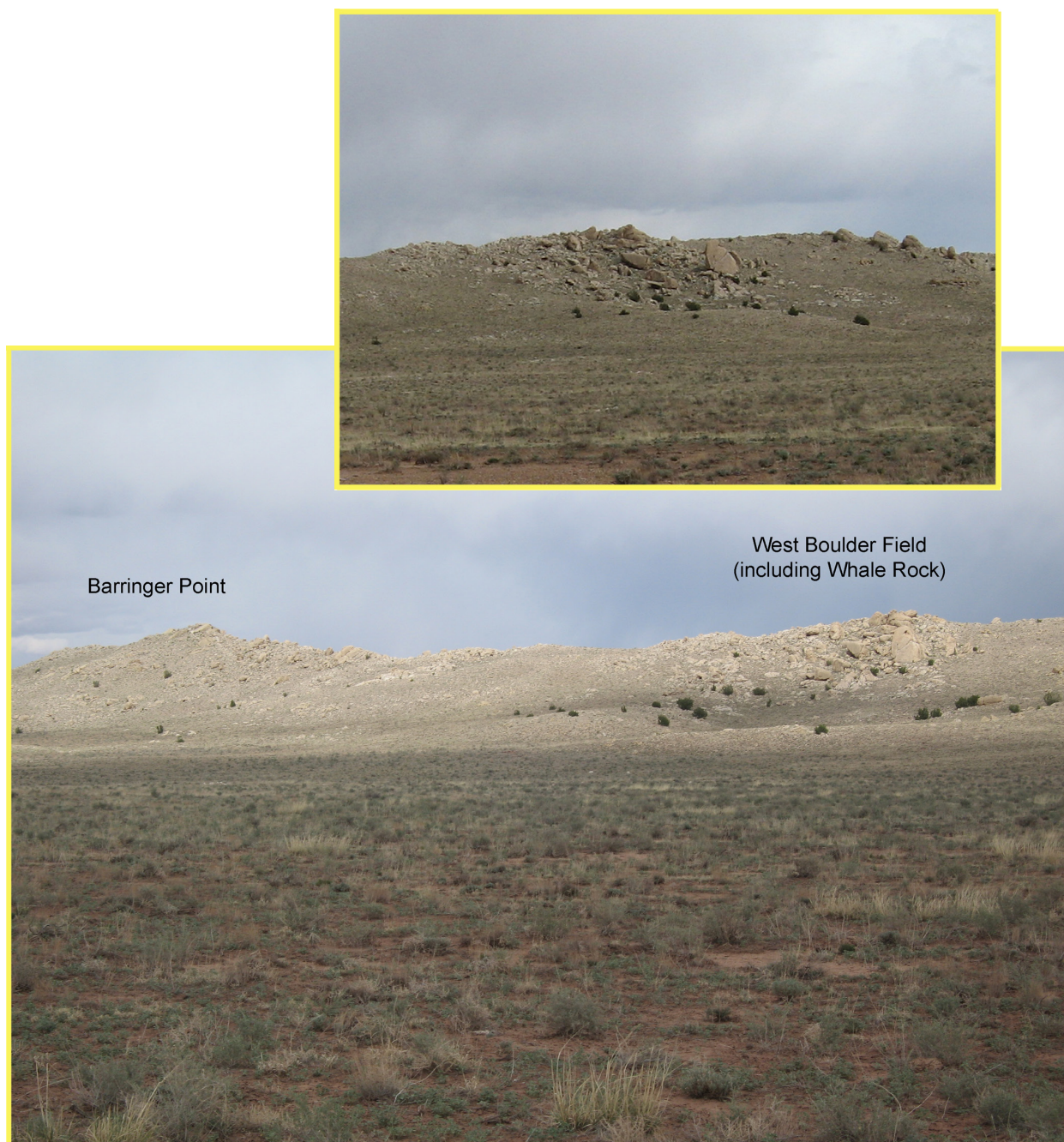


Fig. 8.3. One of two boulder-rich fields within the continuous overturned ejecta blanket. This deposit of boulders is exposed on the west side of the crater, south of Barringer Point. The boulder field contains Whale Rock, which was originally buried within the ejecta blanket. Erosion of finer-grained and more friable ejecta components has exposed the boulders. The inset shows the same boulder field from a southeast-looking vantage point with a slightly different illumination angle. The surface of the surviving ejecta blanket is much steeper on the rim crest than it is at greater radii from crater center.

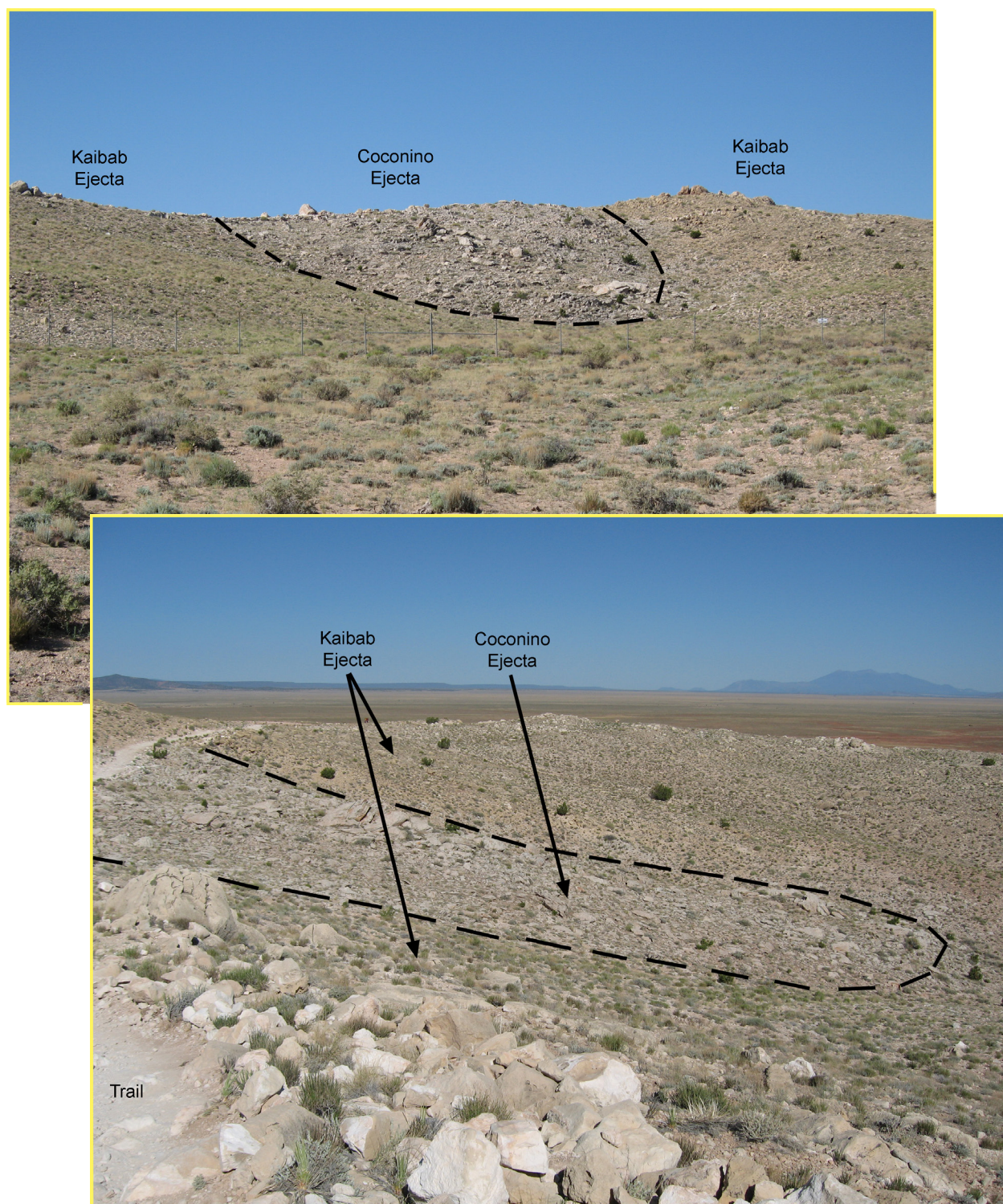


Fig. 8.4. The surface of ejected Kaibab debris was irregular, forming a depression in this location (top panel) that was filled with a wedge of Coconino sandstone debris (top and bottom panels). The deposit is on the north side of the crater. The view of the top panel (looking south) is from the road that leads up to the museum complex. The view in the bottom panel (looking northwest) is from the trail along the north rim, between the current museum complex and remnants of an old museum building.

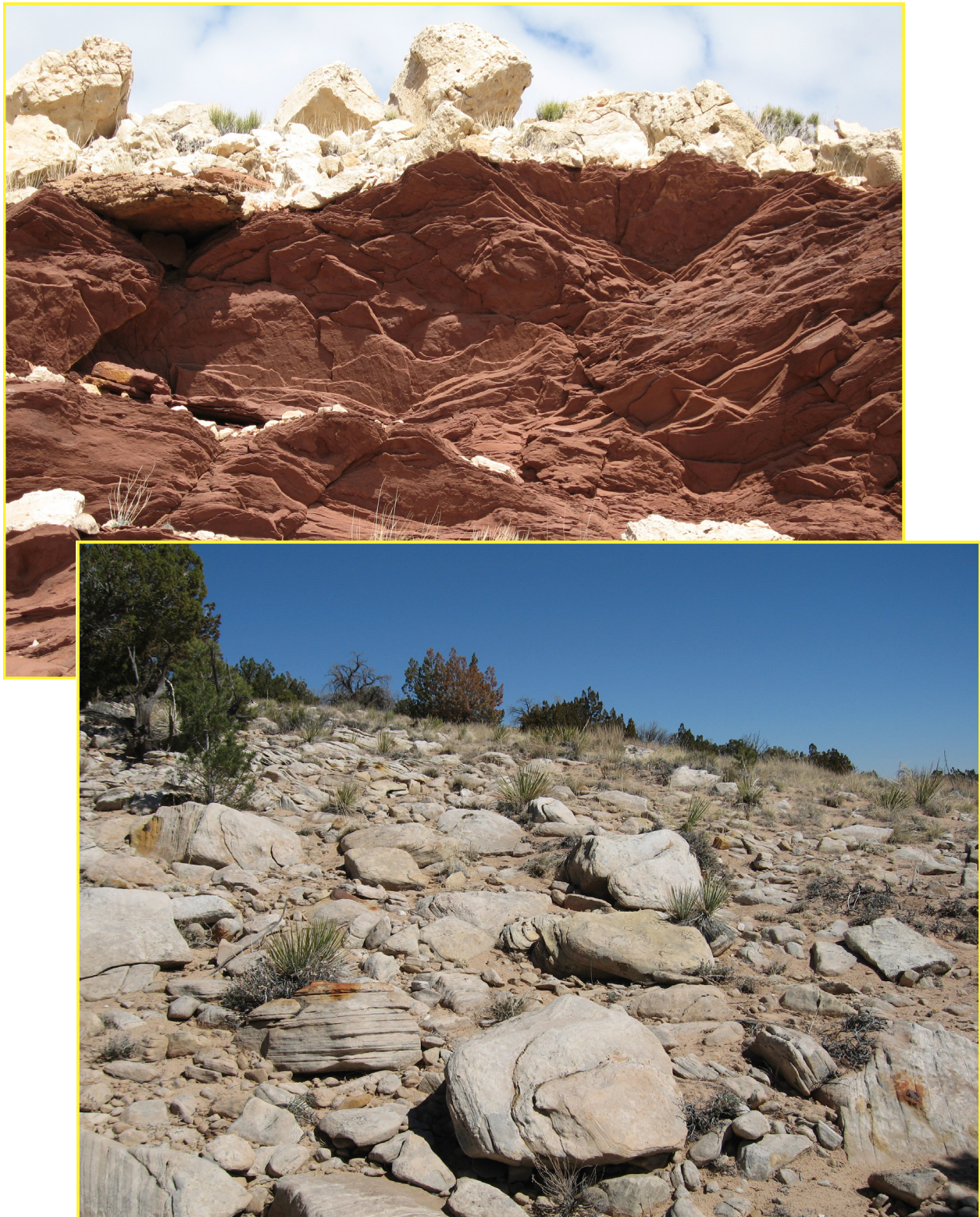


Fig. 8.5. Examples of Moenkopi, Kaibab, and Coconino-Toroweap ejecta in the continuous overturned ejecta blanket. Overturned and ejected Moenkopi is relatively unfractured and forms a coherent unit below a more disrupted layer of Kaibab debris (top panel). This view is along the north wall of the crater. Overturned Coconino-Toroweap ejecta is disrupted even further (bottom panel), with boulders often limited to diameters of only a few tens of centimeters. This view is on the south side of the crater, beyond the crater rim.

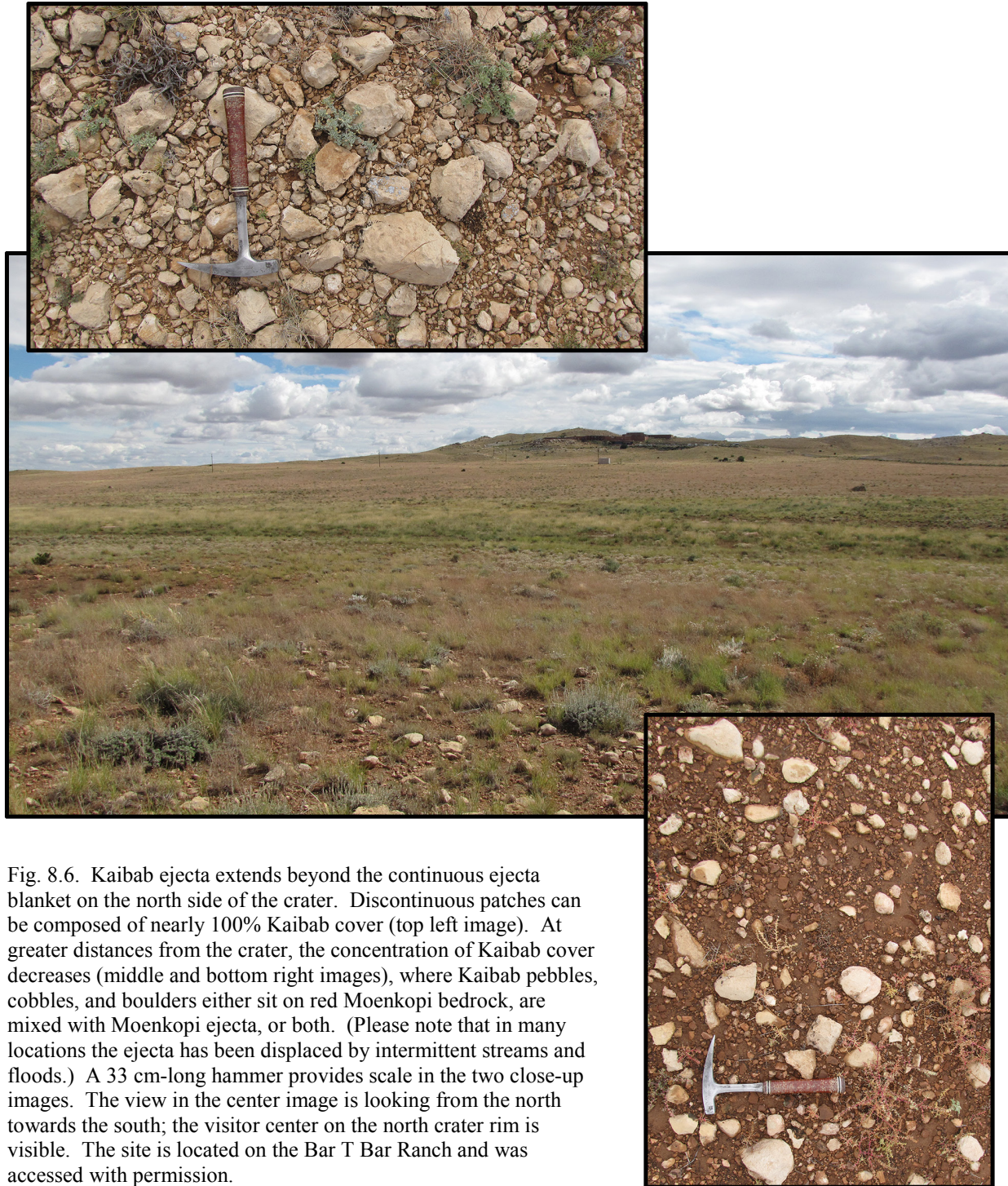


Fig. 8.6. Kaibab ejecta extends beyond the continuous ejecta blanket on the north side of the crater. Discontinuous patches can be composed of nearly 100% Kaibab cover (top left image). At greater distances from the crater, the concentration of Kaibab cover decreases (middle and bottom right images), where Kaibab pebbles, cobbles, and boulders either sit on red Moenkopi bedrock, are mixed with Moenkopi ejecta, or both. (Please note that in many locations the ejecta has been displaced by intermittent streams and floods.) A 33 cm-long hammer provides scale in the two close-up images. The view in the center image is looking from the north towards the south; the visitor center on the north crater rim is visible. The site is located on the Bar T Bar Ranch and was accessed with permission.

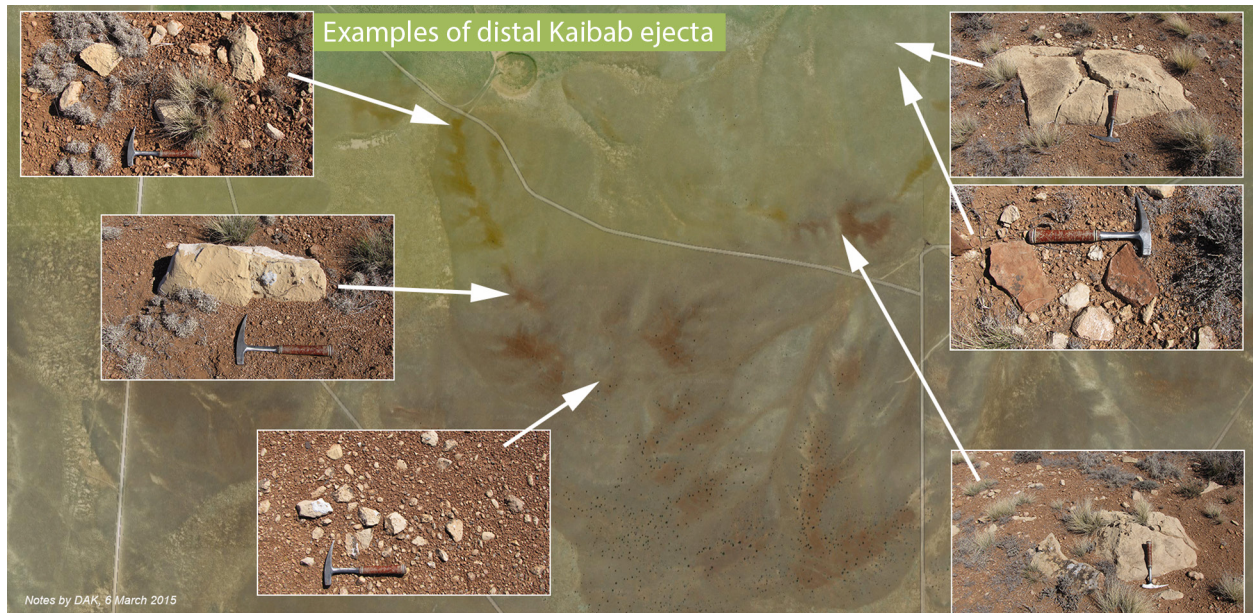


Fig. 8.7. Beyond the continuous ejecta blanket are scattered pebbles, cobbles, and boulders of Kaibab ejecta sitting on a surface of Moenkopi. The atlas of examples shown here are on the south side of the crater on the Bar T Bar Ranch and studied with permission. The example in the upper left is composed of all three particle sizes. Caliche rinds partially surround many specimens, indicating previous burial and exhumation. That is, the ejecta unit used to be thicker than it now appears. The boulder in the second panel (moving counter-clockwise) is on a ridge with vegetation lines, indicating Moenkopi bedrock. In some cases, the Kaibab could be mixed with Moenkopi ejecta too, but that is difficult to discern when sitting on top of a degraded Moenkopi surface. Some of the debris near the boulder in the lower right panel has solution pits (forming tear pants texture), indicating significant subaerial exposure to acidic rain. The most distant example pictured (bottom center) is $2\frac{1}{4}$ km from the crater center. The circular feature in the top center of the frame is a cattle tank. The crater is located farther north, beyond the field of view.



Fig. 8.8. (top panel) Kaibab ejecta on a ~6 m-high Moenkopi ridge ~1.2 km beyond the crater rim. The lobe of material is outlined with a dashed line. The crater is to the left of the image, so the material was flowing radially to the right after landing. (bottom panel) Discontinuous ejecta can be nearly 100% Kaibab (as seen here), although it also contains cobbles of the Kaibab-Moenkopi boundary breccia and pebbles of Moenkopi (as seen outside the frame of this image). This material was initially mapped as alluvium by Shoemaker. Grant and Schultz (1993; see their Fig. 12) subsequently suggested it was ejecta and, I might add, convinced David Roddy who introduced the deposit to me about twenty years ago. See Kring *et al.* (2015) for additional details about the deposit. Note: This outcrop, like all those around the crater, can only be visited with permission. Also, because this material, like nearly all impact-generated material around the crater, is unconsolidated, please do not step on it or otherwise disturb the geologic evidence of the processes that produced the deposit.

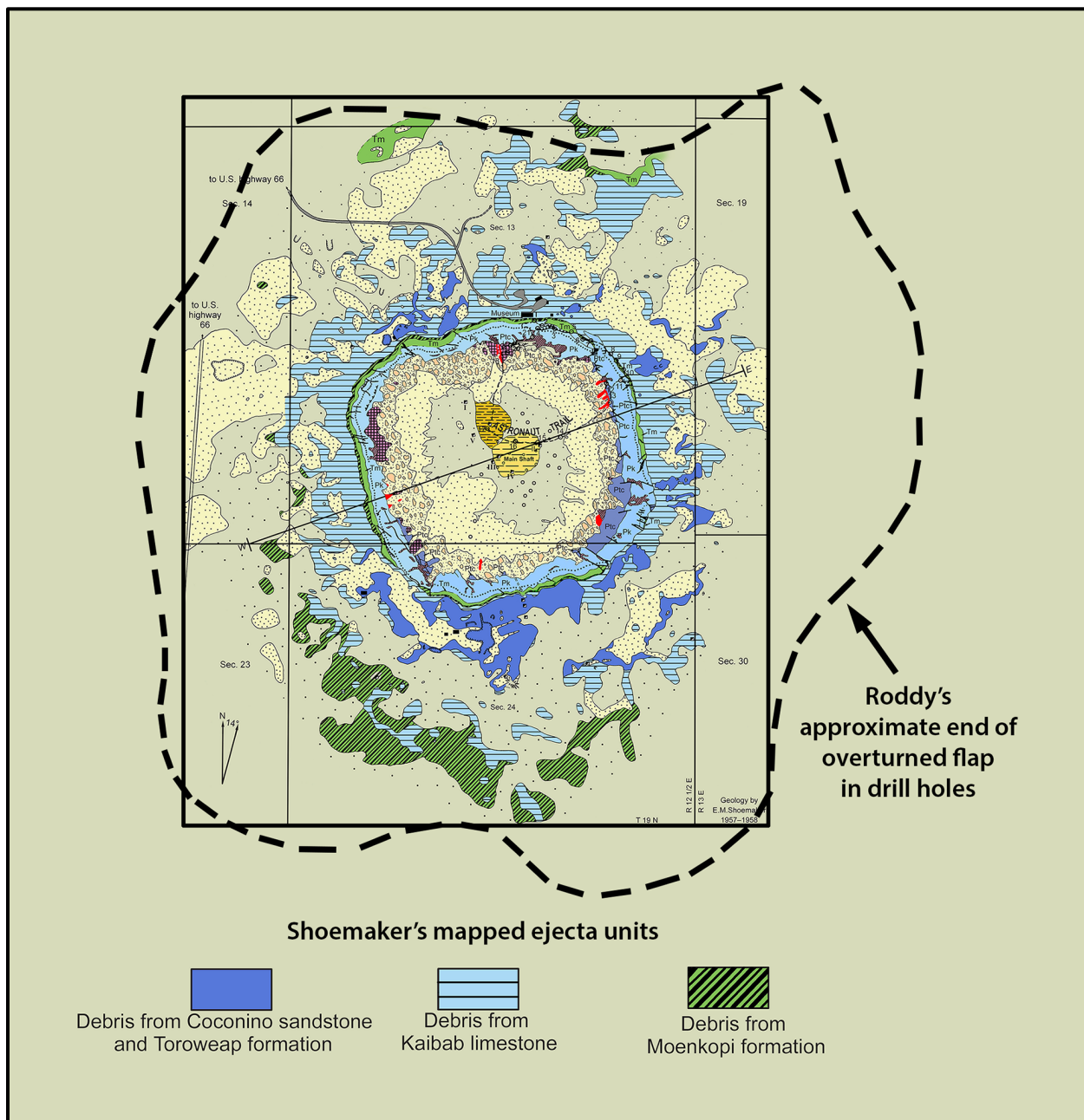


Fig. 8.9. Shoemaker mapped (1957-1958) the impact ejecta units visible in the surface, which provides a minimum estimate of the radial extent of the continuous ejecta blanket. Roddy *et al.* (1975) led a drilling campaign that probed the subsurface, including those areas that are currently covered with alluvium. Based on the cuttings produced by that drilling, he estimated the extent of the overturned flap (*i.e.*, the continuous ejecta blanket) to be significantly larger than that discernable in the surface geology.

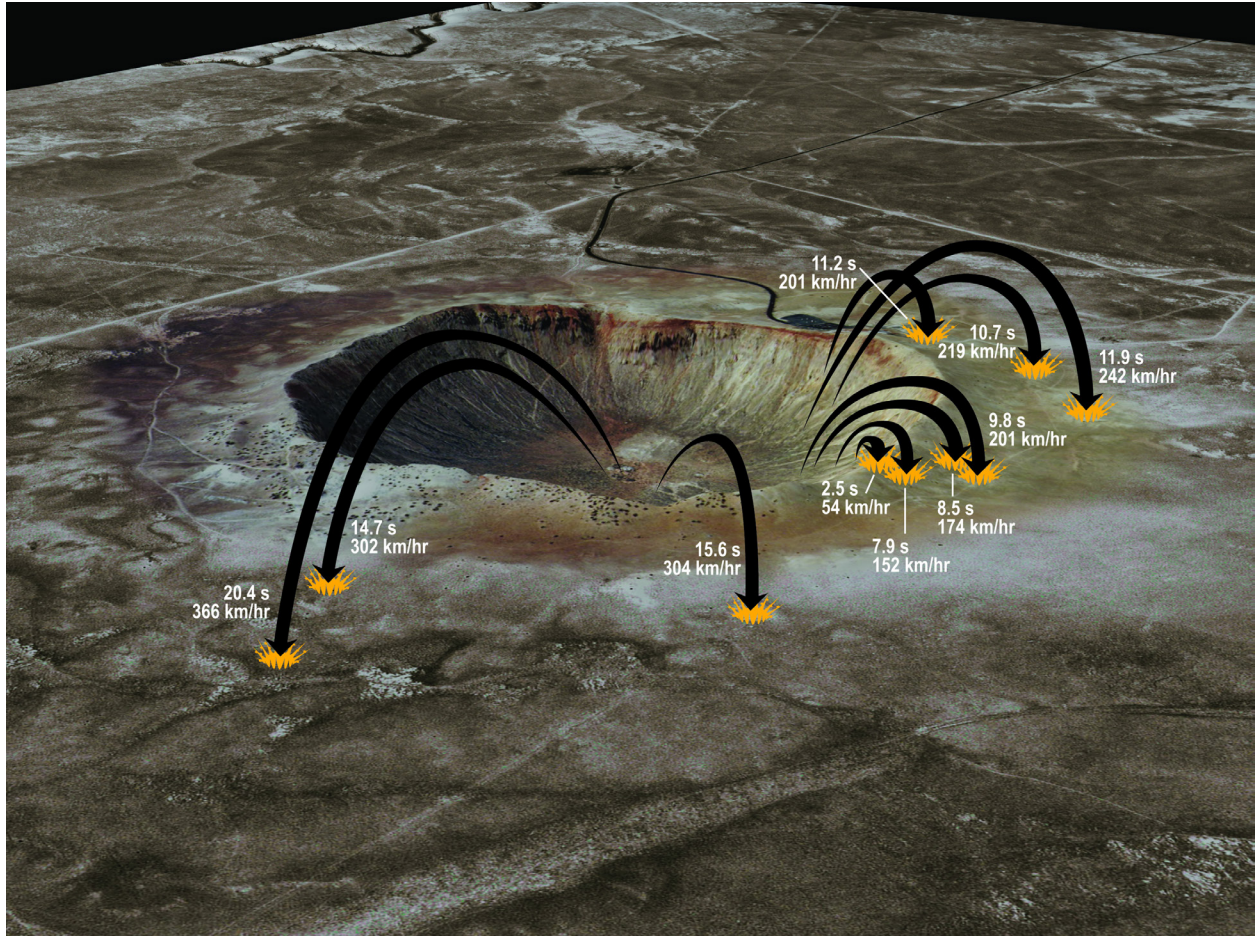


Fig. 8.10. Components in the ejecta curtain are traveling on ballistic trajectories. The debris at the base of the overturned ejecta flap landed first at modest speeds, while more distal portions of the continuous ejecta blanket landed later in time and at higher speeds. For example, one of the largest blocks visible near the crater rim is called Monument Rock or House Rock. It landed about 2 seconds after being launched and hit with a speed of about 50 km/hr. In contrast, a block landing about half a kilometer beyond the crater rim hit with a speed of about 370 km/hr.

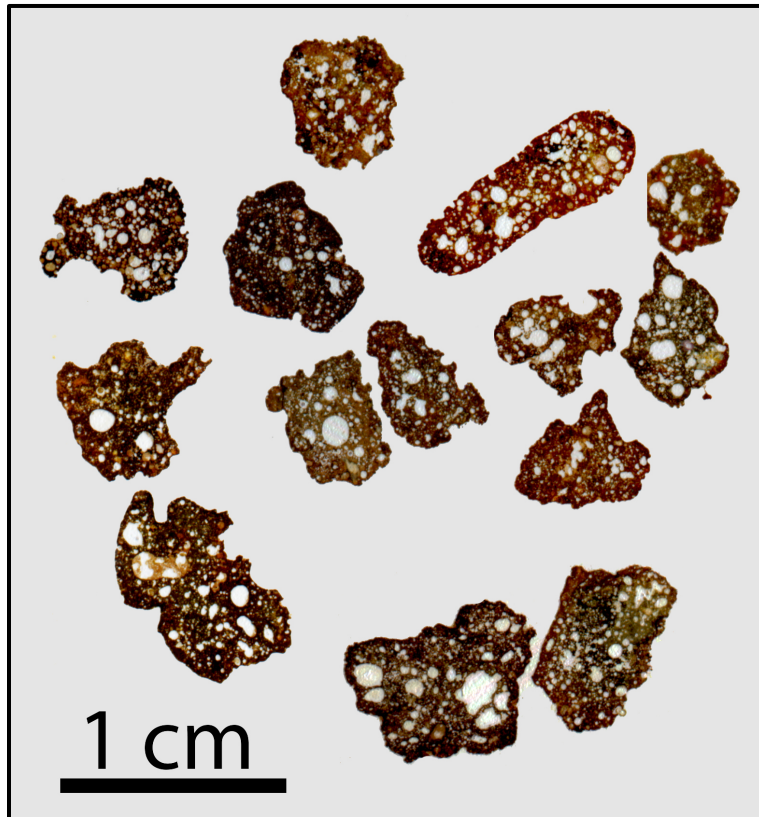


Fig. 8.11. An array of small impact melt particles that were recovered from the eroded surface of the ejecta blanket. The particles are glassy, vesicular, and contain olivine and pyroxene that grew before the melts were completely quenched. The melts are mixtures of degassed target rocks, dominantly the sandy dolomite of the Kaibab, and siderophile elements from the iron asteroid.

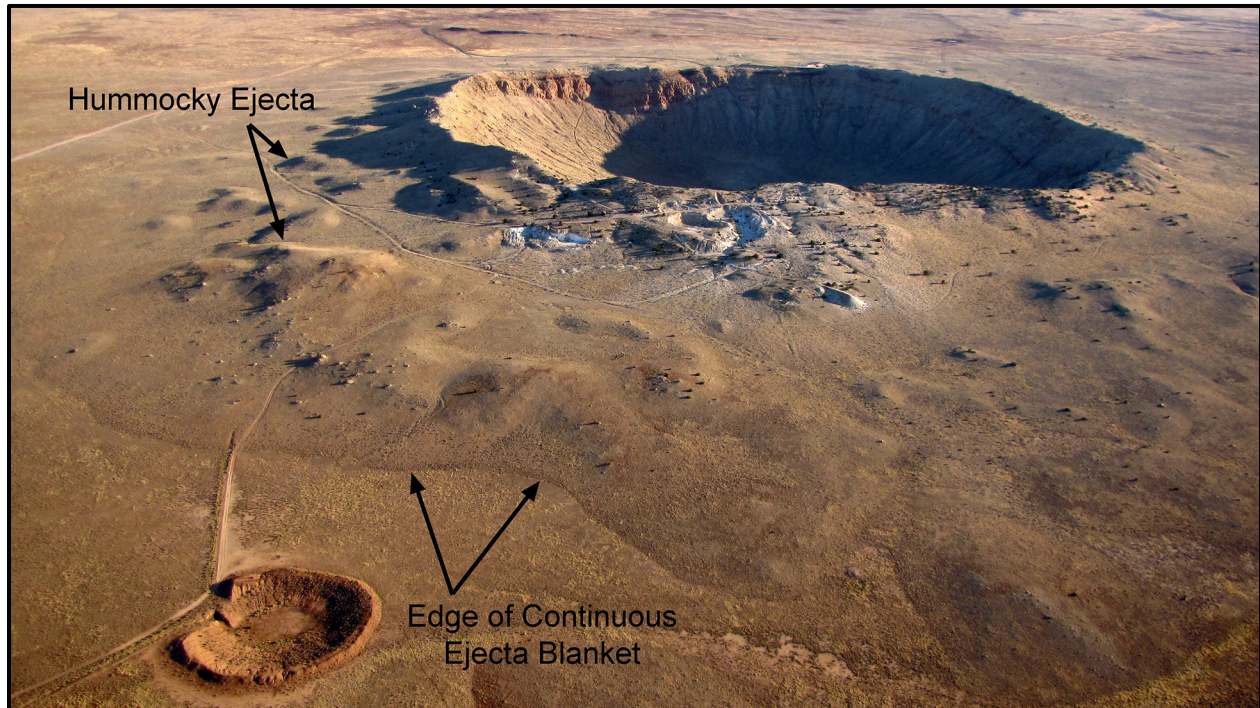


Fig. 8.12. The continuous ejecta blanket around Meteor Crater has a hummocky topography, as illuminated at dawn when the sun angle is very low. Also visible is the edge of the ejecta blanket, which corresponds to the ejecta mapped by Shoemaker (1960), although Roddy *et al.* (1975) argued the ejecta blanket extends farther and lies beneath Quaternary cover. The view is from the south to the north.

9. Projectile



Meteoritic remnants of the impacting asteroid that produced Barringer Crater littered the landscape when exploration began ~115 years ago. As described in Chapter 1, meteoritic irons are what initially captured Foote's interest and spurred Barringer's interest in a possibly rich natural source of native metal. After Foote's description was published, samples were collected by F. W. Volz at a nearby trading post and sold widely. Gilbert (1896) estimated that 10 tons of meteoritic debris had already been recovered by the time of his visit. Similarly, Barringer (1905) estimated that 10 to 15 tons of it were circulating around the world by the time his exploration work began. Fortunately, he tried to document the geographic and mass distribution of that debris in a detailed map, which is reproduced in Fig. 9.1. The map indicates that meteoritic irons were recovered from distances approaching 10 km. Gilbert (1896) apparently recovered a sample nearly 13 km beyond the crater rim. A lot of the meteoritic material was oxidized. It is sometimes simply called oxidized iron, but large masses are also called shale balls. A concentrated deposit of small oxidized iron fragments was found northeast of the crater, although those types of fragments are distributed in all directions around the crater. The current estimate of the recovered meteoritic iron mass is 30 tons (Nininger, 1949; Grady, 2000), although this is a highly uncertain number. Specimens were transported in pre-historical times and have been found scattered throughout Arizona (see, for example, Wasson, 1968). Specimens have also been illicitly removed in recent times, without any documentation of the locations or masses recovered.

These iron fragments are collectively called the Canyon Diablo meteorite, whose namesake is a sinuous canyon west of the crater. This meteorite is a coarse octahedrite (Fig. 9.2) with a bandwidth of 1.2 to 2.2 mm. It is chemically classified as a Group IAB iron. This is a non-magmatic type of iron meteorite. Intriguingly, the IAB irons appear to have been produced in impact craters on at least two early solar system planetesimals. Collisions between planetesimals produced impact melt pools that differentiated (Goldstein *et al.*, 2014; Worsham *et al.*, 2017), allowing the denser metal and sulfide components to sink and, thus, collate into significant volumes. Based on the cooling rates of the iron meteorites, I estimate the craters were 150 to 300 km in diameter on planetesimals >300 km diameter. At some later date, the planetesimals were disrupted, producing iron metal-dominated asteroids, one of which eventually collided with Earth to produce Barringer Meteorite Crater.

The asteroid was dominated by Fe,Ni-alloys, particularly kamacite, reflecting a bulk chemical composition with 6.91 to 7.10 wt% Ni (Moore *et al.*, 1967; Wasson and Ouyang, 1990). The mineralogical diversity, however, is large (Table 9.1), and growing as new techniques identify nanoparticle inclusions composed of platinum group elements, transition metal-rich nitrides, and other phases (Garvie, 2017). As noted in Chapter 1, diamond is one of the mineralogical components of Canyon Diablo specimens. The interpretation of the diamond-bearing specimens led to a firestorm of controversy. Urey (1956) suggested the diamonds were produced in hydrostatic equilibrium and, thus, came from a planet of sufficient size to produce very high pressures. That implies a planetesimal in excess of 2020 km. Indeed, on the basis of diamonds, Urey postulated a series of Moon-sized bodies as the source of meteoritic material. Lipschutz and Anders (1961a,b) correctly argued that the diamonds were formed from carbon-graphite-troilite nodules by high shock pressures generated by the impact. Not everybody was immediately convinced. Carter and Kennedy (1964) were critical, which generated an interesting exchange (Anders and Lipschutz, 1966). The diamonds also caused a brief public sensation when the size of the diamond(s) was errantly equated with that of asteroid. One newspaper (The Indianapolis Star, Sunday, October 6, 1912, page 3) headline read: "Syndicate of Mining Men Sink Shaft in Search for Diamond Half Mile Thick." The article goes on to say "But the most remarkable thing

about this meteorite, apart from its prodigious size, is that fact that in all probability it consists of one huge diamond.”

Some of the carbon-graphite-troilite nodules are cross-cut with veins of metal (Fig. 9.2). It has long been wondered how those veins were produced. Were they a product of the original differentiation and crystallization processes that occurred in a planetesimal crater where the iron formed? Were they the product of impact-remobilization of melt in an event that occurred soon after solidification? Or were they the product of a much younger impact event during the evolution of the planetesimal as it evolved into a near-Earth asteroid that hit Earth? New analytical techniques were recently applied to the metal in one of those graphite nodules to answer that question (Hilton *et al.*, 2017). That study found that the veins have a composition that falls parallel to a primordial Re-Os isochron, suggesting the veins formed during an early event in solar system history. Highly siderophile element abundances in kamacite in the vein, when normalized to abundances in kamacite in the bulk Canyon Diablo meteorite, correlate with partition coefficient, suggesting the vein formed by partial melting of the Canyon Diablo host. Thus, the veined graphite nodules are ancient, not a later evolutionary product.

An analysis of meteorites from the crater rim and surrounding plain (Fig. 9.3) indicated the rim samples are much more strongly reheated than the plain samples and saw much higher shock pressures. Thus, the diamond-bearing specimens are concentrated on the crater rim (Nininger, 1956; Moore *et al.*, 1967). Heymann *et al.* (1966) conducted a detailed study of 56 Canyon Diablo specimens distributed from the crater rim to distances of about 4 mi (6½ km) and used cosmogenic nuclides to determine their original depth in the parent asteroid. Moderately- to severely-shocked specimens came from greater depths (*e.g.*, a mean of 132 cm *vs* 72 cm). Diamond-bearing and rim specimens came from greater mean depths (135 and 127 cm, respectively) than plains specimens (81 cm). They noted that the severely shocked specimens were recovered on top of the NE and SE portions of the continuous ejecta blanket, suggesting a ray-like distribution pattern and preferential distribution of material from slightly deeper levels of the asteroid in those directions.

Table 9.1. Minerals in the Canyon Diablo Meteorite

Mineral Name	Chemical Formula	Type of Mineral
kamacite	Fe,Ni-alloy	metal
taenite	Fe,Ni-alloy	metal
troilite	FeS	sulfide
daubreelite	FeCr ₂ S ₄	sulfide
sphalerite	(Fe,Zn)S	sulfide
mackinawite	(Fe,Ni)S _{0.9}	sulfide
chalcopyrrhotite	(Cu,Fe)S	sulfide
schreibersite	(Fe,Ni) ₃ P	phosphide
cohenite	(Fe,Ni,Co) ₃ C	carbide
haxonite	(Fe,Ni) ₂₃ C ₆	carbide
graphite	C	carbon
diamond	C	carbon
lonsdaleite	C	carbon
olivine	(Mg,Fe) ₂ SiO ₄	silicate
pyroxene	(Mg,Fe,Ca) ₂ Si ₂ O ₆	silicate
plagioclase	(Ca,Na)(Si,Al) ₄ O ₈	silicate
ureyite	NaCrSi ₂ O ₆ silicate	
krinovite	NaMg ₂ Cr ₂ Si ₃ O ₁₀	silicate
chromite	FeCr ₂ O ₄	oxide
rutile	TiO ₂	oxide

Additional details about the Canyon Diablo meteorite appear in V.F. Buchwald's volumes about iron meteorites (1975).

In addition to meteoritic fragments, isolated opaque melt droplets were showered around the crater, either as a direct impact melt product or as a molten condensate from an impact-generated vapor cloud. In an early survey, Nininger (1951) reported a recovery rate of 100 g/ft³ of ejecta and/or alluvium derived from ejecta, which is 3,000 tons of spherules per square mile. He says the total area covered by the spherules is unclear, although there is a "sparse sprinkling...over 100 sq mi." Nininger (1956) later amended these estimates, reporting that 4,000 to 8,000 tons of spherules exist in the upper 4 inches of soil, based on measurements in 60 locations. From these data, he suggests the original asteroid had a mass of 100,000 to 200,000 tons. Most of the spherules are found within 1 ½ mi (2.4 km), although they have been found as far away as 5 mi (8 km) from the crater rim.

The spherules do not have the same composition as Canyon Diablo meteorites and were, thus, somehow fractionated during their formation. The compositional disparity was detected by Nininger (1951), who reported spherules with 17% Ni. Blau *et al.* (1973) found that the spherules are also enriched in S and P. They suggested the spherules formed by preferential shock melting of sulfide-rich portions of the asteroid, rather than oxidation of Fe. Using the dimensions of dendritic crystalline texture in the spherules, they calculated that the 1 mm spherules cooled between 500 and 30,000 °C/sec. They further argued that unshocked "plains" specimens spalled off the asteroid as it approached the surface, that shocked "rim" specimens were blasted off the trailing edge or backside of the asteroid, and that the remainder of the asteroid was dispersed in vapor cloud.

More recently, cosmogenic nuclides have been used to determine the source depths of the spherules on the asteroid. Surprisingly, this signature is preserved, despite the fractionation of the principal siderophile elements. Xue *et al.* (1995) examined the cosmogenic nuclides ¹⁰Be and ²⁶Al in 17 spherules and compared them to meteorite fragments. They concluded that the spherules come from a greater depth than meteorites (or that Al and Be is lost during the spherule-forming process). Leya *et al.* (2002) pursued more cosmogenic noble gases. They also concluded that the spheroids come from a deeper depth than meteorites, but still from within a distance of 2.3 m from the pre-atmospheric asteroid surface.

Other isotope systems were employed to independently assess the relative depths of meteorite and spherule production. Schnabel *et al.* (1999) found that a group of spherules contains 7 times less ⁵⁹Ni than meteorite specimens, implying the spherules came from a depth that is 0.5 to 1.0 m deeper in the impactor than the meteorites. In absolute terms, their results suggest the spherules came from a region that was 1.3 to 1.6 m beneath the pre-atmospheric surface. A model simulation of the impact event in that same study suggested that 1.5 to 2 m of the backside of asteroid (assuming spherical symmetry, 30 m diameter asteroid, and a 20 km/s impact velocity) survives as solid material. This represents 16% of asteroid. The remainder was obliterated and these authors suggest that the bulk of that material was dispersed in a spray of fine molten material and did not involve a significant vapor component. They also argued that the Ni isotope data are consistent with 20 km/s impact simulation, not a slower, 15 km/s simulation; I refer the reader to their paper for details of that discussion.

A crude schematic of the asteroid that summarizes these data is shown in Fig. 9.4. The schematic diagram illustrates a perfectly spherical asteroid. In reality, the asteroid probably had an irregular surface and may have been significantly elongated. To illustrate a possible morphology, model images based on radar data are also included in Fig. 9.4 courtesy of the late Steve Ostro. The model images are of near-Earth asteroid (29075) 1950 DA, which is a suspected metallic asteroid that may pass close by Earth in 2880 and may have a probability of impact as high as 1/300 (Busch *et al.*, 2007). These images were selected rather than those of metallic main belt asteroids, because the Canyon Diablo asteroid was truly a

near-Earth asteroid. The other candidate near-Earth metallic asteroid that has been imaged with radar is 1986 DA (Ostro *et al.*, 1991). Two previously imaged metallic asteroids in the main asteroid belt are 216 Kleopatra and 16 Psyche. NASA has recently approved a spacecraft mission to the asteroid 16 Psyche.

As the model images suggest, metallic asteroids can have irregular surfaces that reflect their collisional evolution. In the case of the Canyon Diablo asteroid, cosmic ray exposure ages suggest the object was liberated in a planetesimal breakup event ~540 million years ago and was subsequently involved in a secondary collision ~170 million years ago (Heymann *et al.*, 1966; Michlovich *et al.*, 1994).

It is not yet clear how surface irregularities or the shape of the asteroid may have affected the excavation of the crater and distribution of debris around the crater (including the distribution of projectile components). This is an area of study that has become approachable only recently with the advent of new computational codes that permit 3-D simulations with asymmetrical components.

The size of (29075) 1950 DA is ~1 km in diameter, which is far larger than the Canyon Diablo asteroid. Previous estimates of its diameter generally fall within the range of 10 to 50 m, but the exact size is still uncertain. To help readers link a discussion of proposed masses with asteroid diameters, I built a table (Table 9.2) of hypothetical spherical projectiles with radii from 10 to 25 m (and, thus, diameters of 20 to 50 m). As noted above, a recent simulation of the impact event assumed a 30 m diameter object, which corresponds to a mass of 1.1×10^8 kg or 110,000 metric tons assuming a density of 7.8 g/cm^3 . The most recent simulation favored a ~42 m diameter object with a mass of $\sim 3.2 \times 10^8$ kg (Collins *et al.*, 2016). Other mass estimates include 400,000 tons (Magie, 1910); 10,000,000 tons (Barringer, 1914); 5,000 to 3,000,000 tons (Moulton, 1931; per Hoyt, 1987); 15,000 tons (Wylie, 1943a,b); 5,000,000 tons (Öpik, 1936; Rostoker, 1953); 100,000 to 200,000 tons (Nininger, 1956); 2,600,000 tons (Öpik, 1958); 30,000 to 194,000 tons (Bjork, 1961); 63,000 tons (corresponding to 25 m sphere; Shoemaker, 1963); and 500,000 to 1,000,000 tons (Shoemaker in Elston, 1990), as discussed in greater detail by Buchwald (1975) and Hoyt (1987). Only a small fraction of this mass survives. As described above, the current estimate of surviving meteoritic material is 30 tons. In addition, Rinehart (1958) estimates 8,000 tons survives as dispersed metallic particles.

The fate of the missing material has been at the center of considerable debate. Barringer, of course, thought it was buried beneath the crater floor. He considered the alternative possibility that the object was vaporized (Barringer, 1910). In that case, he reasoned, the vaporized projectile and target materials would have re-condensed, producing a mass of material (perhaps similar to rock flour) that was stained with iron and nickel oxides. Since this is not observed, he argued the mass must still exist inside the crater. (At this point in the development of his model, he also thought the asteroid was a cluster of fragments rather than a solid mass.)

Others have argued that a large fraction of the object was obliterated, either in the form of a vapor or finely-dispersed molten mist. A quantitative assessment of that fraction and the amount of obliterated material that was truly ejected is still lacking. Or, rather, a consensus has not developed around one of the proposed answers. Shoemaker, for example, maintained that one-third to one-half of the projectile mass is dispersed in material that remains in the crater (Elston, 1990), consistent with his initial assessment of the impact event (Shoemaker, 1963). In contrast, others have suggested nearly all of the projectile was dispersed beyond the rim of the crater as melted and/or vaporized ejecta (*e.g.*, Blau *et al.*, 1973).

The size and strength of the Canyon Diablo asteroid affected the outcome of the impact event. Smaller and weaker objects are often unable to penetrate the atmosphere without catastrophically

Table 9.2. Masses of hypothetical iron asteroids

Radius (m)	Volume (m ³)	Density (g/cm ³)	Mass (kg)	Mass (metric ton)
10	4189	7.8	3.27×10^7	3.27×10^4
11	5575	7.8	4.35×10^7	4.35×10^4
12	7238	7.8	5.65×10^7	5.65×10^4
13	9203	7.8	7.18×10^7	7.18×10^4
14	11494	7.8	8.97×10^7	8.97×10^4
15	14137	7.8	1.10×10^8	1.10×10^5
16	17157	7.8	1.34×10^8	1.34×10^5
17	20580	7.8	1.61×10^8	1.61×10^5
18	24429	7.8	1.91×10^8	1.91×10^5
19	28731	7.8	2.24×10^8	2.24×10^5
20	33510	7.8	2.61×10^8	2.61×10^5
21	38792	7.8	3.03×10^8	3.03×10^5
22	44602	7.8	3.48×10^8	3.48×10^5
23	50965	7.8	3.98×10^8	3.98×10^5
24	57906	7.8	4.52×10^8	4.52×10^5
25	65450	7.8	5.11×10^8	5.11×10^5

fragmenting far above the ground. For example, a 6 to 8 m diameter stony asteroid with L-chondrite affinities fell about ~15,000 years ago in northern Arizona, but fragmented into thousands of stones (the Gold Basin meteorites) that showered more than 225 km² of the Earth's surface rather than create a hypervelocity impact crater (Kring *et al.*, 2001). In the case of Barringer Crater, however, the asteroid was able to collide with the Earth's surface while still moving with a large fraction of its cosmic velocity.

When discussing the size of near-Earth asteroids like the one that produced Barringer Crater, it is also important to keep the density of the objects in mind. For example, when an L-chondrite asteroid exploded near the Russian town Chelyabinsk in 2013, it was often described as being half that of the asteroid that produced the ~1 km crater in Arizona. However, the size of that object (~20 m diameter) relative to the size of the Canyon Diablo asteroid (~40 m diameter) is an incomplete comparison. Because the Canyon Diablo asteroid was denser, it had ~28 times more mass and, thus, was ~28 times more explosive than the Chelyabinsk event (Fig. 9.5)

As noted briefly above, Barringer wondered whether the impacting asteroid hit as a solid iron mass, a cluster of iron fragments, or as iron fragments within a stony or icy matrix. The impact cratering community continues to debate the first two options. Results are in considerable flux at the moment, so I will not try to capture them here and suggest instead that interested students watch the literature.

With regard to Barringer Crater and the projectile that produced it, there are two other observations worth noting. First, with a diameter of ~1 km, the crater approaches the lower limit of hypervelocity craters on Earth (Table 9.3). The atmosphere screens most objects that make smaller craters. That is, the atmosphere shields the surface from objects that are smaller or weaker. Because most small craters are associated with iron asteroids, they appear to be stronger than stony asteroids. Second, the number of craters produced by type IAB irons, relative to other irons, is higher than the ratio of those objects seen in the smaller meteorite population. At least 16 to 17 of the craters in Table 9.3 were generated by irons and, of these, 6 (or ~35%) were produced by type IAB irons. Also, at least 24% of all the small crater impacts were produced by type IAB iron asteroids. In contrast, only 10% of observed iron meteorite falls are type IAB (Grady, 2000). Even in a combined population of iron meteorite finds and falls, type IAB specimens constitute only 15% of the population. The data suggest one of three conclusions: (1) Type

IAB asteroids are stronger than other irons and, thus, better able to penetrate the atmosphere; (2) Type IAB asteroids are less collisionally evolved than other irons and, thus, less populous among meteorite-size objects; or (3) we are falling prey to the vagaries of small number statistics. Because the asteroid that produced Barringer Crater was once part of a larger asteroid that was fragmented, it might be interesting to examine the size distribution of the type IAB asteroids that have hit Earth in the past and infer something about the sizes of type IAB asteroids in that distribution that have either been lost via other processes or still remain in near-Earth space. Thus far, all of the craters unambiguously linked to type IAB impactors are small (<100 m) and young (< 1 Ma). There are suggestions, however, that the ~5 km diameter Gardnos crater, produced at least 385 Ma (Grier *et al.*, 1999), may have been produced by a type IA or IIIC asteroid (Goderis *et al.*, 2009), and that the ~6 km diameter Sääksjärvi crater, produced about 560 Ma, may have been produced by a type IA or IIIC asteroid (Tagle *et al.*, 2009). That data should help assess the collisional evolution of the IAB asteroid that eventually produced Barringer Crater.

Smaller near-Earth asteroids, like the one that produced Barringer Crater, are far more numerous than, say, the asteroid that produced the Chicxulub crater and extinguished most life on Earth 65 million years ago (*e.g.*, Kring, 2007; Schulte *et al.*, 2010; and Kring, 2016 for reviews). Thus, while not as deadly as the dinosaur-killing impact event, Barringer-size impacts occur far more frequently. The detection of those small near-Earth asteroids in space has improved tremendously since the first edition of this guidebook was published. Recently collated data are shown in Fig. 9.6 and 9.7. Thus far, of order 10^3 to 10^4 near-Earth asteroids the size of the Canyon Diablo projectile have been detected. Lurking undiscovered, however, are an estimated million objects.

Table 9.3. Small (≤ 1 km) diameter impact pits and impact craters.

Crater	Locality	Diameter (km)	Projectile	Age (Ma)
Haviland	Kansas, USA	0.011	Pallasite	0
Carancas	Peru	0.013	H-chondrite	0
Dalgaranga	Western Australia, Australia	0.021	Mesosiderite	0.025
Sikhote Alin	Primorskiy Kray, Russia	0.027	IIAB	0
Whitecourt	Alberta, Canada	0.036	IIIAB	<0.0011
Kamil	East Uweinat, Egypt	0.045	Iron ataxite	<0.005
Campo del Cielo*	Gran Chaco Gualamba, Argentina	0.05	IAB	<0.004
Sobolev	Primorye Territory, Russia	0.053	Iron	0
Veevers	Western Australia, Australia	0.08	IIAB	<1
Ilumetsa	Estonia	0.08	?	>0.002
Wabar*	Rub' al Khali, Saudi Arabia	0.097	IIIAB	0.006 ± 0.002
Morasko*	Poznan, Poland	0.1	IAB	0.01
Kaalijarvi*	Saaremaa, Estonia	0.11	IAB	0.004 ± 0.001
Henbury*	Northern Territory, Australia	0.157	IIIAB	<0.005
Odessa*	Texas, USA	0.168	IAB	0.0635 ± 0.0045
Boxhole	Northern Territory, Australia	0.17	IIIAB	0.03
Macha*	Russia	0.3	Iron	<0.007
Aouelloul	Adrar, Mauritania	0.39	Iron or Pallasite	3.1 ± 0.3
Amguid	Algeria	0.45	?	<0.1
Monturaqui	Antofagasta, Chile	0.46	IAB	<1
Kalkkop	South Africa	0.64	?	<1.8
Målingen	Sweden	0.7	L?	458
Wolfe Creek	Western Australia, Australia	0.87	IIIAB	<0.3
Tswaing	South Africa	1.13	Chondrite	0.220 ± 0.052
Barringer	Arizona, USA	1.19	IAB	0.049 ± 0.003

From Grieve (1991), Grieve *et al.* (1995), Koeberl *et al.* (1988, 1994), Holliday *et al.* (2005), Tancredi *et al.* (2009), Kofman *et al.* (2010), Fazio *et al.* (2014), Ormö *et al.* (2014a,b).

*Crater field; diameter of largest crater listed.

DISTRIBUTION OF METEORITIC MATERIAL AROUND METEOR CRATER, COCONINO CO., ARIZONA

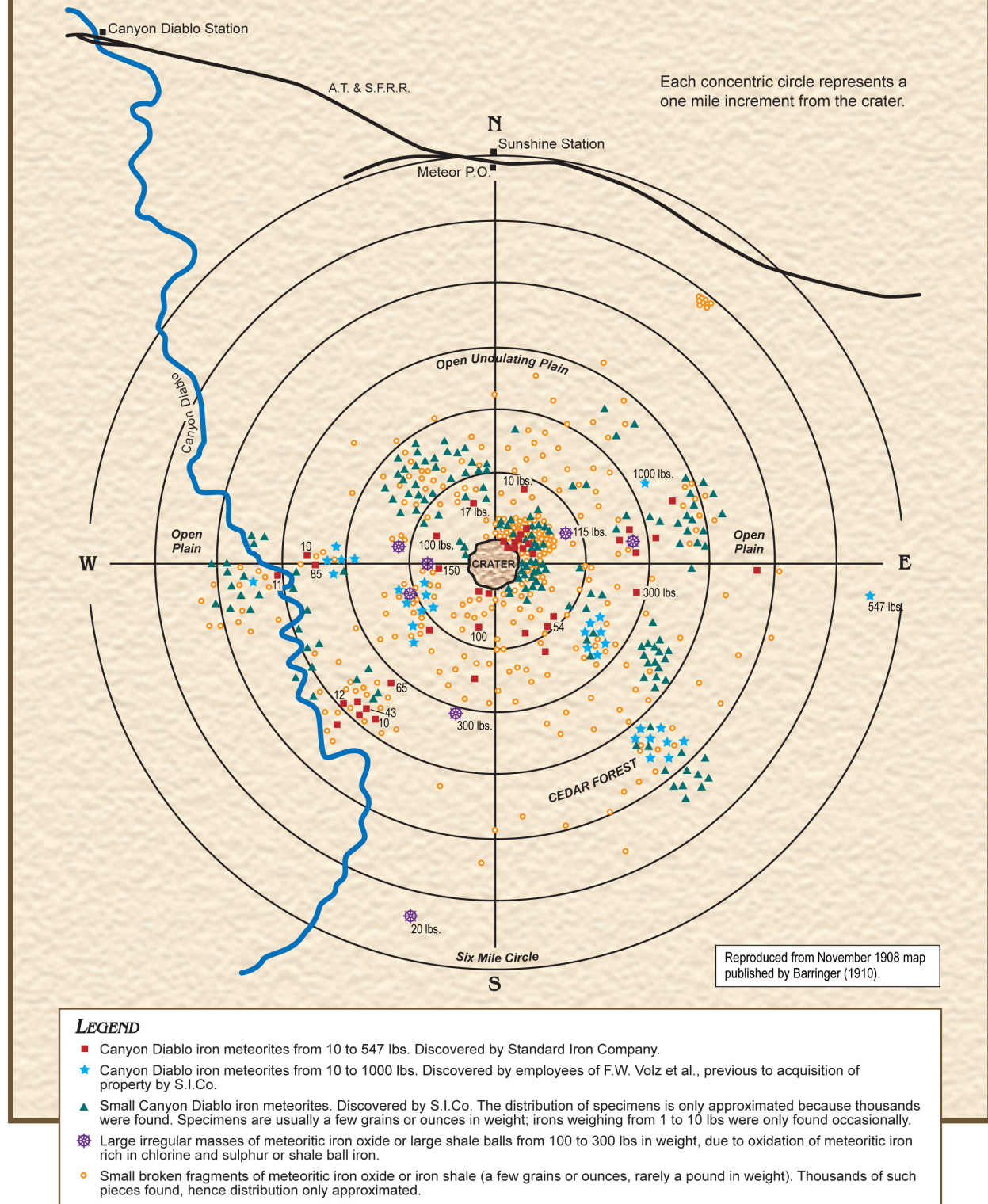


Fig. 9.1. Reproduction of Daniel Moreau Barringer's map of Canyon Diablo meteorite specimens.



Fig. 9.2. Canyon Diablo meteorite. Large fragments of the disrupted iron asteroid were recovered around the crater in the late 1800's and early 1900's as illustrated by a specimen (upper left) in the University of Arizona Mineral Museum, which has material collected when Arizona was still a territory. Etched slices of the meteorite reveal a coarse octahedrite pattern of kamacite and taenite (middle panel with 1-cm cube for scale). This particular slice was taken from a 1,411 g specimen obtained from the descendants of John F. Blandy, the first Arizona Territorial Geologist. Dark troilite and graphite inclusions occur throughout the iron mass and are often rimmed with schreibersite. Some graphite nodules within the meteoritic fragments of the asteroid are cross-cut by veins of metal (lower right, 6-cm-wide specimen).

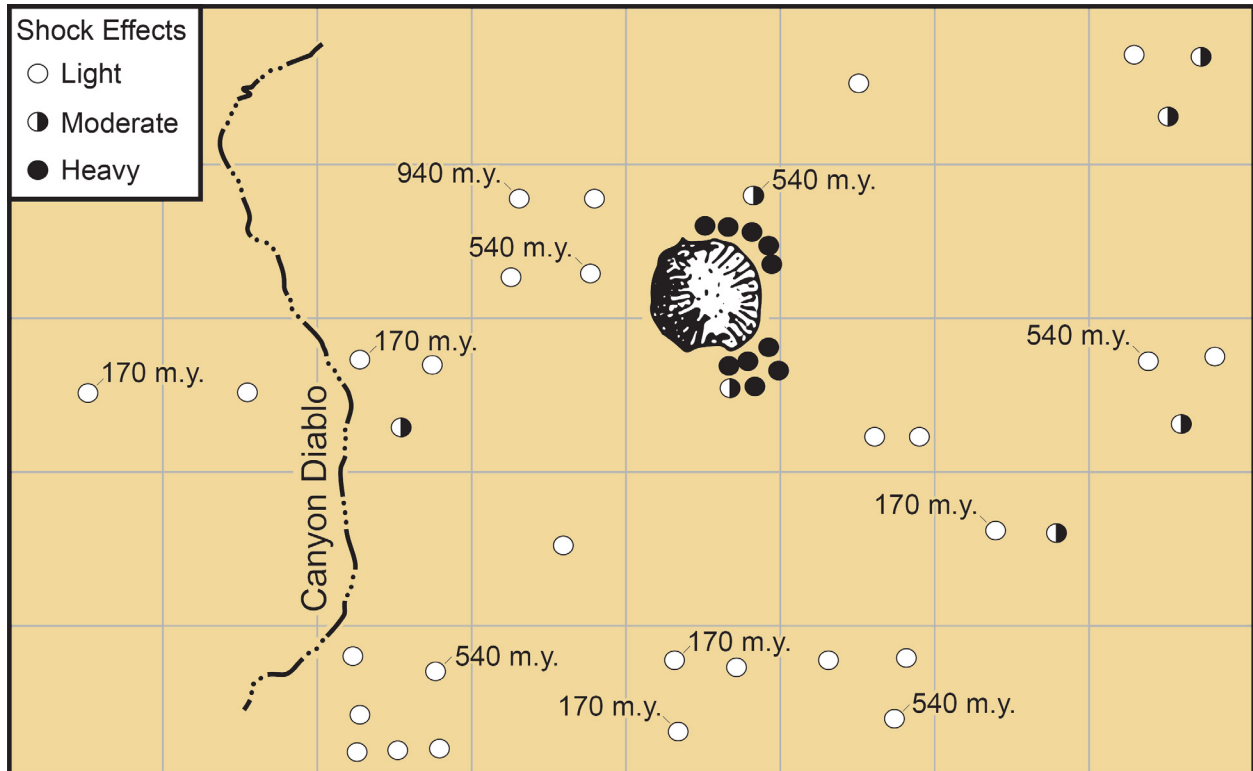


Fig. 9.3. Map of shock effects in rim and plains specimens of Canyon Diablo that were collected in the last century. The specimens with the most severe shock effects were deposited on the crater rim, while low- to moderately-shocked specimens dominated the surrounding plains. Ages reflecting collisional events on the Canyon Diablo asteroid, derived from some of the specimens, are also indicated on the map. (Colorized version of a map published by Heymann *et al.*, 1966.)

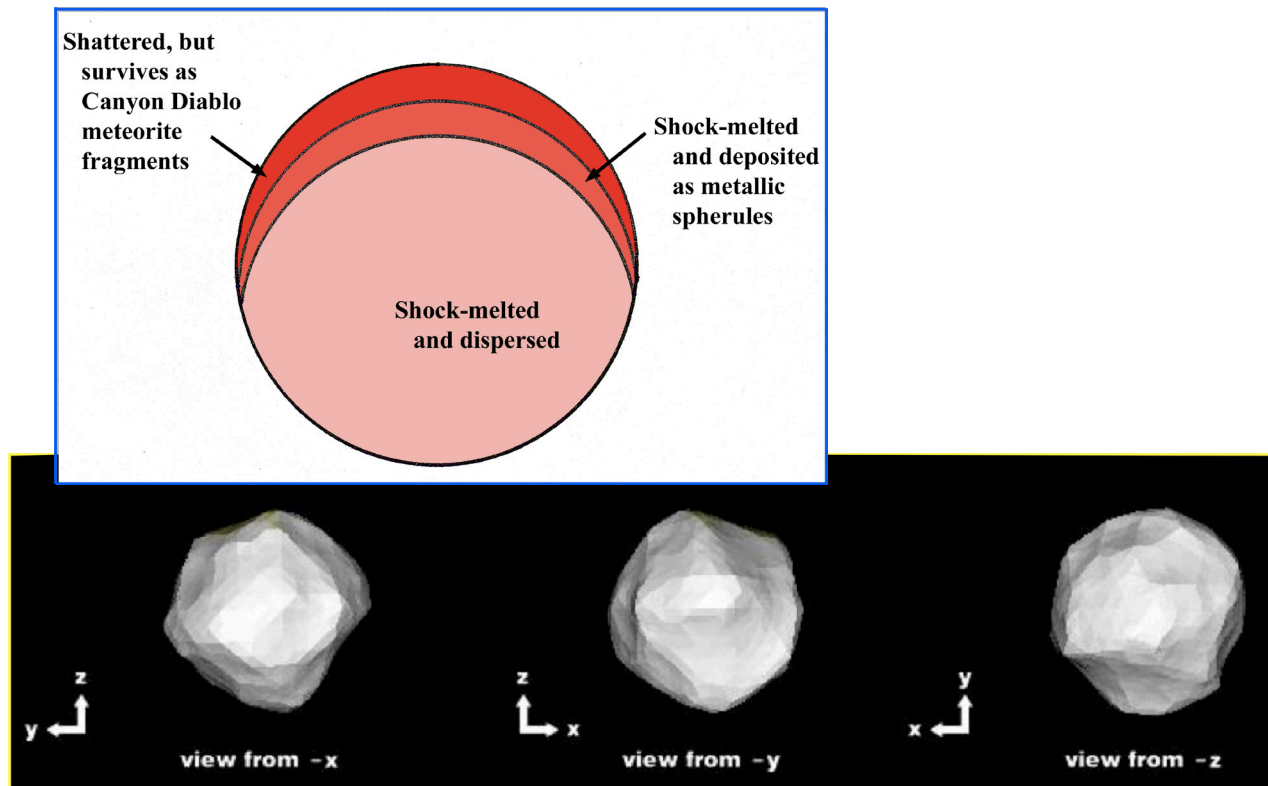


Fig. 9.4. Schematic diagram of the asteroid that produced Barringer Crater (upper left). Cosmogenic nuclides suggest the surviving meteoritic component of the asteroid was derived from a shallower depth (roughly 0.6 to 1.3 m) than molten metallic spherules (roughly 1.3 to 2.0 m depth). Furthermore, lightly-shocked meteorites appear to come from a shallower depth (mean of 0.8 m) than moderately- to heavily-shocked meteorites (mean of 1.3 m depth). The lightly-shocked meteorites are distributed on the plain surrounding the crater, while moderately- to heavily-shocked meteorites are concentrated near the crater rim. Almost all of the diamond-bearing specimens were found on the crater rim. The shape of the asteroid that produced Barringer Crater is unknown, but a suspected metallic near-Earth asteroid is shown (bottom panel) to provide an example of possible morphologies. Three model images based on radar data are shown for (29075) 1950 DA, which were kindly provided by Steve Ostro for our field guide. This object is far larger than the one that produced Barringer Crater (1 km versus 10 to 50 m), but it should help focus our discussion of projectile shape. I refer readers to a paper by Busch *et al.*, 2007) for additional details about asteroid (29075) 1950 DA.

WHEN A NEWSPAPER REPORTS AN ASTEROID BEING TWO TIMES LARGER

Left and center asteroids by Daniel D. Durda

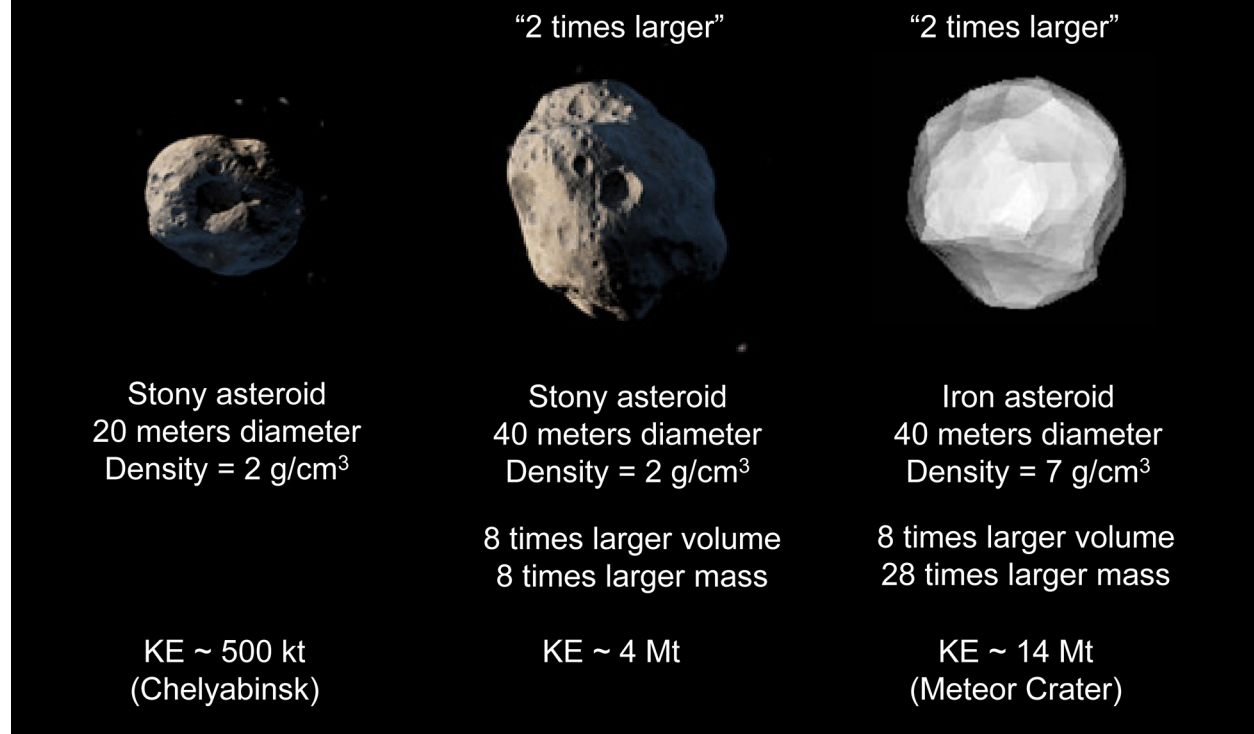


Fig. 9.5. The density of Canyon Diablo meteorite specimens is much higher than that of stony asteroids, like the one that exploded near Chelyabinsk February 15, 2013. That event prompted several comparisons between the Chelyabinsk and Barringer events that did not properly reflect that important property. In news reports, the Chelyabinsk NEA was sometimes described as being half the size of the NEA that produced the famous Meteor Crater in Arizona. That comparison, however, was deceiving, because it did not capture the difference in density and, thus, explosive energy released by the two events. While the NEA that produced Meteor Crater may have been twice the size of the Chelyabinsk NEA, the energy involved was far larger because energy scales with mass, not diameter. The Chelyabinsk NEA was a stony asteroid. A stony asteroid twice that size would have 8 times the volume, mass, and energy of the Chelyabinsk NEA. Meteor Crater was produced by an iron NEA that was much denser. Thus, that NEA, while twice the size and with 8 times the volume, had 28 times more mass and 28 times the kinetic energy of the Chelyabinsk impactor. (Artistic rendering of the two stony NEAs provided by Daniel D. Durda. The iron asteroid is represented by a radar-based shape model of asteroid (29075) 1950 DA that has been dramatically rescaled from 1 km to 40 m for the purpose of this illustration.)

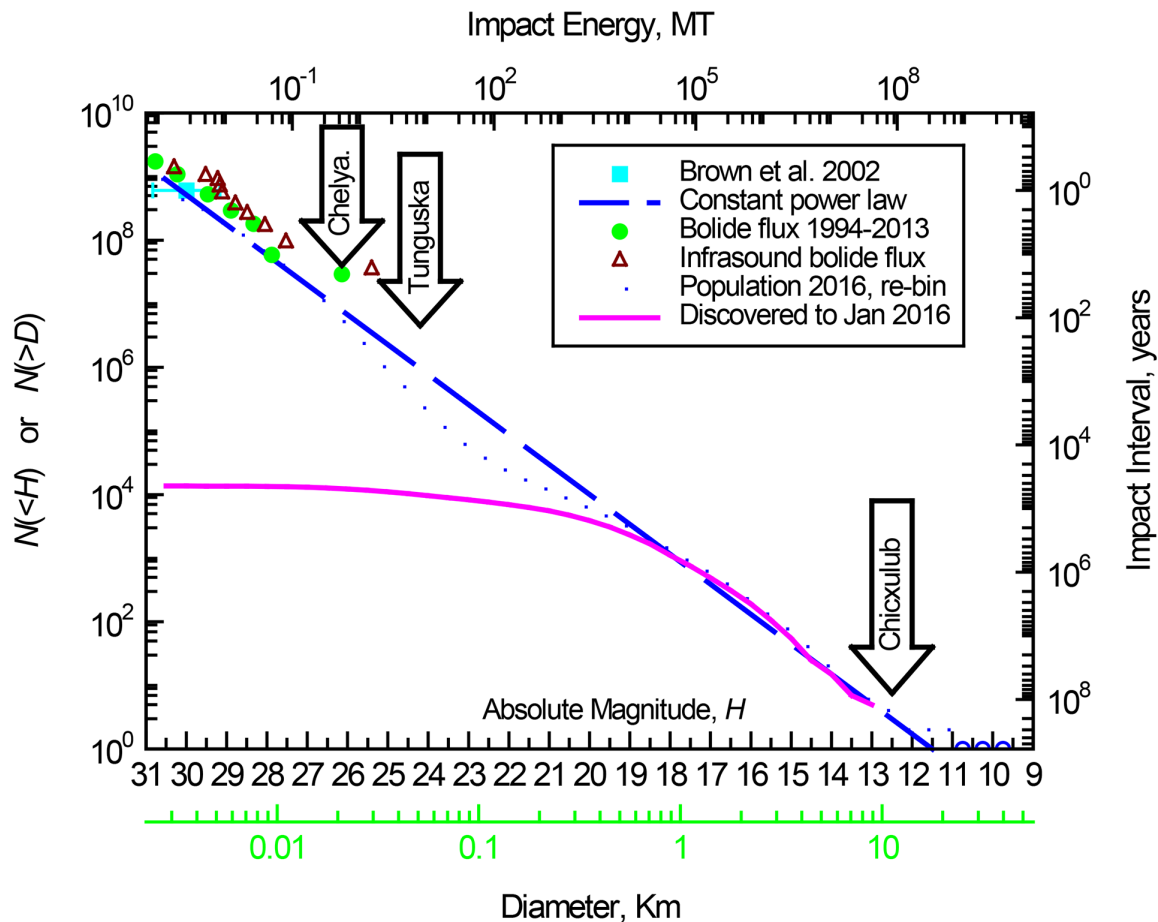


Fig. 9.6. Number (N) of near-Earth objects as a function of absolute magnitude (H) with diameter calculated assuming an average albedo of 0.14 (which makes $D = 1$ km equivalent to $H = 17.75$). This is consistent with the average albedo of NEAs measured by NEOWISE. Ancillary scales are provided for average impact interval (right) and for impact energy (top) in MT of equivalent TNT assuming an impact velocity of 20 km/s. For objects the size of the asteroid that produced Barringer Meteorite Crater, there is a large gap between objects detected thus far (magenta curve) and the anticipated population (blue dots and dashed line). For the smaller asteroids, it is important to note that weaker asteroids (dominantly stony asteroids) break up in the atmosphere, as did the Chelyabinsk event of February 15, 2013, while stronger (dominantly iron asteroids) may reach the surface to produce surface explosions and, if on land, a hypervelocity impact crater, like Barringer Meteorite Crater. The diagram appears courtesy of Alan W. Harris (USA) who kindly updated it for this guidebook.

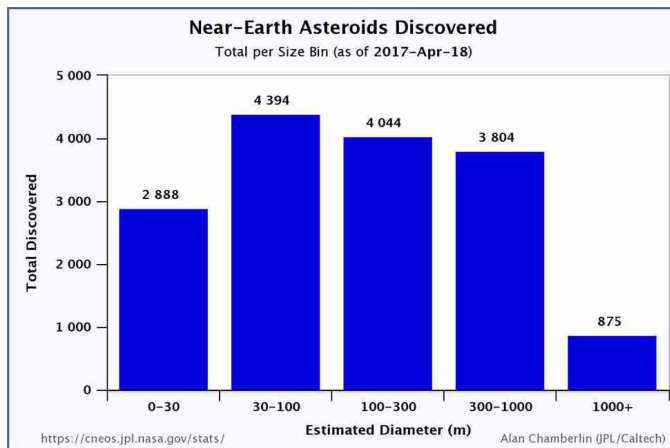


Fig. 9.7. The number of near-Earth asteroids similar in size to the one that produced Barringer Meteorite Crater continues to grow. A few thousand have been discovered thus far: 2,888 in the 0 to 30 m diameter class and 4,394 in the 30 to 100 m diameter class. Data compiled by Alan Chamberlin and current as of April 18, 2017.

10. Trajectory



The trajectory of the impacting asteroid is another issue of considerable debate and still unresolved. Historically, circular plan views of impact craters confounded many investigators who assumed a circular crater requires a vertical impact. They wondered why more craters are not elliptical. Gilbert and Barringer both realized that 45° impacts are the most probable trajectories for meteoritic material. Yet Gilbert, like many of his contemporaries, mistakenly thought a 45° impact produces an oval crater (Hoyt, 1987). Barringer, on the other hand, realized that a 45° impact will produce a round crater (Hoyt, 1987). Despite this insight, Barringer, like Gilbert, initially assumed that the northern Arizona impact had been vertical or nearly vertical and that the asteroid was buried beneath the center of the crater floor.

When extensive drilling did not locate a main mass beneath the crater floor and instead only produced traces of the projectile, Barringer began to consider other options. He had already noted several features that seem to have a directional symmetry. In his 1905 paper, he observed that clusters of immense Kaibab boulders were deposited on the east and west sides of the crater. In his 1910 paper, he argued that the lowermost section of the Coconino only appears in the south-east section of the ejecta blanket and, thus, that the deepest units excavated by the impacting object were ejected in that direction. In that same paper, he also observed that the southern cliffs were uplifted as a single entity by 105 ft. He then suggested that the uplift was caused by a meteoritic mass moving from the north to the south and that the mass remained wedged beneath the cliffs along with a vast amount of shattered rock and Variety A and B shock-metamorphosed Coconino sandstone. He felt vindicated when drilling in 1920-1922 produced a 1,376 ft deep borehole on the southern crater rim that encountered ~30 ft of oxidized meteoritic material, Variety A and B shock-metamorphosed sandstone, and became stuck in what was interpreted to be the main asteroid mass. (See Table 4.2 for the driller's log of that hole.) He published a report (Barringer, 1924), concluding the "mass seems to have approached the earth at an angle of approximately 45°, and from a direction slightly west of north, and to have made a slight curve to the west in its slanting flight through more than 2500 feet or one half-mile of solid rock...."

Shoemaker, on the other hand, was impressed with thrust faults in the crater walls. (See Chapter 6 for more details about the faults.) These faults outlined wedges of rock that are thrust into crater walls, forming anticlines and enhancing crater rim uplift. He and Kieffer (1974) argued that they only occur on the north and west sides of the crater and that they were especially well-developed in the northwest corner. They suggested the features were produced by a bolide moving from the southeast to the northwest.

I agree that the thrust faults are impressive and seem to point to a flow of material through the transient crater margin into the surrounding crater wall in a rough south-to-north direction that encompasses flow towards the northwest and northeast. I have observed a few additional thrust faults along the east margin of the crater, so a purely southeast to northwest flow no longer seems plausible. Taken at face value, the thrusts seem to imply a trajectory roughly from the south to north, with variations to both the northwest and northeast possible. However, I can also imagine the same thrusts produced in reaction to an impact with a projectile trajectory in the opposite direction. I also worry that we are biased by what we can observe. If thrust-faulting occurs low on the hidden portions of the crater walls, we are unable to factor that information into our analysis. The observations only seem truly inconsistent with an east to west or west to east trajectory. Thus, the thrust faults can possibly be reconciled with Barringer's proposed trajectory and the impressive amount of material that may have been injected beneath the rim along the south side of the crater. (See discussion of injected material in Chapter 4.) The uplift of the southern crater wall is a less convincing indicator, because the amount of

uplift along the southern crater wall is much less than that in the east-southeast corner of the crater, as shown in Fig. 17.6 and 17.9 in the trail guide chapters. If uplift is an indicator of trajectory, then the east-southeast corner seems to be at the end of the trajectory. Alternatively, crater wall uplift may be influenced as much by preferential movement along tear faults as trajectory and, thus, not a diagnostic indicator of trajectory.

That was the status of the issue of trajectory when the first edition of the guidebook was published. Since that time, other potential structural indicators of trajectory were measured. In one study, the relative uplift of target strata and the strike of those units were measured along the Kaibab-Moenkopi contact (Poelchau *et al.*, 2009). It was thought that deviations from a perfectly concentric distribution of bedding might indicate the path of the impacting asteroid. The results were ambiguous, but the study concluded a trajectory from the north-northwest to the south-southeast was more likely.

Another structural indicator of trajectory is shearing that has recently been recognized in the crater rim and ejecta blanket (Kring *et al.*, 2011a, 2011b, 2012). In the south crater rim, nearly all (80 m) of the Kaibab ejecta has been sheared radially outward to greater distances from the crater center. (See Chapter 18 for descriptions of the outcrops.) Moreover, in the southwest crater rim, a portion of the ejecta curtain was sheared radially outward, emplacing a rare hinge in the overturned Coconino on top of Moenkopi in the crater wall. That type of shearing is more likely to occur in the uprange or downrange rim of a crater according to cratering experiments (Fechtig *et al.*, 1972; Gault, 1974). For a 45° impact angle, the most probable impact angle and consistent with the symmetrical shape of the crater, shear is more likely to occur in the downrange rim of a crater, suggesting a trajectory from the north to the south.

Other directional indicators have been noted by several investigators: Barringer (1910) pointed to a concentration of iron oxide beyond the northeast corner of the crater; Nininger (1956) and Rinehart (1958) pointed to a concentration of meteoritic soil particles in that same direction; Heymann *et al.* (1966) pointed to a concentration of highly-shocked and diamond-bearing Canyon Diablo meteorite specimens near the northeast and southeast crater rims. Shoemaker and Kieffer (1974) suggested Silica Hill is a small uplift on the crater floor that is offset towards the north. The concentration of meteoritic oxide and iron-rich soil particles in the northeast is the most-often cited evidence beyond the crater rim. Rinehart (1958), for example, wrote that “a highly reasonable hypothesis is that the meteorite approached the earth from a south-westerly direction and, when it struck, pitched forward large quantities of meteoritic material to the position where it now rests.” That would seem to be consistent with a numerical model of the impact (Artemieva and Pierazzo, 2011) that suggests at least 50% of the impacting asteroid was ejected and that it would be concentrated in the downrange direction.

A more distant indicator of impact trajectory may be another young impact crater that some investigators speculate was produced at the same time at the Barringer Crater. This story, too, has its origins with a Barringer. In this case, D. Moreau Barringer Jr. had an opportunity to explore another crater-like structure near the West-Texas town of Odessa. Within a few hours, he found iron meteorites and shale balls and concluded that the structure was an impact crater with at least one satellite impact crater. He telegraphed the news to his father immediately. In private correspondence, Daniel Moreau Barringer wondered if his crater and the Odessa crater could have been produced at the same time by a pair of asteroids traveling together. Several years later, he summarized the evidence for trajectory (Barringer, 1958) and conclude the most likely path was from north or northeast to south or southwest.

The possibility that Barringer and Odessa craters were produced by a pair of asteroids was further explored by Brandon Barringer in a paper presented to The Meteoritical Society in 1965 and published in 1967. Several hints seemed to link the two impact events. (1) Both were produced by similar types of iron asteroids. (2) Although the ages of the craters were imprecisely known, they were approximately

similar. Estimated ages for Barringer Meteorite Crater and Odessa Crater were 20,000 and 25,000 years, respectively, at the time of Brandon Barringer's report. (3) There were hints that both craters were produced by objects with roughly north to south trajectories.

Brandon Barringer recognized problems with some scenarios linking the two events, noting that it was "unlikely that they were formed by the decomposition of a single natural satellite" in the atmosphere. He left the door open, however, to other possibilities. In general, he recommended further study to resolve these and other issues regarding the origin of the craters.

Additional research and newer technology have shed light on the hypothesis. The chemical compositions of the iron asteroids that produced the craters have been analyzed in greater detail and the ages of the two craters have been better determined.

Wasson (1967, 1968) examined the trace element compositions of the iron meteorites at Barringer Crater and those at Odessa. Although both groups of meteorites are part of the same chemical class, there are subtle differences between the meteorites that led Wasson to suggest they formed from two unrelated iron asteroids.

The second set of studies began in the 1980's, when Sutton (1985) examined the crystalline damage caused by naturally occurring radioactive isotopes in crater rocks. Using the isotopes as a clock, he estimated the Barringer Crater was produced approximately 49,000 years ago. Nishiizumi *et al.* (1991) and Phillips *et al.* (1991) used different types of isotopic clocks in crater rocks. They too estimated the crater formed approximately 49,000 years ago. (See Chapter 12 for more information about estimates of the crater's age.)

More recently, techniques similar to those of Sutton were applied by Holliday *et al.* (2005) to the Odessa impact site. They estimated the Odessa craters were produced approximately 63,000 years ago. Although the ages of Barringer and Odessa craters are still not precisely known, these approximate ages suggest Odessa formed earlier, with the caveat that the Barringer crater may be older than 49,000 yrs. (See discussion in Chapter 12). Thus, the two impact events may not be directly related and may not have any bearing on the issue of trajectory.

Nonetheless, several other potential indicators of trajectory survive (and even the Odessa connection might be revived). Unfortunately, those indicators cannot be reconciled at the present time and I think it fair to conclude that the trajectory of the impacting asteroid that produced Barringer Crater remains uncertain.

11. Energy of Impact



The kinetic energy of an impacting asteroid is one-half its mass times velocity squared. As discussed in the previous chapter, the projectile is usually assumed to have a pre-collisional diameter of roughly 10 to 50 m, which represents a mass of ~4,000 to 500,000 metric tons (Table 9.2.). The impact velocity is usually assumed to be between 11 and 20 km/s.

Those dimensions and velocities reflect a wide range of impact energy. Published estimates range from an impact energy equivalent to a few tens of kilotons of TNT to over 60 megatons of TNT (Table 11.1). When Shoemaker (1960, 1963) published his classic study of the crater and analogies with nuclear explosion craters, he estimated an impact energy equivalent to ~1.4 to 1.8 MT. This estimate was based on a cube-root scaling law that he calibrated with the Teapot Ess nuclear explosion. Schmidt (1980) conducted centrifuge experiments, from which he derived a new set of scaling laws. Based on those results, he suggested much higher impact energies, ranging from 22 to 61 MT. At nearly the same time, Roddy *et al.* (1980) developed a new computer model of crater excavation and estimated a 15 MT blast for a vertical impact. Shoemaker (1987) concluded the energy was probably a little higher than 15 MT, because the impact was more likely to have had an oblique trajectory. Roddy and Shoemaker (1995) revised their computer simulations and suggested 20 to 40 MT is a better estimate, which is a rough average of Shoemaker's original estimate and Schmidt's estimates. Unfortunately, the details of those computer simulations only appeared in preliminary form and the details are now lost.

More recently, a family of estimates have been appearing that are dramatically lower and approach Shoemaker's original estimate of the impact energy. These calculations have been emphasizing three features of the impact process: atmospheric deceleration, disruption, and ablation. Before discussing the new results, it may be useful to digress a moment to discuss atmospheric deceleration, disruption, and ablation.

With regard to atmospheric deceleration, it may be best to begin with small isolated iron meteorites. These objects fall to Earth with the same range of velocities as larger, Canyon Diablo-size asteroids, when they first encounter the top of the atmosphere. These small objects are, however, completely decelerated in the atmosphere and eventually fall with a velocity governed by Earth's gravity. Larger impacting bodies with masses substantially greater than the mass of atmosphere they encounter will not be significantly decelerated and will then hit the Earth's surface with most of their cosmic velocity intact. The Canyon Diablo asteroid is at the small end of the range that produces impact craters, so it may represent an intermediate case. It may have been partially decelerated, but still able to maintain enough motion to generate a hypervelocity impact crater.

The Canyon Diablo asteroid is also at the small end of the range of objects that produce impact craters, as discussed briefly in Chapter 9. Smaller objects and weaker objects often catastrophically fragment in the atmosphere. A nearby example is the 6 to 8 m Gold Basin brecciated stony meteoroid that failed to reach the ground intact in northwestern Arizona (Kring *et al.*, 2001). More recent examples are the Tunguska and Chelyabinsk impact blasts (*e.g.*, see Kring and Boslough, 2014, for a popular science summary), in which stony impactors catastrophically fragmented above Russia. None of those events produced a hypervelocity impact crater. Potentially, the Canyon Diablo asteroid began to fragment, but not catastrophically, and reached the ground with a sufficiently large main mass or with a sufficiently dense cluster, while maintaining a significant fraction of its cosmic velocity.

When meteoritic material enters the atmosphere, surfaces are heated dramatically, melt, and slough off. They are ablated. Radiating flow lines generated in the melt are often preserved in meteoritic fusion crusts. Because this is a surface phenomenon, the effect is usually proportionally smaller for larger objects that have larger volume to surface area ratios. However, if a larger object begins to fragment and greatly enlarge the amount of surface area, ablation may consume an increasingly large fraction of the original asteroid.

Calculations that explicitly examine atmospheric deceleration, disruption, and ablation processes are generating new estimates of the impact energy that fall in the range of ~1 to 10 MT (Melosh and Collins, 2005; Artemieva, 2006). Because the asteroid is being decelerated, a larger mass and diameter for the original asteroid are implied. For example, Artemieva (2006) calculates a ~40 m diameter coherent iron asteroid with an 18 km/s collisional velocity has sufficient energy to create the crater. However, if she allows for disruption and ablation, she requires a 57 m diameter asteroid that was decelerated to a final impact velocity of 11 km/s or a 46 m diameter asteroid that was decelerated to a final impact velocity of 15 km/s. Both generate about 10 to 11 MT, which her calculations suggest is sufficient to excavate the crater and fracture the surrounding wall rock. That model continued to evolve (Artemieva and Pierazzo, 2009, 2011) and produced energies of 7 to 15 MT. A more recent numerical model that fit crater morphometry, structural deformation, and the crater's gravity signature (Collins *et al.*, 2016) produced required an energy of 8.6 MT. Thus, the numerical models appear to be converging on surface impact energies of nearly 10 MT, with initial energies at the top of the atmosphere about 50% greater.

Table 11.1. Estimates of Impact Energy

Energy (MT TNT equivalent)	Source
38.8	Magie 1910 (per Hoyt 1987)
38	Moulton (per Hoyt 1987)
2.91	Moulton (per Hoyt 1987)
0.21	Wylie 1943 (per Hoyt 1987)
0.08	Baldwin 1949 (per Hoyt 1987)
4.8	Gilvarry and Hill 1956 (per Hoyt 1987)
64	Opik 1958 (per Hoyt 1987)
1.4 to 1.8	Shoemaker 1963
8.1	Baldwin 1963
4 to 5	Shoemaker 1974
22 to 61	Schmidt 1980
15	Roddy <i>et al.</i> 1980
15+	Shoemaker 1987
20 to 40	Roddy and Shoemaker 1995
5.3	Schnabel <i>et al.</i> 1999 (calc. for their 15 m radius & 20 km/s velocity)
0.44	Ai and Ahrens 2004 (calc. for their 9 m diameter & 33 km/s velocity)
2.5	Melosh and Collins 2005
10 to 11	Artemieva 2006 (calc. for her 46-57 m diameter & 15-11 km/s velocity)
7 to 15	Artemieva and Pierazzo 2009 (calc. for their 46-66 m diameter & 15-18 km/s velocity)
8 to 12	Artemieva and Pierazzo 2011 (calc. for their 40-47 m effective diameter & 16 km/s velocity)
8.6	Collins <i>et al.</i> 2016 (calc. for their 3.2×10^8 kg, 42 m diameter projectile, & 15 km/s velocity)

For cases where kinetic energy is calculated from authors' estimates of projectile size and velocity, I assume a projectile density of 7.8 g/cm³. For the effective diameter of Artemieva and Pierazzo (2011), I used the effective density that they tabulated. Please note there was a typographical error in Collins *et al.* (2016), so the mass was reported at 10⁸ kg rather than 3.2 × 10⁸ kg.

12. Age of the Crater



As any visitor can see, the crater is exceptionally well-preserved. Although talus covers the lower slopes of the crater walls and finer-grained sediments cover the crater floor, the crater still has the sharp edges of a relatively unaltered structure. For that reason, a young age has always been assigned to it. Indeed, Barringer (1905) estimated the age to be 2,000 to 3,000 yrs, not much older than the 700 yr-old rim cedars (junipers). Likewise, Tilghman (1905) commented that the crater looked like it formed yesterday and that it must have an age less than 10,000 yrs and probably less than 5,000 yrs.

Measuring a precise age for the crater, however, was difficult. Even using modern techniques, the question of age was difficult to resolve. The impact did not produce huge volumes of impact melt that might be analyzed using the isotopic systems (*e.g.*, ^{40}Ar - ^{39}Ar) often applied to other igneous rocks, including impact melts. In addition, the crater is too young for many of those radiometric systems to be applied, because they involve half-lives that are too long. For that reason, many early attempts to determine the age of the crater relied on evaluations of erosion and sedimentation.

In a paper titled “The Age of Meteor Crater,” Blackwelder (1932) evaluated the thickness of lake sediments within the crater, the amount of alluvium and finer-grained debris on the crater slopes and crater floor, ravines cut into the crater deposits, and dissolution pitting of ejected limestone blocks. Based on those criteria, he estimated the crater was produced between 40,000 and 75,000 years ago. As described further below, this may be an incredibly accurate estimate.

At about the same time, Jakosky *et al.* (1932) conducted an electrical and magnetic survey of the crater. In the course of that investigation, they evaluated the thickness of lake beds on the crater floor, lag deposits of concretions on Coconino and Kaibab surfaces on the crater rim, and small basins filled with sediment from eroded ejecta. They argued that the “fresh looking cliffs” are not, in fact, fresh, but rather “the products of centuries of erosion.” They also pointed out that the thickness of Moenkopi buried beneath Kaibab and Coconino in the crater walls is much greater than the thickness of Moenkopi on the surrounding plains. They required sufficient time to erode up to 40 ft of Moenkopi on the plains. We now understand that this latter argument is flawed, because the Moenkopi is thickened by an overturned component in the crater walls and, thus, the discrepancy is not an erosional one. Nonetheless, based on all of these criteria, they concluded the crater formed tens of thousands of years ago and probably about 50,000 years ago.

Shoemaker (1960, 1974) compared the Pleistocene and Holocene alluvium that covers the ejecta blanket with deposits elsewhere on the Colorado Plateau. Drawing on those comparisons, he estimated (Shoemaker, 1974) the crater was produced “a few tens of thousands of years ago, as shown by the mid-Wisconsin age of the oldest sedimentary deposits on the rim and in the interior of the crater.” He quantified those words with estimates of 20,000 to 30,000 yrs and $25,000 \pm 5,000$ yrs (Shoemaker, 1983), which were numbers he used for over a decade. His estimate may have been influenced by the first radiometric age of material in the crater. Ives *et al.* (1964) obtained a radiocarbon age for shells from a dump around the crater’s main shaft. The measured age was $24,000 \pm 2,000$ yrs. The shells were believed to be from the basal portion of the lake sediments. Assuming the lake sediments were deposited immediately after the crater formed, the value indicated the age of the crater. However, if either the lake did not form immediately or the shells were from a higher level within the lake sediments, the date only represented a minimum age for the crater.

Those shells and other fossils deposited in lake sediments on the crater floor provide additional clues about the crater's age through correlations with fossil assemblages in other localities and climatic events. The results, however, are ambiguous (Reger and Batchelder, 1971; Forester, 1987) and will not be discussed in any detail here. In addition, a preliminary assessment of pollen from the base of the lake sediments (Davis and Kring, 2002) found an assemblage that is similar to those in 50 ka sediments in Walker Lake near Flagstaff. That, however, is more a measure of climatic conditions and not a diagnostic indicator of age.

Efforts to directly measure the age of the crater resumed in the mid-1980's, when Sutton (1985) measured thermoluminescence ages for shock metamorphosed rocks. He estimated an age of $49,000 \pm 3,000$ yrs for the crater. Similar ages were soon recovered using cosmogenic nuclides that measured the amount of time boulders on the rim of the crater had been exposed. In back-to-back papers, Phillips *et al.* (1991) and Nishiizumi *et al.* (1991) reported $49,700 \pm 850$ and $49,200 \pm 1,700$ yr ages, respectively. Based on the extraordinary agreement between these three independent studies, 49 or 50 ka is widely accepted to be the age of the crater.

The ages based on cosmogenic nuclides are being re-evaluated, because estimates of the production constants and scaling factors needed for the calculations have been improved. The recalibration of production rates was an immense consortium project called Cosmic-Ray Produced Nuclide Systematics on Earth or, CRONUS (Borchers *et al.*, 2016). While that effort was underway, we re-examined the ^{36}Cl -based age determinations of Phillips *et al.* (1991). Splits of the original samples were re-analyzed using modern techniques. The measured values were very similar to the original values. However, application of a preliminary version of the revised production rates produced an older age of 56.0 ± 2.4 ka, which we reported at the 2010 Meteoritical Society meeting (Marrero *et al.*, 2010).

Unfortunately, the final CRONUS production rates have not yet been applied to the ^{36}Cl data, nor to the ^{10}Be - ^{26}Al measurements of Nishiizumi *et al.* (1991). I am told (Kuni Nishiizumi, personal communication, 2017) that the deviation from the original 49 ka age will not be as large for the ^{10}Be - ^{26}Al system as it appears to be for ^{36}Cl . Thus, at the present time, I recommend the age of the crater used in public venues remain at 50,000 yrs, but caution that the age could drift to slightly older ages as geochronological techniques are refined.

Plans for other types of age determinations have been made. The first involves pack-rat middens that are scattered among the rocky clefts of the crater walls. Pack-rat middens have been excellent sources of both age and climate information elsewhere on the Colorado Plateau. Appropriate samples will be collected to determine an age for the deposits, which will provide an additional minimum age for the crater. In addition, the fossil sequence within the lake sediments will be resampled. This latter task, however, is delayed until the walls of Main Shaft and/or Shaft #2 (also called the Science Shaft) in the crater floor can be stabilized. Efforts are underway to raise funds so that the shafts can be re-cribbed and converted into permanent research and educational facilities.

I considered using the thickness of carbonate rinds (caliche) around ejected debris to place a constraint on the age of the crater. While that method has been applied in the southwestern United States (Amoroso, 2006), the uncertainty on caliche production rates is too large to sharpen our assessment of the crater's age. I have, for example, measured caliche layers 0.3 to 0.5 mm thick around pebbles and cobbles in the ejecta blanket (*e.g.*, Cernok and Kring, 2009; also Fig. 15.6). When applying the calibration curve of Amoroso (2006) to the thickest caliche layer (0.5 mm), I derive an age of 54^{+10}_{-8} ka. However, I also note that two of the data points used to derive that calibration curve have ages ranging from 20 to 90 ka for rind thicknesses of 0.5 mm. A related technique that cross-correlates variations in

carbon and oxygen isotopes with U-Th geochronology in layers of pedothem carbonate (*e.g.*, Oerter *et al.*, 2016) is a newly developed option that has yet to be applied.

An effort to determine the age of volcanic ash that fell into the crater is also underway. Deposits of ash fell when a lake filled the crater and after that lake dried up (Chapter 14). If these attempts are successful, they will provide a minimum age for the crater. They will also help calibrate the chronology of geologic events that helped shaped the crater we see today.

13. Environmental Effects of the Impact



The relationship between the Chicxulub impact event and a mass extinction at the Cretaceous-Tertiary boundary has promoted an assessment of the environmental effects of impacts of all sizes. Such studies have two components. First, they must reconstruct the environment at the time of impact. Second, they must determine the effects of the impact on that environment and the plants and animals within it. An initial attempt to resolve those issues at Barringer Crater appeared two decades ago (Kring, 1997) and will be summarized here. As discussed at the time, there were numerous uncertainties in the baseline data being used, so a discussion of possible permutations will also appear below.

Any age for the crater within 20,000 yrs of 50 ka places the impact event within the Wisconsin interstadial, which is a relatively warm interval during the Wisconsin period of glaciation. The topography was similar to that seen today. The average slope was $\sim 0.5^\circ$ to the northeast. Moenkopi ridges had an average relief of ~ 5 to 10 m and the maximum topographic high was no more than ~ 20 m. Drainage systems may have been more active than they are today, because the climate was wetter during the Wisconsin period. Gilbert (1896) even suggested the impact hit a small drainage system. Most of the volcanic features in the region were present, with the possible exception of few cinder cones with age comparable to or younger than that of the crater.

Currently, the vegetation around the crater is dominated by a grassland (Fig. 13.1). At lower elevations to the east, the grassland is replaced by a sagebrush ecosystem. At higher elevations to the west, the grassland is replaced sequentially by a woodland and pine forest. The woodland is dominated by juniper and pinyon, small patches of which can also be found on the south crater rim. The understory of the woodland is composed of grasses and shrubs. The pine forest is dominated by Ponderosa Pine at lower elevations and a mixture of Douglas-fir, White-fir, Limber Pine, and Aspen at higher elevations. Spruce-bearing conifer forests and alpine tundra occur at the highest elevations in the San Francisco Peaks, ~ 60 to 70 km northwest of the crater.

At the time of impact, these vegetation zones were shifted to lower elevations, because of climatic conditions during the interstadial. Pollen deposited in lake sediments throughout the region suggested woodlands may have been established near the crater and possibly at the impact site (Kring, 1997). Efforts to improve this floral reconstruction continue and have benefitted greatly from the expertise of Owen Davis, who is one of the leading palynologists in the American southwest. In a preliminary study (Davis and Kring, 2002), lake sediment deposited on top of the impact breccia lens was recovered ~ 30 m beneath the crater floor. Davis' pollen analysis confirms the climate favored the types of forests now restricted to the highlands of the Flagstaff area. However, the concentration and diversity of the pollen is low and dominated by wind-dispersed pollen types, suggesting long-distance transport and locally sparse vegetation at the crater. The impact may have occurred in a sagebrush community, bordered by a narrow woodland that transitioned to pine and spruce forests over short distances (Fig. 13.2).

The surrounding sagebrush steppe, woodland, and forest terrains were populated with mammoths, mastodons, large ground sloths, tapirs, bison, camels, and horses (Kring, 1997). Mammoths grazed on sagebrush and related vegetation, so they may have been in the immediate vicinity of the impact. They also migrated into nearby spruce forests. Mastodons preferred to browse in spruce forests, pine forests, and woodlands. Large ground sloths preferred to graze and browse in sagebrush and open woodlands, along with bison and camels.

In this type of environment, the most destructive components of the impact event were ejected debris, a fireball, a radiating shock wave, and a closely related air blast. These effects were confined to the region. A small amount of seismic energy was generated and small amounts of climatically-active gases (*e.g.*, CO, CO₂, SO₂ and/or SO₃, H₂O, Cl, and Br) were released, but of little consequence.

The magnitude and radial extent of a radiating shock wave and air blast depends on the energy of the impact event. (It also depends on the trajectory, but that issue will be discussed separately.) At the time of Kring's initial study, Roddy and Shoemaker (1995) estimated the impact energy was equivalent to 20 to 40 MT of TNT. As discussed in Chapter 10, more recent calculations suggest lower energies. For purposes of discussion on the field trip, some of the effects are illustrated (Fig. 13.3) for a 20 MT blast, with the caveat that smaller radii may apply to the effects if lower impact energies are appropriate.

We do not yet know if the impact occurred during the day or night. Nonetheless, a relatively pastoral scene was disrupted when an iron asteroid came hurtling through the atmosphere. The meteor would have split the sky along a bright path of light before slamming into the ground. Plants and animals at ground zero were vaporized, while most of the asteroid and some of the underlying bedrock were obliterated. Bedrock below and around the vapor-melt zone was then ejected and overturned, burying the topography and any plants and animals not already swept away by an air blast.

The collision generated a shock wave, as described previously in Chapter 4. In addition to radiating into target bedrock and the asteroid, a shock wave radiated across the landscape. This created dramatic overpressures. It also generated an air blast. These winds were in excess of 1000 km/hr in the vicinity of the impact event (Fig. 13.3) and decreased with distance. The winds severely damaged trees in any forested area within a diameter of 32 km. Grass, small shrubs, and soil were probably stripped from the area near the crater by these high velocity winds. A small amount of material can potentially have been trapped beneath the overturned ejecta, because roots in soil were preserved in a similar position around the Sedan nuclear explosion crater (Carlson and Roberts, 1963). I have not yet found, however, any material sandwiched in Moenkopi hinges along the crater wall or in drill samples that penetrated that contact beneath the ejecta blanket.

Shock overpressure and wind velocity diminished with distance, falling from 2200 km/hr at a radial distance of 3 km to 800 km/hr at a radial distance of 6 km, but remaining fairly large for distances approaching 30 km. Throughout a circular region up to 32 km in diameter, the large mammals described above would have been killed or wounded by the pressure pulse and air blast. Some of the injuries would have been directly caused by the pressure pulse. For example, it would have caused rapid pressure oscillations in air-containing organs and damaged areas between tissues of different densities (*e.g.*, near joints). This would have generated hemorrhaging and edema in the lungs that caused suffocation, air emboli that may have obstructed blood vessels in the heart and brain, and fibrin emboli in the blood that may have damaged the brain and other organs. In addition to these direct blast injuries, animals would have been injured when the blast wave hit them, accelerated their bodies to velocities on the order of a few to tens of kilometers per hour, and then slammed them back onto the ground or they collided with other objects. The air blast also picked up broken branches, rocks, and other types of missiles that created a fusillade of debris that impaled, lacerated, or otherwise traumatized animals.

These are the effects of the impact and crater-excavating blast. Additional damage was created by the ballistic shock wave. Because we do not yet know the trajectory of the object (Chapter 10), these effects are more difficult to quantify. However, it is likely that a ballistic shock expanded the region affected by many of the processes described above.

As far as we can tell, the northern Arizona impact was not witnessed by or involved any humans in the region. (It is more likely that the Gold Basin event was witnessed, because it occurred ~15,000 yrs ago.) If a similar size impact were to occur over a modern city, however, that city would largely be destroyed. As an example, the effects above have been mapped to Kansas City (Kring, 1997).

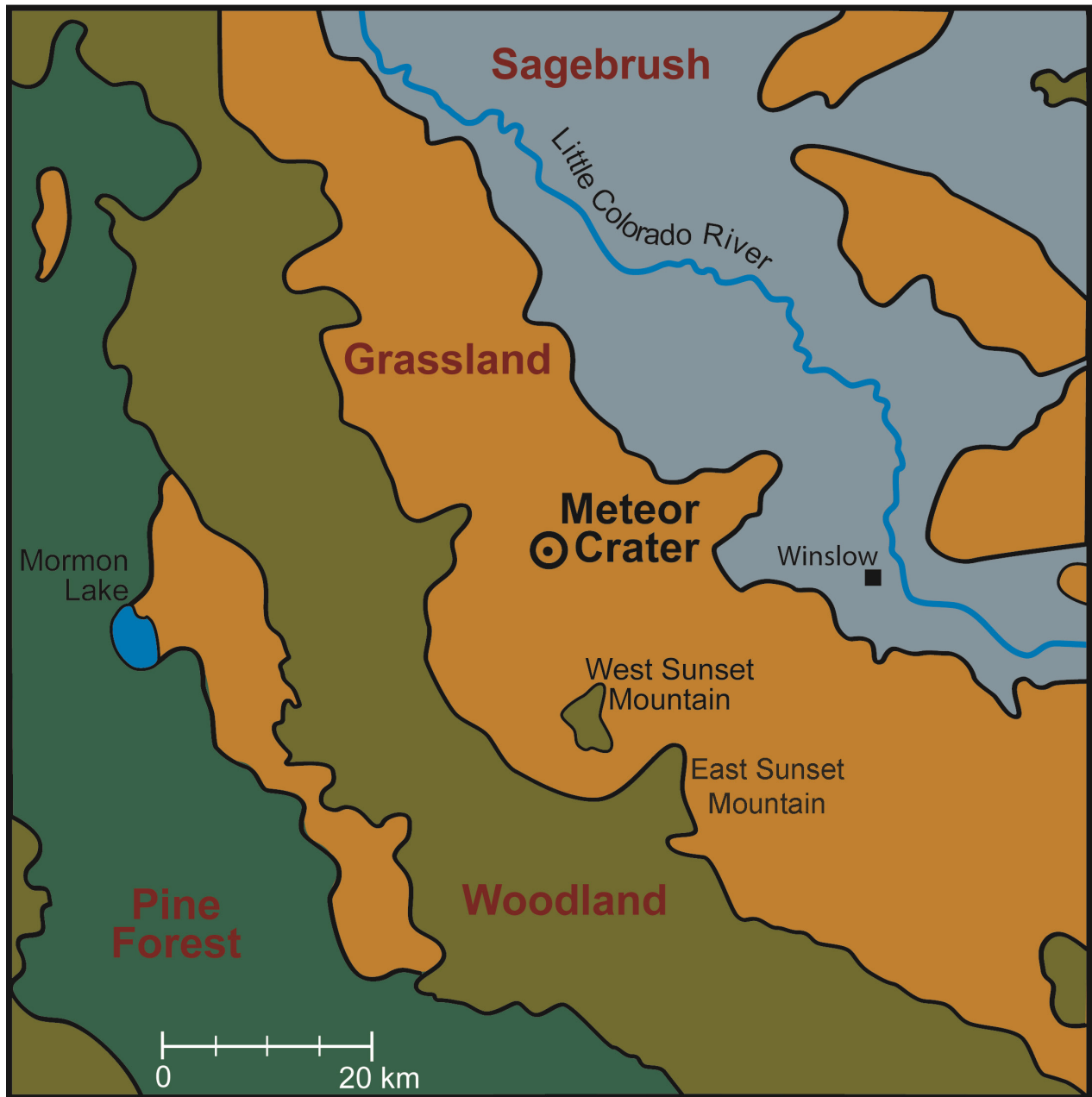


Fig. 13.1. Map showing the distribution of biotic communities in the area around Meteor Crater today. The zones of sagebrush, grassland, woodland, and pine forest are extracted from a map of southwestern biotic communities by Brown and Lowe (1980). This is a slightly simplified and colorized version of a map that appeared in Kring (1997), which should be consulted for additional details about the vegetation in the immediate vicinity of the crater.

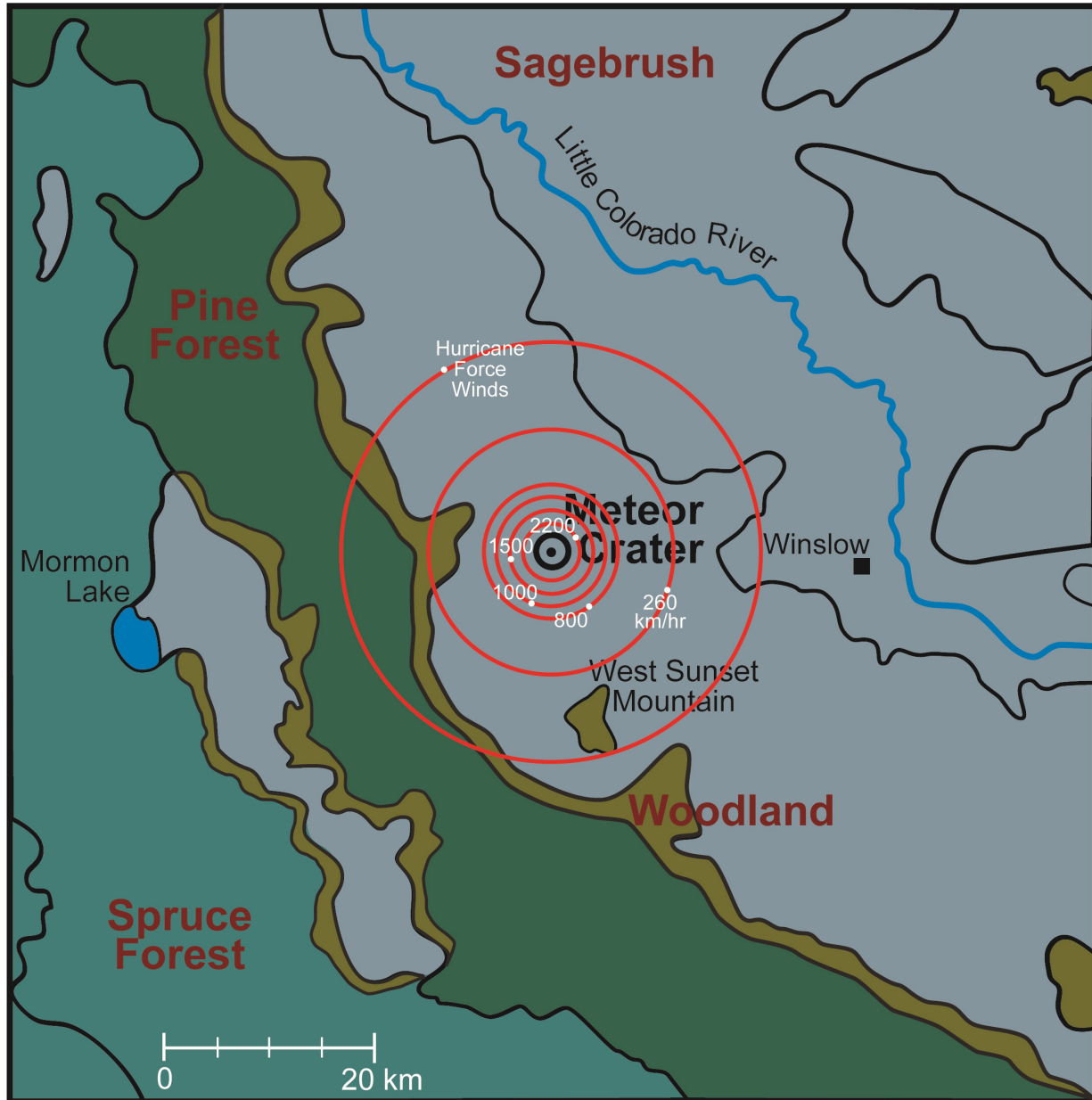


Fig. 13.2. A preliminary palynological study of sediments deposited immediately on top of the mixed debris unit on the floor of the crater has been used to reconstruct the vegetation zones that may have existed at the time of impact ~50,000 years ago (Davis and Kring, 2002). The climate at the time of impact favored the types of forests that are now restricted to the highlands of the Flagstaff area (Kring, 1997). The concentration and diversity of the pollen in the crater sediment is low and dominated by wind-dispersed pollen types, suggesting long-distance transport and locally sparse vegetation at the crater (Owen Davis, personal communication). Thus, upland vegetation near the crater was probably a conifer groveland, with stands of pine, spruce, and fir scattered along a sagebrush steppe. In contrast to a previous reconstruction (Kring, 1997), the new data suggest forests were a few kilometers west of the crater, rather than in the immediate vicinity of the crater at the time of impact. As the new study proceeds, additional samples will be analyzed to further refine our reconstruction of environmental conditions at the time of impact. Also indicated on the map are the wind velocities generated by the impact event, assuming an impact energy of 20 MT. Wind velocities at radial distances of 3, 4, 5, 6, and 12 kilometers were 2200, 1500, 1000, 800, and 260 km/hr (Kring, 1997). Category 3 hurricane-force winds existed at a radial distance of 20 km (outermost red circle). Although not shown, hurricane-force winds extended to a radial distance of 30 km.

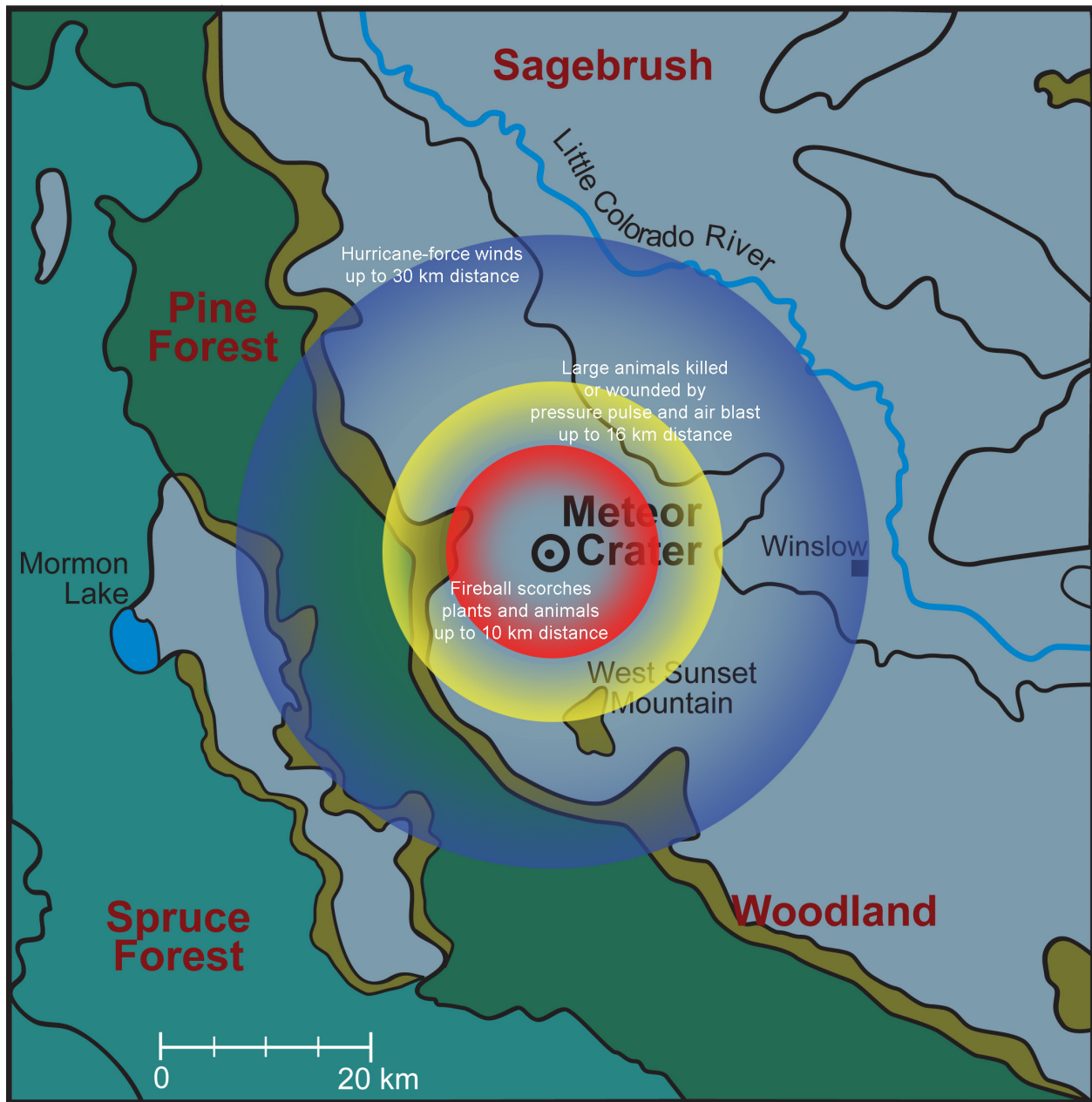


Fig. 13.3. The surrounding sagebrush, woodland, and forest terrains were populated with mammoths, mastodons, large ground sloths, tapirs, bison, camels, and horses. Mammoths grazed on sagebrush and related vegetation, so they may have been in the immediate vicinity of the impact. They also occasionally migrated into spruce forests. Mastodons preferred to browse in spruce forests, pine forests, and woodlands. Large ground sloths preferred to graze and browse in sagebrush and open woodland communities. Similarly, bison and camels migrated through both sagebrush and open woodland communities. Presumably horses did the same, but their distribution 50,000 years ago is less well-known. Shock pressures, wind velocities, and heating were greatest within a few kilometers of the impact. The fireball scorched plants and animals out to a maximum distance of 10 km (red circle). Large animals were killed or wounded by the pressure pulse and air blast out to a distance of 16 km (yellow circle). The air blast decelerated with distance from the crater. The maximum limit of hurricane force winds was 30 km (blue circle). These radial distances assume a 20 MT impact event.

14. Post-impact Lake and Volcanic Ash Deposits



Barringer (1905) recognized ~70 ft of lake sediments on the crater floor and reported they contained fresh-water shells and microscopic organisms with siliceous skeletons. Sketchy reports of the lake sediments were included in several other papers about the crater (*e.g.*, Tilghman, 1905; Fairchild, 1907; Merrill, 1908; Barringer, 1910, 1914; and Jakosky *et al.*, 1932), including the work of Shoemaker (1960), who incorporated them in his cross-section of the crater (Fig. 4.5).

The lake sediments indicate climatic conditions were wetter at some point in the past and potentially at the time of the impact. Today the water table is far below the crater floor. In the well for the museum complex, the water table is 186 m deep, which places it about 183 m beneath the average pre-impact surface. Based largely on the presence of lake sediments, Shoemaker and Kieffer (1974) estimated the water table was about 30 m higher at the time of impact, arguing further that the impact occurred during a pluvial period in the late Pleistocene.

They made two important observations: the lake sediments are deposited directly on the fall-out debris unit without any intervening alluvium; and there is a concentration of fragile, pumiceous lechatelierite in those basal lake sediments, as if it floated before being buried. They concluded the lake must have formed immediately after impact (Fig. 14.1). Roddy (1978) concurred, suggesting the water table may have been as much as 43 m higher than it is today to generate a 10 m deep lake. This puts the water table well up into the walls of Coconino and one can envision a ring of artesian-fed springs or waterfalls around the crater. These springs and the lake they created produced a new habitat in the region. They may have also begun to dissect impact breccias on the crater walls. The lake sediments are continuous laterally across the crater floor based on exploration shafts and drilling. They also are stratigraphically continuous, with breaks only composed of volcanic ash. The lake eventually disappeared as climatic conditions became arid and the water table fell. A series of playa deposits were produced during the transition.

I suspect these lake sediments may provide one of the best climatic records on the Colorado Plateau for the late Pleistocene, at least from the time the impact occurred (~50 ka) until the lake disappeared (~11 ka). For that reason, efforts are underway to restore access to the lake sediments in the two surviving shafts in the crater floor (Fig. 14.2). Access will permit detailed sampling of macro- and micro-fauna and the rich stable isotope record that those types of specimens can provide.

One of the most interesting reports was generated by Reger and Batchelder (1971) who re-examined the collection of fossils that Holsinger made for Barringer. They identified the species of mollusks in two shafts (#1 and #3), a pit and cut near Silica Hill, and drill hole number 28. They separated the mollusks into groups that inhabit terrestrial, fluctuating water, and perennial water environments. Mollusks that favor perennial water habitats were found at all stratigraphic depths, including the deepest level analyzed (73 ft in Shaft #3).

Another interesting report, albeit brief (3 paragraphs), was written by Forester (1987). He received a collection of lake sediments from Shoemaker, who is said to have collected them from the wall of one of the shafts. Unfortunately, no details about sample depths or sample density were available in that report, nor did it say if more than one shaft was sampled. Nonetheless, Forester tried to reconstruct the evolution of the lacustrine system based on available material. The samples contain a diverse assemblage of ostracodes (19 species) and diatoms. One sample also contained benthic foraminifera. Ostracodes are aquatic crustaceans with a hinged bivalve form. Most ostracodes are very small (*e.g.*, 0.5

to 1.5 mm) and calcified. Diatoms are microscopic single-celled aquatic plants related to algae. They secrete silica, which preserves their form. Foraminifera are single-celled planktonic animals with a perforated calcified shell.

Forester suggests the earliest ostracodes are consistent with a saline lacustrine or spring environment, from which he infers the system was shallow. The water freshened resulting in a truly freshwater lake that hosted ostracodes that prefer cold water. He envisions the lake was fed by freshwater springs or seeps around the perimeter. The next ostracode assemblage is dominated by species that only inhabit freshwater springs or seeps, from which he suggests the lake had evolved into a marsh. This assemblage was eventually extinguished, when conditions became too arid to support any aquatic activity and, instead, transitioned to a dry playa environment.

When the first edition of this guidebook was published, I wrote that it was unfortunate that the sample suite was not tied to the stratigraphy of the lake sediments. Taken at face value, the first assemblage suggests a lower water table than that inferred by Shoemaker and Kieffer (1974) and Roddy (1978). It is also seemingly inconsistent with the observations of Reger and Batchelder (1971). In general, it seemed that only a small amount of data survived from previous fossil collections and that the documentation was poor. Many samples were collected from dumps around the shafts and without reliable stratigraphic control. That may have been true then, but I have since been able to recover a portion of the older evidence. Fortunately, I was able to locate the retired USGS paleontologist, Rick Forester, who conducted his study of the lake sediment biota with J. Platt Bradbury. He generously made time for a large number of questions. He provided (personal communication, 2010) a tremendous number of details about his previous work and valuable insights that I want to share here.

The samples he analyzed were part of Shoemaker's thesis collection from the walls of the shafts (collected by Shoemaker and F. M. Byers, January 25-30, 1958; Shoemaker's field notes). The samples contain ostracodes, green algae, rare diatoms, and, surprisingly, marine-type foraminifera that were possible because of the groundwater chemistry that emanating from spring mounds on the crater floor. Forester reported that the first waters to produce ostracodes also had marine solute abundances. He interpreted that to mean, again, that the water was derived from below (groundwater that had interacted with target rocks), rather than being dominated by rain or surface water. He went on to note that some of the ostracodes are similar to those associated with boreal forests. They suggest a cold, wetter, glacial period. There seems to be climate variations recorded in the lake sediments.

Three internal USGS reports were prepared and submitted to David Roddy and Gene Shoemaker. Wright Horton (USGS-Reston) and Bruce Wardlaw (also with the USGS) kindly located those reports for me and gave me permission to publish the findings as long as the reports' authors are credited: Bradbury and Forrester (1983) analyzed Quaternary diatoms and ostracodes; Forester (1983) analyzed Quaternary-late Pleistocene ostracodes and charophytes; and Bradbury (1983) analyzed Pleistocene diatoms. The assemblages derived from each of the crater floor shafts differ, suggesting that several different aquatic centers or zones existed simultaneously on the crater floor. The assemblages also differ stratigraphically, recording environmental changes as a function of time. Table 14.1 collates the data in those three reports with the sample depths recorded by Shoemaker in his field notes.

There appear to be three basic diatom assemblages. (1) A low-diversity assemblage dominated by species that are characteristic of fairly saline (probably $\geq 10^0$ ‰) NaCl-rich water. (2) A low- to medium-diversity diatom assemblage suggestive of fresh to slightly brackish water that probably contained significant Ca, Mg, and HCO_3 , along with Na, Cl, and SO_4 . Many of the organisms in this assemblage attach themselves to emergent and subemergent aquatic vascular plants in shallow water that was likely <5 m deep. (3) A high-diversity assemblage that appears to be a mixture of (1) and (2). It was unclear if

that meant both assemblages co-existed in the lake and were mixed during sediment deposition or whether they reflect mechanical mixing during sampling of the lacustrine strata.

The quality of the diatom data varied between the shafts, as did the environments they represented. The picture that emerged, however, involved several aquatic ecosystems. Lake waters may have been stratified, with a basal saline layer covered with freshwater. The amount of freshwater may have varied seasonally when rain fell. Moreover, contributions from one or more springs, the largest being associated with Silica Hill, constantly fed the aquatic system. There were probably several ponds around that spring during periods of low water levels, but an interconnected lake at other periods. Variations in that system were driven, in part, by an evolving climate.

The record in the shafts may be extraordinarily rich, including a seasonal temporal record. Laminated samples in one area have a variable diatom content correlated with a red-white sediment couplet. The white lamina is dominated by *C. caspia*, a planktonic diatom, that Bradbury inferred to be representative of a bloom of the species in response to a seasonal change in nutrients, light, and water chemistry. A red lamina contains a greater diversity of diatoms, including those preferring fresher water, although saline species still dominate. He suggested that mix of fresh water and saline diatoms may have been produced by a seasonal influx of fresh water. He went on to suggest that spring water from Silica Hill, the dominant source of water in the crater, had a constantly fresher chemistry than the ponds or shallow lakes that occurred nearer the crater center. Furthermore, he suggested that seasonal rains freshened the aquatic ecosystems and delivered nutrients that catalyzed the diatom blooms seen in the white laminae. Bradbury described a sample of flaggy, siliceous limestone from the top of Silica Hill with plant impressions of what he interpreted to be emergent plants such as *Scirpus* or grasses, and flow-like structures indicative of a spring mound environment.

Forester, who studied the ostracodes, was surprised at the number of species in the aquatic system, writing that there “are 19 ostracode species in these sediments, which is at least 17 more species than I would have expected to find in this setting.” He identified four assemblages and three general types of environments: (1) fresh Ca-Mg-HCO₃ springs with moderate and variable quantities of Na-SO₄-Cl; (2) a permanent, slightly to moderately-saline, Na-Cl-(SO₄) lake; and (3) a fresh Ca-Mg-HCO₃-SO₄ lake or pond. The species involved in those assemblages and the variation in those assemblages as a function of time. Furthermore, the strata in the shafts, located in different areas of the crater, also represented different aquatic environments. The chronological pattern he inferred began with an ephemeral-dry environment (seen in shaft #2, which seems to be consistent with a pollen analysis; see Chapter 13), and, elsewhere the evolution of a spring environment that had seasonably variable salinity and solute compositions, a stratified Na-Cl lake, and a freshwater lake or pond, followed, again, with a seasonably variable environment at the end of the lacustrine period that gave way to a dry eolian environment.

He correlated that sequence with sequences in other Southwestern lakes. Based on the calibrated chronology of those lakes, he suggested the crater was older than 25 ka, that the transition to the Na-Cl lake occurred roughly 20 ka, transitioning to a final lacustrine period about 14 to 15 ka. Those ages, I suspect, could be further refined based on the large amount of work that has occurred in biostratigraphy over the past 35 years.

Forester’s collection of samples survives, and I have been given detailed stratigraphic logs of all species previously identified in the crater floor shafts. We hope to use modern techniques (*e.g.*, micro-analytical stable isotope analyses) to further evaluate the biota and their record of post-impact environmental conditions in the vicinity of the crater.

Because of uncertainties involved in existing data and the importance of the issues involved, a new set of samples with good stratigraphic control might further illuminate the climatic changes recorded in the crater. Any new sampling will be coordinated with a large number of investigators to ensure that all fauna and flora in the samples studied are integrated together to provide the best environmental and climatic reconstruction possible. A nascent team has been assembled, but we are still trying to secure funds to re-crib Shaft #2 and the Main Shaft so that the appropriate samples can be collected. In parallel, we are also considering a new drilling campaign on the crater floor.

While the community's studies of Barringer Meteorite Crater are often focused on impact cratering processes, the presence of fossil-bearing lacustrine sediments vividly shows that the crater is also an important site for astrobiological studies. The crater provided a rich array of niches for life that changed over time in ways that may better inform us of the possibility of biological niches on other planets, such as Mars. This is an area of study still being developed at the crater and one that will likely grow in the future.

Important components of the lacustrine fill are interbedded strata of volcanic ash (Fig. 14.2) that were deposited following pyroclastic eruptions in the nearby volcanic field. Shoemaker and Kieffer (1974) drew attention to multiple ash layers. Two layers attributed to the 0.9 ka Sunset Volcanic Crater eruption occur 0.3 m (1 ft) deep in playa sediments. They also described a series of three ash beds ~5 m (15 to 18 ft) deep that they suggested might be a deposit from the Saddle Mountain eruption, which is now thought to have erupted ~17 ka. More recently, the age of the Merriam eruption was revised downward from ~150 ka (Moore and Wolfe, 1987) to ~20 ka (Duffield *et al.*, 2006), so it is a potential source too. The petrology and, importantly, geochronology of ash in the lake sediment sequence are currently being studied.

While conducting a survey of gullies in the crater wall (Chapter 15), Alan Howard, Marisa Palucis, Bill Dietrich, Kuni Nishiizumi, and I discovered a ≥ 86 cm-thick deposit with volcanic ash beneath a layer of colluvium on the south-southwest portion of the crater floor (Fig. 14.3 and 14.4). The ash must have been redistributed by eolian processes and also modified by erosional and sedimentation processes associated with the crater wall. In outcrop, the deposits are horizontally laminated (Fig. 14.3 and 14.4) and interspersed with pebble-rich horizons of debris from the crater walls. Microscopic examination (Altomare *et al.*, 2014) indicates volcanic ash is also mixed with sedimentary particles of quartz, hematite-cemented quartz siltstone, quartz-sand-bearing carbonate, and micritic carbonate (Fig. 14.5); that is, particles from the Moenkopi, Kaibab, and potentially Coconino strata in the crater wall.

The volcanic particles have both glassy vesicular and microcrystalline textures (Altomare *et al.*, 2014). Phenocrysts include olivine, plagioclase, and clinopyroxene (Fig. 14.6). The olivine phenocrysts are also normally zoned. Potentially, the compositions of those phenocrysts can be used to identify the source vent.

The ash was deposited after the lake dried up circa 10 to 13 ka. Vents in the area with younger ages are Sunset Crater at 0.9 ka, potentially SP Crater, although it has a disputed age ranging from nearly 6 ka to ~72 ka (Fig. 14.7); the older age is more likely (Fenton *et al.*, 2013). Saddle Mountain, which has an age of ~17 ka, could be a source of an ash layer interbedded with lake sediments beneath the current crater floor level, as previously surmised by Shoemaker and Kieffer (1974). Likewise, Merriam Crater, which has an age of 20 ka, may be too old to be a primary source of ash on the dried up crater floor. Those older vents are, however, possible (albeit less likely) sources if their ash deposits were reworked and redistributed to the vicinity of Barringer Meteorite Crater.

Of those source vents, the most likely source of the surface ash deposit is Sunset Crater and potentially SP, based on their ages, and West Sunset Mountain and Merriam Crater based on proximity. Sunset Crater is a cinder cone ~57 km from Barringer Meteorite Crater that formed after the impact and after the lake dried up. The mineral compositions of Sunset Crater samples are identical to those found in the Meteor Crater deposit (Fig. 14.6). Also, the mapped distribution of that vent's ash covers ~315 km² and nearly reaches the edges of Flagstaff where layers of ash are up to 10 cm thick (Hooton *et al.*, 2001) (Fig. 14.8). A thin layer of ash produced by the Sunset Crater eruption could have been deposited on the floor of Barringer Meteorite Crater and then reworked by winds. Merriam Crater is closer, ~42 km, and relatively young, ~20 ka (Duffield *et al.*, 2006). Because its age is older than that of Meteor Crater, if it was the source of the ash, then that would require reworking and secondary transport of its ash to Meteor Crater. The mineral compositions of Merriam Crater ash are also similar to those found in the Meteor Crater deposit (Fig. 14.6). The closest cinder cone to the crater is only 14 km south of the crater on West Sunset Mountain (Fig. 14.9). Because it is older than the crater, with an estimated age from 3 to 9.3 Ma, that eruption cannot be a primary source of the ash. However, its ash, like that at Merriam, could potentially have been reworked and blown to the crater. Thus far, that vent has not been sampled and its potential as a candidate petrologically assessed.

Table 14.1. Compiled sedimentary and paleontological logs of shafts in crater floor

Sample Depth (ft)	Sample # (EMS-- 58)	Notes
Shaft I (or #1)		
3.3-4.7	1	Calcareous sand with root casts; barren of diatoms. Parallel study of ostracodes and charophytes revealed: <i>Candona caudata</i> , <i>Cypridopsis vidua</i> , <i>Ilyocypris gibba</i> , <i>Potamocypris granulosa</i> ; plus snails, largely aquatic, bivalves, charophyte stems, carbonate coated plant stems
4.7-4.9	2	Dark calcareous sandy silt with root casts. Parallel study of ostracodes and charophytes revealed: <i>Candona caudata</i> , <i>Cypridopsis vidua</i> , <i>Potamocypris granulosa</i> ; plus <i>Chara sp.</i> , snails, terrestrial and aquatic, and carbonate coated plant stems
4.9-8.0	3	Brown calcareous sandy silt with snails (<i>lymmaea</i> and <i>gyralus</i>). Parallel study of ostracodes and charophytes revealed: <i>Candona caudata</i> , <i>Cypridopsis vidua</i> , <i>Potamocypris granulosa</i> ; plus snails, terrestrial and aquatic, and carbonate coated plant stems
	3A	Snails (<i>lymmaea</i> and <i>helisoma</i>)
8.0-9.4	4	Alternating beds of silt and marl; snails and ostracodes, very rare specimens of <i>epithemia argus</i> septae and corroded sponge spicules in situ samples of marl and silt. Parallel study of ostracodes and charophytes revealed: <i>Candona caudata</i> , <i>Cypridopsis vidua</i> , <i>Candona renoensis</i> , <i>Potamocypris granulosa</i> ; plus snails, largely aquatic, and carbonate coated plant stems
9.4-11.0	5	Red silty sand. Parallel study of ostracodes and charophytes revealed: <i>Potamocypris granulosa</i> , <i>Candona sp.</i> indet. juveniles; plus snail shell fragments
13.4-13.7	6	Basaltic ash
Shaft II		
34.35	200	Volcanic ash
85.8	108	Fine white silt and sand; BOD
88.0-88.5	107	Fine white silt and sand, with melted glass; BOD
88.5-88.7	106	White, fine sand and silt, slightly calcareous; BOD. Note: rare individuals of <i>navicula huefleri</i> var. <i>leptocephala</i> were found in an earlier cut of this sample. They may represent contaminants.
	106	Sample is near the base of the Pleistocene lake bed sequence (per Bradbury and Forrester); a marl with rare occurrence of diatom <i>Navicula huefleri</i> var. <i>leptocephala</i> .
88.7-95.5	105	Fine white sand; BOD
100	104A	Qd (breccia with Coconino, Kaibab, and Moenkopi)
110	104	Qd (breccia with Coconino, Kaibab, and Moenkopi)
126	103	Shattered blocks of Coconino
126	103A	Mostly fused Coconino
134	102	Coconino fragments and powder
141.3-148.5	101	Coconino sandstone block
26 V 83-1	Spoils	Fine, paper-like laminations in alternating red and white couplets; diatomite.
		Red lamina: <i>Scoliopleura peisonis</i> (r), <i>Anomoeoneis costata</i> (c), <i>Epithemia argus</i> (c), <i>Cyclotella caspia</i> , <i>Campylodiscus slypeus</i> (c), <i>Cocconeis placentula</i> (r), <i>Navicula oblonga</i> , <i>Nitzschia obtusa</i> (c), <i>Mastogloia braunii</i> (r), <i>Nitzschia denticula</i> , <i>Cyclotella bodanica</i> , <i>Amphora coffaeiformis</i> (c), <i>Synedra capitata</i> , <i>Denticula elegans</i> , <i>Cymbella pusilla</i> , <i>C. mexicana</i> , <i>Synedra ulna</i> , <i>Amphora veneta</i> , sponge spicule.
		White lamina: <i>Anomoeoneis costata</i> (c), <i>Cyclotella caspia</i> (dd), <i>C. bodanica</i> , <i>Denticula elegans</i> , <i>Amphora coffaeiformis</i> , <i>Mastogloia braunii</i> , <i>Epithemia argus</i> , <i>Scoliopleura peisonis</i> .
26 V 83-2	Spoils	Laminated marly diatomite with plant impressions: <i>Denticula elegans</i> (a), <i>Amphora coffaeiformis</i> (d), <i>A. arcus</i> , <i>A. commutata</i> , <i>Mastogloia smithii</i> , <i>Fragilaria brevistriata</i> , <i>Cymbella affinis</i> , <i>Scoliopleura peisonis</i> , <i>Epithemia argus</i> (c), <i>Navicula oblonga</i> , <i>Nitzschia obtusa</i> , cysts.

26 V 83-3	Spoils	Thin-bedded marly diatomite: <i>Nitzshia obtusa</i> (a), <i>Cyclotella caspia</i> (a), <i>Scoliopleura peisonis</i> (a), <i>Epithemia argus</i> (c), <i>Navicula oblonga</i> , <i>Mastogloia braunii</i> (c), <i>Amphora arcus</i> , <i>Cyclotella bodanica</i> , <i>Compylodiscus clypeus</i> , sponge spicule.
Shaft IV		
10.5-15.3	100A	Vertebrate fossil; antelope fossil (not seen by Bradbury)
	100B	Pinkish brown silt and fine sand with some weakly calcareous sediment pieces; BOD. Parallel study of ostracodes and charophytes revealed: <i>Limnocythere friabilis</i> , <i>Candona caudata</i> , <i>Candona patzcuaro</i> , <i>Ilyocypris gibba</i> , <i>Heterocypris salinas</i> , <i>Cypridopsis vidua</i> ; plus snails, aquatic, carbonized plant stems, and gypsum
	100C	Fine white sand; BOD. Parallel study of ostracodes and charophytes revealed: <i>Candona caudata</i> , <i>Limnocythere friabilis</i> ; plus carbonate coated plant stems
15.3-21.0	99A	White calcareous sand (Coconino ss?); common, well preserved diatoms: <i>Fragilaria brevistriata</i> (d), <i>Cymbella affinis</i> , <i>Navicula oblonga</i> , <i>Synedra capitata</i> , <i>Denticula elegans</i> . Parallel study of ostracodes and charophytes revealed: <i>Candona candida</i> , <i>Candona acuminata</i> , <i>Candona paraohioensis</i> , <i>Limnocythere friabilis</i> , <i>Heterocypris incongruens</i> , <i>Potamocypris granulosa</i> , <i>Cypridopsis vidua</i> , <i>Cypricercus</i> sp. indet. poorly preserved single valve; plus snails, aquatic, bivalves, carbonate coated plant stems, ooids, and carbonate grains
	99B	Red silty sand; BOD. Parallel study of ostracodes and charophytes revealed: <i>Limnocythere friabilis</i> , <i>Candona candida</i> ; plus snails, aquatic, carbonate grains, and red clastics
	99C	Light red silty sand; BOD. Parallel study of ostracodes and charophytes revealed: <i>Limnocythere friabilis</i> , <i>Candona accuminata</i> , <i>Candona paraohioensis</i> , <i>Candona patzcuaro</i> , <i>Candona candida</i> , <i>Potamocypris granulosa</i> , <i>Heterocypris incongruens</i> ; plus carbonate coated plant stems and red clastics
21.0-21.3	98	Light buff diatomaceous marl; abundant diatoms, well preserved: <i>Fragilaria brevistriata</i> (d), <i>Denticula elegans</i> , <i>Anomoeoneis costata</i> (c), <i>Cymbella affinis</i> (?), <i>C. cymbiformis</i> , <i>C. cistula</i> , <i>Navicula oblonga</i> (c), <i>Cyclotella caspia</i> (c), <i>Amphora coffaieformis</i> , <i>Cyclotella</i> sp., <i>Synedra capitata</i> , <i>Synedra puchella</i> , cysts, sponge spicules, <i>Cocconeis placentula</i> , <i>Amphora ovalis</i> ; plus gypsum and snail shell fragments
21.3	97	White marl with sharp contact to basaltic sand ; abundant, fairly preserved diatoms, especially at basalt contact: <i>Anomoeoneis costata</i> (c), <i>Cyclotella caspia</i> (d)
	97A	Volcanic ash; scraps of basalt , silt (BOD), and diatomite: <i>Anomoeoneis costata</i> (d)
21.5	96	White diatomaceous marl, powder and pieces; common, fairly preserved diatoms: <i>Anomoeoneis costata</i> (c), <i>Cyclotella caspia</i> (d), <i>Mastogloia braunii</i>
21.8	95	White, platy diatomaceous marl; abundant fairly preserved diatoms: <i>Anomoeoneis costata</i> (d), <i>Cyclotella caspia</i> (dd), <i>Navicula subinflatooides</i> (o), <i>Cymbella pusilla</i> , <i>Scoliopleura</i> (?)
22.4	94	White, laminated diatomaceous marl; abundant fairly preserved diatoms: <i>Cyclotella caspia</i> (d), <i>Anomoeoneis costata</i> (c), <i>Entomoneis alata</i>
22.7	93	White, homogeneous, marly claystone; rare, fairly preserved diatoms: <i>Navicula oblonga</i> , <i>Anomoeoneis costata</i>
23.3	92	White powdery marl and marly pieces of diatomite; abundant, well preserved diatoms: <i>Amphora coffaieformis</i> , <i>Anomoeoneis costata</i> , <i>Cymbella pusilla</i> (a), <i>Cyclotella caspia</i> , <i>Syndera tabulata</i> (?), <i>Fragilaria brevistriata</i> , <i>Nitzschia frustulum</i> . The marly diatomite pieces are dominated by <i>Fragilaria brevistriata</i> , <i>F. construens</i> var. <i>venter</i> , and <i>Anomoeoneis costata</i> . They also contain <i>Cyclotella caspia</i> (a), <i>Fragilaria construens</i> var. <i>subsalina</i> , <i>Nitzschia obtusa</i> , <i>Navicula rhynchocephala</i> , and <i>Epithemia argus</i> .
23.5	91	White, rock-like limestone or marl, MnO stains, accicular crystals of CaCO ₃ ; BOD
23.6	90	White calcareous sand; BOD
25.6	89	Light tan-orange silt; BOD
25.7	88	Hard, laminated sandy marl; occasional poorly preserved diatoms: <i>Anomoeoneis</i> sp. <i>zsl</i> (d)
26.2	87	White, noncalcareous sandstone; BOD
26.4-28.5	86	White, clayey, gypsiferous marl, acicular crystals CaCO ₃ ; BOD
28.5-28.6	85	Light tan calcareous sand; BOD
28.6-30.2	84	White crusty granular marl; occasional poorly preserved diatoms: <i>Entomoneis alata</i> , <i>Amphora coffaieformis</i> . Parallel study of ostracodes and charophytes revealed: <i>Heterocypris incongruens</i> ; plus <i>Chara</i> sp. abundant and carbonate coated plant stems
30.2-31.7	83	Light brown sandy marl; BOD
	83A	Fossilized monocot stem (<i>Scirpus</i> perhaps) and gypsum crystals

31.7-32.4	82	Buff powdery marl; BOD; carbonate coated plant stems and snail shell fragments
32.4-33.5	81	Buff marl; very rare, poorly preserved diatoms: <i>Denticula elegans</i> . Parallel study of ostracodes and charophytes revealed: <i>Limnocythere friabilis</i> , <i>Heterocypris incongruens</i> ; plus carbonate coated plant stems
33.5-39.3	80	Buff granular marl, accicular crystals of CaCO ₃ ; abundant, well-preserved diatoms: <i>Fragilaria brevistriata</i> (d), <i>Navicula oblonga</i> (c), <i>Campylodiscus chypeus</i> , <i>Epithemia argus</i> , <i>Anomoeoneis</i> sp. zlc, <i>Denticula elegans</i> , <i>Apithemia turgida</i> , <i>Cymbella affinis</i> , <i>Mastogloia aguilegieue</i> , <i>pinnularia microstanron</i> . Parallel study of ostracodes and charophytes revealed: <i>Candona acuminata</i> , <i>Limnocythere friabilis</i> , <i>Heterocypris incongruens</i> ; plus snails, aquatic and terrestrial, and carbonate coated plant stems
Shaft V		
6.4-8.8	39	White marl and fine to medium sand. Abundant, well-preserved diatoms: <i>Fragilaria brevistriata</i> (d), <i>Fragilaria construens</i> var. <i>venter</i> (c), <i>Navicula oblonga</i> (c). Parallel study of ostracodes and charophytes revealed: <i>Candona caudata</i> , <i>Cypridopsis vidua</i> , <i>Sarscypridopsis aculeata</i> , <i>Heterocypris incongruens</i> , <i>Potamocypris unidcaudata</i> , <i>Potamocypris granulosa</i> , <i>Candona albicans</i> ; plus snails, aquatic, carbonate coated plant stems, and carbonate grains
8.8-9.1	38	Reddish tan crusty marl: BOD. Parallel study of ostracodes and charophytes revealed: <i>Heterocypris incongruens</i> ; plus snails, aquatic, and carbonate grains
9.1-10.2	37	White marl, well-preserved diatoms: <i>Epithemia argus</i> (c), <i>Denticula elegans</i> (c), <i>Navicula oblonga</i> (r), <i>Fragilaria brevistriata</i> , <i>Cocconeis placentula</i> , <i>Rhopalodia gibberula</i> , <i>Mastogloia smithii</i> , <i>Nitzschia frustulum</i> , <i>Nitzschia denticula</i> , <i>Chaetoceras</i> , <i>Amphora</i> sp., sponge. Parallel study of ostracodes and charophytes revealed: <i>Heterocypris incongruens</i> , <i>Cypridopsis vidua</i> , <i>Limnocythere friabilis</i> ; plus snails, aquatic, carbonate coated plant stems, and mite
10.2-11.6	36	Grey-tan, platy marly silt and tufa. Abundant well-preserved diatoms: <i>Anomoeoneis costata</i> (d), <i>Chaetoceras</i> (o), and <i>Rhopalodia gibberula</i> (c)
11.6-11.7	35	White-tan, finely bedded, aragonitic(?) marl with gypsum crystals. Sharp contact with basaltic sand ; the contact lamination (only) diatomaceous: <i>Anomoeoneis costata</i> , poorly preserved
11.7-11.9	34	White diatomaceous sandy marl: <i>Anomoeoneis costata</i> (c), <i>Cymbella pusilla</i> , <i>Chaetoceras</i> , <i>Nitzschia frustulum</i>
11.9-12.1	33	Light orange calcareous sand; BOD
12.1-13.2	32	Tan crusty marl with plant stem molds; BOD
13.2-13.9	31	White marly diatomite; <i>Nitzschia obtusa</i> , <i>Anomoeoneis</i> sp. zsl. (a-d), <i>Cymbella pusilla</i> , <i>Anomoeoneis costata</i>
13.9-14.6	30	Aragonitic(?) marl and layers of felty diatomite, white; <i>Nitzschia obtusa</i> (d), <i>Cyclotella caspia</i> (d), <i>Anomoeoneis</i> sp. zsl., <i>Mastogloia braunii</i> , <i>Cymbella pusilla</i> , <i>Anomoeoneis costata</i> , <i>Mastogloia aquilegiae</i> ?
14.6-14.9	29	White powdery aragonitic(?) marl and fragments of grey silt, some fine bedding; essentially BOD, fragment of <i>Anomoeoneis costata</i>
14.9-15.2	28	White calcareous claystone, rare, poorly preserved diatoms: <i>Cyclotella caspia</i> (d), <i>Anomoeoneis costata</i> (o)
15.2-15.9	27	Tan, finely bedded marl; very poorly preserved diatoms: <i>Anomoeoneis costata</i> , corroded <i>Entomoneis alata</i> (d) in white layers
15.9-16.5	26	Orange fine calcareous (acicular CaCO ₃ crystals) sand: BOD; mollusk shell fragments
16.5-16.6	25	Tan crumbly, platy marl with plant stem molds; poorly preserved diatoms: <i>Cyclotella caspia</i> (d), <i>Rhopalodia gibberula</i> (r), and <i>Anomoeoneis costata</i> (r) in gray laminae
16.6-16.9	24	Tan thin bedded gypsiferous marl, acicular crystals of CaCO ₃ , plant stem molds: BOD
16.9-17.15	23	Orange-tan calcareous sand, acicular CaCO ₃ crystals: BOD; carbonate coated plant stems
17.15-17.2	22	Tan granular marl, acicular crystals: BOD
17.2-17.55	21	White marly claystone, thin bedded, gypsiferous: BOD
17.55-17.6	20	Tan fine sand: BOD
17.6-18.2	19	White marly claystone, thin bedded, gypsiferous: BOD
18.2-18.45	18	Light tan marl with acicular crystals of CaCO ₃ and plant stem molds: BOD. Parallel study of ostracodes and charophytes revealed: <i>Limnocythere friabilis</i> , <i>Heterocypris incongruens</i> (?) juveniles
18.45-18.6	17	White marl: BOD

18.6-19.6	16	Yellowish silty sand, root casts and daccicular CaCO ₃ crystals: BOD
19.6-20.7	15	Red sandy silt, weakly calcareous; BOD
20.7-21.1	14	Light reddish brown silty sand, calcareous; BOD; snail shell fragments
21.1-22.2	13	Reddish calcareous silty sand: BOD; carbonate coated plant stems
22.2-24.1	12	Tan calcareous silty sand; BOD. Parallel study of ostracodes and charophytes revealed: <i>Canadona sp.</i> indet. internal mold; plus snail shell fragments and carbonate coated plant stems
24.1-26.0	11	Tan calcareous sand; BOD; carbonate coated plant stems
26.0-27.9	10	Granular sandy marl with plant stems; BOD. Sample from near the top of the Pleistocene lake bed sequence (per Bradbury and Forrester); sample is a marl with abundant calcified molds of monocotyledenous plant stems, like <i>Scirpus juncus</i> or related plants in the family Cyperaceae. Also contains ostracodes; <i>Candona sp. cf. C. elliptica</i> . Parallel study of ostracodes and charophytes revealed: <i>Candona sp.</i> indet., valve fragments; plus snail shell fragments and carbonate coated plant stems
27.9-28.9	9	Tan calcareous sand; BOD; snail shell fragments and carbonate coated plant stems
28.9-31.6	8	(upper half) Light reddish brown calcareous sandy silt; BOD. Parallel study of ostracodes and charophytes revealed: <i>Candona sp.</i> indet. juveniles; plus snails, largely terrestrial, and carbonate coated plant stems
	7	(lower half) Light tan marl, powdery, BOD. Parallel study of ostracodes and charophytes revealed: <i>Heterocypris incongruens</i> , <i>Cypridopsis vidua</i> , <i>Limnocythere friabilis</i> , <i>Candona acuminata</i> ; plus snails, largely aquatic, and carbonate coated plant stems
Shaft VI		
0	79	Buff, granular marl, few plant stem molds; BOD. Sample is from an intermediate level of Pleistocene lake bed sequence (per Bradbury and Forrester); sample is a marl with plant stem fragments that are presumably of the family Cyperaceae.
0.7	78	Buff, granular marl with many plant stem molds: BOD; gypsum
1.7	77	White, marly clay, acicular CaCO ₃ crystals: BOD
2.1	76	White, thin bedded or banded marly clay with root pores; BOD
2.4	75	Granular, crusty marl, plant stem molds, acicular CaCO ₃ crystals; BOD; carbonate coated plant stems
2.8	74	Red-orange rocky colluvium; BOD
4.2	73	Dark red medium sand; BOD; rare, abraded carbonate coated plant stems
5.4	72	Rocky reddish sand; BOD; rare, abraded carbonate coated plant stems
6.5	71	Dark red coarse sand; BOD; rare, abraded carbonate coated plant stems
7.5	70	Reddish gravelly sand; BOD; rare, abraded carbonate coated plant stems
9.1	69	Reddish calcareous sand; BOD; rare, abraded carbonate coated plant stems
9.3	68	Buff, granular sandy marl with plant stem molds; BOD; snails, terrestrial, and carbonate coated plant stems
9.6	67	Reddish, marly sandy silt; BOD; rare, abraded carbonate coated plant stems
10	66	Crusty, granular marl with plant stem molds; BOD. Parallel study of ostracodes revealed: <i>Heterocypris incongruens</i> , plus carbonate coated plant stems
10.9	65	Buff calcareous sand; BOD
11.1	64	Light buff sandy marl; BOD. Parallel study of ostracodes revealed: <i>Heterocypris incongruens</i> , plus carbonate coated plant stems and carbonate grains
11.3	63	Buff sandy marl with plant stem molds; BOD. Parallel study of ostracodes and charophytes revealed: <i>Heterocypris incongruens</i> , <i>Cypridopsis vidua</i> , <i>Candona acuminata</i> , <i>Limnocythere staplini</i> ; plus <i>Char sp.</i> , carbonate coated plant stems, snails, aquatic, gypsum, and ooids
12.6	62	White powdery marl with plant stem molds; BOD. Parallel study of ostracodes and charophytes revealed: <i>Heterocypris incongruens</i> , <i>Cypridopsis vidua</i> , <i>Candona acuminata</i> , <i>Limnocythere friabilis</i> ; plus snails, aquatic, carbonate coated plant stems, and ooids
13.3	61	Buff sandy marl; BOD
14.4	60	Reddish sand; BOD
14.8	59	Buff calcareous sand; BOD. Parallel study of ostracodes and charophytes revealed: <i>Heterocypris incongruens</i> , <i>Limnocythere friabilis</i> ; plus snails, aquatic, carbonate coated plant stems, and charophyte stems

15.9	58	Buff calcareous sand; BOD; snail shell fragments and gypsum
16.1	57	Buff silty marl; BOD; gypsum
17	56	Buff, fine granular marl and sand; BOD; snails, terrestrial, and carbonate coated plant stems
17.5	55	White powdery marl; abundant, well-preserved diatoms: <i>Epithemia argus</i> , <i>Cymbella affinis</i> (a), <i>Campylodiscus clypeus</i> (c), cysts, sponge spicules, <i>Denticula elegans</i> , <i>Cyclotella caspia</i> , <i>Navicula oblonga</i> , <i>Synedra capitata</i> (?), <i>Fragilaria construens</i> var. <i>subsalina</i> , <i>Amphora commutata</i> , <i>A. coffaeiformis</i> , <i>Nitzschia amphibia</i> . Parallel study of ostracodes and charophytes revealed: <i>Heterocypris incongruens</i> , <i>Limnocythere friabilis</i> ; plus carbonate coated plant stems, gypsum, and ooids
18.3	54	Light brown, silty to sandy marl; BOD; snail shell fragments and carbonate coated plant stems
18.7	53	Buff granular marl; BOD. Parallel study of ostracodes and charophytes revealed: <i>Candona</i> sp. indet. valve fragments; plus carbonate coated plant stems
19.6	52	Reddish brown powdery marl; BOD. Parallel study of ostracodes and charophytes revealed: <i>Candona</i> sp. indet. valve fragments; plus carbonate coated plant stems and gypsum
19.9	51	White, powdery marl; common, poorly preserved diatoms: <i>Campylodiscus clypeus</i> , <i>Denticula elegans</i> (c), <i>Fragilaria construens</i> , <i>Cymbella affinis</i> (c), <i>Mastogloia</i> sp., <i>Navicula oblonga</i> , <i>Synedra filiformis</i> (?) (a), <i>Anomoeoneis</i> sp. zsl, <i>Nitzschia amphibia</i> , <i>Cymbella pusilla</i> , <i>Epithemia argus</i> . Parallel study of ostracodes and charophytes revealed: <i>Heterocypris incongruens</i> , plus carbonate coated plant stems
20.4	50	Tan granular marl with plant stem molds; common, poorly preserved diatoms: <i>Mastogloia</i> sp. (fragment), <i>Cyclotella caspia</i> , <i>Mastogloia smithii</i> , <i>Anomoeoneis costata</i> , <i>Nitzschia communis</i> (?), <i>Denticula elegans</i> , <i>Nitzschia frustulum</i> , <i>Amphora</i> sp.; carbonate coated plant stems
20.5	49	White diatomaceous marl, common poorly preserved diatoms: <i>Denticula elegans</i> (c), <i>Epithemia argus</i> (a), <i>Navicula oblonga</i> (c), <i>Mastogloia smithii</i> , <i>Anomoeoneis costata</i> , <i>Amphora coffaeiformis</i> , cysts, <i>Nitzschia obtusa</i> , <i>Mastogloia elliptica</i> , <i>Cymbella affinis</i> (?) (c), <i>Pinnularia microcephala</i> , <i>Synedra</i> sp. Parallel study of ostracodes and charophytes revealed: <i>Candona acuminata</i> , <i>Limnocythere friabilis</i> , <i>Heterocypris incongruens</i> , <i>Potamocypris granulosa</i> ; plus snails, aquatic, carbonate coated plant stems, and gypsum
21.3	48	Light tan diatomaceous marl, abundant poorly preserved diatoms: <i>Mastogloia braunii</i> , <i>Nitzschia obtusa</i> (a), <i>Cyclotella caspia</i> , <i>Anomoeoneis costata</i> , <i>Fragilaria brevistriata</i> , cysts, <i>Campylodiscus clypeus</i> , <i>Denticula elegans</i> , <i>Epithemia argus</i> , <i>Nitzschia denticula</i> , <i>Amphora coffaeiformis</i> , <i>Cymbella pusilla</i> , <i>Mastogloia aquilegiae</i> , <i>Anomoeoneis</i> sp. zsl, <i>Rhopalodia gibberula</i> , <i>Synedra filiformis</i> (?) (a), <i>Amphora commutata</i> , <i>Diploneis interrupta</i> (?), <i>Nitzschia accicularis</i> , <i>Navicula odiosa</i> (?), <i>N. graciloides</i> . Parallel study of ostracodes and charophytes revealed: <i>Heterocypris incongruens</i> ; plus carbonate coated plant stems and gypsum
21.7	47	Tan, fine-grained, earthy marl; BOD; carbonate coated plant stems and gypsum
21.8	46	Tan sandy marl, acicular crystals; BOD. Parallel study of ostracodes and charophytes revealed: <i>Candona eriensis</i> (?), <i>Candona</i> cf. <i>C. acuminata</i> , <i>Limnocythere friabilis</i> ; plus snails, aquatic, and carbonate coated plant stems
22.4	45	Reddish tan diatomaceous marl; common diatoms, poorly preserved: <i>Nitzschia obtusa</i> (r), <i>Mastogloia smithii</i> (o), <i>M. elliptica</i> (o), <i>Amphora commutata</i> (r), <i>Amphora coffaeiformis</i> (c), <i>Amphora hyalina</i> (?), <i>A. arcus</i> (a), <i>Campylodiscus clypeus</i> , <i>Pinnularia abaujensis</i> (r), <i>Denticula elegans</i> (r). Parallel study of ostracodes and charophytes revealed: <i>Heterocypris incongruens</i> , plus carbonate coated plant stems and gypsum
22.6	44	Reddish tan sandy diatomaceous marl; abundant diatoms, fair preservation: <i>Amphora coffaeiformis</i> (a), <i>A. commutata</i> , <i>Nitzschia obtusa</i> (a), <i>Navicula oblonga</i> (o), <i>Nitzschia frustulum</i> , <i>Rhopalodia gibberula</i> , <i>Mastogloia smithii</i> , <i>Cymbella cymbiformis</i> , <i>Denticula elegans</i> (c), cysts, <i>Fragilaria brevistriata</i> (r), <i>Campylodiscus clypeus</i> , <i>Anomoeoneis costata</i> , <i>Bacillaria paradoxa</i> , <i>Amphora arcus</i> . Parallel study of ostracodes and charophytes revealed: <i>Heterocypris incongruens</i> , <i>Cypridopsis vidua</i> ; plus charophyte stems, carbonate coated plant stems, gypsum
24.5	43	Reddish tan laminated diatomite, poor preservation: <i>Nitzschia obtusa</i> (d), <i>Epithemia argus</i> , <i>Anomoeoneis</i> sp. zsl, cysts, <i>Cyclotella caspia</i> (c), <i>Amphora coffaeiformis</i> , <i>Mastogloia smithii</i> , <i>Denticula elegans</i> , <i>Cymbella pusilla</i> (c), <i>Amphora commutata</i> , <i>Amphora arcus</i> ; plus carbonate coated plant stems
25.3	42	Reddish tan marl + grey silty marl, rare, very poorly preserved diatoms: <i>Nitzschia lineris</i> (?), <i>Nitzschia</i> sp., <i>Rhopalodia gibberula</i> ; BOD.
25.5	41	Reddish tan marl, rare poorly preserved diatoms: <i>Amphora coffaeiformis</i> (c), <i>Nitzschia frustulum</i> (c), <i>Navicula subinflatoideis</i> (c), <i>Nitzschia obtusa</i> (r), <i>Nitzschia linearis</i> (?), <i>Melosira</i> sp.(?), <i>Anomoeoneis costata</i> ; plus snails, terrestrial.

Light tan powdery marl; diatomaceous: *Mastogloia smithii*, *M. braunii*, *M. elliptica*, *Epithemia argus* (c), *Cymbella cymbiformis*, *Campylodiscus clypeus*, *Denticula elegans*, *Cyclotella caspia* (a), *Synedra ulna*, *Navicula oblonga*, *Cymbella pusilla*, *Anomoeoneis* sp. zsl, *Nitzschia obtusa*, *Nitzschia* sp. spicules, cysts, *Cyclotella quillensis*, *C. bodanica*, *Navicula salinarum*, *Amphora hyalina*, *Cocconeis placentula*, *Amphora ovalis*. Parallel study of ostracodes and charophytes revealed: *Candona acuminata*, *Candona eriensis*(?), *Cypridopsis vidua*, *Candona acutula*(?); plus snails, aquatic, *Chara* sp., carbonate coated plant stems, carbonate grains, and *Elphidium* sp. foram

BOD = barren of diatoms

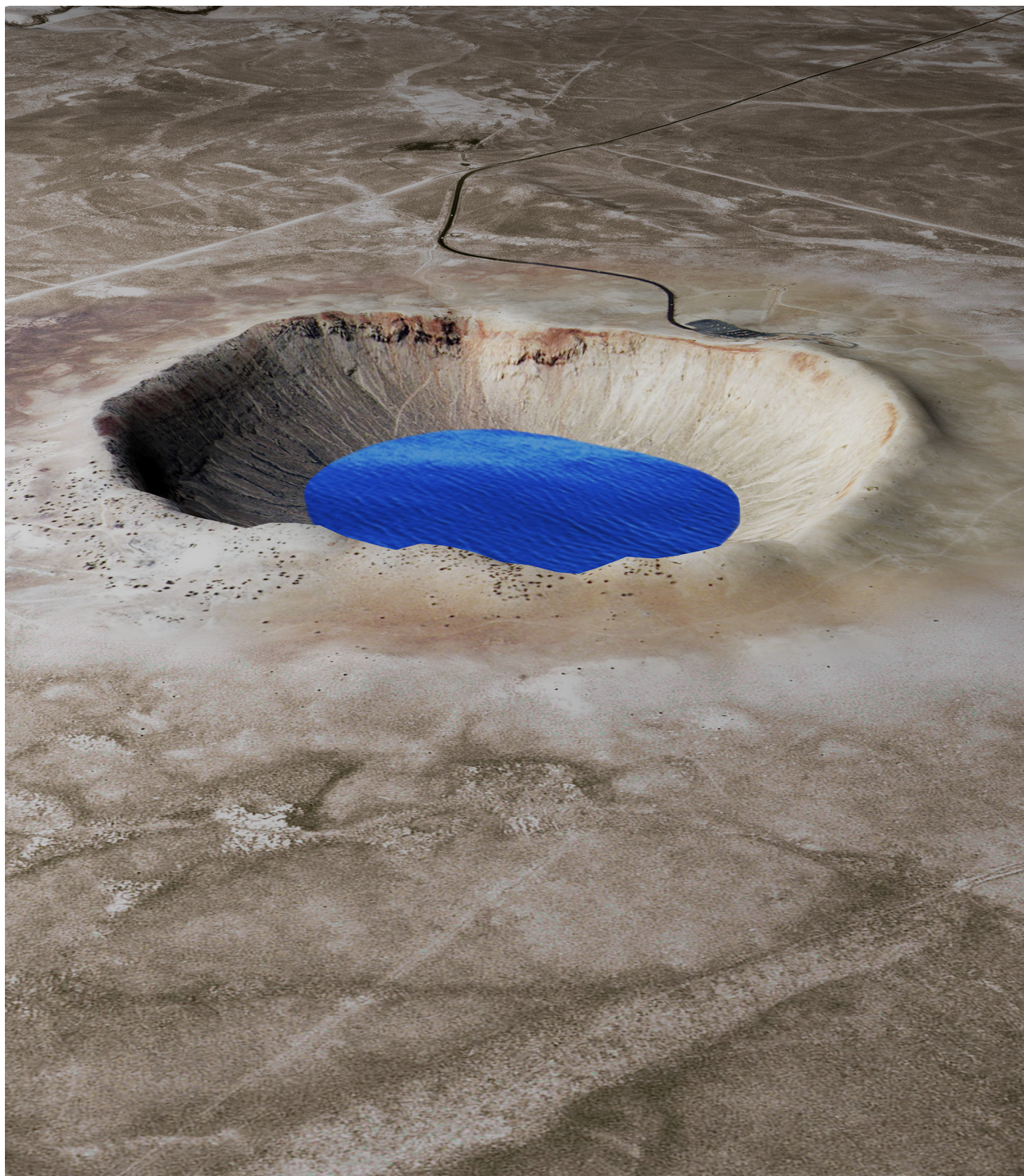


Fig. 14.1. Ground water and precipitation partially filled the crater during the Late Pinedale of the latest Pleistocene, producing a crater lake. Sediments deposited on the floor of the lake preserve fossil assemblages and horizons of volcanic ash.



Fig. 14.2. The Science Shaft (shaft II or #2) contains an exquisitely preserved sequence, beginning with the breccia lens at the bottom, followed by mixed fallback debris and lacustrine sediments deposited on the floor of the crater lake. The contact between the fallback breccia (with Coconino, Kaibab, and Moenkopi debris) and first lacustrine strata are shown in the lower panel. The lacustrine sediments are very finely laminated (middle panel) and may contain seasonal varves. The lacustrine sediments are also interbedded with volcanic ash horizons (top panel). I am trying to stabilize the shaft so that it can be a permanent teaching and research laboratory. In the meantime, a consortium effort is underway to conduct a preliminary study of those materials.

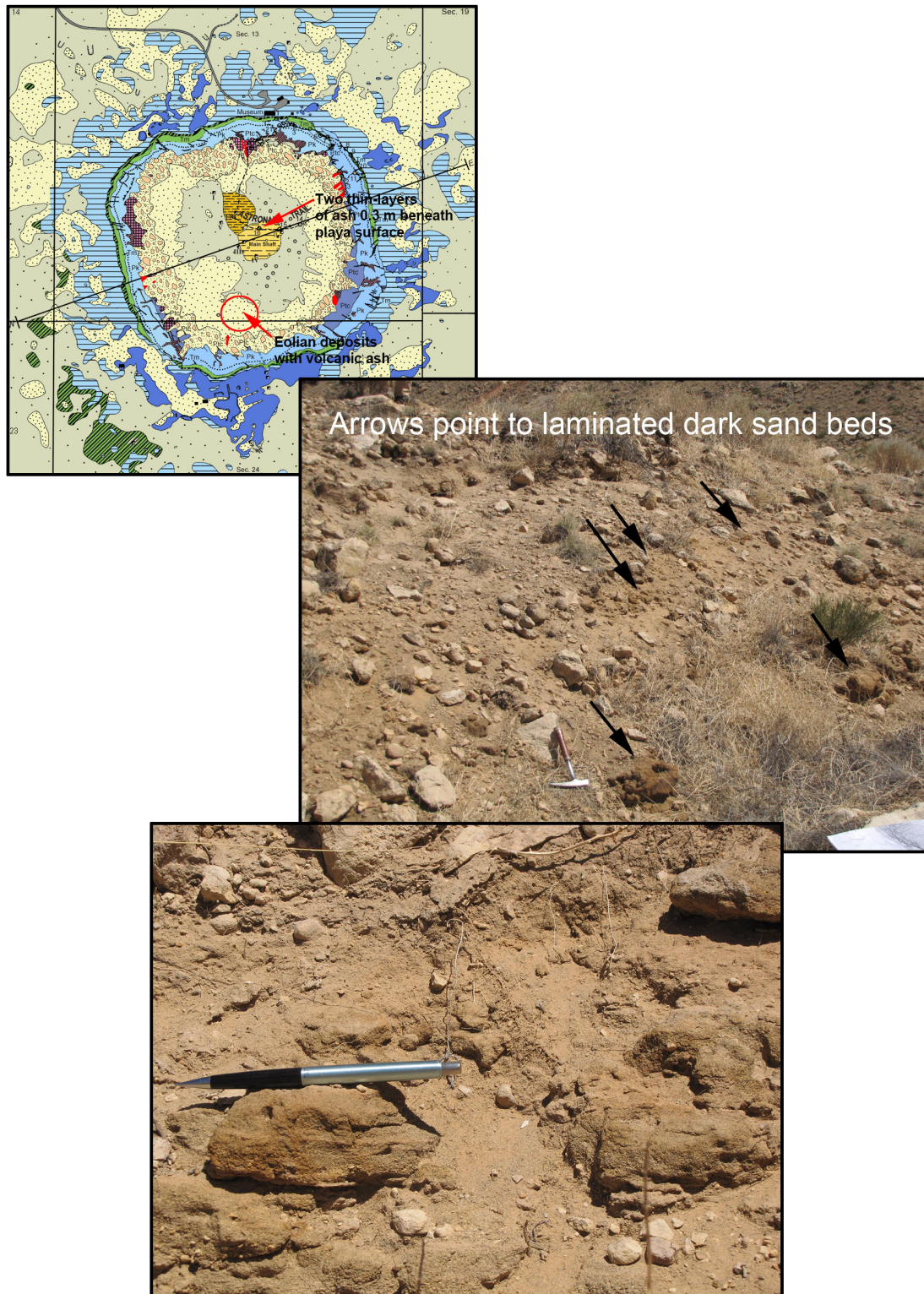


Fig. 14.3. A thick sequence of volcanic-ash-rich sediments is buried beneath colluvium in the south-southwest section of the crater floor, as indicated in map form (top left). That map also indicates the location where Shoemaker described two thin layers of ash from the Sunset Volcanic Crater eruption. A view of one of the outcrops is shown in the middle panel with five arrows pointing to exposures of ash and a 33-cm-long hammer for scale. A close-up view of the sediments, which are affected by modern plants, is shown in the bottom panel with a 14-cm-long pencil for scale.



Fig. 14.4. Several outcrops of ash-rich sediment buried beneath colluvium can be found in the south-southwest section of the crater floor (bottom panel), indicating the deposit covered a large portion of that part of the crater floor. A 33-cm-long hammer is shown for scale. That fine-grained sediment is sometimes mixed with pebbles and cobbles of rock (upper right) that likely fell from the crater walls. A 14-cm-long pencil is shown for scale. These sediments may be a grand analogue for basaltic eolian deposits on the floors of impact craters on Mars.

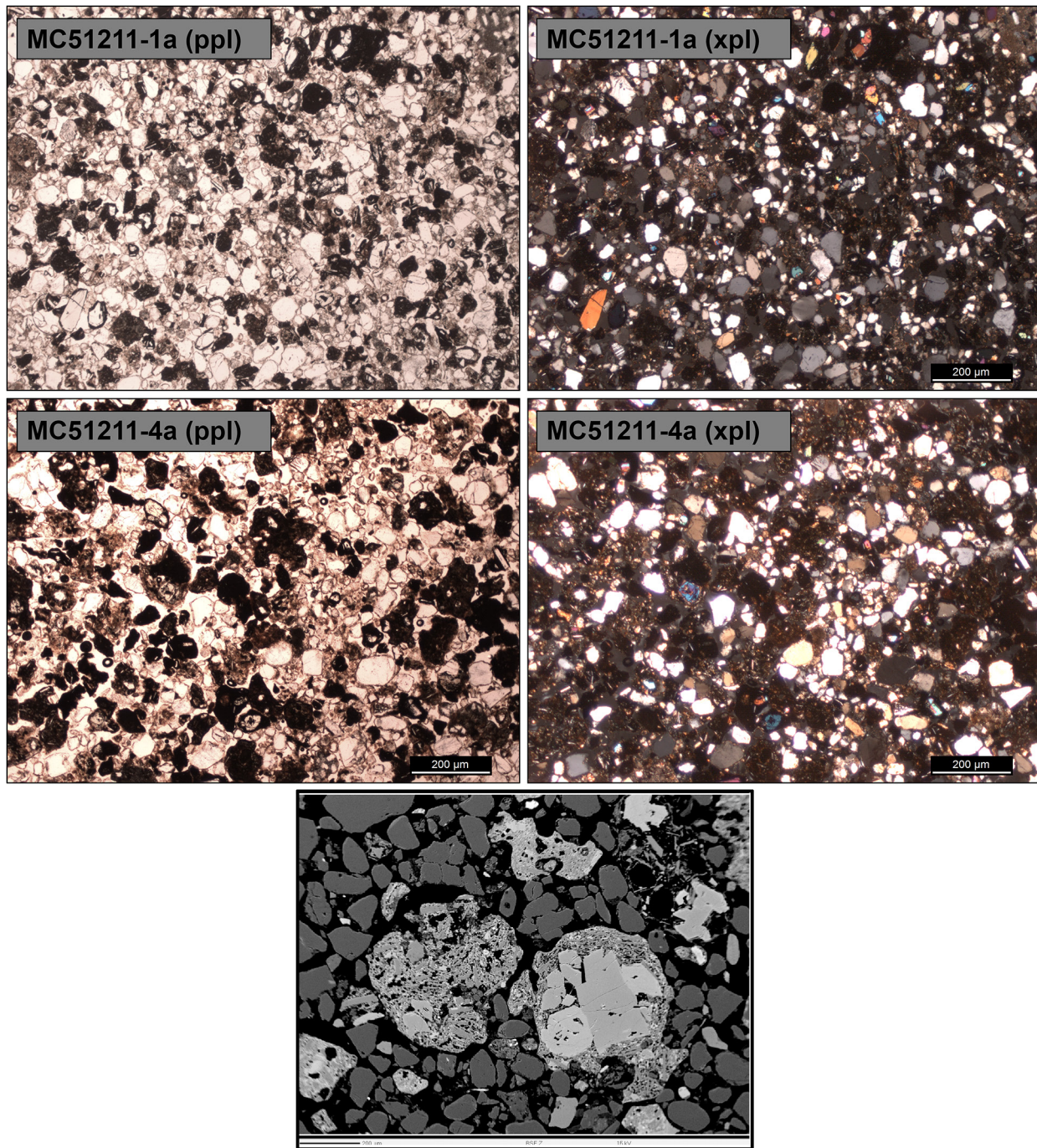


Fig. 14.5. Volcanic particles are a major component of sands in the south-southwest portion of the crater floor. Microscopic views of two samples are shown here. The top row is sample MC51211-1a in plane polarized light (left) and cross-polarized light (right). The second row is sample MC51211-4a, also in plane- and cross-polarized light. The volcanic particles are generally dark in plane-polarized light. A backscattered electron image of several volcanic particles in MC51211-1a is shown on the bottom. The volcanic particles are the brighter particles; phenocrysts of olivine and pyroxene are clearly visible in a particle in the right center of the image. The medium gray particles in the field of view are dominated by quartz. Scale bars in the plane- and cross-polarized light images are 200 microns and that in the backscattered electron image is 500 microns. These samples were part of the study by Altomare *et al.* (2014).

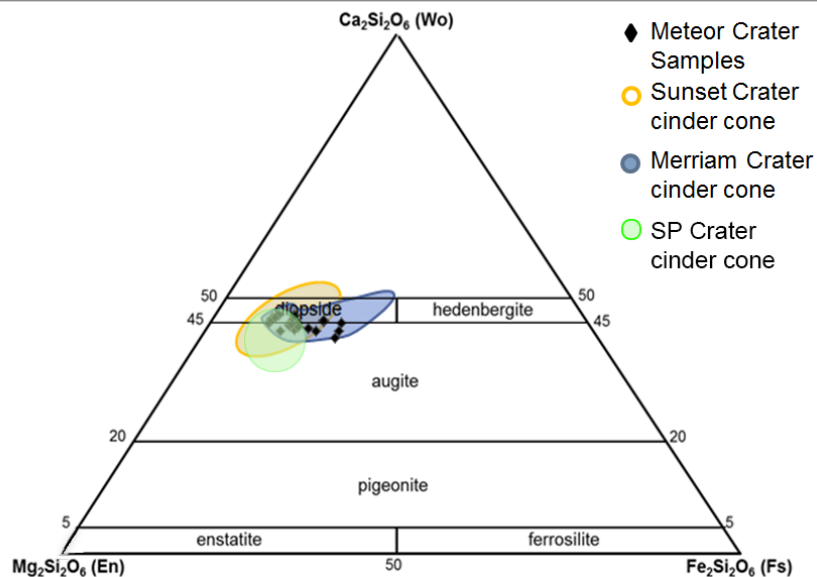
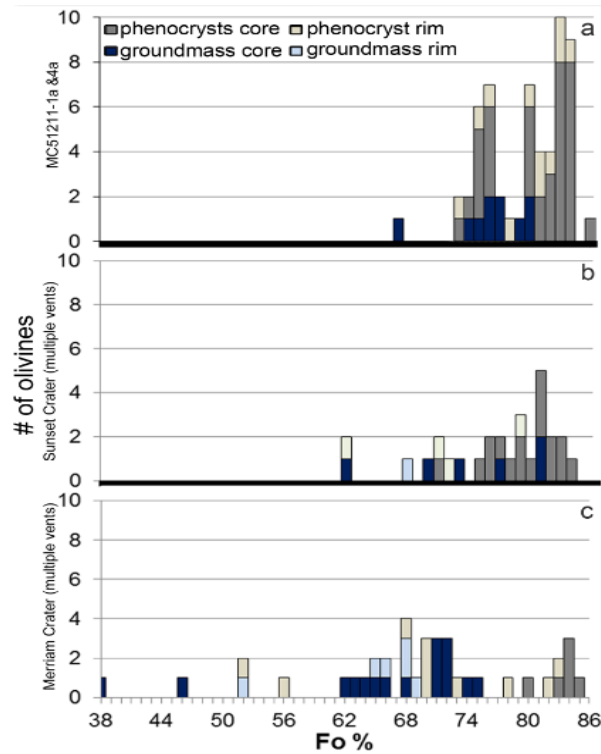


Fig. 14.6. Potentially, the phenocryst compositions in the volcanic particles within Meteor Crater can be used to determine the source vent. In the top diagram, olivine compositions are plotted for (a) Meteor Crater samples, (b) Sunset Volcanic Crater samples, and (c) Merriam crater samples. In the bottom diagram, pyroxene compositions are plotted for Meteor Crater samples, Sunset Volcanic Crater samples, Merriam Crater samples, and SP Crater samples. The phenocryst compositions are similar, probably because all of the vents tapped the same magmatic source. Thus, the phenocryst compositions are not a strong diagnostic tool in this case. While the petrology of other potential vent sources is being done, qualitative and quantitative geochronology, which is also in progress, may be needed to identify the source vent for the volcanic particles in Meteor Crater. Analyses by Caitlin Altomare and Amy Fagan, supplemented with literature sources in Altomare *et al.* (2014).

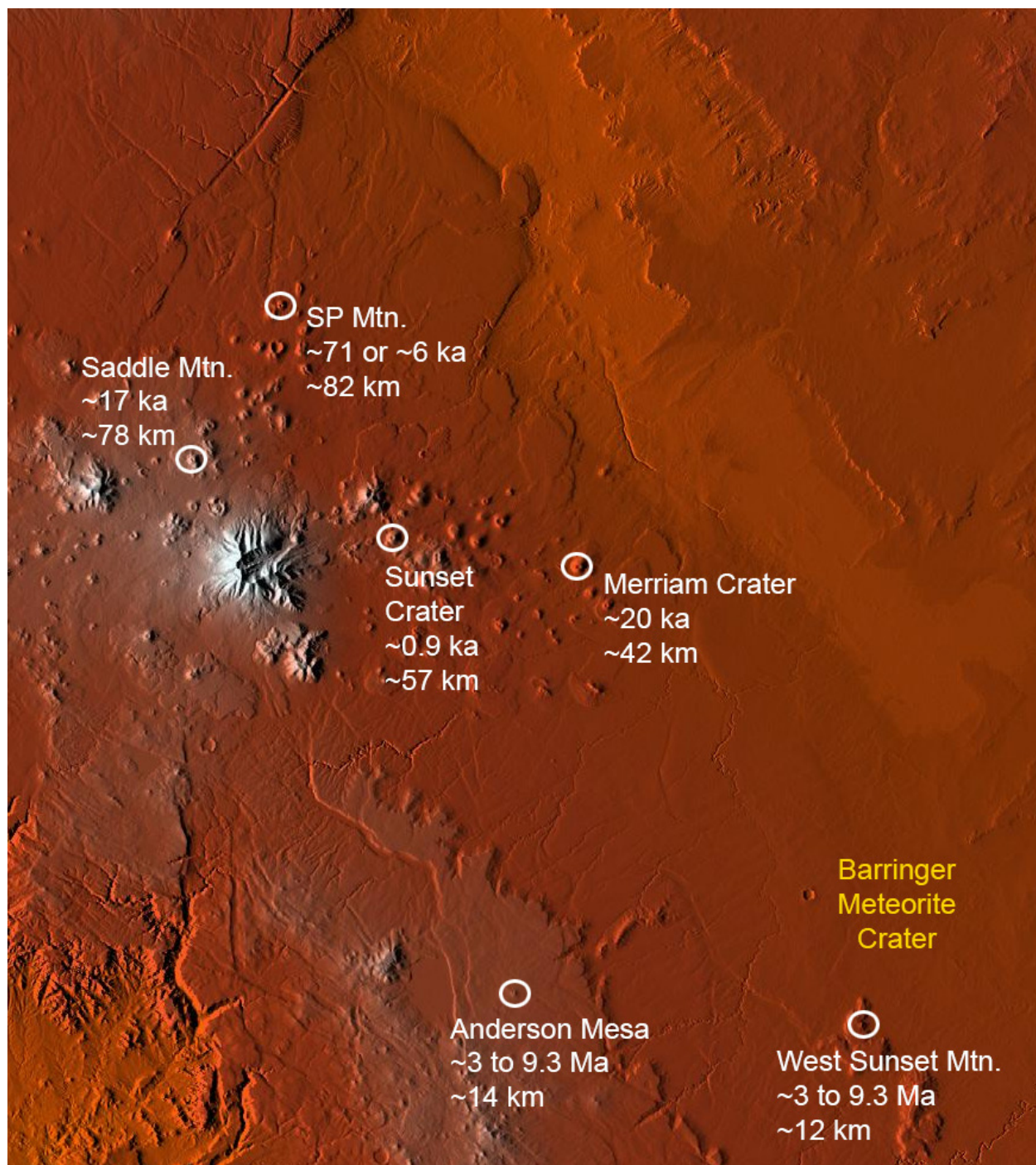


Fig. 14.7. Volcanic vents that spewed ash during the last ~50 ka (after Barringer Meteorite Crater formed) are Sunset Crater at ~0.9 ka, Saddle Mountain at ~17 ka, Merriam Crater cinder cone complex at ~20 ka, and potentially SP Mountain, although the age of the latter is disputed with estimates ranging from a little under 6 ka to ~71 ka. Of those vents, only Sunset Crater appears to have erupted after the lake in Meteor Crater dried up circa 10 to 13 ka. Nearby vents (Merriam and West Sunset Mountain) have ages older than the impact event, but potentially could have provided ash if winds reworked those older deposits.

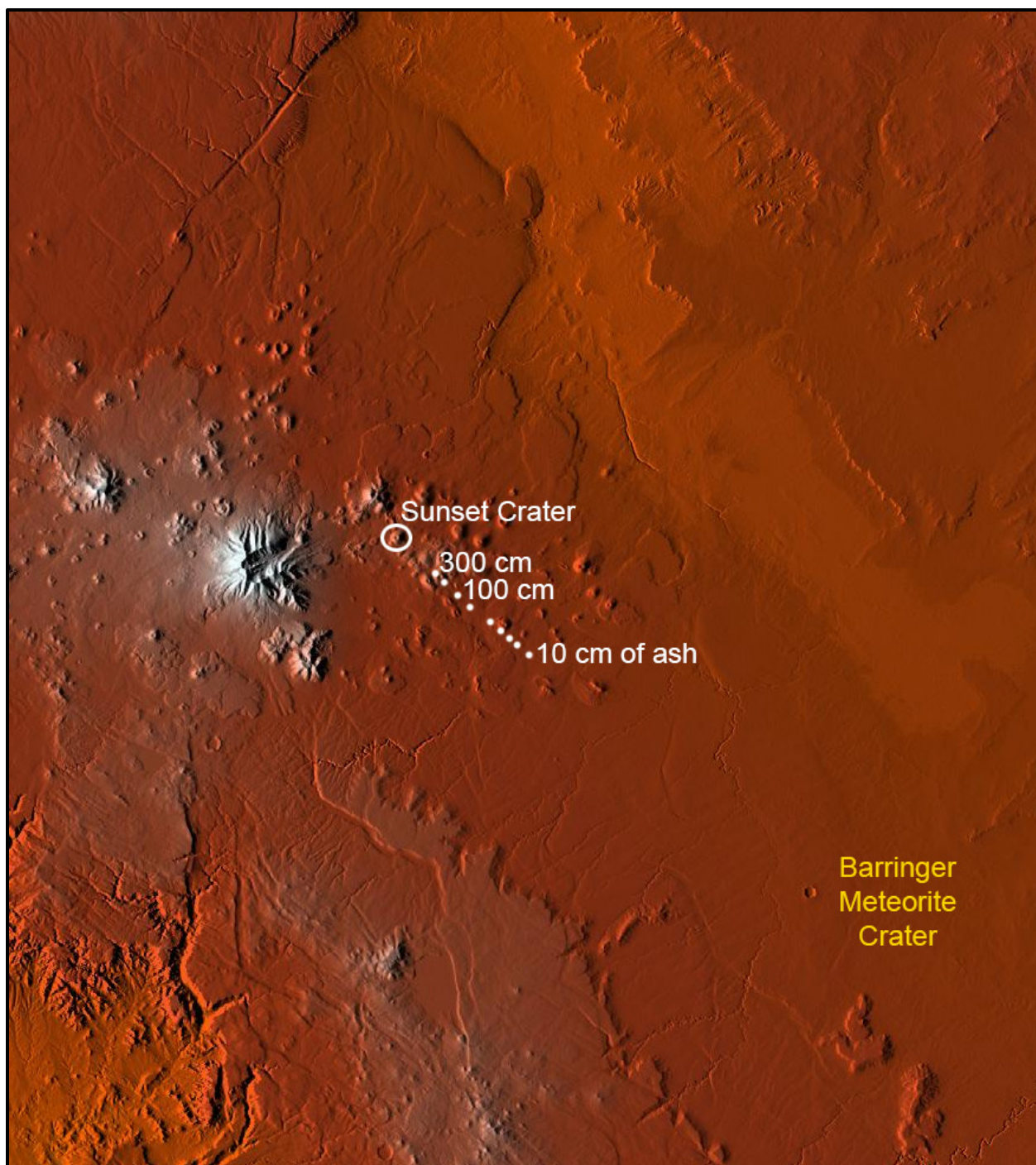


Fig. 14.8. Isopachs of ash deposited by the Sunset Crater eruption ~ 0.9 ka have been mapped by Hooten and Ort (Hooten *et al.*, 2001; Elson and Ort, 2003) down to a thickness of 10 cm at a location that is still ~ 35 km northwest of Barringer Meteorite Crater. If Sunset Crater is the source of ash on the floor of Barringer Meteorite Crater, then eolian processes blew that and other sand-size particles into a thick deposit on the south-southwest side of the floor of Barringer Meteorite Crater.

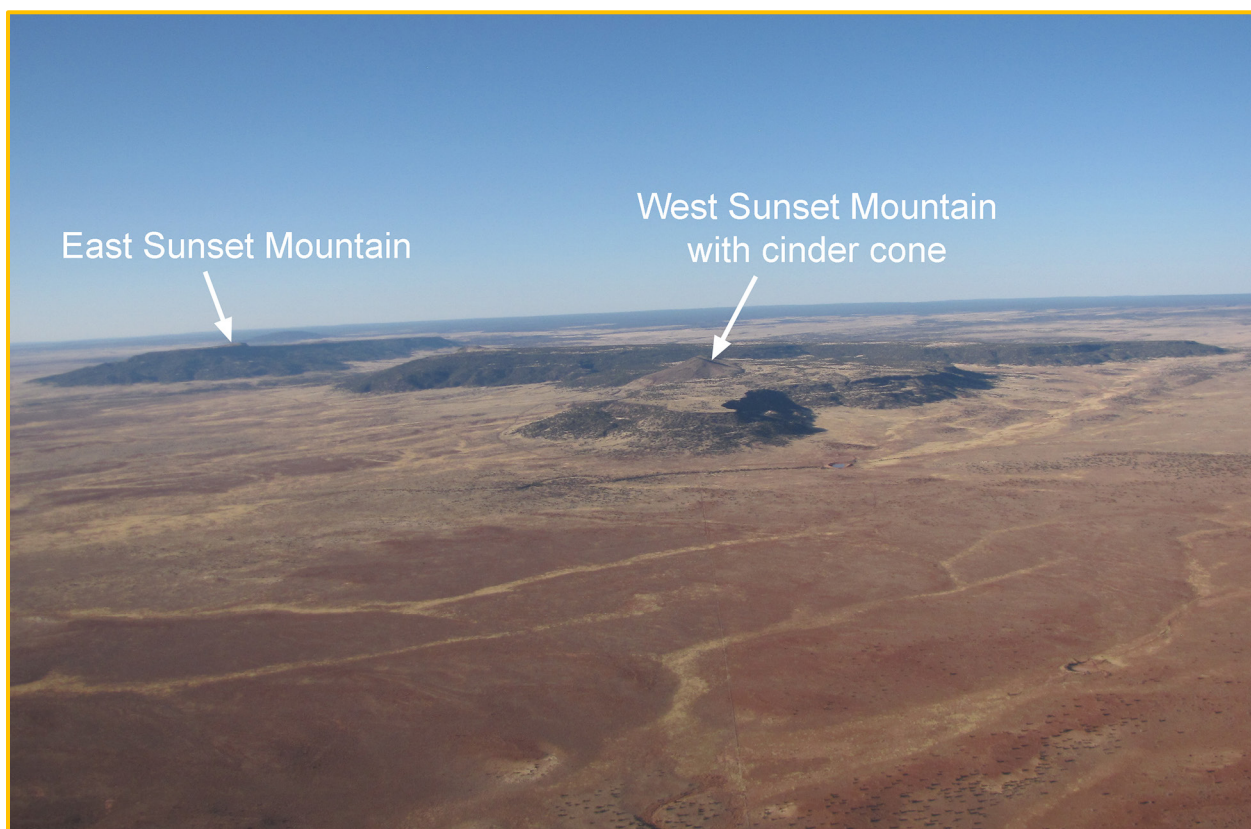


Fig. 14.9. The closest cinder cone to Barringer Meteorite Crater is ~14 km south on West Sunset Mountain. It has an estimated age between 3 and 9.3 Ma (Weir *et al.*, 1989), so it is not a likely primary source of ash in a crater only 50,000 years old. However, it is possible ash from that cinder cone was remobilized and blown north into the crater. Thus far, samples of that cinder cone and its ash deposits have not been collected and petrologically assessed.

15. Post-impact Erosion and Sedimentation



Although the crater is often described as the best preserved impact site on Earth, it has, nonetheless, been weathered, eroded, and modified by secondary sedimentary deposits. Our attention is usually riveted by the geologic processes associated with impact cratering, but it is necessary to also understand how post-impact processes modified the surviving evidence. Also, those secondary processes are, themselves, interesting and a few of them can be used as proxies for crater modification elsewhere in the Solar System, such as Mars.

I begin with some of the most commonly observed features seen on the crater rim. I also begin with the processes that affect Kaibab ejecta, because that is the material that dominates the crater rim and ejecta blanket. As already noted in Chapter 2, the surface of Kaibab is often textured with dissolution pits (Fig. 15.1). One can find near-vertical alignment of solution pits reflecting water flow downward along the face of boulders. In some cases, the orientations of those features indicate the boulders have shifted or rolled. Dissolution also accentuates fractures in Kaibab and can, in extreme cases, reduce a large boulder to several smaller boulders that fit together like puzzle pieces, separated only by fissures opened by that dissolution (Fig. 15.2).

The dissolution pits in Kaibab are also sometimes called tafoni. In a study of pits in rock at the crater, Norwick and Dexter (2002) used the term tafoni for pits of all sizes, ranging from small, centimeter-scale dissolution pits to larger, meter-scale cavernous openings in the crater wall. Cavernous features occur in both the Kaibab and Moenkopi (Norwick and Dexter, 2002; Kring and Andes, 2015). Examples of tafoni at all scales are shown in Fig. 15.3 and 15.4. The depth of tafoni is a potential geochronometer of rock surface ages throughout the American Southwest. Because Barringer Meteorite Crater has a relatively well-known age, it was used to calibrate that geochronometer. For more details, I refer readers to Norwick and Dexter (2002). In contrast to the nomenclature of Norwick and Dexter (2002), other investigators will reserve the term tafoni for only the largest (m-scale) pits, using instead the term alveoli for cm-scale features. I might add that a new study of cavernous weathering and other rock breakdown features in the Moenkopi and Coconino is underway by a student, Ankit Verma, and his advisor, Mary Bourke, so interested readers should look for those results in the near future.

Caliche is commonly associated with Kaibab pebbles, cobbles, and boulders along the rim and in the ejecta blanket. These bright white coatings are produced when calcium, dissolved from surface-exposed rocks, re-precipitates in the soil (Fig. 15.5). Exposed caliche around the base of boulders indicate up to 12 inches of erosion has occurred along the rim trail due to people passing. Microscopically, one can see the layers of carbonate are commonly 0.3 to 0.5 mm thick (Fig. 15.6). The coatings may entrain other particles in the soil around a cobble. The coatings may also include phyllosilicates (clay). Multiple layers with variable proportions of carbonate and clay may reflect changing climate. While caliche is most commonly seen around Kaibab, it also coats Moenkopi and Coconino (Fig. 15.5). As noted in Chapter 11, the thickness of these coatings is another potential geochronometer of the crater's age. Based on an observed thickness of 0.5 mm, an age of 54^{+10}_{-8} ka can be calculated. Comparisons of caliche around Barringer Crater samples and caliche around other lithologies (*e.g.*, basalt; Fig. 15.4 and 15.7) in the Flagstaff area exist for those wanting to examine this issue further (Cernok and Kring, 2009; Hörz *et al.*, 2016).

Percussion marks is another signature of rock breakdown, but their occurrence is rare as sediment transport is not very energetic and occurs over short distances. Percussion marks are usually found at the base of crater wall cliffs and in the levees of debris flows (see below).

Barringer Meteorite Crater is a closed basin that provides a fascinating opportunity to study erosion caused by variable climate and hydrological conditions. Significant mass wasting is evident along the crater walls, which are cut by dramatic gullies that feed boulder-rich deposits on the crater floor. Two major studies of those processes (Kumar *et al.*, 2010; Palucis *et al.*, 2012a,b; Palucis *et al.*, 2015) occurred during the past decade and, in both cases, implications for gullies on Mars were explored.

Each gully is composed of an alcove, a channel, and a depositional zone. The alcoves are excavated from bedrock exposures near the upper and middle portions of the crater walls. Most occur along the rim crest, but several are located immediately below the contact between the Kaibab and Toroweap (Kumar *et al.*, 2010). The widths of the alcoves range from ~10 to ~120 m, the largest of which are associated with the portions of the crater affected by tear faults (*e.g.*, as in the southeast and southwest corners of the crater). These alcoves would have formed from precipitation falling directly on the rim of the crater.

A few small alcoves exist at the base of a fracture system through the Kaibab appear to have been carved by precipitation that flowed down through that fracture system where it was then discharged through the underlying Toroweap sandstone. The pathways through the Kaibab are so efficient at dewatering the unit that there are no perennial streams on the Kaibab plateaus surrounding the Grand Canyon (Huntoon, 2000).

In general, the alcove-channel erosional process removed material from the rim and upper wall of the crater, transported it downward along channels <1 to ~5 m wide, and deposited it along the base of the crater wall or on the crater floor (Kumar *et al.*, 2010). The channels produced by that flow cut through a veneer of colluvium on the crater wall, reworking that material a second time. Incision was also greatest in the weakest lithologies on the crater wall: *e.g.*, in authigenic fault breccias and impact breccias.

Some of that sediment transport occurred (and still occurs) in an ephemeral alluvial process that produced meandering channels and outwash deposits on the lowest slopes and crater floor. However, the lower walls of the crater are also cross-cut by dramatic m-scale boulder-levee channels indicative of debris flows (Fig. 15.8 through 15.10). That type of rock flow and levee construction is common in arid environments following short bursts of precipitation that mix relatively small amounts of water (*c.* 20%) with unconsolidated debris (*c.* 80%). While those debris flow channels were briefly described by Kumar *et al.* (2010), they were the focus of the mass wasting study of Palucis *et al.* (2012a,b; 2015).

LiDAR maps (Fig. 4.3) were used to map the distribution of those debris flow channels around the crater. Field studies of representative channels were then made to assess the type of debris involved, its size distribution, the contrast in size distributions between the channel fill and levees, and the point in the channel where the transition from entrainment to deposition began. For example, in a debris flow channel in the northeast quadrant of the crater (Fig 15.9), levees were ~4 to 6 m apart and ~0.5 to 0.7 m tall. Some boulders in the levees are more than 0.5 m in diameter (Palucis *et al.*, 2012a). Cosmogenic nuclide analyses of boulders in the levees produced ages of ~10.1 to 18.7 ka, suggesting the debris flow channel was last active during the Pleistocene.

Those field observations then guided a series of rotating drum experiments to determine the amount of water needed to transport the debris. Assuming a water-to-rock ratio of 0.3 in the debris flows, Palucis *et al.* (2015) estimated ~150,000 m³ of water transported ~500,000 m³ of debris. The erosional events required <0.4 m of total runoff over the 0.35 km² upslope source area of the crater, which corresponds to ~26 mm of runoff per debris flow event. Based on the measured cosmogenic nuclide ages of a boulder

levee, the debris flow activity apparently ceased in the early Holocene when the crater lake disappeared and the surrounding region became more arid.

Those two studies were tremendously illuminating, but several questions still remain. Which type of process, fluvial or debris flow, dominated erosion? Did the debris flows reach the edge of the lake and, if so, what happened? Can the lengths of debris flows or the morphologies of their distal ends be used to determine the size of the lake over time? Did the lake shrink monotonically or did it oscillate in size? Additional studies of the gully system and its channels, like studies of the lake sediments (Chapter 14), should provide a better assessment of the post-impact modification of the crater and the evolution of the Colorado Plateau climate during the past ~50,000 years.

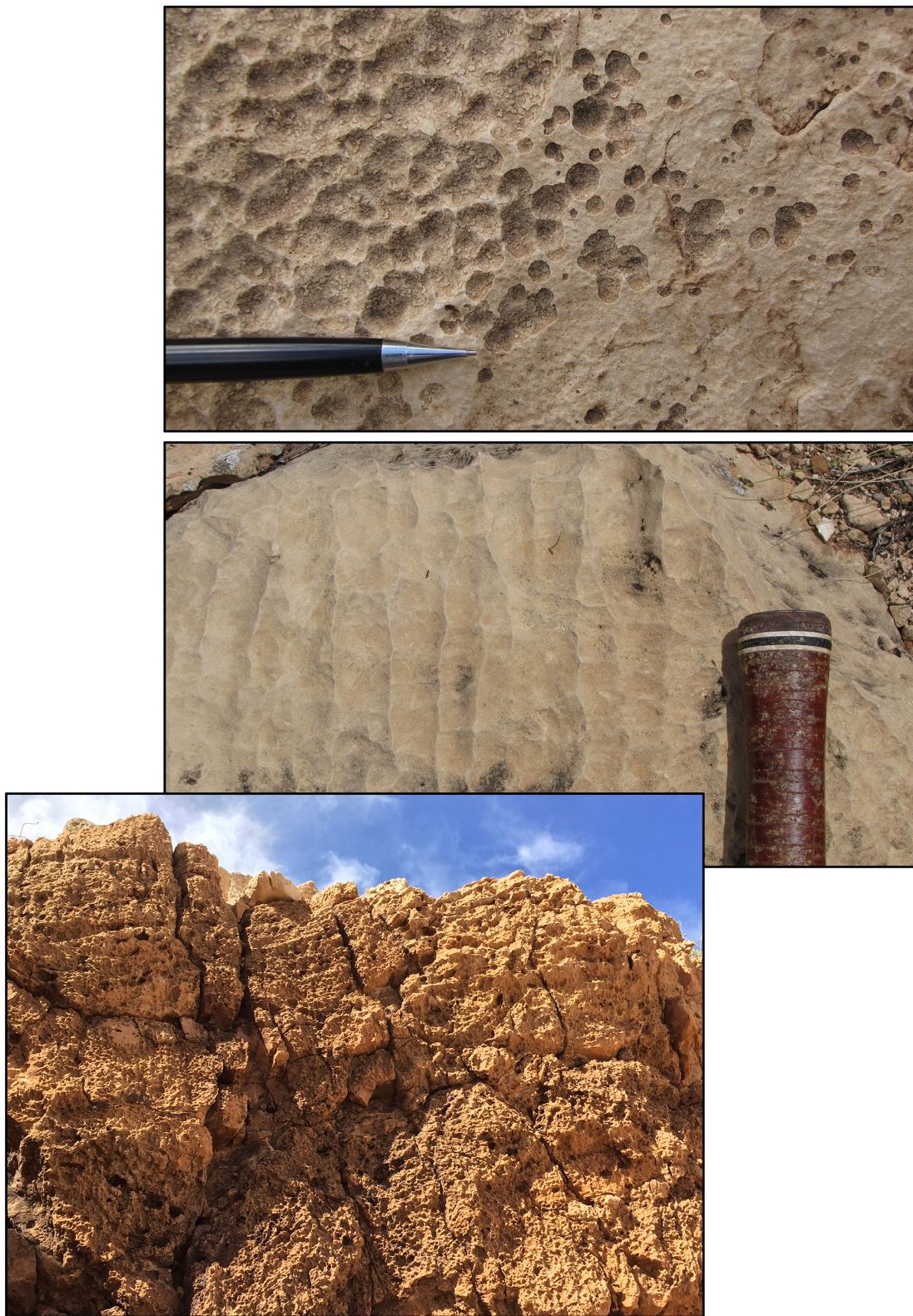


Fig. 15.1. Differential dissolution and flaking on surface of ejected Kaibab boulder (top panel), where incipient solution pits in case-hardened surface (right) occurs adjacent to well-developed solution pits (left). Near-vertical alignment of solution pits reflecting water flow downward along the face of an ejected Kaibab boulder (middle panel). Extreme example of dissolution in bedrock Kaibab in crater wall, along trail to the crater floor in the northwest portion of the crater.



Fig. 15.2. Differential erosion (top panel) where the top of the rock has been exposed to weathering far longer than the lower portion of rock, which was likely buried. The top of the rock has lost a significant layer of material (where hammer sits) and also has much deeper solution pits. Dissolution of an ejected Kaibab boulder (bottom two panels) has completely separated small breakdown blocks, as illustrated in the bottom image where the loose segments have been manually overturned.



Fig. 15.3. Tafoni at three different scales in the Wupatki Mbr of the Moenkopi Formation. Centimeter-scale pits occur on the surface of an ejected boulder (top). Decimeter-scale pits occur in bedrock on the south crater wall (middle panel). Meter-scale cavernous openings also occur around the crater, as seen here on the south crater wall. The interior of the cavern is being utilized by fauna. See Kring and Andes (2016).



Fig. 15.4. Pre-impact features on target Moenkopi can affect its post-impact breakdown in the ejecta blanket. Tafone will sometimes form along laminae in the cross-bedded siltstone (top). Also, joints and bedding planes are weaknesses that accelerate breakdown (bottom). A student, Ankit Verma, and his advisor, Mary Bourke, are currently studying the breakdown of Moenkopi and Coconino. A 33-cm-long hammer for scale.



Fig. 15.5. Caliche coatings on (from top to bottom) Moenkopi siltstone, Kaibab sandy carbonate, Coconino sandstone, all from Barringer Crater, and a porphyritic olivine basalt from the San Francisco Volcanic Field near Flagstaff. Samples MC71108-4a, MC71108-1b, MC71108-3, and SFVF71008-2a. A 1-cm cube is included for scale.

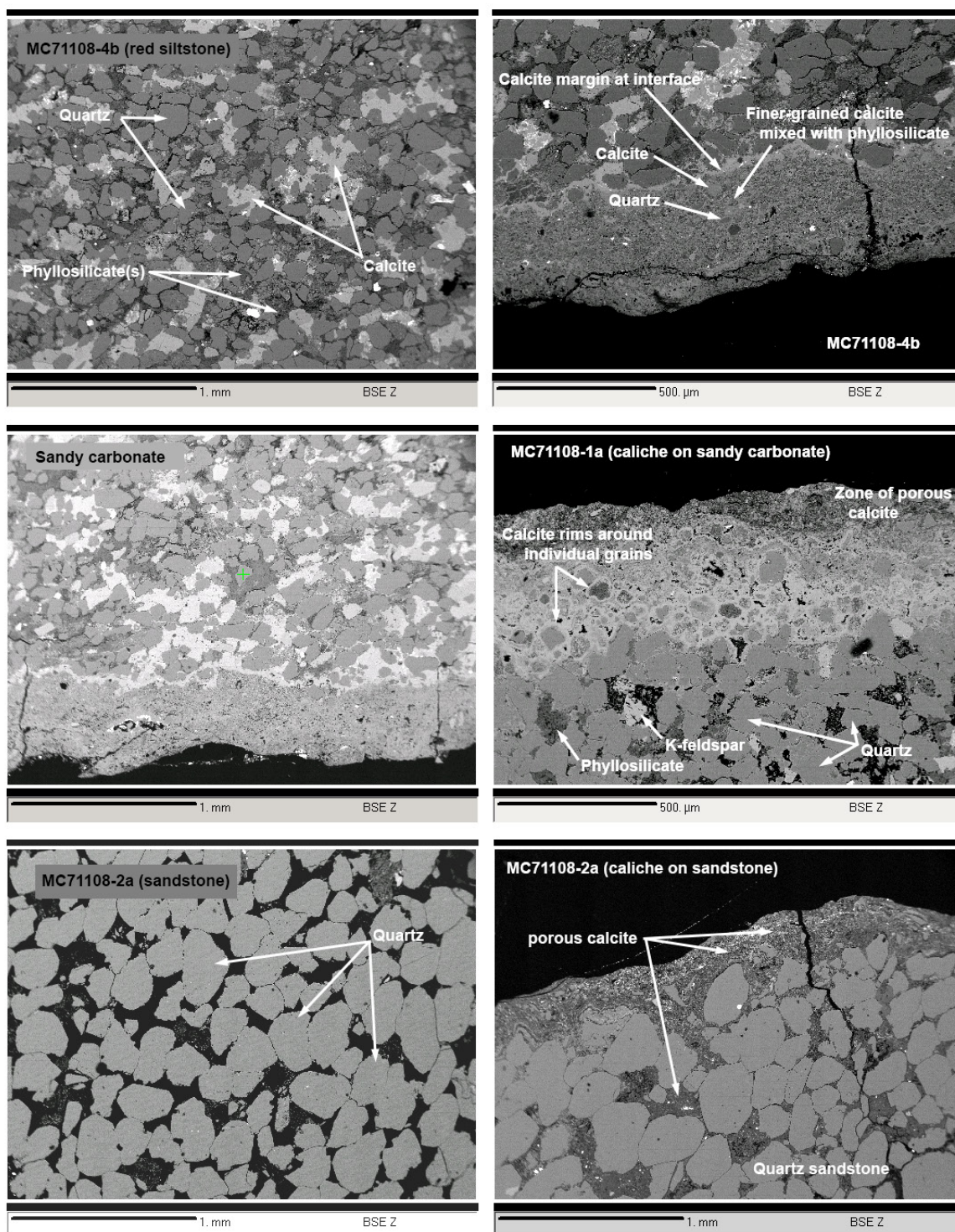


Fig. 15.6. Ejected sample of Moenkopi red siltstone (top left) with a caliche coating (top right). Ejected sample of Kaibab sandy carbonate with caliche coating (second row). Multiple layers indicate changing diagenetic (likely climate-related) conditions (second row right). Ejected sample of Coconino sandstone (third row left) with a caliche coating (third row right). Phyllosilicates (clay) can also be comingled, in variable proportions, with the carbonate in the caliche coatings. Backscattered electron images. Samples MC71108-4b, MC71108-1a, and MC71108-2a. Scale bars are either 1 mm or 0.5 mm (500 μm).

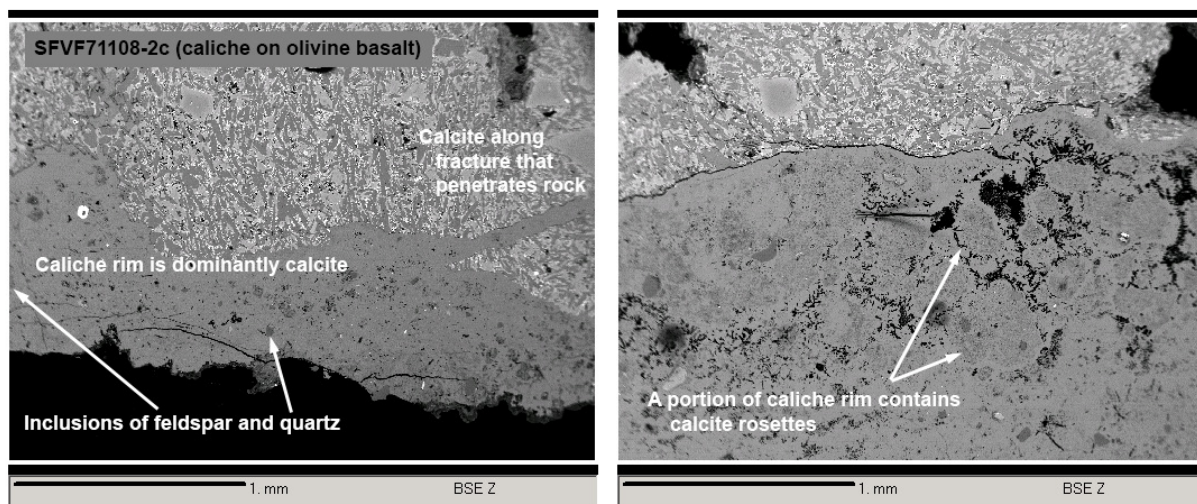


Fig. 15.7. For comparison with the Barringer Crater samples shown in Fig. 15.6, here are shown caliche coatings on a porphyritic olivine basalt from the nearby San Francisco Volcanic Field. When the calcium carbonate precipitated around the basalt, it also entrained and cemented other phases in the soil; *e.g.*, feldspar and quartz (bottom left panel). Phyllosilicates (clay) can also be comingled, in variable proportions, with the carbonate in the caliche coatings. Backscattered electron images. Sample SFVF71008-2c. Scale bars are 1 mm.



Fig. 15.8. Leaved debris flow channels can be seen from the crater rim. An example appears here in the center of the field of view. Several older leaved channels are also visible. Sometimes a channel will cut across an older channel. East side of the crater.



Fig. 15.9. Below gully alcoves, gullies often transition to debris flow channels with boulder levees. The lower left panel is a view looking down a channel on the east crater wall that flows out onto the crater floor. The upper right panel is a close-up view of a boulder-rich levee along one of these types of channels. A person is in the field of view in the lower left panel for scale. A 33-cm-long hammer is shown for scale in the upper right panel.



Fig. 15.10. In this perspective view, a debris flow channel with a boulder-rich levee is in the foreground and rises in the distance towards its source region on the south crater wall. Yellow arrows point to the margin of the gully as it rises up the crater wall.

16. Modern Atmospheric Conditions at the Crater



The crater continues to be modified in the current arid environment, so it is important to understand the meteorological conditions operating today. Those conditions are also important because they govern the distribution of biologically attractive niches in the crater and, thus, are critical parameters for any assessment of astrobiological conditions that might be applicable to other planetary (*e.g.*, Martian) systems.

In 2009, an extensive set of meteorological measurements were made in an NSF-sponsored campaign called the Meteor Crater Experiment (METCRAX). The consortium team chose Meteor Crater for their experiment, because it was a near-perfect topographical basin and, thus, suitable for a study of the structure and evolution of temperature inversions and cold-air pools that form on a daily basis in larger topographic basins and valleys, such as Phoenix. The physical processes leading to the buildup and breakdown of temperature inversions and the formation of atmospheric seiches (atmospheric oscillations caused by wind disturbances at the basin crest) were studied in the crater without the complications introduced by more complex topography. The experiment produced a large number of papers relevant to atmospheric sciences (Whiteman *et al.*, 2008, 2010; Fu *et al.*, 2010; Hoch and Whiteman, 2010; Mayer *et al.*, 2010; Doring *et al.*, 2011; Haiden *et al.*, 2011; Hoch *et al.*, 2011; Lehner *et al.*, 2011; Adler *et al.*, 2012; Lehner and Whiteman, 2012) and, importantly for the planetary science community, an immense amount of data that can be used for astrobiological purposes.

The implications of those results for microniches on Mars immediately followed (Whiteman *et al.*, 2008). Two sets of observations are relevant. First, measurements of wind found that horizontal-axis eddies were produced by the crater rim and vertical-axis eddies formed over the crater floor during the daytime. In contrast, at night, a large drainage flow from the higher terrain of the Mogollon Rim southwest of the crater would sometimes pour over the rim of the crater. Second, measurements of temperature over a year (Fig. 16.1 and 16.2) showed how it varied between the crater rim and crater floor, between opposing crater walls, and between seasons.

Temperature inversions formed in the crater late in the day. During those periods, temperatures were similar from one side of the crater to the other at the same altitude. A 30-m thick stable cold-air pool formed on the crater floor with a temperature increase of $\sim 5^\circ\text{C}$ over that distance, covered by a nearly isothermal layer that extended to the altitude of the crater rim. The thermal inversions were destroyed within $2\frac{1}{2}$ hours of sunrise and replaced by a convective layer of air that grew upward as the crater floor and crater walls grew hotter. The daytime growth of that convective layer created strong winds at the crater by carrying strong winds from aloft downward. Those conditions would have been moderated in the crater when a lake was present, because of differences in the thermal properties of the soil (today) and water (then), except when the lake was frozen.

The experiment suggests that cold air may pond on crater floors, deepening thermal inversions seen in craters on Mars (Smith *et al.*, 2004). Those inversions, like the ones in Meteor Crater, may have been less severe on early Mars when lakes were filled with water, if that water was not capped by a frozen shell of ice (Whiteman *et al.*, 2008). The variation in temperature each day is greater on the crater floor than on the crater rim and the average temperature is less on the crater floor than on the crater rim at Meteor Crater and similar patterns should apply on Mars. Downslope winds may enhance the ablation of volatiles from bedrock, caves, and talus on crater walls, particularly in gully channels (Chapter 15).

It also seems reasonable that the condensation of volatiles is more likely on shadowed slopes and where

large-scale nocturnal drainage flows spill over a crater rim.

Those nocturnal drainage flow winds were an unexpected observation at Meteor Crater and prompted NSF to support a second experiment called METCRAX II in 2013 to study the flow as an analogue for downslope windstorm-type flows. In the case of Meteor Crater, the process begins with katabatic winds draining the Mogollon Rim and flowing towards the crater where they spill over the rim in higher-velocity downslope flows along the southwest crater wall (Fig. 16.3). To study those winds, an array of meteorological equipment was temporarily installed (Fig. 16.4). This experiment, like the first experiment, generated a wealth of meteorological data that will be useful for astrobiological and planetary analogue studies. That data is still being evaluated, but two papers describing the experiment in greater detail (Cherukuru *et al.*, 2015; Lehner *et al.*, 2016a) and an initial result relevant to atmospheric sciences (Lehner *et al.*, 2016b) have appeared. The data confirm the inferences drawn for Mars from the original METCRAX experiment, but I expect to see a broader application of the data to conditions on early and modern Mars as the METCRAX II data is processed further.

The data produced by both experiments can be accessed through the LPI website that complements this guidebook (http://www.lpi.usra.edu/publications/books/barringer_crater_guidebook/).

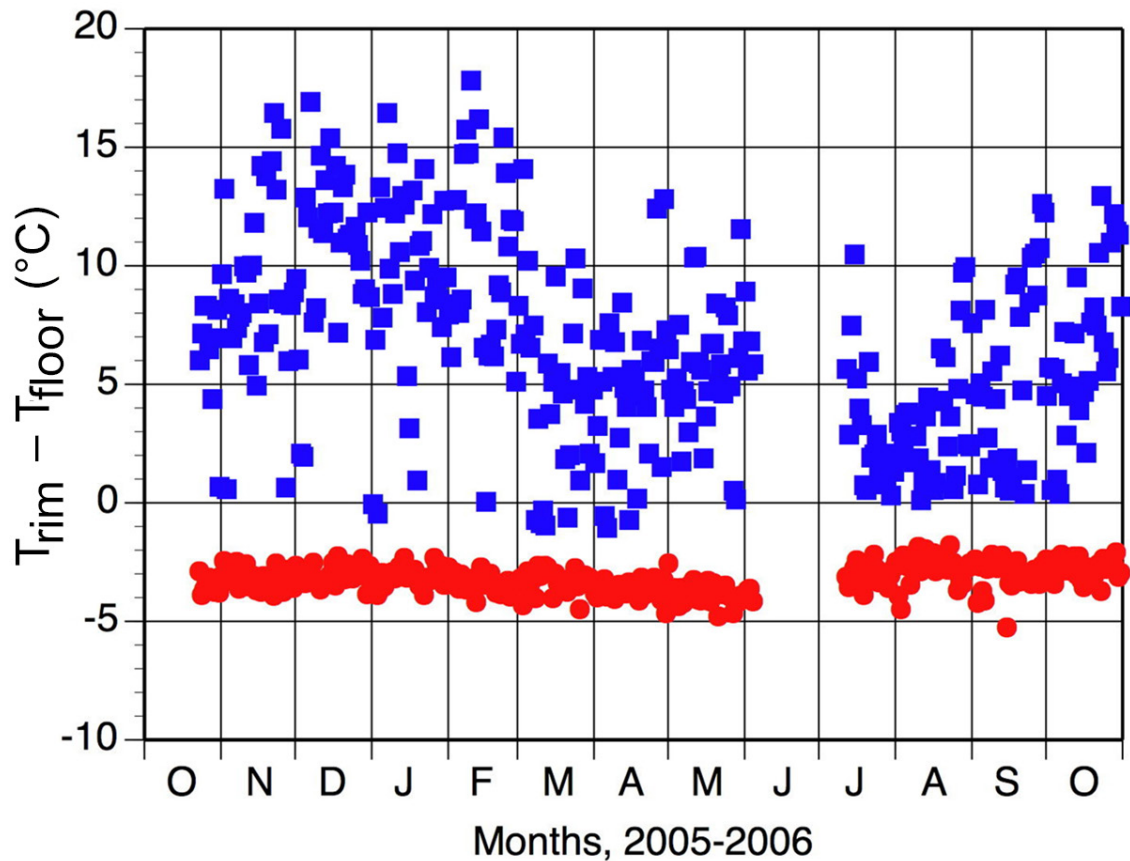


Fig. 16.1. The METCRAX experiment documented the temperature differences between the crater rim and crater floor as a function of time from October 22, 2005 through October 31, 2006, albeit with a data gap between June 4 and July 11, 2006. The data represent daily maximum (blue) and minimum (red) temperature differences between the rim and floor. The data indicate a daily temperature inversion, wherein the rim is hotter than the floor. Those inversions form in the late afternoon and evening. The minimum daily temperature differences (red) are always negative, indicating the nocturnal temperature inversions are broken up daily. The strongest inversions occur in the winter months, when temperatures increase by 15 $^{\circ}\text{C}$ from the floor to the rim. Illustration from Whiteman *et al.* (2008).

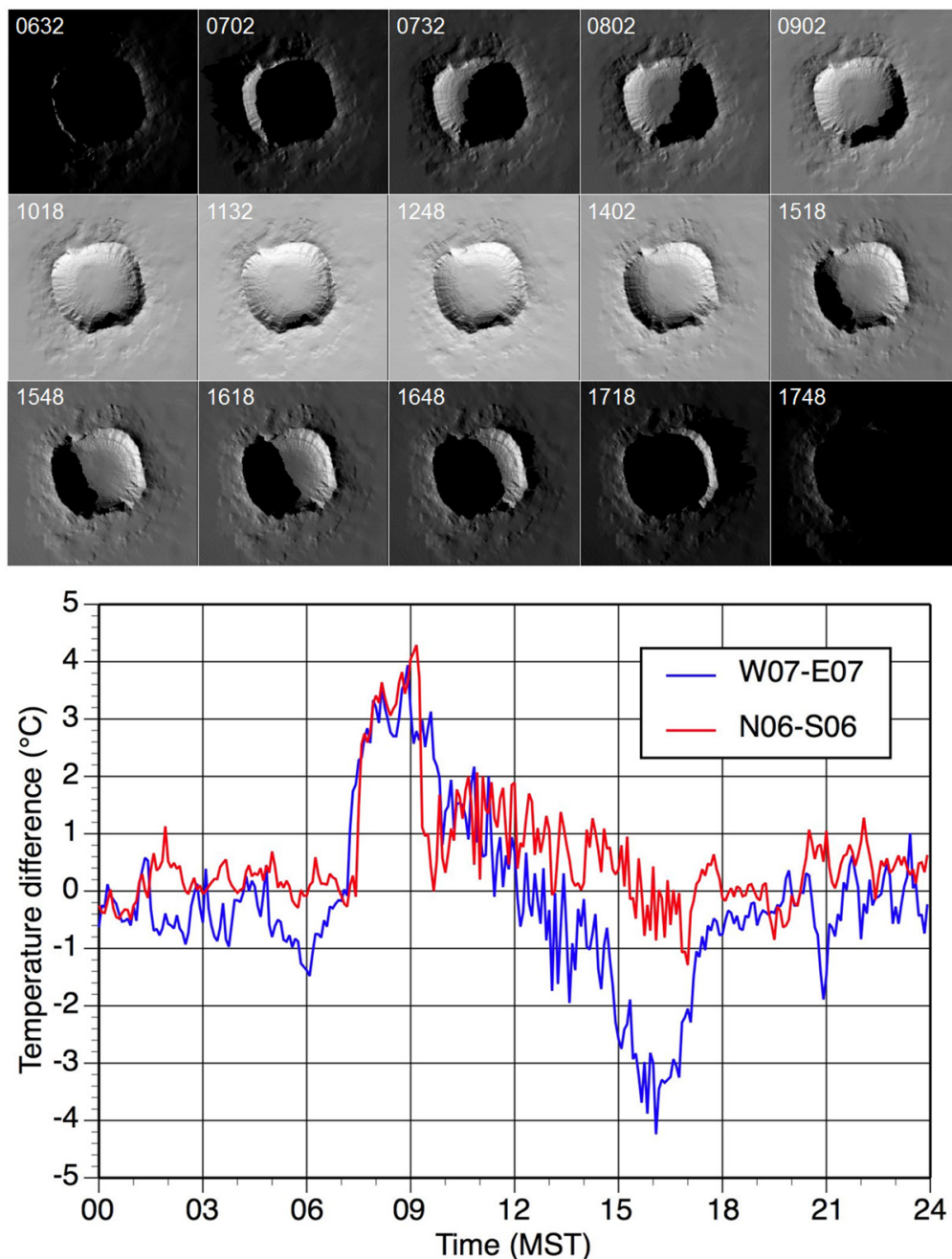


Fig. 16.2. The METCRAX experiment documented the diurnal air temperature differences caused by oblique sunlight and shadows on the crater walls. The upper panel shows the modeled progression of sunlight and shadowing in the crater on October 15, 2006, with time stamps in units of Mountain Standard Time (MST). That differential solar radiation created differential air temperatures that were measured. To illustrate those differences, the bottom panel shows the temperature differences between opposing west-east (blue line) and north-south (red line) crater walls at about 75 m above the crater floor on October 22, 2006, as recorded as a function of MST. At night, temperature differences between the same heights on the crater walls are small. (Although not shown here, that is not the case at the level of the rim, where a large scale cold air drainage flow from the southwest can produce temperatures that are 3 °C colder on the southwest rim than on the northeast rim.) During the day, temperature differences rise to 4 °C when a crater wall is in sunlight and the opposing crater wall is shadowed. In general, the north and west crater walls are relatively warmer in the morning and the east crater wall is relatively warmer in the afternoon. Illustrations from Whiteman *et al.* (2008) and their poster presentation.

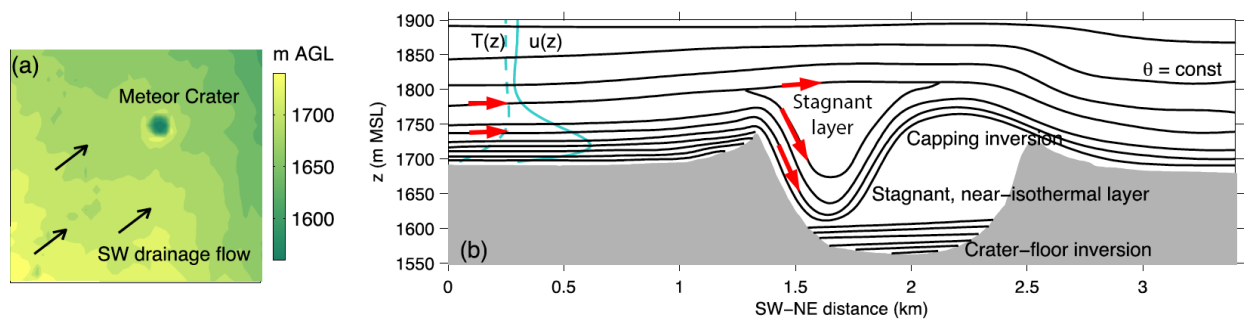


Fig. 16.3. The METCRAX II experiment was designed to study downslope flows to better understand windstorms in mountainous areas; *e.g.*, the chinook winds that sometimes level forests and damage buildings in the Rocky Mountain region. Similar winds, called föhn winds, affect areas within Europe's Alps. Meteor Crater provides an analogue environment, because winds blowing southwest to northeast (left panel) plunge over the crater rim (right panel). On clear, undisturbed nights, cold air pools on the plain southwest of the crater, forming a near-surface inversion (*i.e.*, warm air over colder air). That air flows downhill over the slightly-sloping plain towards the northeast. When the cold air reaches the crater rim, it spills over the rim and drains to the crater floor. When that cold air layer deepens, warmer air aloft also spills over the rim, producing a wavelike flow structure with higher wind speeds. That warm-air intrusion creates a large horizontal temperature gradient from the southwestern crater wall towards the crater center. The METCRAX II experiment, designed to study a modern meteorological problem, provided data relevant to our understanding of environmental conditions within impact craters and possible microniches in localities as distant as Mars. This illustration is used with permission and is modified slightly from its form in Lehner *et al.* (2016), which amplified the work of Adler *et al.* (2012).



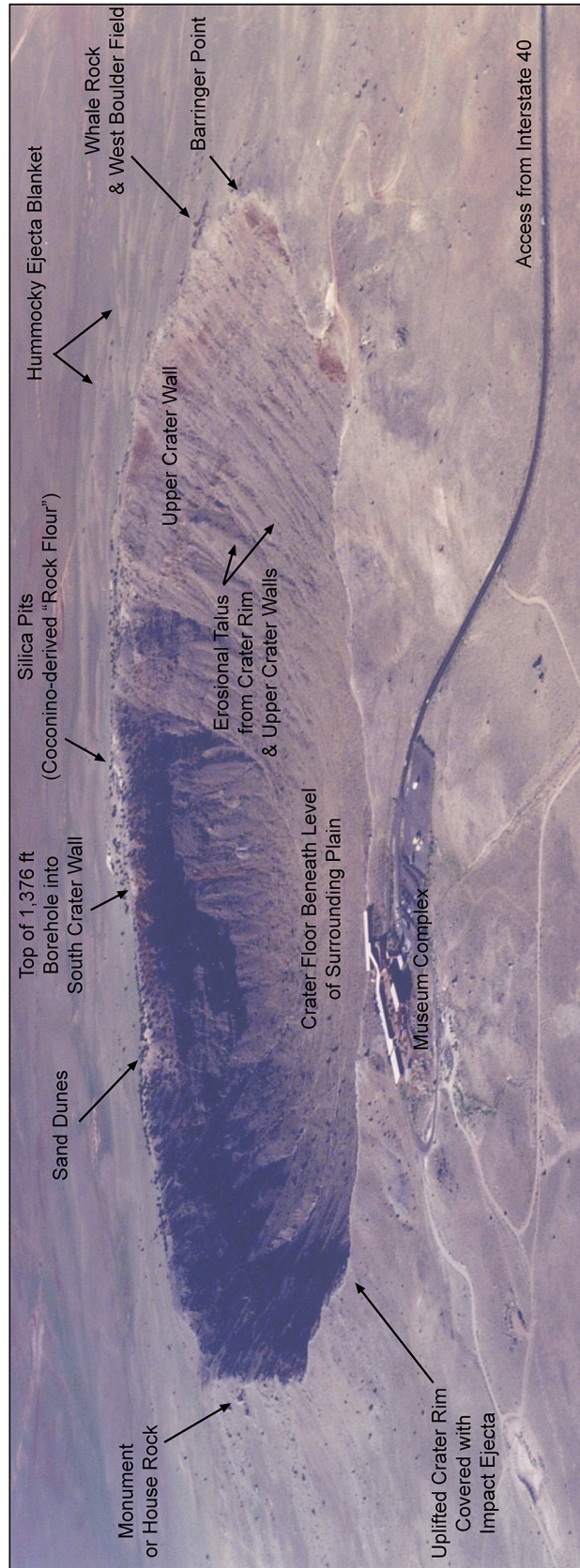
Fig. 16.4. The METCRAX II experiment deployed instruments in the crater and on the surrounding plain. Instruments were secured to booms at several different heights on a tower (upper left) to measure differences in atmospheric properties as a function of height above the crater rim. Six arrays of HOBO temperature data-loggers (left side of middle panel) were temporarily installed on the crater floor, crater walls, and rim. Infrared and LiDAR cameras were deployed (right side of middle panel) to measure air flow into and within the crater. Towers were also erected on the surrounding plains to evaluate the atmosphere before air reached the vicinity of the crater. Data are accessible from the guidebook's website http://www.lpi.usra.edu/publications/books/barringer_crater_guidebook/.

Trail Guides

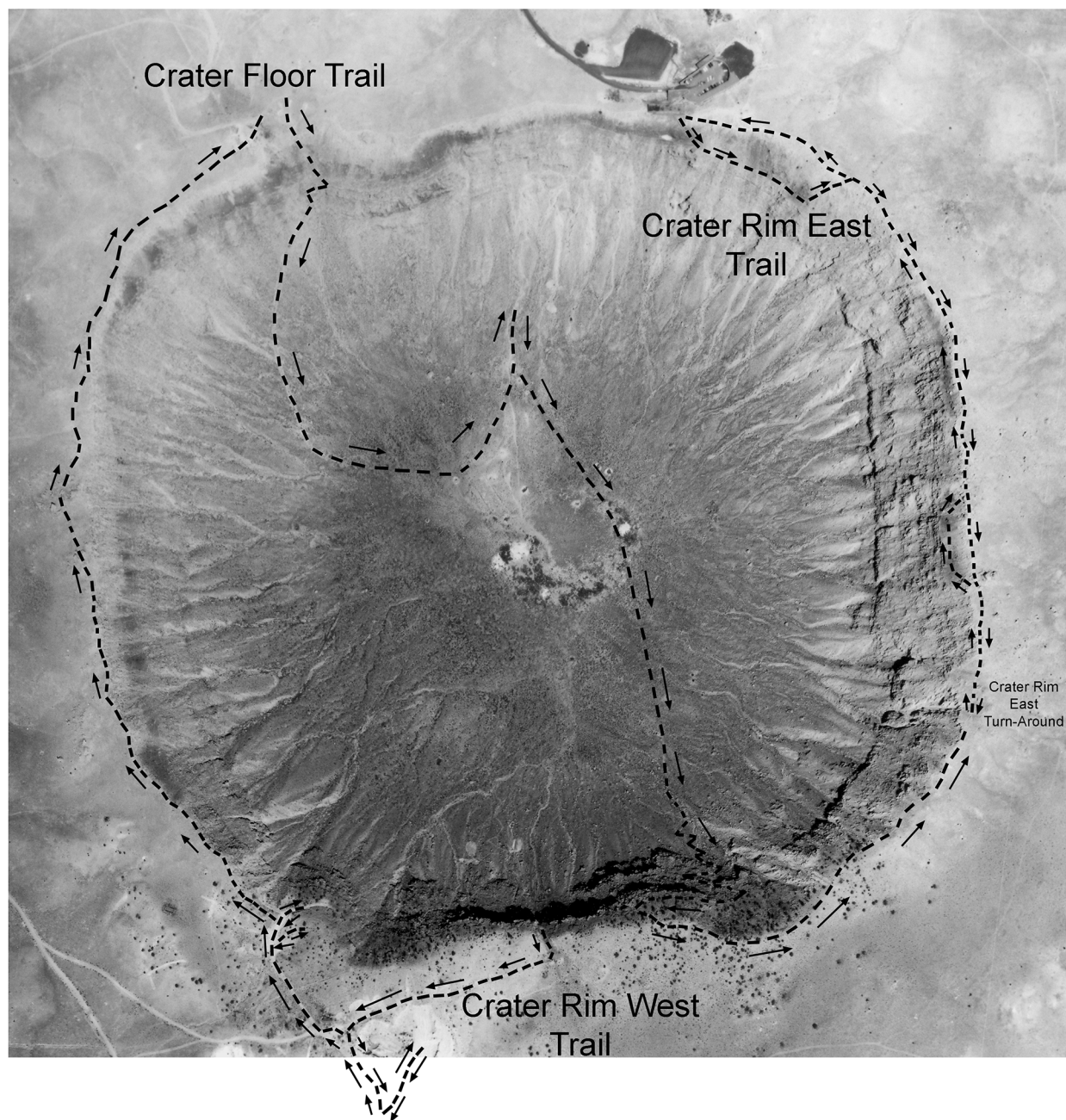
Crater Rim East

Crater Rim West

Crater Floor



Aerial view of Meteor Crater with some of its features labeled. Photograph is courtesy of Meteor Crater Enterprises.



Trail Guide Routes

17. Trail Guide 1: Crater Rim East



We begin our excursion along a paved trail that leads to the museum's overlook platform. Walk down that trail and pause before walking out onto the platform. The bedrock adjacent to the paved trail is red Moenkopi siltstone. It has been uplifted from its pre-impact horizontal configuration. Moenkopi a few meters farther up the slope has been overturned and forms the base of the impact ejecta or debris unit. Overturned Kaibab debris rests on top of the Moenkopi debris. The precise location of the axis of the fold will be obscure here. We will revisit this overturned sequence at several other locations along the east wall of the crater.

With permission of crater staff, we will step from the paved trail onto the Moenkopi and then follow a faint trail (the Astronaut Trail), proceeding roughly east along this portion of the crater's north rim. The path drops down into the Alpha Member of the Kaibab Formation where we will have our first stop.

Crater Stratigraphy

Before taking a closer look at the rock beneath our feet, it will be useful to examine the crater stratigraphy in a dramatic exposure in the southern cliffs of the crater (Fig. 17.1). The basal Kaibab (or Gamma Mbr) outcrops as a cliff-forming unit immediately above lower, talus-covered slopes in the crater wall. The Gamma Mbr is a medium- to thick-bedded sandy dolomite that is normally gray to buff yellow in color. The cliff, however, is stained. A moderately bright red stain comes from the overlying Moenkopi. A dark, nearly black stain also coats large sections of the cliff-face. Although not visible from this vantage point, a small patch of the Toroweap Fm can be found in a cave at the base of the Gamma Mbr. Pleistocene talus and a small amount of mining debris covers the Gamma Mbr and Toroweap Fm to the right (west) of the cave.

The uneven slope above the Gamma Mbr is produced by the Beta Mbr of the Kaibab Formation. It is composed of sandy dolomite that does not outcrop around the crater as well as the underlying Gamma and overlying Alpha Mbrs. This tendency to be a poorly-outcropping and slope-forming unit can be seen particularly well on the slope with a stripe of red drilling mud.

The sharp, cliff-forming unit above the Beta Mbr is the Alpha Mbr. This unit is dominated by medium- to thick-bedded sandy dolomite at its base and an interbedded sequence of medium-bedded dolomite and sandstone at the top. A key marker bed within the Alpha Mbr is a 2-m-thick white sandstone, which Shoemaker traced around the crater and used extensively when identifying fault displacements in the crater wall. It is not the only sandstone horizon in the Alpha Mbr, however.

Although historically called the Kaibab Limestone, the formation is better described as a dolomite or interbedded sequence of sandy dolomites and sandstones. The entire formation is ~80 m thick in the crater walls. I refer readers to Chapter 2 for additional details.

Above the Kaibab is the red Moenkopi Formation. The basal Wupatki Mbr outcrops in relatively massive orbicular knobs and ledges. That unit is covered by a more fissile Moqui Mbr. There is also a very thin, ~30 cm-thick section of fissile Moenkopi at the base of the Wupatki Mbr, although it is not always visible in outcrop. These units formed the eroded, and, thus, uneven pre-impact surface. For that reason, they are not the same thickness in all locations around the crater, although they can be traced

continuously along most of the southern crater wall. Additional details of these units can be found in Chapter 2.

Above this pre-impact stratigraphic sequence is a thick deposit of impact ejecta composed of Moenkopi, Kaibab, Toroweap, and Coconino. We will be taking a closer look at those units later in the field excursion.

Museum or Moon Mountain Anticline

The uppermost Kaibab unit in the walls of the crater is chaotic, irregular, and, in places, missing. Here one will find a dolomitic sandstone with individual sandstone and sandy dolomite clasts in a bed about 1 m thick. Shoemaker and Kieffer (1974) interpreted this to be a residual deposit formed on a karst surface. That is, it formed by partial solution of the Kaibab over a fairly long period of time. The unit is sometimes called the “leached Kaibab” unit. Below the unit is an ~4-meter-thick sequence of medium-bedded sandy dolomite, sandstone, and minor limestone. Below that interval is an important marker bed at the crater: the yellow vuggy dolomite. This unit can easily be traced around the uplifted crater walls and found in overturned ejecta debris.

In front of us (Fig. 17.2), two thrust faults cut through the Alpha Mbr, duplicating part of the section and enhancing the uplift of the crater rim. The yellow vuggy dolomite marker bed in the lower plate of the thrust plane is in contact with a duplicate of the same bed in the overlying plate. Fault gouge can be found along the thrust fault, particularly on the west (or left) side of the exposure in Fig. 17.2. The thickness of the gouge is variable, but ranges up to 15 cm thick. The contact is also covered in some places. Farther to the east, the fault and the yellow vuggy dolomite marker bed bend sharply and angle downward. These beds of the Alpha Mbr are arched over a wedge of additional Alpha Mbr rock about 15 m across. This wedge was thrust outward from the center of the crater during crater excavation and crater wall uplift. Shoemaker measured a 30° outward dip on the crest of the arch and estimated ~45° dip on the fault. He also measured 2 m of Kaibab that was repeated in the section, implying ~5 m of throw on the fault.

These types of faults occur in several locations around the crater, in both the Alpha and Beta Mbrs of the Kaibab, and are responsible for a significant portion of crater rim uplift. Shoemaker noted them on the west and north sides. Examples also occur on the east side. Multiple thrusts occur beneath the highest anticlines around the crater, which remain the topographical high-points on the crater rim, such as the northwest corner of the crater (*e.g.*, Barringer Point). The thrusts are often small (as here), but occur multiple times, producing a cumulative effect. Bedding within the Kaibab (particularly the Beta Mbr) is often indistinct, so the amount of bedding repetition cannot always be measured quantitatively. Nonetheless, most of the uplift in the largest anticlines appears to be a direct consequence of the thrusts. Shoemaker suggested that the concentration of these thrusts to the northwest suggests the trajectory of the projectile may have been moving from southeast to northwest.

If we turn around, a thrust fault can be followed down the crater wall to the west, passing beneath a prominent dolomite outcrop, from where it continues to a point beneath the observation platform (Fig. 17.3). Also visible in this section is the white marker sandstone in the middle of the Alpha Mbr of the Kaibab Fm and the yellow vuggy dolomite near the top of the Alpha Mbr of the Kaibab Fm. These previously horizontal units have been sharply uplifted in the walls of the crater and now dip outward. If the field party is small, it can follow the thrust fault to the west and peer beneath the observation deck. Erosion along the thrust fault has formed a chute. If the field party is large, this extra view should probably be avoided.

Next, we want to return to our trek to the east. Follow the trail, which should stay above a small section of near-vertical outcrops within the Alpha Mbr of the Kaibab. The trail will pass into a section of Moenkopi that tracks across and diagonally down the crater wall (Fig. 17.4). We will stop here to discuss the Moenkopi.

Identifying Overturned Bedrock in the Crater Rim

As discussed in Chapter 2, Moenkopi siltstone was deposited in a coastal environment that was constantly being processed by water currents and wind. This generated cross-bedded laminae that can be used to separate uplifted strata and overturned strata. Normally-bedded units will be sitting on top of Kaibab-Alpha. Somewhere up-slope, those units are overturned and duplicated. We will use the cross-bedded laminae to identify that point.

Begin by examining large blocks of Moenkopi near the contact with the Kaibab-Alpha. The top of many cross-bed sets will be sharply truncated, typically at an angle of $\sim 30^\circ$ (see Fig. 2.6d for an example). At the base of these sets, however, the cross-bedded laminae are truncated at very shallow angles, typically less than 5° . The laminae will appear to tangentially or asymptotically approach the base of the set. The distinct difference between the base and top of a cross-bed set can be used to identify units that are oriented normally or overturned. A schematic illustration of these features and their relationship to parental dunes is also provided (Fig. 17.5).

I invite the group to migrate across the slope, moving increasingly upward in section, to study the cross-bedded laminae and identify the level where blocks have been overturned.

Not all blocks will have an unambiguous indicator of orientation. Some blocks of Moenkopi may have, for example, horizontal rather than cross-bedded laminae. In addition, some blocks have rotated and shifted slightly downhill, obscuring their original orientations. Nonetheless, with careful scrutiny, the duplicated and overturned sequence of the Moenkopi on this portion of the upper crater wall is identifiable.

After locating the overturned section of Moenkopi, follow the Moenkopi across the slope to the east with your eyes. You will see that the trace of Moenkopi disappears. It is replaced by yellow to buff-colored Kaibab. The Moenkopi in that section of crater wall is at a much higher elevation near the top of the crater rim. The jump from Moenkopi to Kaibab in this section of the crater wall was created by differential uplift along a tear fault. Shoemaker (1960) and Roddy (1978) argued that these tear faults formed along pre-existing sets of joints that are particularly prominent in the Kaibab and accentuated by dissolution along those joints.

Additional faults can be seen from this location along the east crater wall (Fig. 17.6). The relative structural displacements can best be seen by following the cliff-forming Kaibab-Gamma unit. The displacements are modest along the crater wall, but dramatic in the southeast corner of the crater where another large tear fault (or, rather, a complex set of tear faults) was produced during crater formation. The additional uplift generated on the north side of this tear fault provides the best exposure of the Toroweap and Coconino Fms in the entire crater. As the excursion proceeds, we will hike above those faults and it will be evident that they are easily eroded and an important structural source for major gully formation in the crater walls.

From this vantage point, we can also glimpse the path we will be taking along the remainder of our excursion (Fig. 17.7). We will be walking along the east rim of the crater. Similar outcrops of uplifted

Kaibab-Alpha are visible along that portion of the crater wall. Also visible is a particularly large block of Kaibab ejecta called Monument or House rock. We will be visiting that location. We will also hike beyond that point to a location near a gate in a fence line that is visible slightly further to the south. We will then turn around. Our hike to the southeast will utilize a trail on the rim of the crater. On the return, we will dip down the crater wall again.

From our current position in the field of Moenkopi blocks, the field party should climb up the slope of the crater wall to the crater rim trail that circumnavigates the crater.

If time allows, however, the field party can follow the Moenkopi to the tear fault before climbing to the rim. Exposures indicate the fault is complex, diverging into several sub-parallel faults, particularly as it cuts through the Moenkopi. Where the fault cuts through the Kaibab, gouge is visible in the walls of a ravine that has been eroded deeply into the fault.

Relative displacement on the tear fault along the gully is ~24 m (Shoemaker and Kieffer, 1974). It has juxtaposed the overturned Moenkopi debris layer (this side of fault) against the white marker sandstone in the middle of Kaibab-Alpha (far side of fault). Farther down the slope, it has juxtaposed the upper part of the Kaibab-Alpha (this side of fault) against the upper part of the Kaibab-Beta (far side of fault).

The group still needs to reach the trail on the crater rim before continuing the excursion. From the tear fault, the climb up to the crater rim is very steep and over unstable rock. It may be prudent to return to the Moenkopi boulder field and climb to the rim from that point.

Once on the rim trail, follow it to the southeast along the east wall of the crater.

Traversing Impact Ejecta

This portion of the rim trail weaves over and through blocks of Kaibab that were excavated from the crater. Roddy *et al.* (1975) calculated that 175 million metric tons of rock was deposited on the crater rim and the surrounding landscape. The debris is composed of angular to sub-angular blocks. The smallest debris components identifiable in the field are millimeter in scale and range to blocks that are several meters in size. Shoemaker and Kieffer (1974) report that the size frequency of this debris follows a classic fragmentation law, such that the cumulative mass of debris is a simple power function of the particle size. The exponent of this power function is such that 50% of the total mass falls in the largest 3 phi intervals. The data, however, appears to be lost. Size frequency data for the smallest size fractions (0.03 to 16 mm or +5 to -4 phi units) of Kaibab and Coconino ejecta were independently gathered by Grant and Schultz (1993). They found modes at 0.074 and 0.21 mm for Kaibab and Coconino samples, respectively, without any identifiable power-law distribution. The mode for this fine fraction of Coconino ejecta is approximately equal to the average grain size in the original Coconino target rock (~0.19 mm; Table 2.1).

A cursory comparison of the size-frequency data at the crater suggests the power law exponent may be different than that for ejecta observed around some experimental explosion craters. For example, less than 25% of the ejecta mass is in the 3 largest phi intervals (smallest grain sizes) at the ~230 m diameter Pre-Schooner II crater (Frandsen, 1967), compared to the 50% reported for Meteor Crater by Shoemaker and Kieffer (1974).

A careful examination of bedding features within the *in situ* Kaibab beds below and the Kaibab debris here on the crater rim can be used to demonstrate that the debris is largely overturned, although we will not take the time to repeat this exercise. It is, however, worth noting that additional rotation of some blocks can produce diverging orientations. We will be discussing other details of the ejecta blanket later in the excursion.

Additional Views of Crater Interior

Approximately mid-way to the fence line in the southeast corner of the crater, it is worthwhile to stop and re-examine the crater interior from this perspective. In the foreground, slightly south of our present position, we see that the Kaibab continues to sandwich red Moenkopi along the east wall of the crater (Fig. 17.8). All three members of the Kaibab are visible below the Moenkopi. The uplifted and outward dipping orientations of those strata are also clearly visible here. Keen-eyed observers may also spy small thrust faults in the Kaibab-Alpha.

Sweeping our gaze around the crater towards the south crater wall, we see that the Kaibab is truncated against a large tear fault (Fig. 17.9). This is the same section we examined earlier from our perspective on the north crater rim (Fig. 17.1 and 17.6). The Kaibab is uplifted much higher on our side of the tear fault. That additional uplift provides the best exposure of the Coconino Fm in the walls of the crater. Beyond the tear fault, all three members of the Kaibab can be traced across the face of the southern cliffs.

Looking across the crater to the west, we see the same simple Kaibab-Moenkopi-ejecta stratigraphic sequence repeated (Fig. 17.10). The lower crater walls are covered with Pleistocene talus, so very little exposure of the Toroweap and Coconino Fms are found there. Barringer Point is one of the highest points along the crater rim. From this vantage point, the anticlinal nature of that feature and underlying thrusts in the Kaibab-Beta are visible.

Remnants of mining operations are visible on the crater floor. White patches of disturbed debris mark the locations of several shafts and boreholes. The top of the Main Shaft is enclosed in a large fence, as is the nearby Shaft #3. The top of the East Shaft is covered. This shaft was crudely cribbed and has been used in the past for studies of the crater's subsurface. That is, for example, the source of the pollen being used to reconstruct the environment at the time of impact (Chapter 13). Collectively, the shafts reveal that ~30 m of lake sediments sit on top of an impact breccia lens. The breccia lens is ~175 m thick and was produced when the excavation flow stopped and remaining allogenic breccias along the transient crater wall collapsed. At the time of impact, the water table was within the Coconino, so artesian spring flow filled the crater with a small lake. As the climate became arid ~11,000 yrs ago, the lake dried and a small amount of playa sediments were deposited. Silica Hill is a small knoll on the crater floor with the highest level of lake sediments. Shoemaker and Kieffer (1974) hypothesized that the knoll of lake sediments is on top of a topographic high or "central peak" that formed when allogenic breccias collapsed.

Kaibab, Toroweap, and Coconino Ejecta on Crater Rim

In the east-southeast portion of the crater rim, one finds an immense block of uncovered Kaibab ejecta (Fig. 17.11) that Barringer called Monument Rock. The block is often called House Rock today. We approach this boulder from the north. We want to walk past the rock, turn around, and look at it from the south for the best view. While standing next to the rock, it is usually a worthwhile exercise to

imagine the energy necessary to excavate it from the crater, carry it upwards, and deposit it many meters beyond the crater rim. The block, however, is only one among countless numbers of blocks that were excavated, form a blanket of debris that was ~20 m thick on the crater rim, and that stretches from the rim of the crater to distances in excess of a kilometer. The enormity of the energy involved in crater formation often begins to become tangible at this location. This is also a region where some of the most heavily-shocked Canyon Diablo specimens were recovered (*e.g.*, Heymann *et al.*, 1966), including diamond-bearing meteorites that Nininger (1956) and Moore *et al.* (1967) found to be concentrated on the crater rim and virtually absent on the distant plains. See Chapter 9 for additional details.

While at Monument Rock, let's also pause for a moment to discuss a couple of features that astronauts encountered in the impact-cratered terrain of the Moon. Monument Rock is often called House Rock for two reasons. First, from the observation platform at the museum, there is a telescope trained on the rock labeled "house-size rock." Second, and more importantly for our discussion, it is reminiscent of House Rock at North Ray Crater, which was explored by John Young and Charlie Duke during the Apollo 16 mission. North Ray Crater is similar in size to Meteor Crater, ~1 km in diameter, although it is older and suffered more (and different types of) erosion (Fig. 17.12). On the southeast side of the crater, there is a large rock that the astronauts called House Rock (Fig. 17.13). The astronauts approached the rock, but, because of the steepness of the slope, they were unable to reach it. Nonetheless, it is a memorable feature in a memorable mission and has lent its name, at least informally, to Monument Rock.

This is also a good point to consider how impact cratering has affected the landscape. Here, in northern Arizona, the impact crater is an isolated feature. One can look in all directions and not see another impact crater. The uniqueness of Meteor Crater is misleading. One might conclude, wrongly, that impact cratering is a minor geologic process. On Earth it may seem to be a minor process, but that is simply because Earth is such a dynamic geologic planet that other processes (*e.g.*, erosion, sedimentation, volcanism, plate tectonics) constantly destroy evidence of impact cratering. If we go back to the Apollo 16 landing site, we would find North Ray Crater in a field of impact craters (Fig. 17.12D). Two craters of nearly the same size, Kiva and Ravine, are immediately adjacent to North Ray Crater. Imagine that scene here: if, while standing on the rim of Meteor Crater, we could see two other impact craters of similar size and, moreover, a surface covered with hundreds to thousands of smaller impact craters. It is clear the Moon provides a better record of impact cratering than does the Earth.

A short distance south of Monument Rock we encounter additional mounds of impact debris (Fig. 17.14). The character of the debris changes, however. The trail crosses or passes adjacent to sandstone debris. This is our first encounter with sandstone from the Toroweap and Coconino sandstones that underlie the Kaibab Fm. This material was excavated from a pre-impact depth of at least 80 m.

This material, and another patch of sandstone on the north rim, intrigued Barringer and his colleagues with the Standard Iron Company. He describes them as impact-ejected rays of material. He was essentially describing what we now understand to be heterogeneities that can develop in ejecta blankets, leading to hummocky ejecta blankets and concentrated rays of ejected debris. In some cases, however, a transition from Kaibab to Coconino debris can reflect erosional remnants of ejecta that were deposited on a topographically variable surface that was created by tear faults in the underlying crater walls. A clear map identifying the source of this type of ejecta patchiness has not been developed in past studies. An example of the first source of the patchiness, however, is visible on the north rim. Although we will not visit that locality on this excursion, it is illustrated in Chapter 8 (Fig. 8.4).

Tear Fault in Crater Wall

If we continue south on the rim trail and pass through a gate in the fence line, we encounter additional Coconino- Toroweap ejecta. Coconino and Toroweap lithologies are not easily separated in these deposits and were mapped together by Shoemaker. We will stop near a winch (Fig. 17.15) that was used to haul supplies to and from the crater floor during mining operations. It is a nice historical reminder of original focus of exploration activities at the crater and the impetus for understanding the structure's origins. The winch sits above the tear fault that is responsible for the dramatic off-set in the Kaibab-Gamma Mbr that we viewed from the north and east rims of the crater (Fig. 17.1 and 17.6). A tremendous amount of fault gouge is visible in a ravine below the rim that continues nearly all the way down to the crater floor. The structural complexity of the crater rim along tear faults will also be visible. A number of small faults, one of which may reflect the partial collapse of the crater rim, is visible in the flank of the ravine. In my previous edition of this guidebook, I wrote that a detailed structural map of this section of the crater wall and rim is still needed, with an interpretation of the kinematics implied by those structures. An undergraduate student accepted that challenge and prepared a short report (Denton and Kring, 2016), the results of which are illustrated in Figs. 18.18 and 19.13.

This is also a useful vantage point for peering again at the northwest “corner” of the crater. That “corner” is also cut by a large tear fault. Slightly west of that tear fault the crater rim rises to Barringer Point. The thrusts in the Kaibab-Beta that underlie the anticline are sometimes easier to see here (Fig. 17.16) than from the stop earlier on our excursion.

From this point, we want to retrace our steps through the gate. When we reach Monument Rock, we will descend the crater wall in a diagonal line towards the north, until we reach outcrops of Moenkopi.

Fold Hinge in Moenkopi

Erosion and the angle of light hitting south-facing slopes makes a study of folds in the overturned rim sequence easier on our return hike. A good example of a hinge within the Moenkopi is visible on the slope north of our position (Fig. 17.17). The Moenkopi core is enveloped by a fold in Kaibab, whose apex is in the sky. Once the hinge has been located, we will walk to it. Please be careful when approaching the hinge. The fissile Moqui shale is fragile and we want to avoid damaging it so that its orientation will be apparent to future visitors. We also do not want to dislodge any of the adjacent blocks of vertical to near-vertical Kaibab limestone.

In the immediate vicinity of the Moenkopi hinge, we can see that the Moqui core is surrounded by blocks of Wupatki, which is, in turn, surrounded by blocks of Kaibab-Alpha. As illustrated in a schematic diagram in Chapter 7 (Fig. 7.2), the units are both structurally and stratigraphically overturned.

Hinges in the Moenkopi are not everywhere visible around the crater. Indeed, in some sections of the crater wall, the Moenkopi is not exposed because it lies encased within folded Kaibab. Erosion after the impact has cut into the overturned sequence, however, and occasionally exposed Moenkopi cores. This is illustrated schematically in Fig. 7.4.

Next we want to hike uphill and return to the trail on the crater rim.

Kaibab Ejecta beyond the Crater Rim

We return to the trail in the midst of a Kaibab boulder field that extends outward from the crater rim towards the surrounding plain (Fig. 17.18). Although this material was visible on the hike out, it is easier to appreciate with the sun behind us.

This is one of two boulder fields that impressed Barringer. The other boulder field sits on the west flank of the crater and contains the charismatic Whale Rock. The symmetry of these boulder fields is one of the reasons he favored a north to south trajectory for the impacting asteroid.

Beyond the immediate boulder field, one can also see isolated mounds of debris that are often pinnacled by a large block of Kaibab (Fig. 17.19). These features accentuate the hummocky topography of the ejecta blanket. In a larger impact event, ejected boulders like those visible will produce secondary craters.

We continue our return trek to the museum along the rim trail.

Fold Hinge in Kaibab

As we begin to turn the “corner” along the crater wall, another fold hinge is visible (Fig. 17.20). In this case, the fold hinge occurs in Kaibab, rather than Moenkopi. Beds on the lower limb of the fold have vertical dips. Tracing those beds around the hinge, they become increasingly overturned. Beds on the top of the slope mirror perfectly the beds on the lower limb and are clearly inverted or upside down. Within the Kaibab fold is a pale red core of Moenkopi. Erosion has barely reached that level, so very little of the Moenkopi is visible. Nonetheless, it nicely illustrates how Moenkopi is sandwiched within the overturned Kaibab sequence.

Breccia Deposits and Pleistocene Talus on Crater Walls

En route to the museum, we will have several opportunities to view the interior face of the crater’s north wall. Breccia deposits and post-impact alluvium are easily seen, particularly when highlighted by shadows in the late afternoon (Fig. 17.21). The upper portion of the crater wall is composed of near vertical cliffs. The lower 2/3 of the wall, however, has a much shallower slope. Those slopes are defined by Pleistocene talus, but they have a core of allogenic and fall-out breccia. Lechatelierite and meteoritic debris is included within the fallback breccia. Large blocks of debris that slid with the allogenic breccias towards the crater floor during the modification stage can also be seen along the crater wall. Authigenic breccias along shear planes within and at the base of those blocks can be found when examined more closely. Ravines with a fairly regular spacing cut through the fallback and allogenic impact breccias. Although that provides for good exposure of the breccias, erosion along the ravines is slowly destroying the deposits.

Hopi Buttes

Before climbing over Moon Mountain and returning to the museum, one has a good view of the Hopi Buttes northeast of the crater (Fig. 17.21). If we begin our scan directly to the east, we are peering towards the Painted Desert, which is dominated by the Chinle Fm, which sits on top of the Moenkopi Fm. Towards the north, sequentially younger Jurassic and Cretaceous strata are found. The highest and most-

distant mesas towards the northeast are capped with Cretaceous bedrock, which records the recession of the Cretaceous Seaway that once cut through the middle of North America, connecting the Gulf of Mexico and Arctic Ocean. Many of the mesas and buttes towards the northeast are carved from the sandstones and shales of the Jurassic-Cretaceous sequence. However, a large number of the buttes are, instead, Tertiary diatremes, which are called the Hopi Buttes. These diatremes contain fragments of the mantle, lower crust, middle crust, and the sediments that encompass them, providing a fascinating cross-section of the Earth. Despite the diatremes' similarities to kimberlites in South Africa, they do not contain any diamonds. Those are only found in the shock-metamorphosed specimens of Canyon Diablo found here on the rim of Barringer Crater.

Unfortunately, samples of those meteorites and related shock-metamorphosed target rocks are not found (or no longer found) on the rim of the crater. They are, however, displayed in the museum and I invite everyone to examine them there.

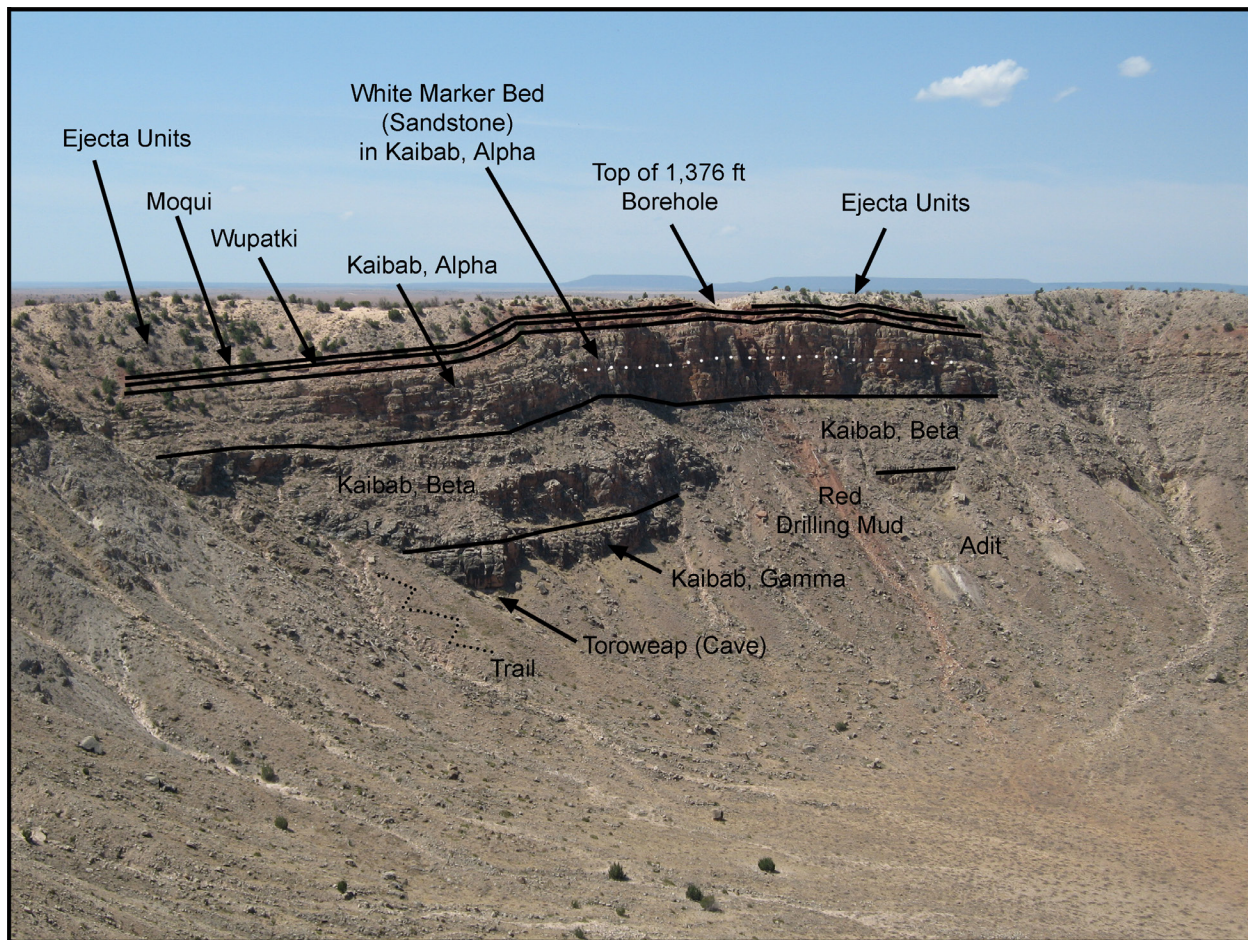


Fig. 17.1. Stratigraphy of the upper crater wall, as viewed towards the south. Target units shown are the Toroweap Fm, Gamma Mbr of the Kaibab Fm, Beta Mbr of the Kaibab Fm, Alpha Mbr of the Kaibab Fm, Wupatki Mbr of the Moenkopi Fm, and Moqui Mbr of the Moenkopi Fm. The Coconino Fm is not visible in this particular exposure (but is visible in the southeast corner of the crater). The position of a white marker sandstone bed in the middle of the Alpha Mbr of the Kaibab Fm is shown with a dotted white line. Ejecta from the target lithologies is visible on top of the Moenkopi beds. Also visible is the top of a 1,376 ft deep borehole through target lithologies on the south side of the crater. That borehole encountered fractured rock with meteoritic debris. See Chapter 4 for details.



Fig. 17.2. Museum or Moon Mountain thrust faults. Thrust faults within the Kaibab-Alpha duplicate part of the section, generating a wedge of material that creates an anticline and additional uplift of the crater rim. The thrust fault can be traced using the yellow vuggy dolomite unit within the Kaibab-Alpha (top panel). The wedge of material injected beneath the anticline is ~15 m across (bottom panel). The thrust fault was mapped by Shoemaker (1960) and described by Shoemaker and Kieffer (1974).



Fig. 17.3. View of outward-dipping beds in the wall of the crater and a thrust fault that cuts across a slope of Kaibab-Alpha towards the west. The yellow vuggy dolomite marker bed is visible in the upper plate (upper right of image) and the white marker sandstone bed is visible in the lower plate (lower center of image). The fault continues beyond the field of view and continues to cut down the slope beneath the observation deck of the museum complex.

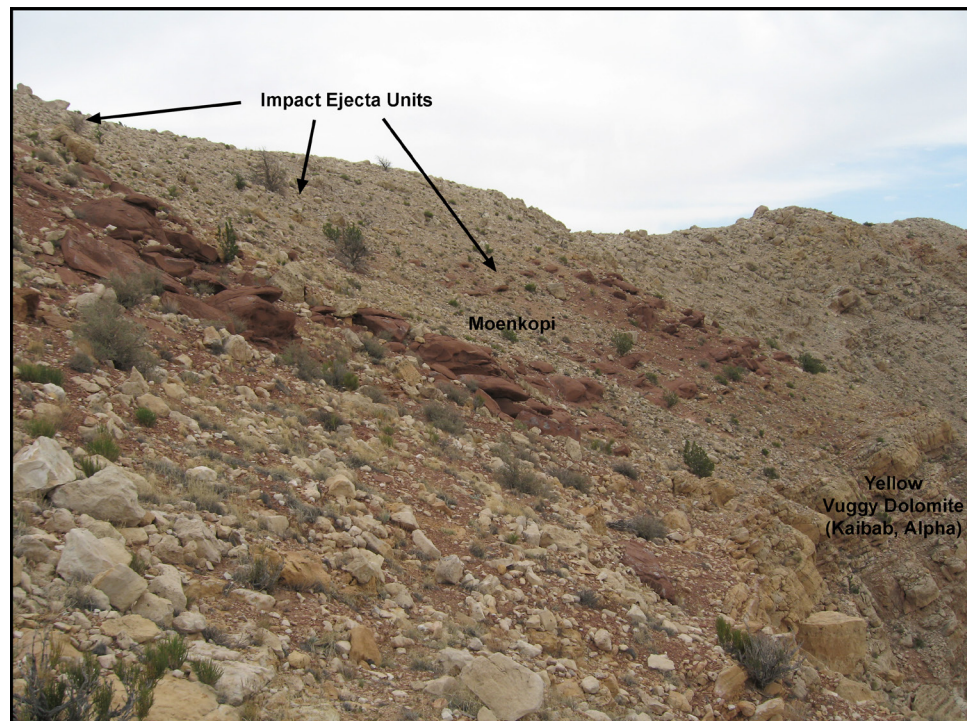


Fig. 17.4. A sequence of Moenkopi units with cross-bedded laminae that can be used to demonstrate the overturned sequence that characterizes the ejecta units at the crater. In this particular view to the east, the stratigraphic sequence begins with normal Kaibab-Alpha (including the yellow vuggy dolomite marker bed), normal Moenkopi, overturned Moenkopi, and overturned Kaibab at the top.

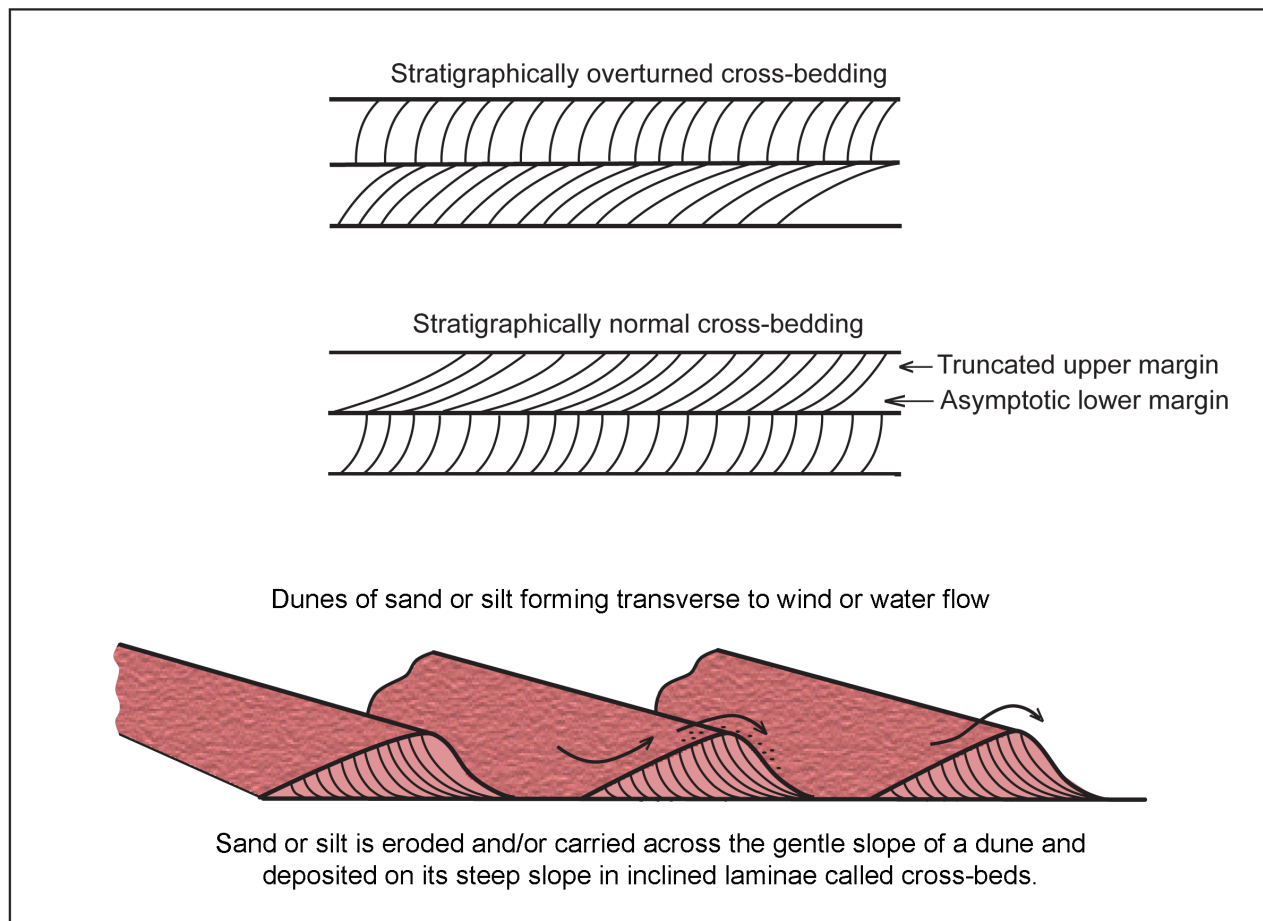


Fig. 17.5. Schematic diagram illustrating the formation of cross-bedded laminae in the Wuptaki Member of the Moenkopi Formation. The geometry of the cross-bedded laminae can be used to determine the orientation of the Moenkopi strata in the rim of Barringer Crater. When the strata are in their normal orientation, the cross-bedded laminae asymptotically approach the lower margin of each set and are truncated at the top of each set. In the overturned part of the crater rim, the truncated margin of a set is below the asymptotic margin. This is an illustration of simple cross-bedding. Within the Moenkopi one can find more complex forms of cross-bedding (like trough cross-bedding), which can also be used to determine the orientation of strata. However, some silt was deposited in higher velocity currents, producing horizontal laminae. In these cases, one has to find other geopetal features (like mud cracks) to determine the orientation of strata.

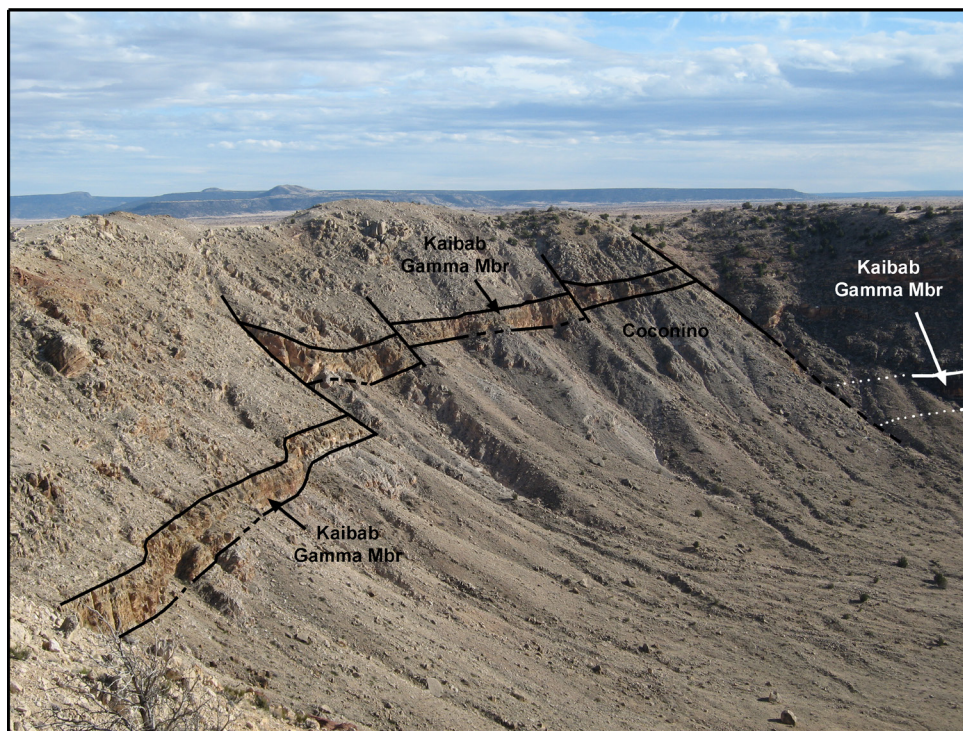
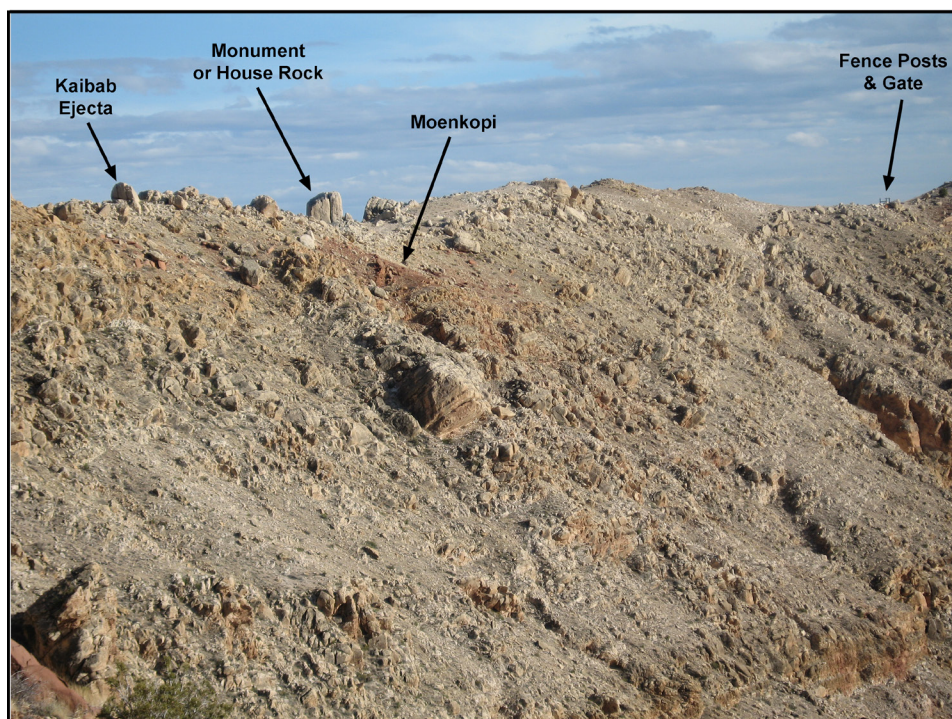


Fig. 17.6. View towards the southeast corner of the crater. The Gamma Mbr of the Kaibab Fm is outlined to help show tear fault displacements along the east crater wall. A very large displacement occurs in the southeast corner of the crater. On this side of that large tear fault, the Coconino Fm is visible. It is the thickest sequence of Coconino exposed in the crater wall. The crater wall farther to the west (right) is shown in Fig. 17.1.

Fig. 17.7. Zooming in on the east rim of the crater, one can spy Monument Rock within a boulder field of Kaibab ejecta that was deposited above normally-bedded and overturned Moenkopi. We will be hiking along the crater rim and will eventually stop within that boulder field. We will then continue towards the south and turn around near the fence posts and gate. We will backtrack along the inner crater wall.



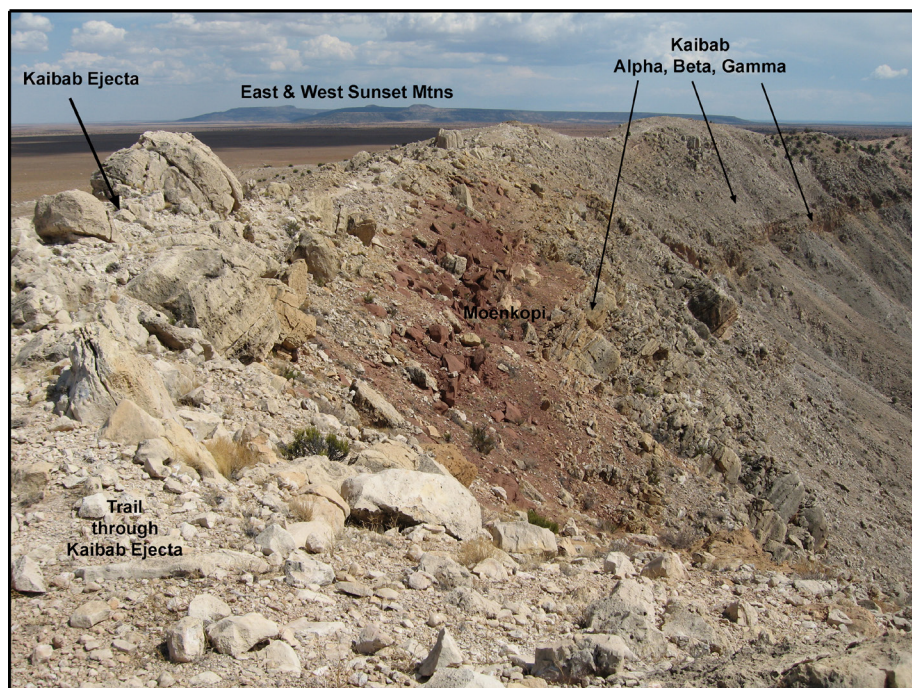
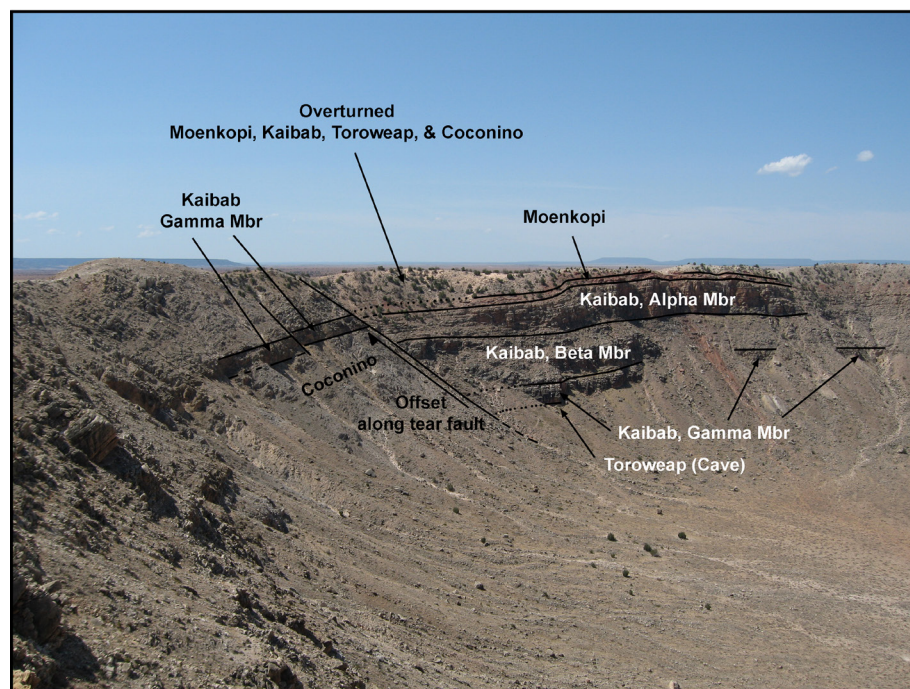


Fig. 17.8. View of upper crater wall from a trail along the rim of the crater. The trail is winding through Kaibab ejecta. Lower on the crater slopes, one can see the outward dipping normally-bedded strata of the Kaibab Fm, including all three members of that formation (Alpha, Beta, and Gamma). If one looks carefully, small thrust faults that thicken the Kaibab sequence will be visible from this location. The bedded and ejected Kaibab units sandwich the red Moenkopi. Farther to the south, the Quaternary volcanics of East and West Sunset Mountains are visible.

Fig. 17.9. This is a closer view of the stratigraphy and one of the fault displacements that were previously seen in Fig. 17.1 and 17.6. The total displacement along the tear fault is more than 45 m. On this side of the fault, ~90 m of the upper Coconino Fm are exposed.



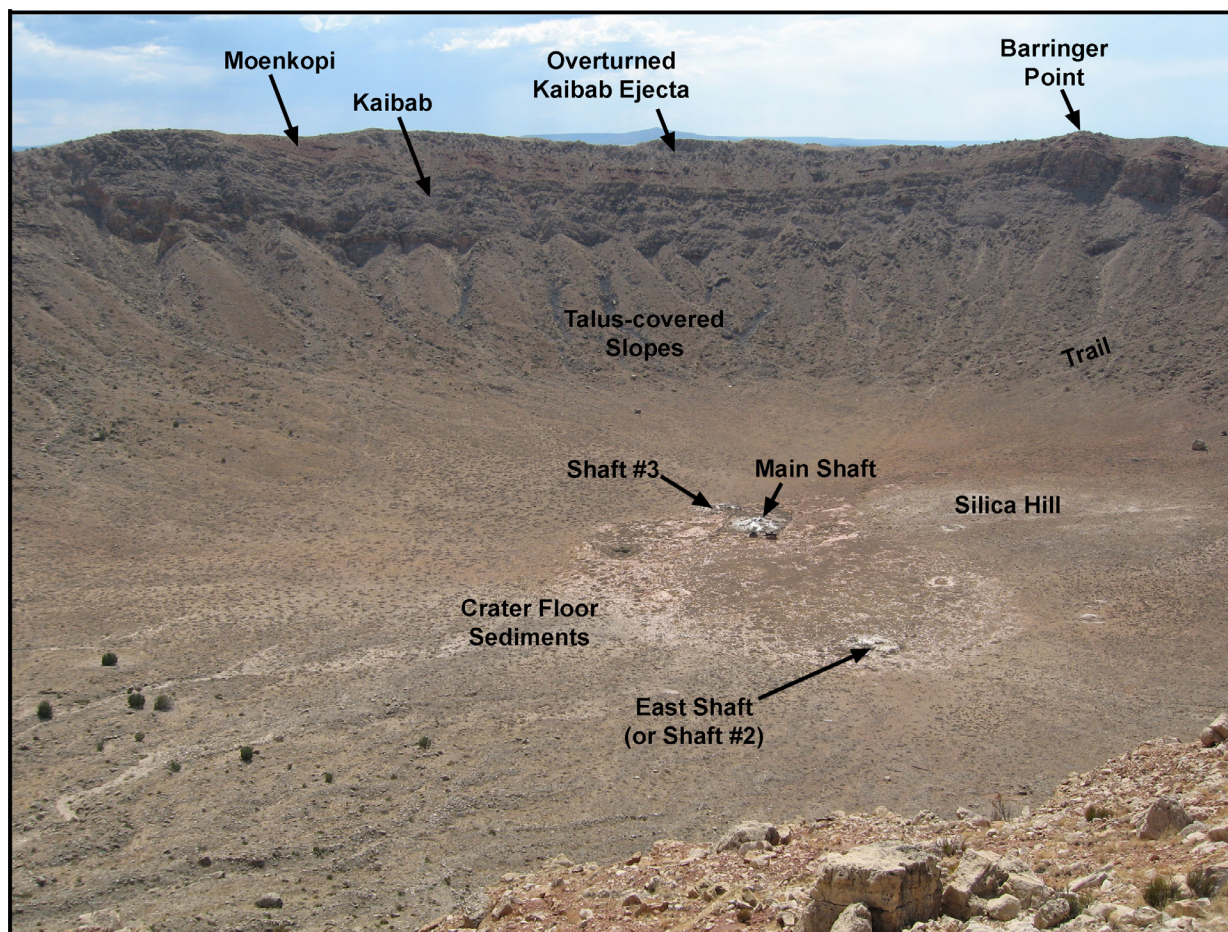


Fig. 17.10. View of the west crater wall and the crater floor from the trail on the east rim of the crater. The stratigraphy of the upper west crater wall is similar to that on the east crater wall. The highest point along the rim of the crater is visible on the horizon. Thrust faults have thickened the Beta Mbr of the Kaibab Fm beneath Barringer Point, creating an anticline. A trail from the northwest crater rim to the crater floor traverses talus-covered slopes. On the floor of the crater, one can see a topographic high (Silica Hill) surrounded by playa sediments. Several exploration shafts were sunk into the crater floor, three of which are identified in the image. The Main Shaft and East Shaft penetrated ~30 m of lake sediments, ~10 m of fall-back breccia, and bottomed in an ~175 m thick allogenic breccia lens that is dominated by blocks of Coconino sandstone, including one slab with an area of 20,000 square meters.



Fig. 17.11. Monument or House Rock is one of the largest boulders that is visible in the ejecta blanket. It is a large block of Kaibab within a boulder field of ejected Kaibab. A small, dark green tree is growing at the base of the rock in the foreground. Over 7,000 metric tons of rock are exposed in the block above erosional surface at the base of the exposure. This is one of the blocks used to determine a cosmogenic exposure age and, thus, an approximate age for the crater. (See Chapter 12 for details.)

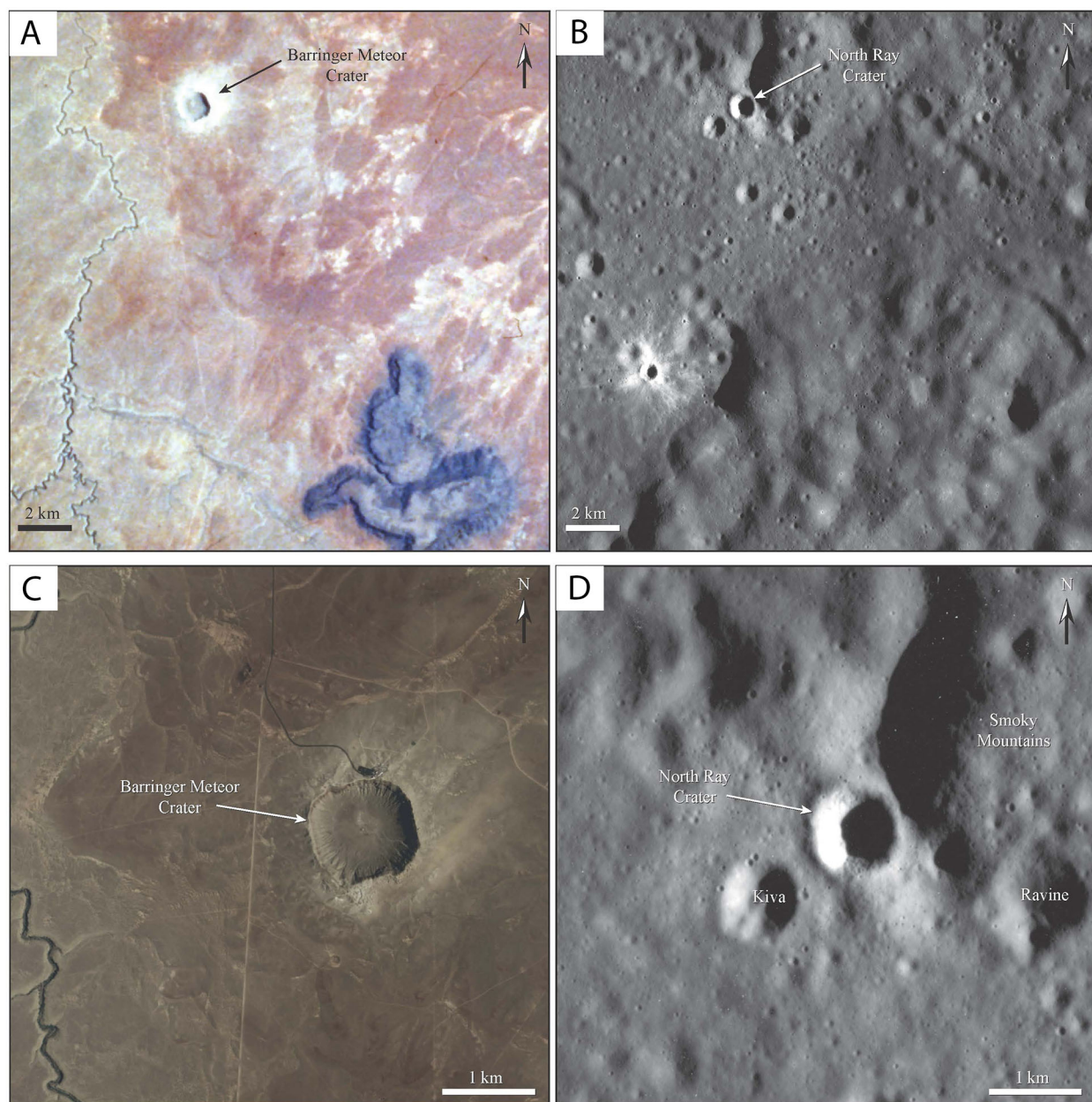


Fig. 17.12. Comparing the ~1 km diameter Barringer Meteorite Crater in northern Arizona with the ~1 km diameter North Ray Crater at the Apollo 16 landing site on the Moon. (A) Barringer Meteorite Crater region, with the sinuous Canyon Diablo to the west and the dark basaltic West Sunset Mountain to the southeast. Scale bar is 2 km. Space Shuttle Columbia image STS 040-614-058). (B) Shown at the same scale is the Apollo 16 landing site with North Ray Crater. South Ray Crater is a younger, bright-rayed crater to the southwest. Apollo Image Atlas AS16-P-4558). (C) Barringer Meteorite Crater stands alone in this USGS photograph. Scale bar is 1 km. (D) Shown at the same scale, North Ray Crater is adjacent to Kiva and Ravine craters, both of comparable size. Apollo Image Atlas AS16-P-4558. As one gazes from the rim of Barringer Meteorite Crater, imagine a landscape with two additional craters of comparable size and countless numbers of smaller impact craters. I thank Celeste Mercer for collating these images for one of our training exercises at the crater for postdoctoral researchers.

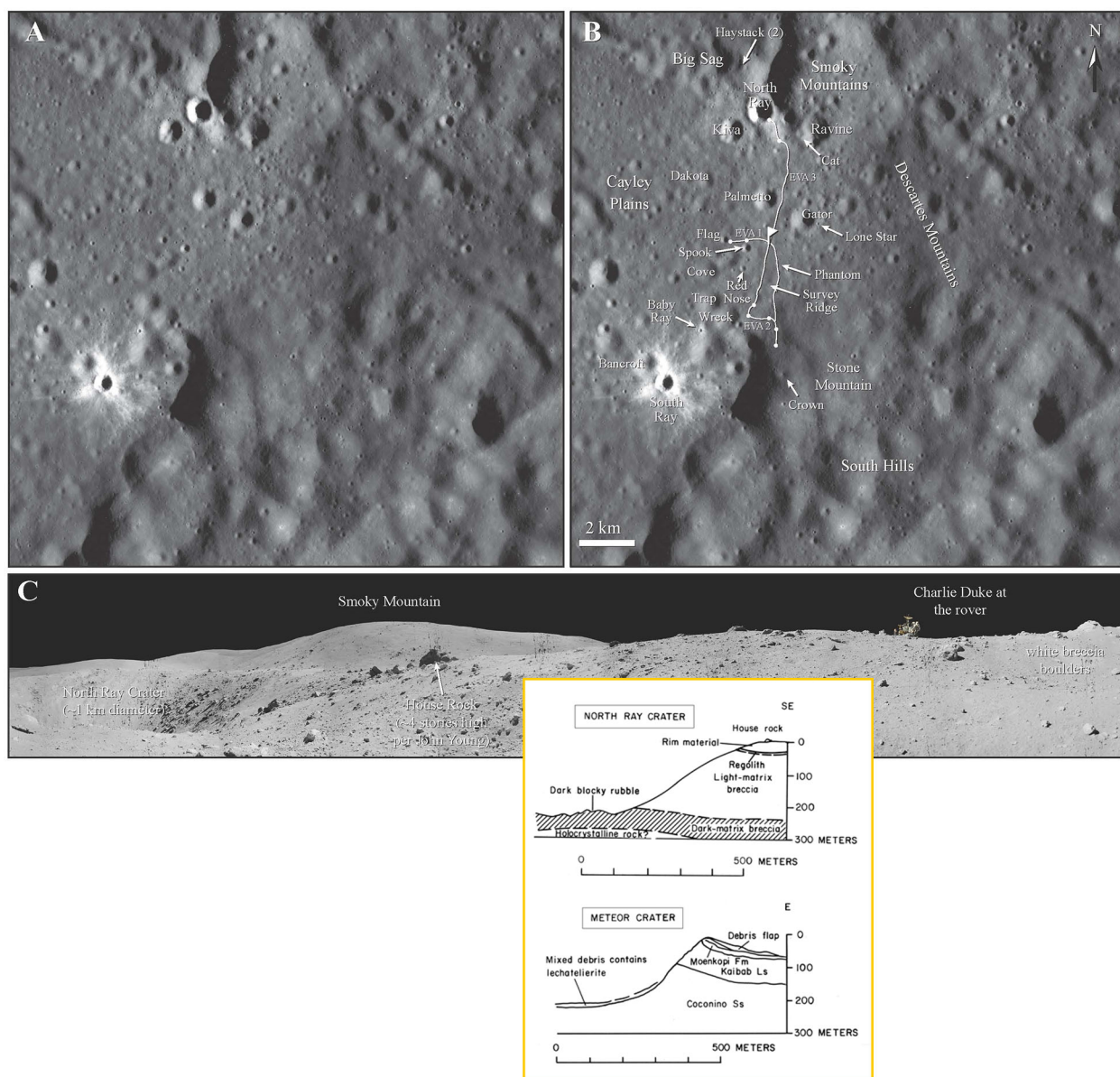


Fig. 17.13. Comparing the ~1 km diameter Barringer Meteorite Crater in northern Arizona with the ~1 km diameter North Ray Crater at the Apollo 16 landing site on the Moon. (A) The Apollo 16 landing site with North Ray and South Ray craters. Apollo Image Atlas AS16-P-4558. (B) The traverse that the Apollo 16 astronauts implemented (modified after Stooke, 2007). (C) A ground-level view taken by astronauts from Apollo 16 station 11 at North Ray Crater. NASA image JSC2007e045381. House Rock is labeled near the rim of the crater. The inset shows a cross-section of the rim of North Ray Crater, with the location of House Rock, and a similar cross-section of Barringer Meteorite Crater (a.k.a. Meteor Crater) at the same scale. I thank Celeste Mercer for her help obtaining digital copies of the photographs.

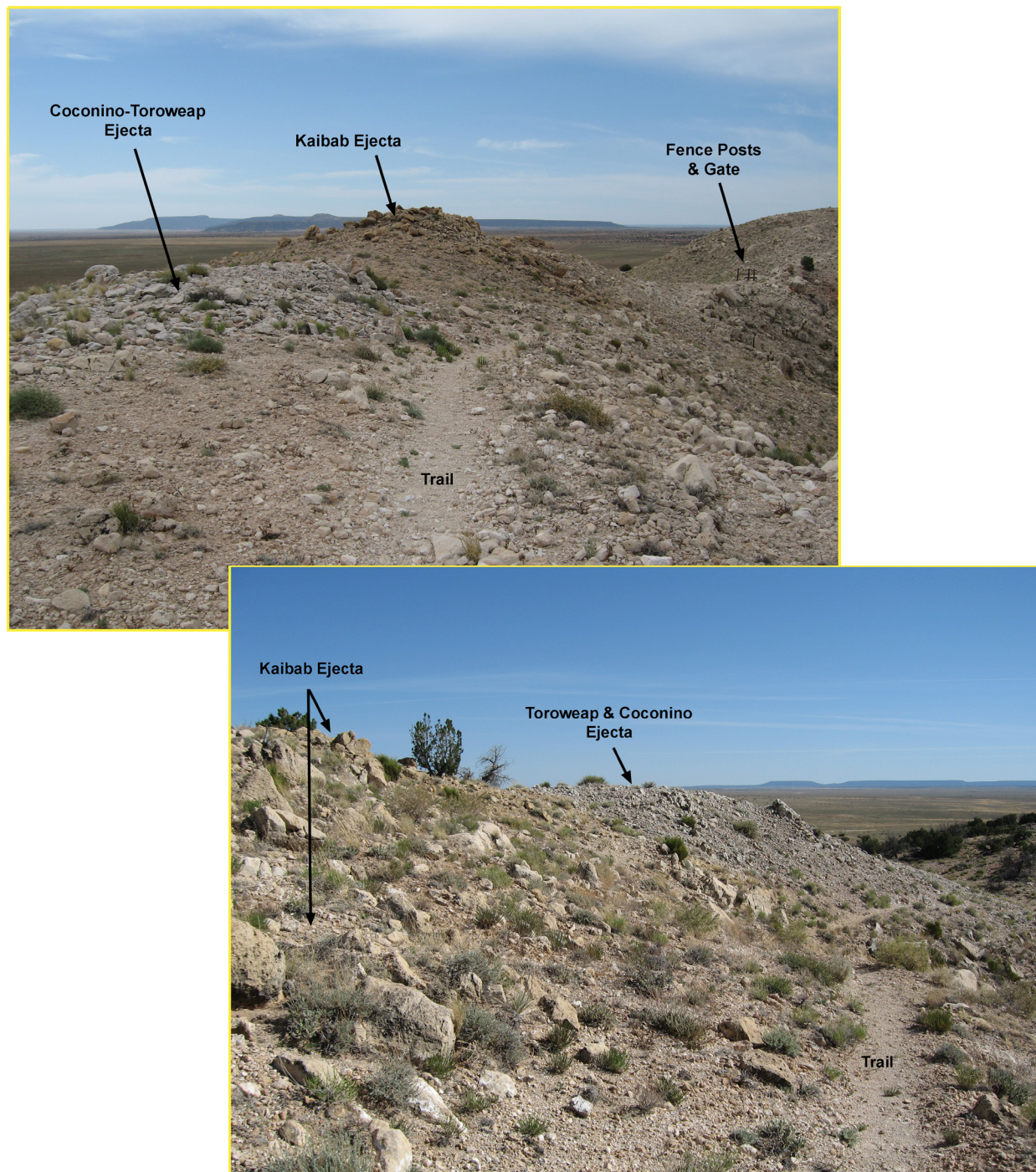


Fig. 17.14. Trailside outcrops of co-mingled Kaibab and Coconino-Toroweap ejecta deposits. The Coconino-Toroweap deposit was first mapped by Barringer (1910) as a ray of debris. There are two potential sources for this type of juxtaposition: (a) Coconino debris fills depressions in a hummocky surface on the ejected Kaibab debris unit (as shown in Fig. 8.4) or (b) material drapes a rim sequence with differential uplift (*e.g.*, on either side of a tear fault), which may be modified further by differential rates of erosion (as shown in Fig. 7.4).



Fig. 17.15. A winch on the crater rim is a reminder of the mining exploration that once occurred at the crater. This winch was probably mule-driven and transported supplies down a slide raised above the rocky crater wall below. The winch is at the top of a large tear fault in the crater wall and rim (which is not visible in the photograph). In the middle distance, one can see blocks and mounds of Kaibab ejecta.

Fig. 17.16. View from southeast crater “corner” of the Barringer Point anticline in the west-northwest portion of the crater wall and rim. Thrust fault(s) within the Kaibab-Beta have thickened that part of the sequence, creating additional uplift of the overlying Kaibab-Alpha, Moenkopi, and ejected debris. Barringer Point is one of the highest topographic points on the crater rim.

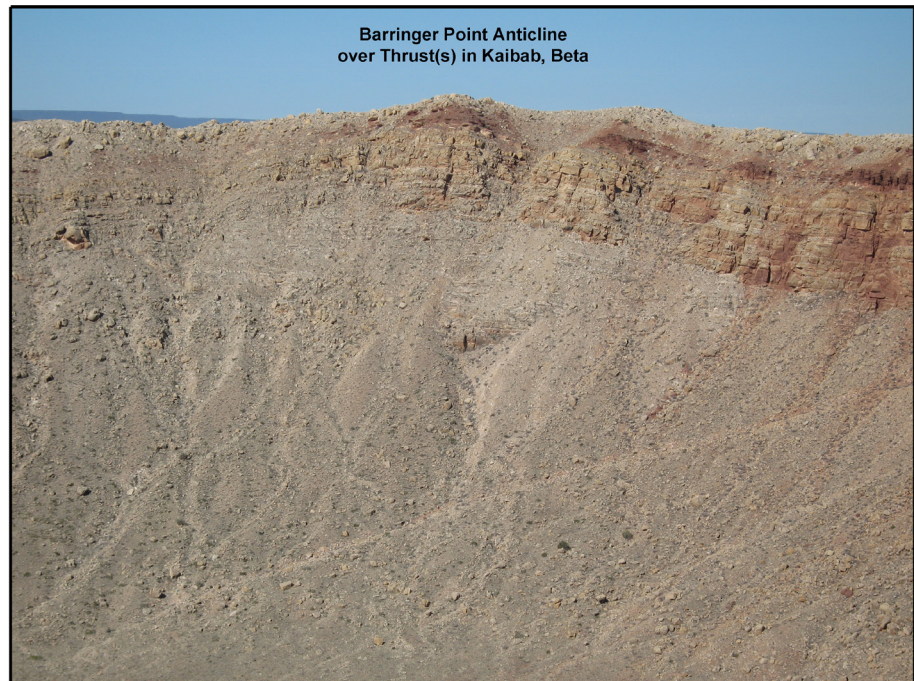




Fig. 17.17. Structurally and stratigraphically overturned Kaibab and Moenkopi, with an exposed hinge within the Moenkopi. Crater center is to left and the ejecta blanket lies beyond the top of the crater rim on the right. As can be seen in the lower left (above), the crater wall rocks have been uplifted so that they have an outward dipping slope. The top of the Kaibab reaches near vertical dips. The hinge within the Kaibab is eroded, but a trace of the fold is indicated with a dashed line. At the upper far right, the Kaibab is overturned. Within that Kaibab fold is a Moenkopi fold. Erosion has exposed the hinge in the Moenkopi fold. The location of the hinge within the overturned rim is shown above and a close-up of that hinge is shown to the right. The hinge is visible within the fissile Moqui Member of the Moenkopi. The orbicular Wupatki Member is visible between the Moqui and Kaibab (right).



Fig. 17.18. A field of Kaibab boulders is strewn across the east flank of the crater. Finer-grained ejecta has probably been eroded from the ejecta blanket, exposing larger blocks within the shattered and overturned sequence. Subtle mounds of additional ejecta are visible in the middle distance, including a mound of Coconino-Toroweap debris (near bushes and a pole in the upper left corner).

Fig. 17.19. A mixture of large blocks and finer-grained debris within the ejecta blanket is accentuated among the erosional remnants of distant mounds of Kaibab ejecta. The light-colored soil in the fore- and middle-ground is dominated by Kaibab detritus. A transition to red Moenkopi-derived material is visible in the distance.





Fig. 17.20. Uplifted and overturned portion of the Kaibab Formation in the crater rim. In a context view (above), the dip of Kaibab in the upper crater wall is near vertical (e.g., left side of image). It is then overturned (center and upper right). Erosion has exposed the fold hinge. Thomas Kenkmann and Michael Poelchau appear for scale in a close-up view of the core of that fold hinge (right).

Fig. 17.21. Impact debris coats the interior wall of the crater (right). Within the shallower-sloping deposits on the lower crater walls, an allogenic breccia is draped over bedrock. The allogenic breccia is draped, in turn, by fall-out breccia. Both are mantled by Pleistocene talus that eroded from the steep upper crater walls. The allogenic breccia is dominated by Coconino and Kaibab debris, whereas the fall-out breccia has a large Moenkopi component. Lechatelierite and meteoritic debris are found within the fall-out breccia. A final view towards the northeast (below) reveals the Hopi Buttes and several mesas. The mesas are carved from Triassic, Jurassic, and Cretaceous sandstones and shales. The Hopi Buttes are the erosional remnants of Tertiary diatremes.



18. Trail Guide 2: Crater Rim West



While this trail guide traces the western route from the south side of the crater to the north side of the crater, most of the field stops will be on the south and southwestern sides of the crater. The south side of the crater provides an outstanding set of clues about crater excavation and emplacement of ejecta, both in the continuous ejecta blanket and fallback breccia that covered it, that were not recognized until recently. Many of these clues were documented by graduate students participating in the Field Training and Research Program at Meteor Crater over the past decade. Their work is gratefully acknowledged.

1,376 ft Deep Borehole

Units of the crater rim were exposed when a 1,376 ft-deep churn drill hole was drilled in 1920-1922. Although the outcrop is over 100 years old, the extraordinary nature of the outcrop was not recognized until recently (Kring *et al.*, 2011a).

Peering past the top of the churn hole, one can see the contact between the uplifted Kaibab and Moenkopi in the crater wall. The base of the Moenkopi is composed of 1.2 m of shale and 3.6 m of massive, cross-bedded siltstone of the Wupatki Member. Five meters of shaly siltstone of the Moqui Member follows. The stratigraphy is then overturned along an axial plane within the Moqui. The basal portion of the overturn Moenkopi is incomplete and represented, instead, by a 0.3 to 0.7 m-thick unconsolidated breccia that contains blocks of both Moqui and Wupatki lithologies (Fig. 18.1). That breccia is covered by a ~1.4 m-thick unconsolidated breccia of both Moenkopi and Kaibab fragments, and then intermittent blocks of lithified breccia, similar to the P-T boundary breccia in the normal stratigraphic sequence (*e.g.*, Fig 19.15). There is, however, no other Kaibab before being covered, in turn, by overturned Coconino and Toroweap. Approximately 80 meters of Kaibab is missing.

The loss of Kaibab from the rim sequence requires shearing to a more distant portion of the ejecta blanket and requires a pair of faults at the lower boundary of the overturned Coconino and Toroweap sandstone (Kring *et al.*, 2011a). The underlying mixed breccia wedge might then be interpreted as a fault breccia of a combination of ejecta and fault breccia. Shearing and faulting may not be quite the correct terms if the units were devoid of cohesion when separation of the Kaibab occurred. Nonetheless, the effective result is the displacement of Kaibab past both the Moenkopi and Coconino. Furthermore, the stratigraphic hiatus that it produced has the mappable attributes of faults.

The lack of Kaibab near the rim is confirmed in the DDH log for Meteor Crater Core #4 (see Chapter 2). That log records a sequence, from bottom to top, of dolomite, red sandstone, dolomite, and sandstone, representing target Kaibab, target and ejected Moenkopi, ejected Kaibab, and ejected Coconino. The ejected Kaibab is anomalously thin, reportedly <5.1 m and probably <2.4 m (Haines, 1966). I confirmed the thinness of that unit by examining the core, which is now curated at the USGS Astrogeology Science Center. Thus, the core indicates the Kaibab ejecta is also thinned to a distance of 10 m from the topographical crater rim and ~50 m west-southwest of the current field stop at the top of the 1,376 ft borehole.

If the Kaibab dolomite was sheared from the rim sequence on the south side of the crater, then it was displaced to greater radial distances. Interestingly, Roddy *et al.* (1975) reported that drilling into the ejecta blanket “shows the overturned flap is the thickest on the southern side of the crater where low hummocky hills composed of blocks of Kaibab lie as far as 1500 m from the center of the crater.” This is

consistent with field observations that suggest unusually large amount of Kaibab occurs lower on the ejecta slopes than elsewhere around the crater and that the topographic profile of the original ejecta deposit was less steep to the south. This displacement of Kaibab seen in the measured section appears to extend to distances of at least 50 m from the crater rim, because it is not visible in debris around a ~100-year-old exploration shaft that is located ~50 m south of this field stop.

We recently conducted a geophysical survey along a south-bearing transect from this location (Roy *et al.*, 2011). A 645 m 2-D single component seismic line was run radially outward. A total of 228 shots spaced 3 m apart were acquired using a truck-mounted Accelerated Weight Drop. This was the first reflection seismic study conducted at the crater. We also acquired a new set of p-wave velocity data on crater rock samples that augment those tabulated in Chapter 2. They, along with other details of the work, will be described in a paper still to be prepared. That geophysical imaging of the subsurface is consistent with the radial displacement of ejected Kaibab to larger distances than is inferred from geological observations at the crater.

Silica Pits, Extension of Overturned Ejecta, and Fallback Breccia

Note: It is essential that one enter the silica pits along an existing path. PLEASE do not walk along the east margin of the silica pit, as you could easily destroy critical evidence of ejecta emplacement. See the illustration with the trail guide routes; the silica pit should be entered from the south side.

Coconino ejecta is absent from most of the north, east, and west sides of the crater, but forms a continuous deposit on the south side of the crater. The details of its emplacement and internal structure received very little attention until recently. At two stops located in the vicinity of the silica pits, we can see how shock affected the unit, see that normal faulting was a factor in its extended distribution around the crater, and see that faulting had the secondary effect of preserving a small amount of fallback breccia.

From the top of the 1,376 ft borehole, we will follow the remnant of an old road to the west. Along the way, we will pass through typical Coconino ejecta (Fig. 18.2). Our first stop is a small pit on the north side of the road (Fig. 18.3). There is no need to step off the road into the pit. The key features are evident from the road. The pit exposes the interior of the overturned Coconino ejecta blanket. As can be seen, it is very bright white; *i.e.*, has a high albedo. Within the bright white unit are blocks of gray, normal-looking Coconino. Thus, as is so often the case with shocked rocks, we see the juxtaposition of rock affected differently by shock. The higher albedo portion of the unit has been crushed by shock. That is, quartz grains in the unit are fragmented. The additional reflective surfaces produced by the fragmentation are probably the reason for the higher albedo. Although the quartz has been shattered and the character of the rock obviously affected, you might note that the laminae of cross-bedding survives. As with all stops, this is a no-sampling location. Please do not disturb the exposed rock and features just described.

To reach our second stop in the main silica quarry, it is important to follow a specific path, shown on the photograph at the beginning of the trail guide section of this book, to avoid destroying the walls of the silica pit and key geological features in those walls.

Once on the floor of the silica quarry, we will focus our attention on the east wall. Here, the students in one of our Field Training and Research Programs carefully mapped the geology (Kring *et al.*, 2012), supplementing the thesis work of Gray (1977). The quarries expose ~5½ to 7½ m of monomict Coconino breccia, which is composed of rotated clasts of sandstone that is variably affected by shock;

some clasts are gray-colored and appear to be unaffected by the impact, except for minor fracturing, while the bulk of the material is less coherent, bright white, and microscopically deformed. The floor of the quarry does not reach the base of the Coconino ejecta. Three boreholes drilled ~20 m east-southeast of the quarry (Fig. 2.5) indicate the total thickness of the monomict Coconino breccia is 9 to 13 m at this distance from the crater rim.

As can be seen along the top of the quarry wall, the monomict Coconino ejecta is sometimes covered with a polymict breccia containing a chaotic assemblage (in order of abundance) of Kaibab, Moenkopi, and Coconino debris (Fig. 18.4-18.6). In four locations in the quarries, this polymict breccia forms the down-dropped hanging walls of normal faults. Strikes of the fault planes range from 80 to 105° (generally E-W) and dips are to the south. Three faults have standard normal fault dips (52 to 59°), while one is shallower (34°). The vertical displacement along two of the faults is at least 140 to 180 cm. The polymict breccia can be traced beyond the quarry wall in two elongate exposures that lie between outcrops of Coconino ejecta. These exposures imply the faults seen in the quarry walls extend east ~150 m parallel to the crater rim (Fig. 18.7). While Shoemaker mapped the material as alluvium, we suggest that it is fallback breccia. The faulting of the Coconino was likely a process that occurred during emplacement of the ejecta blanket, as it was an extensional process. Fallback breccia immediately covered the fault. Subsequent erosion of the surface of the ejecta blanket over much longer periods of time removed most of the fallback breccia, except for that portion protected in the lee of the fault scarp.

The preservation of fallback breccia beyond the crater rim is a relatively new concept and will require some adjustments to Shoemaker's map. In addition to these quarry deposits, several other polymict breccia deposits south of the crater rim are on topographic highs and likely have a similar origin as primary fallback breccia deposits (Kring *et al.*, 2012).

Elsewhere along the quarry wall the monomict Coconino ejecta is covered with a ~½ m-thick unit that has the characteristics of alluvium. The base of the unit has a series of rounded Kaibab cobbles that are covered by an assortment of small clasts of all three target lithologies. The clasts are aligned and imbricated. This unit cross-cuts one of the faults that juxtaposes the polymict breccia with the monomict breccia, indicating the deposition of the polymict breccia and the faulting preceded the deposition of this unit.

Please return to the rim trail via the same route used to enter the quarry.

Buildings

The western margin of the quarry was once covered with buildings needed to support the mining camp. Most structures have been removed, but two remain (Fig. 18.8). These wood-frame structures provided a home for those living and working at the crater. We ask that you respect the buildings and do not enter them. They are an important historical element of the crater.

Coconino Hinge

*PLEASE do not climb up the slope with the hinge described at this stop. The ejected and overturned sequence is composed of disarticulated strata that are still geologically young and, thus, not lithified or otherwise consolidated. **Even approaching the hinge can cause rock movement that would destroy the outcrop.***

Here we have the first (and only) hinge in the Coconino and Toroweap sandstones (Kring *et al.*, 2011b), which were the basal target units overturned and ejected onto the crater rim by the impact.

The structural relationships are exposed along a short road. At the east end of the outcrop, one finds the Wupatki and Moqui members of the Moenkopi Formation (*e.g.*, at the left edge of Fig. 18.9). As one begins to walk along the road towards the west (or right as seen in Fig. 18.9), those units are overlain by an overturned sequence, with the fold axis hidden within the shale-bearing Moqui. The overturned Moenkopi is followed by a breccia of Kaibab and Moenkopi. That sequence is then cut by a fault that juxtaposes those units with a hinge of Coconino and Toroweap sandstone (Fig. 18.10). The sandstone is thinly bedded like that found at the top of the sandstone section where it appears lower in the crater walls. Within the fold hinge is an abbreviated sequence of Kaibab sandy dolomite that is repeated five times in exposures along the road where it cuts through the crater rim towards the southwest (Fig. 18.9).

Hinges in overturned Coconino and Toroweap are not normally preserved, because they either collapsed to form the breccia lens on the crater floor or they were eroded from the upper crater wall soon thereafter. Indeed, the loss of that material was necessary to expose the hinges seen in Kaibab and Moenkopi (*e.g.*, as illustrated in Fig. 7.4) elsewhere around the crater (*e.g.*, Fig. 17.17 and 17.20). The Coconino and Toroweap hinge seen here must have been closer to the crater center during the excavation phase of the impact event and then faulted radially outward during the emplacement of the ejecta blanket. That motion requires up to 100 m of outward displacement during the emplacement of the ejecta blanket (Fig. 18.11). The displacement occurred along a fault that parallels the road, except towards the east where it cuts up across the upper crater wall (Fig. 18.9). That displacement is illustrated in Fig. 18.11. Towards the west, the fault approaches and is probably buried in a tear fault that shapes the southwest corner of the crater.

The faults that repeatedly cut through the Kaibab effectively thinned the unit in a radial direction from the crater center. The result is qualitatively similar to the displacement of Kaibab on the south side of the crater near the 1,376 ft-deep borehole. Thinning of the Kaibab (and other overturned units) is needed to form the continuous ejecta blanket, because it now covers an order of magnitude more surface area than it did before the impact. This is the first location, however, where a mechanism for that structural thinning is visible in outcrop. Evidence of extension was once also evident in a series of conjugate fractures in overturned Coconino along the rim trail nearby (Fig. 18.12). Sadly, somebody recently destroyed that outcrop, so it is no longer available for study.

This stop is the third location on this particular portion of the crater where extension of the ejecta has been observed. Here we see five normal faults in the Kaibab. At the top of the 1,376 ft churn hole, we saw dramatic shearing of the Kaibab to greater radii. A smaller example of extension was also discernable in the Coconino seen in the walls of the quarry. That type of extension clearly helped the ejected material cover a larger area around the crater. I suggest, too, that the extension is the source of hummocky topography in the ejecta blanket, producing blocks of Kaibab-rich material at variable distances around the crater. Thus, while hummocky topography around craters is sometimes described as a product of undefined instabilities in the ejecta curtain, the extension seen in these outcrops suggest it is

caused by simple structural extension of the overturned units, separating blocks of material along normal faults.

Potential Fold in Ejected Coconino

If we walk back towards the buildings, we will find a small trail that goes to the top of the hill with Coconino ejecta. On top of the hill, we will find an apparent fold in the alignment of Coconino sandstone (Fig. 18.13 and 18.14). There appear to be two limbs around a hinge. This feature may have caught Shoemaker's attention too, because there is a small, albeit unclear, mark on his geologic map at this location. Potentially the structure was produced when Coconino was overturned, ejected, and spreading over the landscape around the crater. Because the ejecta covers nearly an order of magnitude more area around the crater than it occupied within the crater, it was spreading radially and circumferentially. The structure here may capture both those movements, as illustrated schematically in Fig. 18.14. On the other hand, we need to be mindful that the Coconino has enormous cross-bedding. Thus, the apparent structure may be cross-bedding. This is a good location for discussion.

METCRAX Experiments

We return to the road along the trail. Before moving on, it is worth noting that this is the site where air flows over the crater rim into the crater late in the day and through the night. I refer readers to Chapter 16 for additional details.

Highest Point on Crater Rim

We immediately begin an ascent on the rim trail, which will take us to the highest point along the crater rim (Fig. 4.2). As we move up the trail, good views of steeply dipping Kaibab can be seen in the crater wall (Fig. 18.15). These units were uplifted adjacent to one of the tear faults that give the crater its square shape in plan view.

From the summit, one has good views of Canyon Diablo and Anderson Mesa ~3 and ~20 km to the west, respectively. Canyon Diablo is cut into the Kaibab Formation. It was the source of water when Daniel Moreau Barringer was conducting mining operations in search of asteroid fragments. A trace of a pipeline from the canyon to the crater can still be seen. Anderson Mesa is a Quaternary basalt complex. Potentially the mesa would have been a dramatic site from which to see the impact event. On the other hand, if the energy of impact was sufficiently high and/or the trajectory had a southwestern component, it may not have been a safe site to view the impact.

Fallback Breccia (or not)

As we approach Whale Rock, fragments of red Moenkopi shale and siltstone will appear on the ground adjacent to the trail (Fig. 18.16). The nearest outcrop of Moenkopi is inside the crater, in the crater wall, below the rim trail. Because the Moenkopi in that outcrop could not erode uphill and over the rim, the trailside Moenkopi must have some other origin. Like the polymict breccia along the top of the silica quarry wall, this material is likely fallback breccia or alluvium from a fallback breccia deposit that has seen only a few meters of transport. Because the material is virtually at the rim and would only move downhill if eroded, it clearly has not moved far if at all.

From this location, we also have a good view of two large boulders that were used to assess the age of the crater (Fig. 18.16). Those boulders were chosen because they may have been exposed at the top of the ejecta blanket when the crater formed or the first surfaces to be exposed early in the erosion of the ejecta blanket. The polymict breccia at our feet is a few meters below those two points. That may mean the fallback breccia filled in gaps between Kaibab (and overlying, now eroded, Coconino) ejecta, producing pockets several meters thick. Alternatively, as Coconino and Kaibab ejecta were eroded, remnants of fallback breccia, which was also being eroded, filled in. Shoemaker apparently preferred the latter, because he mapped the material as alluvium. If alluvium, the lateral transport was limited to a few meters.

Whale Rock and the West Boulder Field

One of the two boulders for which an age of ~50 ka was derived is called Whale Rock, because of its similarity in shape to the head of a whale (Fig. 18.17). It is also part of the west boulder field, which is roughly opposite the east boulder field. Also, the largest boulders represent the same pre-impact stratum: Whale Rock is from the same stratigraphic horizon as Monument or House Rock on the east side of the crater.

In Chapter 3, the joints that cross-cut the impact target were described. They may have several effects on crater formation, including one that produced this boulder field (Kring, 2015). The west and east boulder fields bisect the major and minor joint orientations. Although this distribution could reflect the trajectory of the impacting asteroid, it is also possible that excavation flow, oblique to both sets of joints, created blocks with dimensions of the joint spacing and deposited them relatively close to the crater rim, because excavation flow was not as effective in that direction. The scales of the blocks seen in the east and west boulder fields are similar in size to the spacing of joints seen in Kaibab elsewhere in the region.

Barringer Point Thrust Wedge and Anticline

Barringer Point is one of the highest summits on the rim of the crater and, like Moon Mountain, is high, in part, because a wedge of rock was thrust into the crater wall beneath it. That thrust wedge is not visible from the summit. Rather, it is best seen from an opposing point on the crater rim. I refer readers to Fig. 6.3, 6.4, and 17.16. The depth of the thrust wedge is, however, evident from the summit. If one looks at the sloping surface of the ejecta blanket radially outward from the summit, there is a sharp change in that slope. That is the topographical expression of the terminus of the thrust wedge. We ran a short seismic line across that area which confirmed the thrust wedge thins at that location.

Barringer Point provides an excellent view of another structure on the opposing, southeast portion, of the crater wall (Fig. 18.18). During excavation flow, there was differential uplift of crater wall rock. That differential displacement produced stratigraphic offsets up to 45 m. There are two large faults in the southeast corner, both with right lateral offsets. That differential motion also has a radial component that is more difficult to see from this location, but can be inferred by the differential outcroppings of Moenkopi, and is shown schematically in an inset of Fig. 18.18. Another view of that portion of the crater wall is shown in Fig. 19.13. See Denton and Kring (2016) for more details.

From this point along the trail we return to the museum.

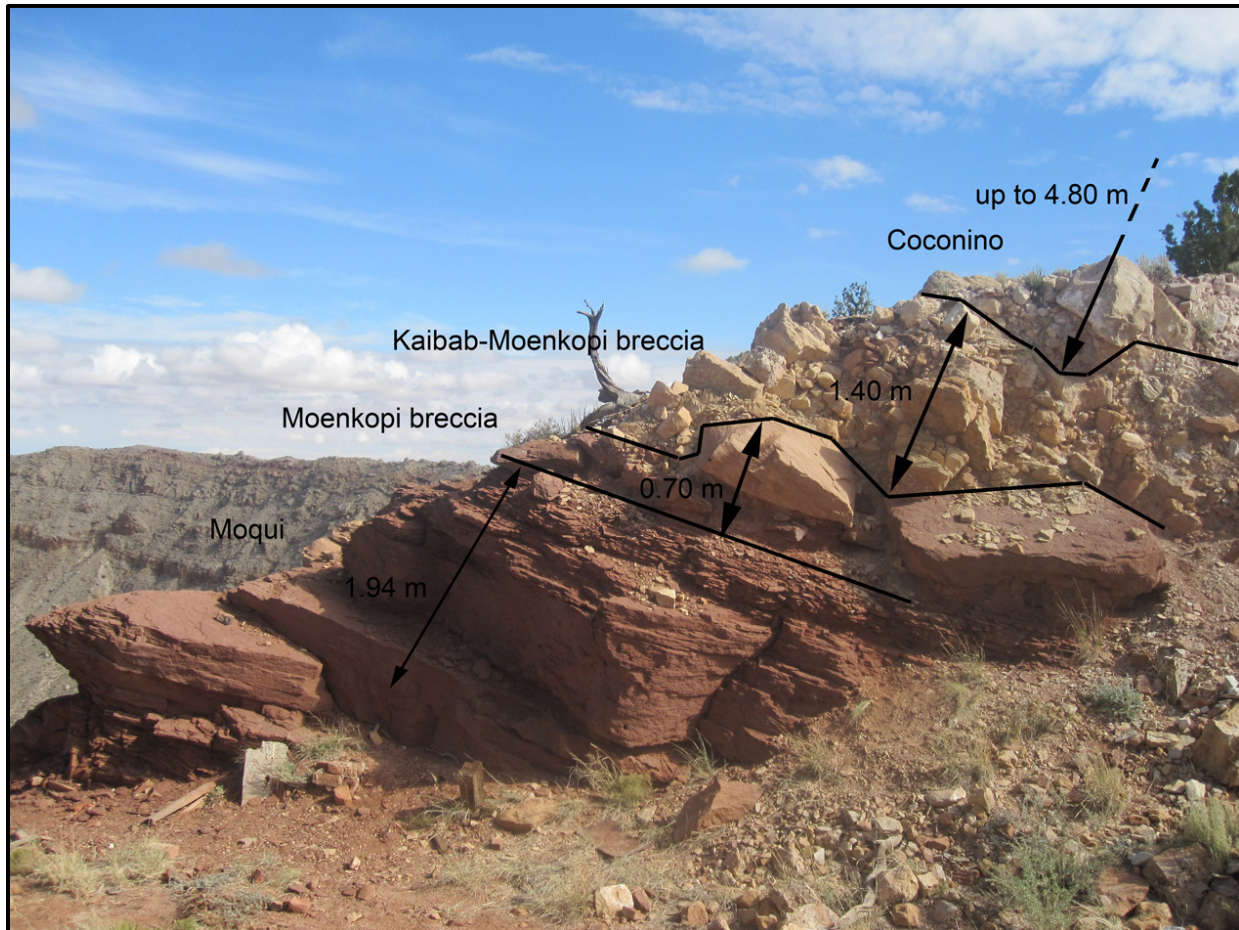


Fig. 18.1. Upper portion of the section measured by Kring *et al.* (2011a) on the south rim of the crater adjacent to the 1,376 ft-deep churn hole. The outcrop, from bottom left to upper left, is composed of 1.94 m of Moqui, 0.70 m of Moenkopi breccia, 1.40 m of mixed Kaibab and Moenkopi breccia, and up to 4.80 m of Coconino sandstone. Approximately 80 m of Kaibab dolomite are missing from the overturned section in the crater rim.



Fig. 18.2. The surface of the ejecta blanket on the south side of the crater is dominated by Coconino sandstone debris, as seen here along the road. See Fig. 8.5 for another perspective. Some sections of this unit have been disturbed by mining operations and by USGS scientific drilling and excavation.



Fig. 18.3. Examples of the disparate appearance of overturned and ejected Coconino in a small pit (top panel) next to a road on the south side of the crater. This monomict breccia is composed of normal-looking gray blocks of Coconino that are adjacent to units that are bright white in color due to a modest amount of shock damage. A close-up view of one of the bright white blocks is shown in unshadowed (bottom left) and partially shadowed (bottom right) illuminations.

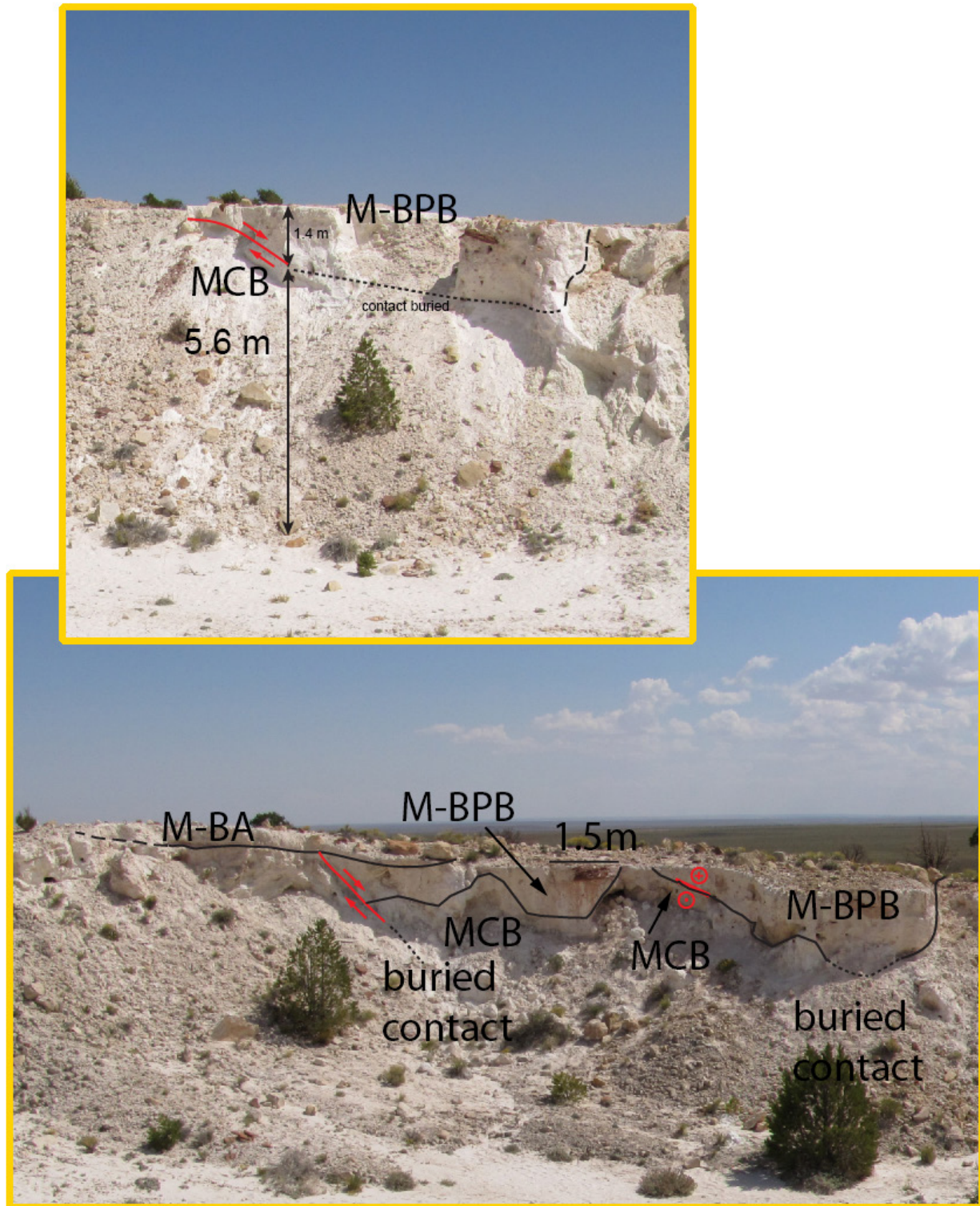


Fig. 18.4. The east wall of the Silica Quarry exposes contacts between the overturned Coconino ejecta and overlying debris units. The Coconino ejecta is a monomict Coconino breccia (MCB) in the upper panel. It is truncated by a normal fault that dips south, away from the point of impact. A Moenkopi-bearing polymict breccia (M-BPB) lies above the fault. A similar pattern is seen farther south in the quarry (bottom panel). In places, the M-BPB is covered with Moenkopi-bearing alluvium (M-BA, bottom panel) and Coconino-bearing alluvium (not shown). Shoemaker mapped the M-BPB as alluvium too, but as argued by Kring *et al.* (2012b), that material is likely fallback breccia.

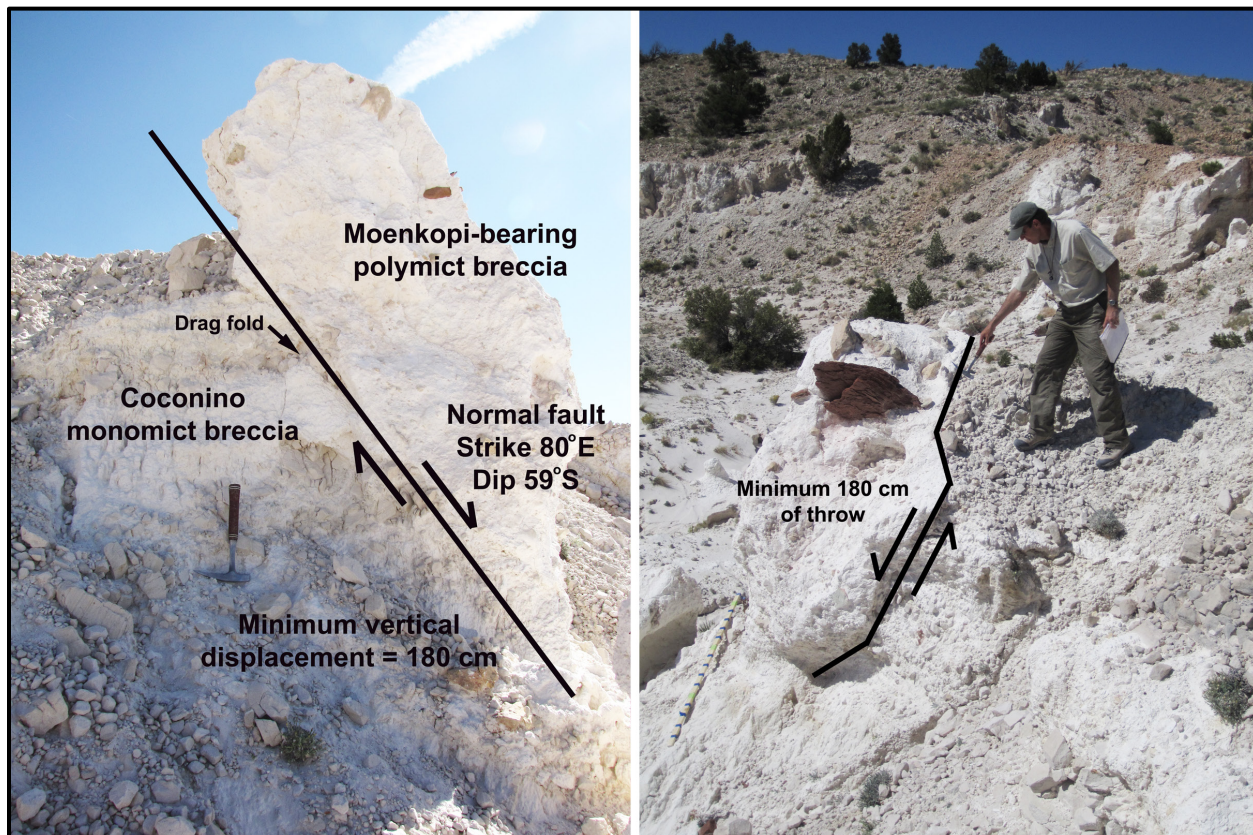


Fig. 18.5. A close-up view of a normal fault that cuts through the monomict Coconino breccia (MCB). This site is located to the far left of the top panel in Fig. 18.4. The side-by-side photographs show two sides of the same fault. Motion along the fault caused a drag fold in a semi-coherent layer of Coconino in the breccia (left panel). The throw on the fault is at least 180 cm. Moenkopi-bearing polymict breccia (M-BPB) lies above the fault. Shoemaker mapped the M-BPB as alluvium, but it may be fallback breccia (Kring *et al.*, 2012b).

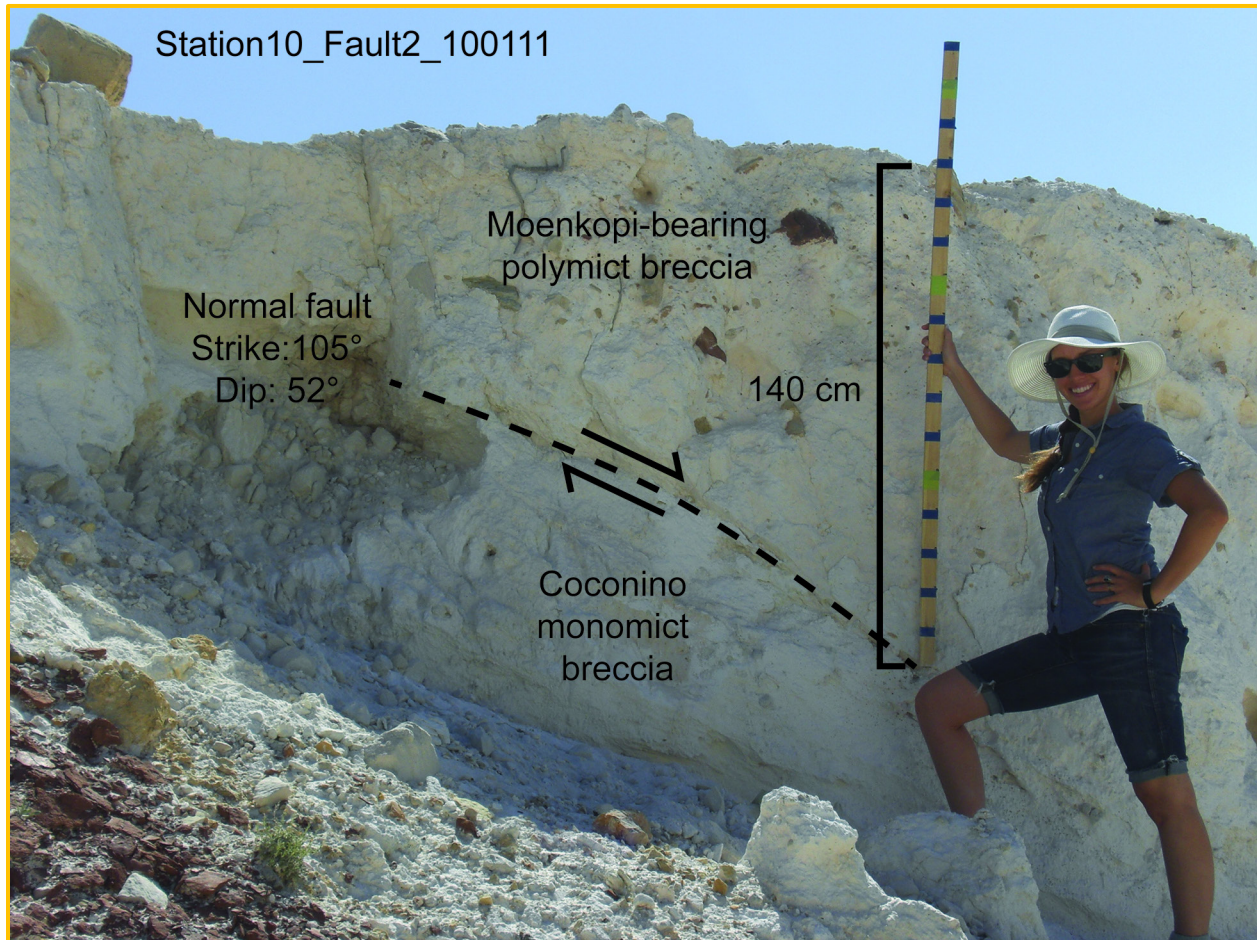


Fig. 18.6. A normal fault juxtaposes Moenkopi-bearing polymict breccia on the hanging wall with Coconino monomict breccia on the footwall. That fault displacement, interpreted to occur during deposition of the ejecta blanket, carried fallback breccia to a depth where it survived subsequent erosion. Photograph by Sarah Crites and pictured is Christine Jilly holding a Jacob's staff for scale during the 2011 Field Training and Research Program at Meteor Crater.

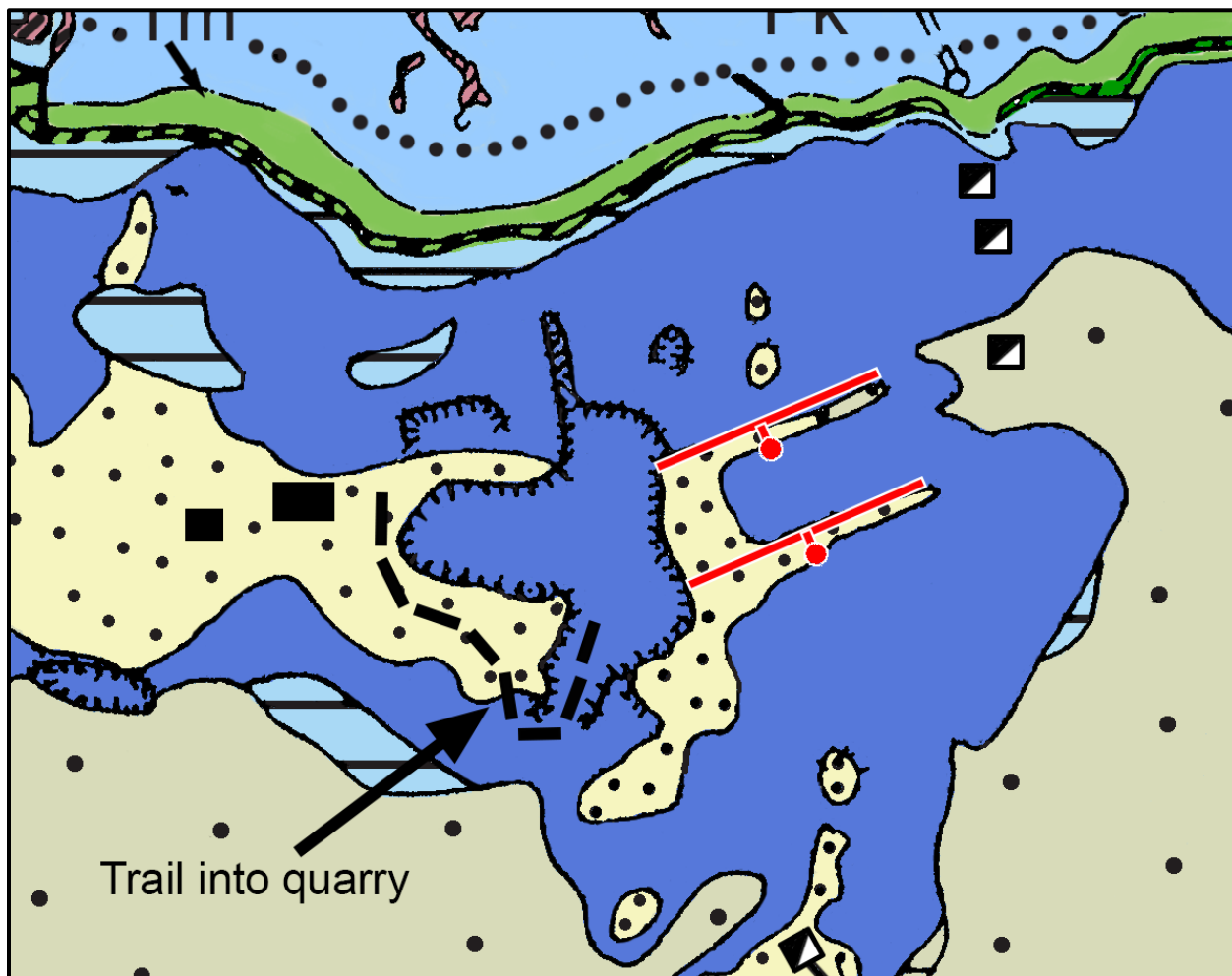


Fig. 18.7. The faults visible in the east wall of the quarry can be traced to the east, as shown here in red and added to a detail from Shoemaker's geology map (Fig. 4.4). Those faults seem to be responsible for two linear deposits of material that Shoemaker mapped as alluvium, but that may instead be fallback breccia. Those faults dip to the south, away from the crater center, and, thus, reflect extension of the overturned ejecta blanket when it was emplaced. It is the same sense of extension seen closer to the crater rim at two other stops described in the guidebook. The trail to be used for this field stop enters the quarry from the south, as shown with a dashed line.



Fig. 18.8. Relics of the living quarters and packing house used by miners and subsequent curators of the crater. The trail described in this guidebook runs between the two buildings in the upper photograph. A close-up view of the building in the background is shown in the lower photograph. Many buildings were erected around the crater, most of them on the south side in the vicinity of these two structures. Several structures were constructed with vertical wood planks on a wood frame, as seen here, while at least two other buildings utilized Moenkopi as a building stone.

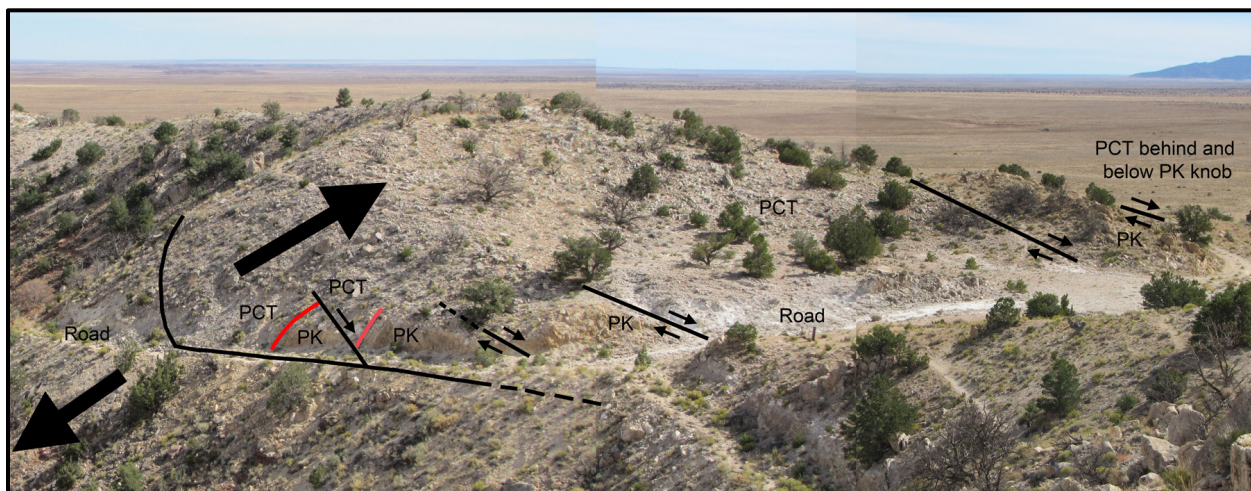


Fig. 18.9. A hinge (red curves) in the Coconino-Toroweap (PCT) is exposed in contact with the Kaibab (PK) in the southwest portion of the crater. The hinge was faulted outward from the crater center by up to 100 meters (with relative motion indicated by large black arrows), although that motion may have also had a lateral (west-directed) component that carried it towards a tear fault (not labeled) that cut through the crater rim in the lower right corner of the field of view. The overturned PK, below the overturned PCT, was thinned in a series of outward-dipping normal faults (with relative motion indicated by small black arrows), one of which cut through the hinge, producing a duplication of the hinged PCT-PK contact. Apparent displacements along the faults (from left to right) are ≤ 100 m, 3 m, 6 m, 30 m, 2 m, and ~ 20 m. The viewer is looking towards the southeast. See Kring *et al.* (2011b) for other details.

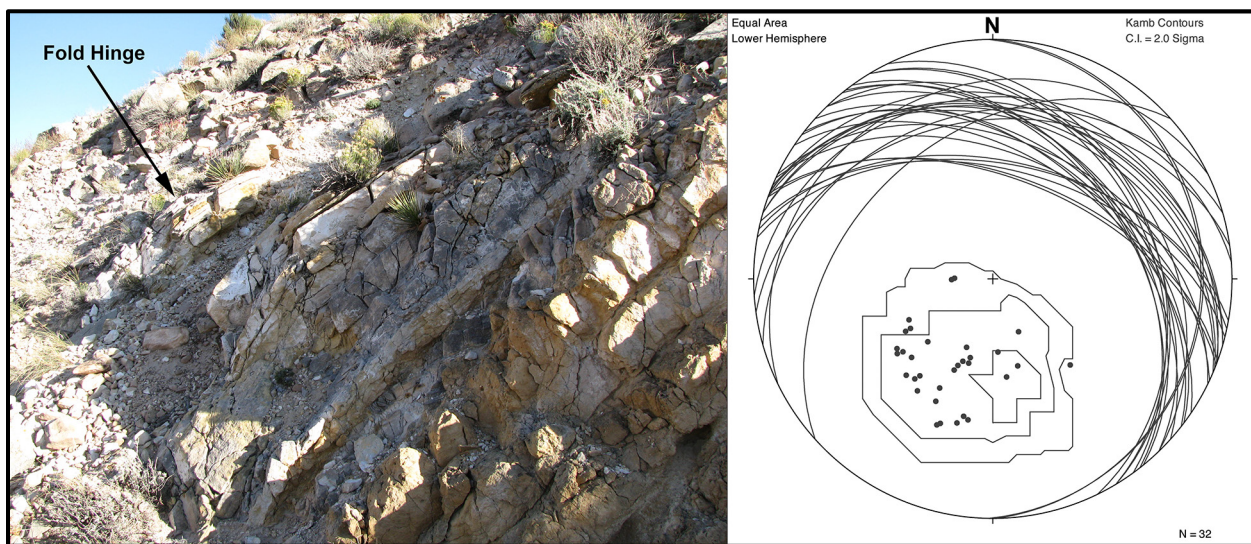


Fig. 18.10. (left panel) View of hinge in Coconino-Toroweap (upper left) and transition to sandy dolomite within the fold (lower right). (right panel) Planes, poles, and 2-sigma Kamb contours around poles measured for the orientations of Coconino, Toroweap, and Kaibab in the fold hinge and upper limb shown in the left panel. A portion of the units are dipping towards the crater E, NE, and N at an inclination of ~ 30 to 50° , but most units are dipping away or nearly flat, reflecting the transition from the hinge to that of the structurally overturned limb. These data were collected by students in the 2010 Field Training and Research Program at Meteor Crater and plotted by Josh Garber.

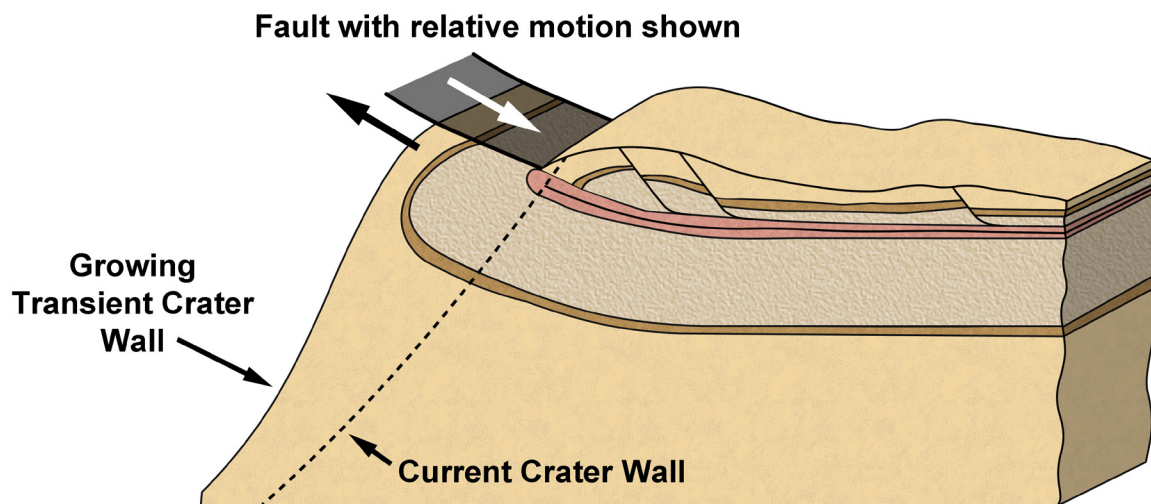
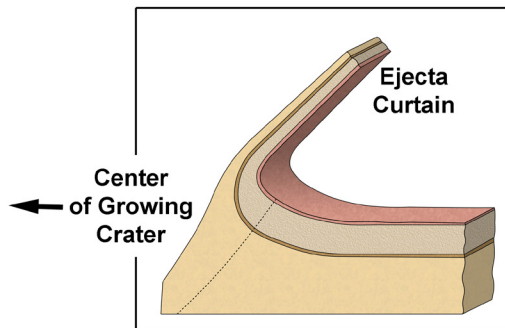


Fig. 18.11. Because the curving outcrop that reveals the faults in Fig. 18.8 make the geometry difficult to assess in the picture, a cross-sectional view is schematically shown here. The inset shows a partial cross-section of Meteor Crater, illustrating the orientation of ejected units during the growth of the transient crater. Overturning is beginning to occur and the ejected material will soon fall down and towards the right onto the red landscape surface. The units are, from bottom to top, Coconino (golden brown), Toroweap (brown), Kaibab (mottled beige), and Moenkopi (red). During the emplacement of ejecta, the overturned unit is faulted outward (main figure). This is shown with a semi-transparent black plane, with two opposing arrows illustrated the relative motion along that fault. As shown in outcrop (Fig. 18.9), the ejected and overturned units are also extended along a series of normal faults that dip away from the crater center, which is shown schematically here with three normal faults. The current position of the crater wall is shown with a dashed line. The thickness of the Kaibab (mottled beige) in the crater wall is ~80 m.

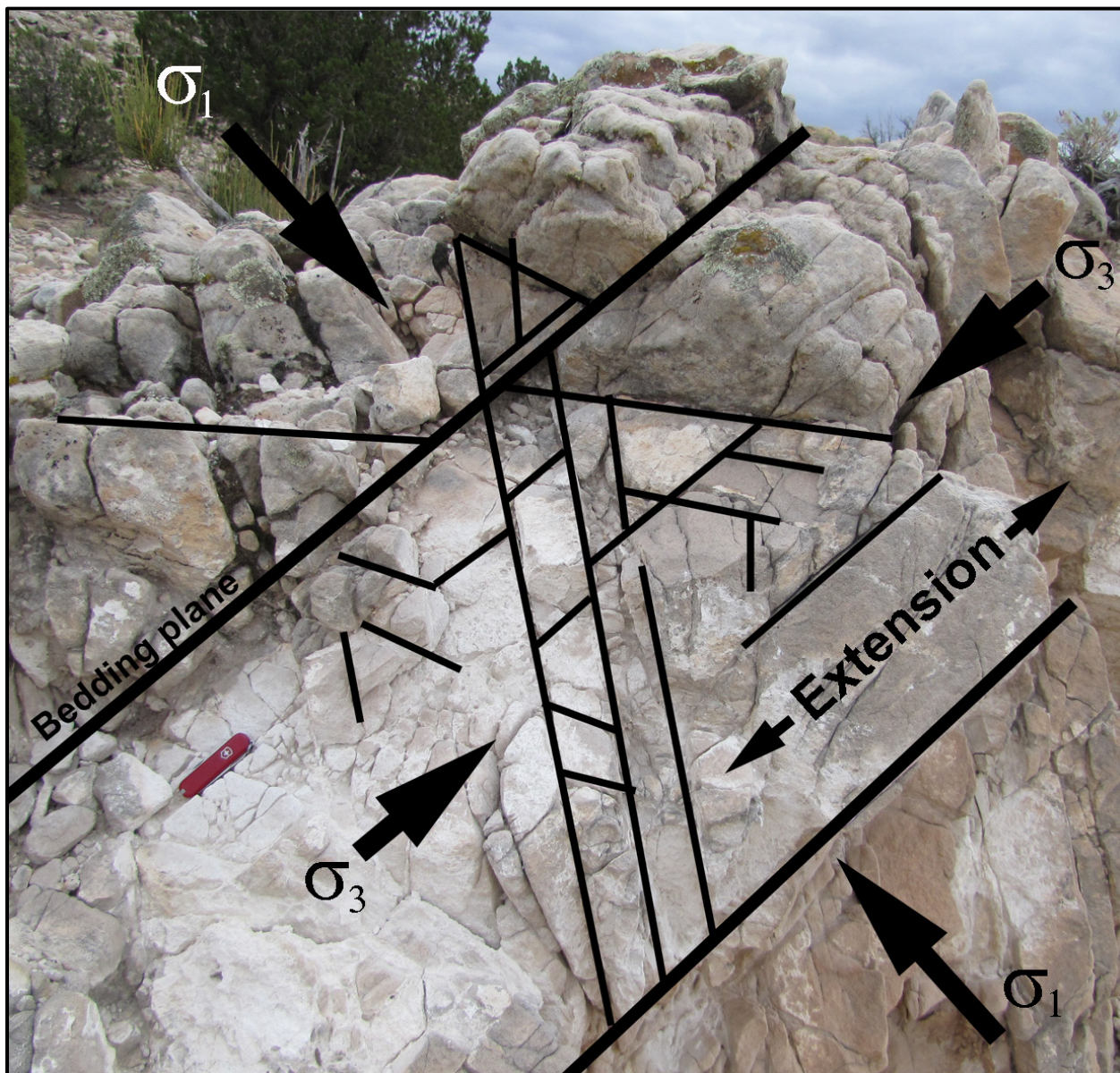


Fig. 18.12. Conjugate fractures (highlighted with black lines) in ejected Coconino sandstone illustrating maximum extension parallel to bedding. The crater is to the left of the picture. A 6-cm-long red knife provides scale.



Fig. 18.13. Coconino-Toroweap sandstone on the south crater rim. As we will discuss in the field, the aligned blocks may represent the limb of a fold or, alternatively, a cross-bedded unit within the sandstone.

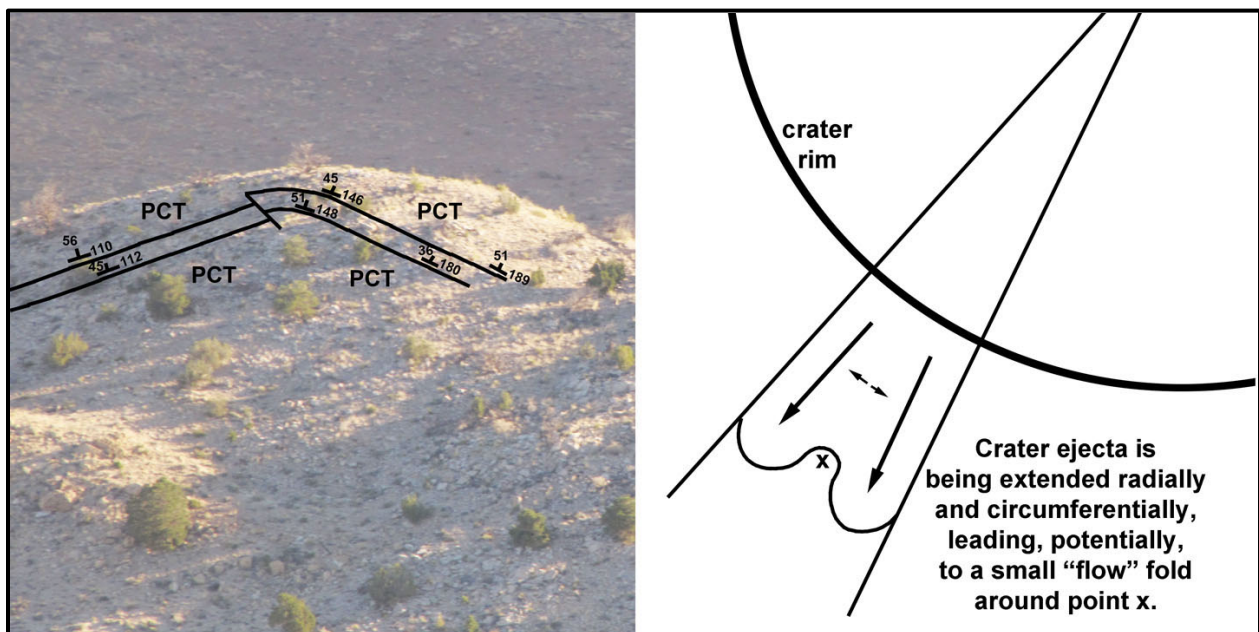


Fig. 18.14. (left panel) There is an apparent fold in the Coconino sandstone that was ejected and emplaced on the south crater rim. The photograph is annotated with apparent strikes and dips. The structure is also cross-cut by a small offsetting fault. It is left to students to determine if this is truly a fold in the ejected Coconino or whether the change in apparent strike is an artifact of massive cross-bedding in the Coconino sandstone. (right panel) If the fold is real, then it might reflect the flow of ejecta as it expands radially and circumferentially. The large arrows represent radial extension while the small arrows represent circumferential extension. That combination of movements could produce an apparent fold in disarticulated blocks of Coconino sandstone around point "x" in the diagram.



Fig. 18.15. Below the rim trail, in the southwest corner of the crater and adjacent to a tear fault, the Kaibab is dipping steeply into the crater wall. The dip varies from near-vertical near bottom of the field of view to lower, albeit still steep dips higher up the slope, and is being overturned on the rim. These variable dips may be accommodated with one or more fault planes within the wall of the crater.



Fig. 18.16. As one approaches Whale Rock, fragments of red Moenkopi begin to appear in the ejecta (top and bottom panels). This material, while mapped as alluvium by Shoemaker, is virtually in place, because it is near the crater rim (right margin of the bottom panel) and any erosional transport would have carried it downhill (to the left in the bottom panel). This is also a location with cosmogenic nuclide ages (Nishiizumi *et al.*, 1981). Two ages on boulder summits are among the oldest at the crater and it is often assumed the points analyzed represent exposed ejecta soon after impact.



Fig. 18.17. Whale Rock is so named because of its shape (upper left panel). The Kaibab boulder is part of the west boulder field (middle panel). Whale rock is the largest boulder seen in that field (right center of the middle panel). This boulder is from the same stratigraphic horizon as Monument or House Rock on the east side of the crater. The face of one bed is covered with a characteristic trace fossil (bottom panel).

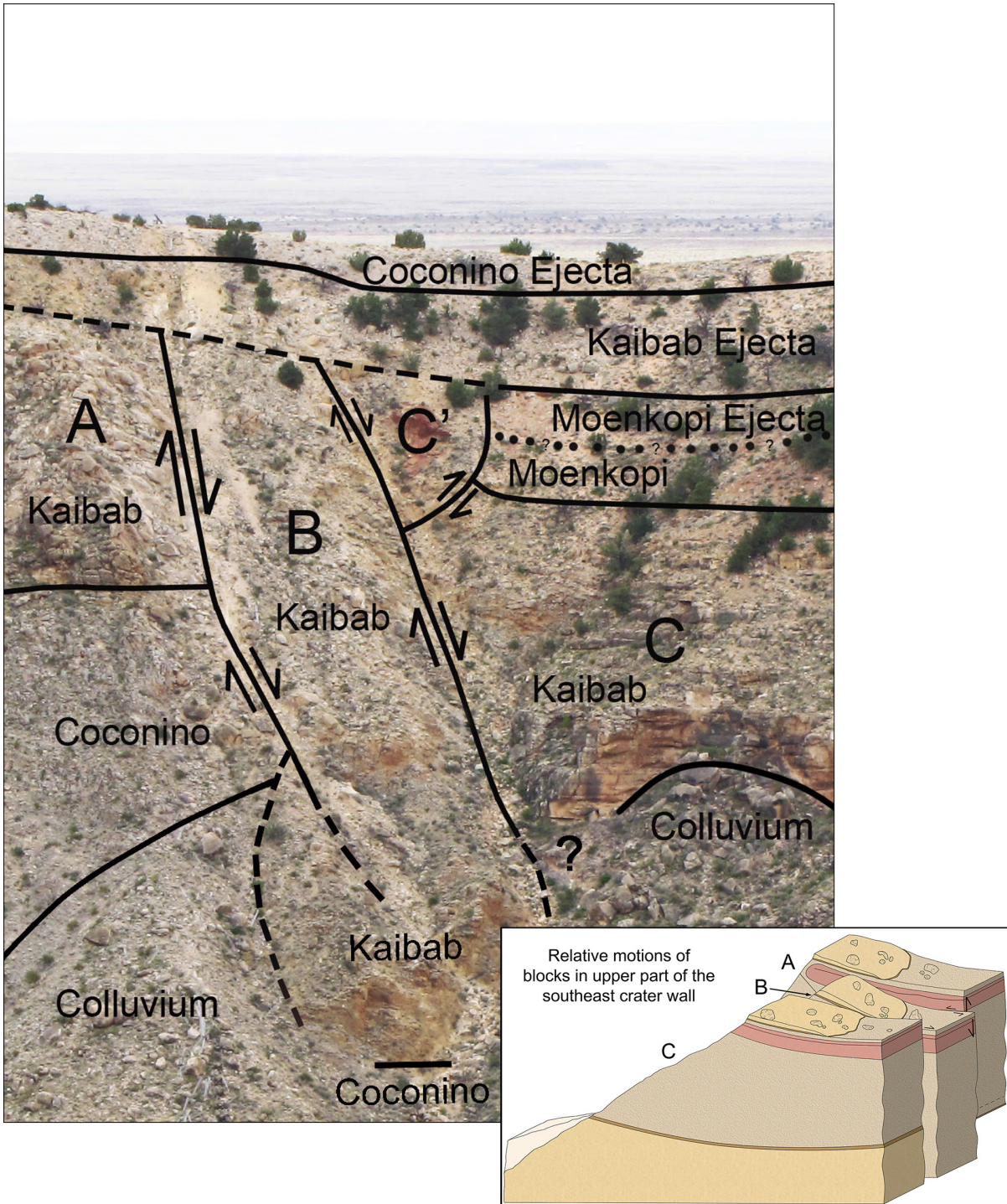


Fig. 18.18. Looking towards the southeast corner of the crater, differential vertical and radial displacement can be seen along faults in the crater wall (Denton and Kring, 2016). Geologic contacts and relative fault movement are shown on an image as seen from Barringer Point. The inset shows, schematically, the differential movement of blocks A, B, and C. The relative motion along both faults separating the blocks is the same: right lateral. The differential motion between the two faults rotated and tilted Kaibab strata, lifting the eastern edge of Block B ~5 m higher than the western edge, and shattering the strata throughout the block. The faults do not appear to extend into the ejecta (see image), indicating the motion along those faults stopped before ejecta was emplaced. To avoid obscuring the fault displacement in the schematic diagram, that feature is not shown. The Coconino ejecta in the schematic inset should, however, be continuous across the three blocks.

19. Trail Guide 3: Crater Floor



To reach the trail-head for the crater floor excursion, we exit the museum and hike west along a trail on the north rim of the crater. This is the same trail that the public uses when guided by museum staff to the northwest corner of the crater. When we reach the northwest corner, however, we will be stepping off that trail so that we can hike down to the crater floor. Permission to leave the public trail must be obtained from museum staff. Once off the public trail, I ask that you walk softly. Try to avoid stepping on vegetation and do not unnecessarily disturb the soil. After we descend below the ejecta blanket, we will reach and follow a 100-year-old trail into the crater that was developed by the Standard Iron Company. You will see a lot of debris from those mining operations while we descend. A decision was made several years ago to leave those artifacts in place for historical purposes, rather than discard them. Please do not disturb the artifacts. The trail-head is also marked by the remnants of a building constructed of red Moenkopi (Fig. 19.1). That building is the original crater museum.

Coconino and Kaibab Ejecta

This excursion begins in a gap along the crater rim. The gap represents the top of a tear fault through the crater wall that has facilitated erosion, providing an excellent cross-section through the rim sequence. At the top of the gap, just a few feet from the public trail, an incredibly white outcrop is visible (Fig. 19.2). The material in the outcrop is weakly consolidated. It is a mass of shocked and ejected sandstone that is transitional to a type of rock flour that was described by Barringer (1905). The material in the outcrop is heterogeneously damaged. Cores of surviving Coconino with traces of cross-bedding can be found in it. Outcrops like this one also contain his Variety A shock-metamorphosed sandstone, which has a higher density than normal sandstone.

This sandstone deposit is in the midst of Kaibab dolomite ejecta. A patchy distribution of both lithologies occurs along this portion of the crater rim, in part because there is a hummocky surface to the Kaibab ejecta blanket. Coconino-Toroweap ejecta fill depressions in that surface. En route to the trail-head, we passed a classic example of this hummocky structure (Fig. 8.4). There is a sharp contrast between the level of impact-induced damage in the Kaibab dolomite and this outcrop of sandstone. Several multi-meter-diameter Kaibab boulders are resting on the rim around us and seem to be completely unaffected by the impact event (albeit upside down), yet the sandstone in the outcrop at our feet is almost pulverized. The same contrast exists in the crater walls beneath the ejecta. Kaibab maintains good bedding and is cross-cut with few fractures, whereas the Coconino is often shattered into angular blocks that are only a few centimeters to decimeters in size.

Continue to descend along the tear fault until you reach the Standard Iron Company's trail and a nice bench in the red Moenkopi.

Crater Rim Uplift and Overturning Along a Tear Fault

From this vantage point, we can easily see that the target strata were uplifted by the impact blast and now have a steep outward dipping orientation (Fig. 19.3). Dips of strata in the crater walls are often 30 to 40°. At the top of the normally-bedded portion of the sequence is red Moenkopi siltstone. Below the Moenkopi is Kaibab dolomite and some minor sands. The Kaibab is a buff to yellow-colored rock, but

its surface in the cliff is stained red from the overlying Moenkopi. The Moenkopi and Kaibab are overturned on the upper part of the slope.

Offset along the tear fault is also visible from this location. The rock in the cliff on the far side of the fault was uplifted farther than the rocks on this side of the fault. Tear faults around the wall of the crater have given it a pseudo-square shape in plan view (*e.g.*, Fig. 4.1). Shoemaker (1960) suggested the tear faults were activated along pre-existing sets of joints. In this portion of the Colorado Plateau, there is a strong SE-NW trending set of joints and a weaker SW-NE trending set of joints (Chapter 3). Some of the joints that cut through the Kaibab have been accentuated by carbonate dissolution, creating cavernous seams that extend all the way to the underlying Coconino-Toroweap. Several of these large crevices can be found within a few kilometers of the crater.

The tear fault in front of us is not a simple fault plane. The fault surface curves as it climbs up the crater wall and is actually composed of multiple fault surfaces (Fig. 19.3). Drag along the tear fault folded the bedrock on the far side of the fault. Although not shown in the figure, there are also two small thrust faults in the Kaibab-Alpha sequence that are roughly orthogonal to the tear fault. These types of thrust faults contributed to rim uplift and can be found in both the Kaibab-Alpha and Kaibab-Beta units. One of the largest thrust fault systems is below Barringer Point, which is slightly farther to the west along the crater wall. It thickened the Kaibab-Beta, producing an anticline in the Kaibab-Alpha and overlying units. The anticline is one of the highest topographic points around the crater rim. We will have a good view of the Barringer Point anticline from the crater floor and southeast crater rim later in our excursion.

This tear fault, plus the regional distribution of joints and dissolution through the Kaibab, led Hager (1953) to propose an alternative origin for the crater. He envisioned the crater was originally an anticlinal mound. That is, the dipping strata in the cliffs once arched over the crater in a broad dome of rock. He argued that the dome was cross-cut with fractures similar to those visible in Kaibab today. Water infiltrated those fractures and dissolved subsurface lithologies. The dome then collapsed downward along faults (the tear faults), forming a graben that was subsequently modified by erosion. Like Gilbert (1896), he argued the meteoritic debris was coincidental. He also argued silica glass found around the crater is the erosional remnant of a pure silica volcanic lava flow.

Continue down the trail towards the crater floor where we will re-assemble. As you hike down the trail, you will encounter a landslide. Climb over the landslide with care. Do not descend directly above another person, in case a rock is dislodged. The first time this trail washed out occurred over 100 years ago in September 1906. An interesting report of the event survives (Fairchild, 1907): A “cloudburst” opened up over the crater and the “northern trail leading down the crater wall was obliterated and trains of boulders were swept far out on the floor of the crater, while the shaft-house, tool-house, and other buildings in the middle of the pit had their floors buried in mud.” If you look to the crater floor below, you can still see some of those boulders. However, it is also important to note that a couple of the largest boulders were on the crater floor during G. K. Gilbert’s trip to the crater years before that cloudburst.

Once we reach the crater floor, we will hike to the north wall of the crater and climb up to an outcrop of impact breccias. Be careful when hiking across the crater floor, because the soft sediments have been burrowed by animals. You may fall through the roof of a burrow system and find yourself knee-deep in the soil. If you move too quickly, you risk breaking a leg.

Allogenic and Fall-out Impact Breccias

A gully dissects debris on the crater wall, exposing two types of impact breccia and a layer of

Pleistocene talus (Fig. 19.4). The best view of the units is on the west wall of the gully. The lowest unit is Shoemaker's allogenic breccia. Patches of this material are found scattered around the crater (Fig. 4.4) and form the thick breccia lens on the floor of the crater. Depending on location, allogenic breccia is composed of Coconino, Kaibab, or a mixture of those two lithologies. It tends to be dominated by Kaibab on the crater walls and Coconino in the breccia lens. At this locality, Kaibab dominates the breccia. Shoemaker and Kieffer (1974) identified most of the clasts as being from the Beta Mbr of the Kaibab Fm. Clasts within the breccia are angular and have irregular surfaces. There was not sufficient energy to eject this type of material from the crater. Most of it slipped into the bottom of the crater to form a thick breccia lens. If one were to coat the entire transient crater with the material in the breccia lens, it would produce a layer c. 20 m thick.

Draping the allogenic breccia is a fall-out or fallback breccia unit that is up to 1½ m thick where it fills a local depression on the surface of the allogenic breccia. This unit has a mixture of target lithologies, including bright red fragments of Moenkopi and brilliant white fragments of shocked Coconino sandstone. Lechatelierite and meteoritic debris occurs in this unit and have been recovered from this particular outcrop.

The impact breccias are buried beneath Pleistocene talus. Elsewhere along the gully, the talus rests directly on allogenic breccia. The fallback breccia appears to have been eroded from those surfaces prior to the deposition of talus.

From this vantage point, we also have a good view of the east and southeast walls of the crater (Fig. 19.5). The Gamma Mbr of the Kaibab Fm forms a cliff that can be traced around the crater wall. Several displacements of the Gamma Mbr are visible, including a huge displacement along a tear fault in the southeast corner. This tear fault is similar to the one that occurs in the northwest corner, but the displacement is greater. The units on the left (north) side of the tear fault were uplifted 45 m higher than those on the right side of the fault, which exposed 90 m of Coconino sandstone.

Return to the crater floor and hike towards a covered shaft on the east side. Stop at the mid-point.

Sedimentation on the Lower Crater Wall and Crater Floor

Looking east, we see two sedimentary units on the lower crater wall (Fig. 19.6). The oldest debris occurs in triangular patches that begin near the base of Gamma Mbr of the Kaibab Fm (or at the top of the Coconino-Toroweap Fms) and descends towards the crater floor. The Toroweap Fm is only 1½ m thick at the crater, so most of the sandstone visible near the patches of talus is Coconino sandstone. Shoemaker and Kieffer (1974) correlated soil profiles within the talus with soil profiles in the Hopi Buttes region northeast of the crater. They determined that the talus formed at the same time as the late Pleistocene Jeddito Fm. They surmised that the talus was deposited during a pluvial episode during the Wisconsin glacial period. After the talus was deposited, the slope stabilized and a soil formed before the deposits were cut by deep gullies.

Coarse alluvium pours through those gullies and onto the crater floor. This deposit also has a soil of late Pleistocene age and corresponds to the highest soil within the Jeddito Fm (Shoemaker and Kieffer, 1974). The alluvial fans were produced in another pluvial episode during the Wisconsin glacial period. The flow of material through the fans produced levied channels that are still preserved. Although erosion has been modest since the alluvial fans were deposited, it has consumed the lower margins of the fans. Small alluvium-filled channels are dissecting the alluvial fans where they interface with playa sediments

on the crater floor. The relative role of fluvial and debris flow processes is being studied; readers are referred to Chapter 15 for a discussion of those processes.

If we turn around and look west, we see a small hill protrudes from the crater floor (Fig. 19.7). This feature is called Silica Hill. It is composed of Pleistocene lake beds and spring deposits, which imply the level of a lake in the crater was once higher than the hill. The top of the lake sediment is 69 m above the current water table, indicating the water table has fallen dramatically since the late Pleistocene.

Several exploration shafts surround Silica Hill and one of them penetrates the hill. Most of the shafts have been filled in, but Shoemaker was able to examine the walls of the shafts before they were lost. In four shafts (I, II, IV, and V) around Silica Hill, he found three basaltic volcanic ash layers about 5 m below the surface. These are late Pleistocene ashes that were deposited during eruptions in the San Francisco Volcanic Field near Flagstaff, possibly from Saddle Mountain (Chapter 14). In contrast, he did not find any ash in Shaft VI on the top of Silica Hill, which suggests the lake level had fallen below the summit of Silica Hill prior to the volcanic eruptions. Any ash that fell on the island was eroded into the surrounding lake.

Shoemaker correlated lake sediments in Silica Hill with the lower to middle stratigraphic levels of lake sediments elsewhere on the crater floor, implying that the base of the lake sediments of Silica Hill is 15 m higher than elsewhere in the crater. Based on this correlation, Shoemaker and Kieffer (1974) suggested the lake sediments of Silica Hill were deposited on top of a topographic high or off-centered “central peak” on the original crater floor. Structural uplift of underlying bedrock is not expected in a crater this small, nor is there evidence of it in exploration boreholes and geophysical surveys. However, observations of lunar craters suggest uneven topography can form on the surface of the breccia lens during collapse of that debris from the walls of the transient crater.

Silica Hill is surrounded by playa sediments that were deposited after the lake disappeared. They are beneath our feet (Fig. 19.8). In the walls of the Main Shaft, Shoemaker measured a total thickness of 1.8 m. The playa sediments are composed of pink eolian silt that blows in from outside the crater. In a trench cut into the playa beds, he found two volcanic ash layers that he correlated with the eruption of Sunset Crater. Using that ash as a chronometer, he determined that 30 cm of playa sediments have been deposited since the eruption. The eruption occurred ~900 years ago, possibly in 1064 or 1065 (Smiley, 1958), between A.D. 1040 and 1100 (Ort *et al.*, 2002).

Continue hiking across the crater floor towards the southeast corner of the crater, where we will begin our hike up to the crater rim. En route, we will pass several remnants from mining operations. We will stop at Shaft II on the east side of the crater floor. If time allows, one can also detour to the Main Shaft in the crater center.

Probing the Crater Floor in 100-Year-Old Exploration Shafts

A large steam boiler and winch sits in the center of the crater floor (Fig. 19.9), immediately east of the Main Shaft, which is enclosed by a safety fence. (Do not enter this fenced area.) The Main Shaft is a large 2-compartment shaft suitable for commercial production of meteoritic ore. Unfortunately, water was encountered at a depth of 210 ft (63 m). Pumps were installed, but they could not mitigate the flow of water and work ceased at a level of 230 ft (69 m) when the walls at the bottom collapsed. A building used to stand over the main shaft (Fig. 19.10). Shaft III is adjacent to the Main Shaft and also surrounded by a safety fence.

Shaft II is on the east side of the crater floor and now covered by a set of doors (Fig. 19.9). The shaft is 43.3 m (145 ft) deep. The upper 30 m (100 ft) of the shaft is composed of lake sediments with the volcanic ash described above. Below the lake sediments is 10.3 m (35 ft) of fallback breccia. The unit is generally massive, but there is a subtle grading upwards from coarse debris at the bottom to finer-grained debris at the top of the unit. The basal 1.3 m (5 ft) is particularly coarse. The shaft penetrates 3 m (10 ft) into the allogenic breccia lens on the crater floor, where it bottoms. The allogenic breccia is composed entirely of Coconino sandstone. Some of the blocks are more than a meter in size. Superficially, the blocks look like they represent several levels of shock, indicating that there was a lot of mixing on the walls of the transient crater before the material was deposited.

A dump around the top of the shaft contains debris from all levels in the shaft. Much of the dump has an inverted stratigraphy, because material removed from the bottom of the shaft was dumped on material previously removed from the top of the shaft. However, the miners also dumped material on different sides of the shaft as they plunged deeper. Fallback breccia dominates the surface on the east side of the dump. Allogenic breccia dominates the surface on the southwest side of the dump. Lacustrine sediments dominate the northwest side of the dump.

Material from the fallback unit contains severely shocked Coconino sandstone, including vesicular silica glass. Shocked Coconino is also found in material from the allogenic breccia, but shock levels are less severe. Microscopic examination might be needed to classify the shock level. The lacustrine sediments are dominated by thinly-laminated, calcareous siltstones with fossils of the organisms that lived in the lake. Although not apparent in the dump, the lake sediments also contain shock-metamorphosed debris. In the shaft, the lower 1.5 m (5 ft) of lake sediments contain many blocks of lechatelierite. Shoemaker measured one block of lechatelierite that was 30 cm across. These low density materials were able to float while water flooded the crater and a lake grew. Eventually they became water-logged, sank, and were buried by the first lake sediments. Lechatelierite blocks may have floated up directly from fallback breccia deposited on the crater floor, but some of them may have also been washed into the lake from the crater walls.

The contact between the fallback breccia and lacustrine sediments is sharp (Fig. 14.2). There is no intervening alluvium. Based on this observation, Shoemaker and Kieffer (1974) concluded the lake formed immediately after the impact event and, thus, that the water table was at least 30 m higher in the Coconino sandstone than it is today.

Unfortunately, the cribbing in this shaft is no longer safe and work in it has been suspended. Before the shaft was closed, however, I was able to sample the first horizon of lake sediments deposited on top of the fallback breccia on the original crater floor. Pollen in that sample was used to improve an environmental reconstruction of the vegetation at the time of impact. (See Chapter 13 for more details.) Plans have been made to replace the cribbing, so that we have a permanent research and educational facility that provides access to both the impact breccia lens and overlying lake sediments. We are still working to acquire the necessary funds for the project.

Continue hiking towards the southeast corner and begin climbing out of the crater along an old mule trail. The trail will switch back and forth across Pleistocene alluvium. We will stop when we reach the base of the cliffs along the southern wall of the crater.

Toroweap Cave

The Toroweap Fm is much thinner at the crater than it is in the Grand Canyon. Only 1.5 m is found

between the underlying Coconino Fm and overlying Kaibab Fm. A small cavernous exposure is visible to the right (southwest) of the trail (Fig. 19.11). Large fractures in the Gamma Mbr of the Kaibab Fm feed water into the boundary region, enhancing erosion of the Toroweap. The dissolution of Toroweap appears to be a post-impact phenomenon. However, elsewhere in the region, large subsurface caverns have been found immediately below the Kaibab-Toroweap contact. Thus, caverns may have existed in the target sequence prior to impact.

Continue hiking up the trail. Four stops are planned for the remainder of the climb to the crater rim.

Hauling Supplies

During mining operations, a lot of supplies had to be transported into the crater. Mules carried some of that material on the trail we are following. Material was also winched to and from the crater floor along a slide that was built on the crater walls. Remnants of the wooden staging can still be seen on the slope (Fig. 19.12). A mule-driven winch sits at the top of the slide on the crater rim. The primitive elevator is no longer in service.

Mining activity within the crater was widely followed by newspapers across the country. In 1906, The Arizona Republican published a summary of the operations and Barringer's impact hypothesis after the first four holes had been drilled in the crater floor and concluded: "It is fortunate indeed for Arizona, that this wonder came into the possession of the men who became deeply interested in it and who at the time had the money and pluck enough to exploit it (February 26, 1906)." Newspaper stories sometimes had a few facts wrong or were intentionally exaggerated. For example, based on the presence of diamonds in Canyon Diablo meteorites, The Indianapolis Star reported (October 6, 1912) that the mining syndicate was trying to recover a half-mile thick diamond.

Differential Vertical and Radial Displacement in Uplifted Crater Walls

As we climb out of the crater, we are afforded an excellent view of the complex geology in the southeast "corner" of the crater. Sections of Coconino-Toroweap, Kaibab, and Moenkopi bedrock are visible in the crater wall beneath Kaibab and Coconino ejecta. The bedrock units are uplifted and, as can be seen, dip at high angles into the crater wall. Fig. 19.13 is a perspective view of the scene, showing that movement along two large, vertically-oriented faults has juxtaposed Coconino with Kaibab and Kaibab with Moenkopi. For ease of discussion, the crater wall has been subdivided into three blocks: A farthest to the north and east, B in the center, and C closest to our current position south and west of the three blocks. If we begin by looking at Block B (Fig. 19.13), the strata in it were uplifted 78 m relative to their pre-impact positions during the excavation phase of the crater-forming event. The strata in Block A were uplifted 45 m farther, juxtaposing Coconino with Kaibab. The uplift along the two faults bounding Block B was different, producing torque in the block that distorted the strata. That can be seen from this vantage point by tracing the white sandstone marker bed of the upper Kaibab (Fig. 19.13).

Comparing the overlying Kaibab sections in blocks A and B, it is also evident that the Kaibab in Block A is truncated, indicating a large section of the unit was, at that location in the crater wall, sheared radially outward during the crater-forming process. There are 3 large cracks in the upper crater wall that are missing the uppermost Kaibab and they are all on the south side of the crater. That type of radially-directed shearing was not recognized until relatively recently (Kring *et al.*, 2011a), when it was described in overturned Kaibab. The first stop in the Crater Rim West trail guide (Chapter 18) is a locality with that type of shearing.

The particular section of the crater wall in front of us was exquisitely mapped by Shoemaker (Fig. 4.4) and the relative displacements along the faults measured by Denton and Kring (2015). For another view of this section of the crater wall, please also refer to Fig. 18.18.

Thrust Faults and Anticlines in Crater Walls

Looking towards the northwest corner of the crater (Fig. 19.14), we can see the tear fault that we utilized in our earlier descent to the crater floor. The drag fold on the west side of the fault is easily visible from this perspective. Scanning around the crater wall to the west, we see Barringer Point, which is one of the highest point on the crater rim. The Beta Mbr of the Kaibab Fm is unusually thick beneath Barringer Point because of one or more thrust faults. The thickened sequence contributes to the uplift of the crater wall and has created an anticline.

Another thrust fault can be seen beneath Moon Mountain (Fig. 19.14). In this case, a section of the Alpha Mbr of the Kaibab Fm has been duplicated, forming another anticline and topographic high.

These types of faults occur in several locations around the crater, in both the Alpha and Beta Mbrs of the Kaibab, and are responsible for a significant portion of crater rim uplift. They occur on the west, north, and east sides of the crater. The thrusts are often small, but can occur multiple times, producing a cumulative effect. Bedding within the Kaibab (particularly the Beta Mbr) is often indistinct, so the amount of bedding repetition cannot always be measured quantitatively. Nonetheless, most of the uplift in the largest anticlines appears to be a direct consequence of the thrusts. Shoemaker and Kieffer (1974) suggested that a concentration of thrust faults in the northwest wall of the crater indicates the impacting asteroid was moving from southeast to northwest.

Breccia at the (Permian-Triassic) Kaibab-Moenkopi Boundary

In some parts of the crater, a breccia occurs at the Kaibab-Moenkopi boundary. An example is visible along the trail (Fig. 19.15). The breccia is often dominated by Kaibab clasts, as is the lower portion of the outcrop here. Another outcrop of this breccia occurs along the north wall of the crater (Fig. 19.16) where it can be traced for over 100 m. Several other outcrops occur on the south wall of the crater near our present location. The matrix is often sandy and weathers differently than enclosed dolomite clasts.

There are three possible origins for the breccia: (1) the breccia is a karst product that existed at the top of the Kaibab before impact; (2) the breccia was formed by shear between the Kaibab and Moenkopi during the impact; and (3) the breccia was produced when debris on the transient crater wall was injected between the Kaibab and Moenkopi during impact.

Shoemaker and Kieffer (1974) described a similar unit adjacent to the museum complex. At that locality, the uppermost unit of Kaibab has irregular to chaotic bedding with clasts of sandstone and sandy dolomite. They interpreted the unit to represent a karst surface that developed during the late Permian and/or early Triassic. Breccias in the uppermost interval of Kaibab have been described elsewhere on the Colorado Plateau, particularly in Utah. Paul Knauth (personal communication, 2007) told me that several examples also occur in the Grand Canyon region. Those breccias, however, are dominated by chert pebbles.

Although the outcrop described by Shoemaker and Kieffer (1974) is composed entirely of Kaibab clasts, some outcrops elsewhere in the crater contain red clasts. These are sometimes red-stained Kaibab clasts, but in many cases are true Moenkopi clasts (Fig. 19.17), which is inconsistent with scenario (1). The sand matrix does not appear to be a simple sediment deposit, infiltrating and burying karst dolomite cobbles. Rather, it sometimes appears to be injected through fractures in clasts (Fig. 19.16). The unit is sometimes compressed into small folds, whose limbs can be sheared (Fig. 19.18). Fractures and displacements also occur within Kaibab-dominated outcrops of the breccia unit (Fig. 19.19 and 19.20). Elongated clasts are sometimes aligned, as if part of a flow (Fig. 15.20). The presence of Moenkopi and Kaibab clasts, injection textures, and internal shearing of clasts seems to point to scenarios (2) and (3). The folding of breccia horizons, however, suggests the breccia unit already existed. That either points to scenario (1) or requires formation and lithification of the breccia early in the cratering process and then folding late in the cratering process. A block of Kaibab-dominated breccia was found on the rim of the crater. If it was not moved during earlier exploration phases at the crater and is a part of the ejecta blanket, then it points to scenario (1) or the special circumstance of formation and lithification of an impact breccia early in the cratering process. In addition, several cobbles of the breccia have been found in distal ejecta, such as on a Moenkopi ridge on the north side of the crater (Kring *et al.*, 2015), also pointing to scenario (1) in which the breccia was a stratigraphic unit in the impact target. Alternatively, there may be two types of breccias at the Kaibab-Moenkopi boundary, one that existed in the target sequence and another that was generated during the impact.

Continue hiking towards the crater rim.

Coconino-Toroweap Impact Ejecta

When we reach the rim of the crater, the ground will be paved with ejected debris from the Coconino-Toroweap Fms (Fig. 19.21). Those sandstones dominate the surface of the ejecta blanket on the south side of the crater. Only small patches of that type of debris are found on other sides of the crater.

The sandstone ejecta is dominated by cobble- to small boulder-size fragments. These fragments are much smaller than the immense boulders of Kaibab that we observed at the beginning of our excursion. Immediately after the impact event, this Coconino debris was probably covered with a layer of fallback debris. Erosion removed it.

The Coconino is formed from an eolian sand. The blocks of debris on the surface are laminated, but it is sometimes difficult to determine if the laminae are cross-beds. Rare examples of the truncated interface of a cross-bed can be found, however (Fig. 19.21 inset). Appropriately, the sandstone is being eroded to produce another generation of eolian sands. The new sand forms small dunes on the southern flank of the crater. Long wind streaks of sand stretch from the crater towards the northeast, reflecting the prevailing southwest wind. The sand dunes lap up against two-needle pinyon pine and juniper trees. The latter were examined by Barringer's team. Tree-rings indicated some of the trees are more than 700 years old (in 1905), or more than 800 years old now. This is the minimum age of the crater.

A short distance to the west is the top of the 1,376 ft deep borehole that was drilled through the crater wall and into a fractured and/or brecciated sequence contaminated with meteoritic debris. (See Chapter 4 for details.) Even farther to the west are the "Silica Pits," which are composed of finely comminuted Coconino. At that location, fractured versions of the blocks at our feet occur in a massive and brilliantly white matrix of "rock flour."

That deposit is covered with a breccia that contains red Moenkopi fragments. Because the only outcrops of Moenkopi on the south side lie below the crater rim on the interior crater wall, those Moenkopi-bearing deposits are candidates for surviving fallback breccia. Shoemaker (1960), however, mapped them as post-impact alluvium. Although they may be secondary deposits, they contain many of the eroded remnants of fallback debris, including Class 4 and 5 shock-metamorphosed Coconino sandstone.

To examine hinges in overturned Moenkopi and Kaibab, however, we need to follow the rim trail towards the east. We will use the Crater Rim East trail guide for the remainder of the hike back to the museum.



Fig. 19.1. The remnants of a stone building sit at the top of a tear fault through the crater rim. The building was the original museum at the crater. It sits on top of the impact ejecta blanket, which has an inverted Moenkopi, Kaibab, and Coconino sequence.





Fig. 19.2. Outcrop of shocked and ejected Coconino sandstone. The sample is transitional to “rock flour” and may contain remnant cores of relatively unshocked Coconino sandstone. Shock may have created a slaty cleavage within these types of units that is distinct from pre-existing target cross-bedding. This outcrop of Coconino debris was deposited in a depression on a hummocky surface of Kaibab ejecta. The Coconino debris in this outcrop is more severely damaged than Kaibab material in the area.

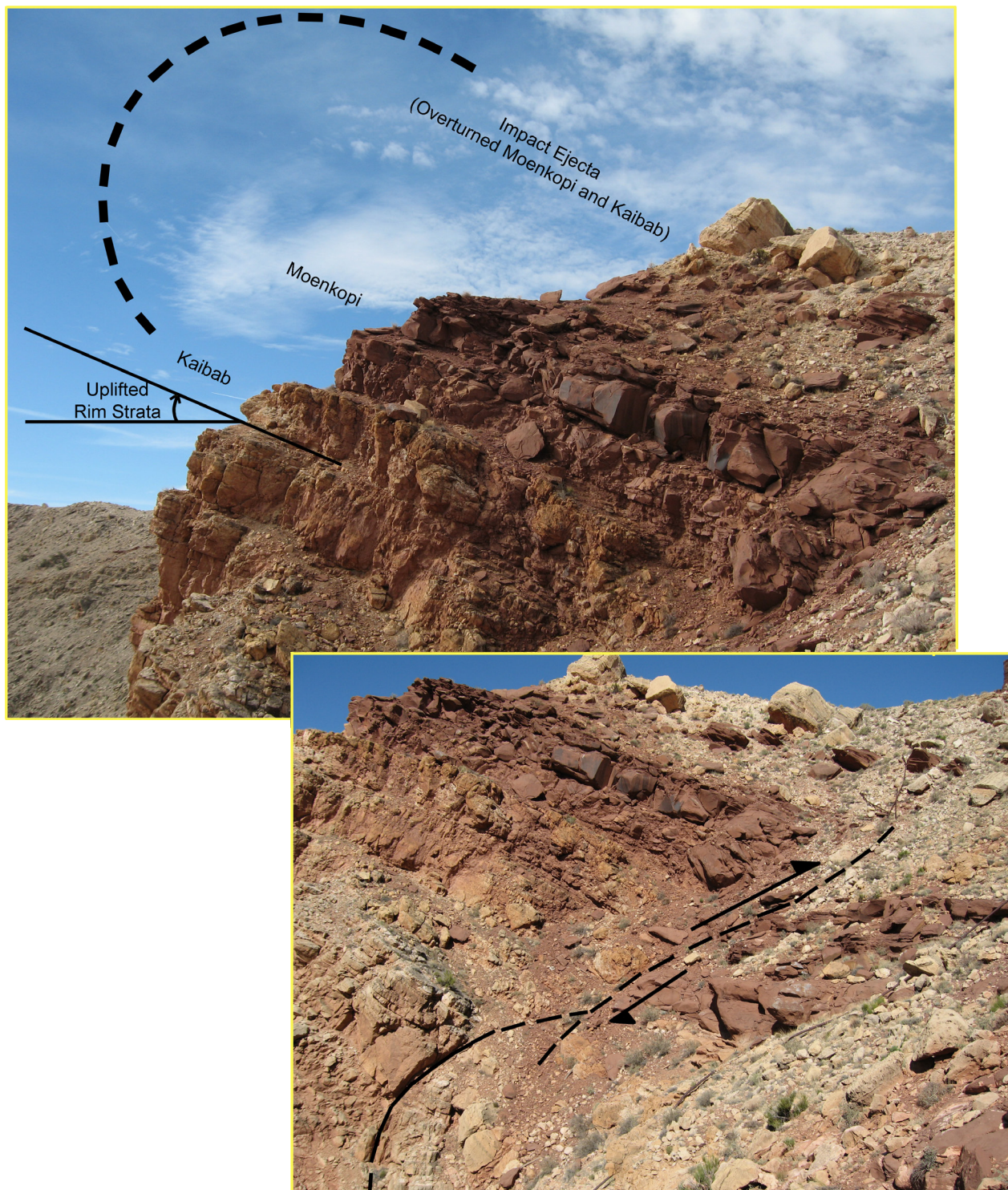


Fig. 19.3. View of structure in the crater wall. Strata that had a horizontal pre-impact orientation were uplifted during crater excavation (top left). Dips are often 30 to 40 degrees. The strata were also overturned and ejected. This further enhanced rim height and distributed debris over the surrounding landscape. Crater wall uplift was not uniform. Differential uplift was accommodated (or facilitated) by tear faults (bottom right) that may have been produced along pre-existing joints. Offsets along these tear faults range from meters to several tens of meters. The structure illustrated (bottom right) is simplified. Small thrust faults, for example, also occur in this part of the crater, but are not easily seen in this image.



Fig. 19.4. Outcrop of allogenic breccia, fall-back breccia, and Pleistocene talus (upper left). Close-up views of allogenic breccia (bottom left), fall-back breccia (above), and fragment of impacting asteroid eroding out of fall-back breccia (left center). Fall-back breccia contains Moenkopi, whereas allogenic breccia is dominated by Kaibab and Coconino.

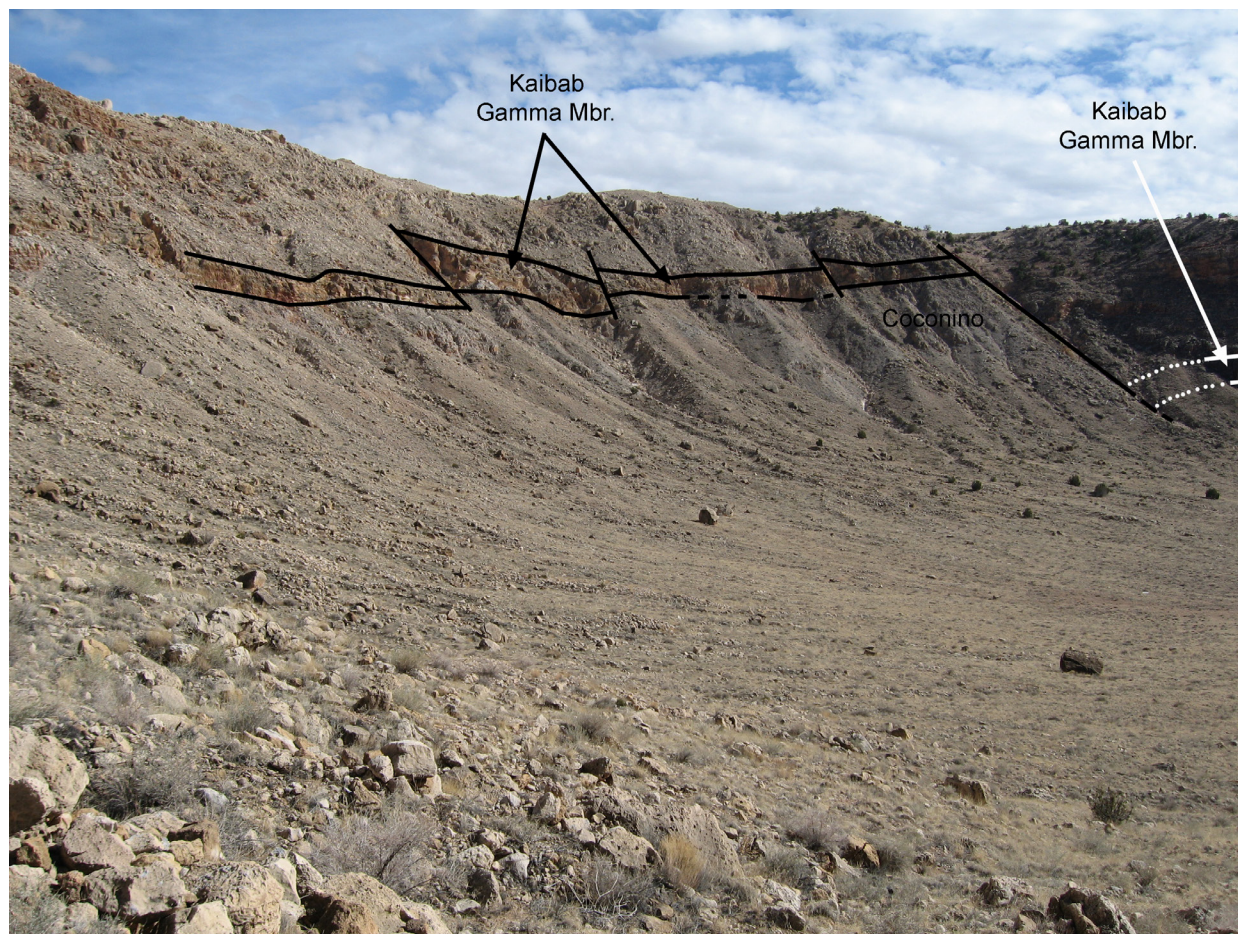


Fig. 19.5. From this vantage point we can trace the Gamma Mbr of the Kaibab Fm along the east crater wall, into the southeast corner of the crater, and part way across the south crater wall. The unit is off-set by several faults, including a large tear fault in the corner. The displacement along that tear fault is 45 m. On the north side of the tear fault, 90 m of Coconino sandstone is exposed. Coconino is not exposed on the south side of fault and only traces of Coconino and Toroweap can be found along the south crater wall. Those units along the south crater wall were buried by allogenic and fall-out breccia (like the deposits examined in the previous figure) and Pleistocene talus (like that in the foreground of this photograph).



Fig. 19.6. The lower walls of the crater are covered by Pleistocene sediments. Talus derived from the upper crater walls was produced first (Qpt) and then dissected, so that only small remnants survive. A younger alluvium (Qp) spilled through the dissecting gullies and flowed towards the center of the crater. Two periods of wetter climatic conditions than we have today are implied. The margins of the younger alluvium deposit are now being dissected and overlapped by recent playa deposits. View is to the east from the crater floor.

Fig. 19.7. A hill composed of Pleistocene lake sediments rises on the north side of the crater floor and is surrounded by recent playa sediments. The lake sediments imply at least one period of wetter climatic conditions, sufficient to raise the water table >69 m above its current level. The lake sediments are nearly 30 m thick and cover the original floor of the crater. View is looking west. The trail that descends from the northwest corner of the crater rim cuts across the slope in the background.

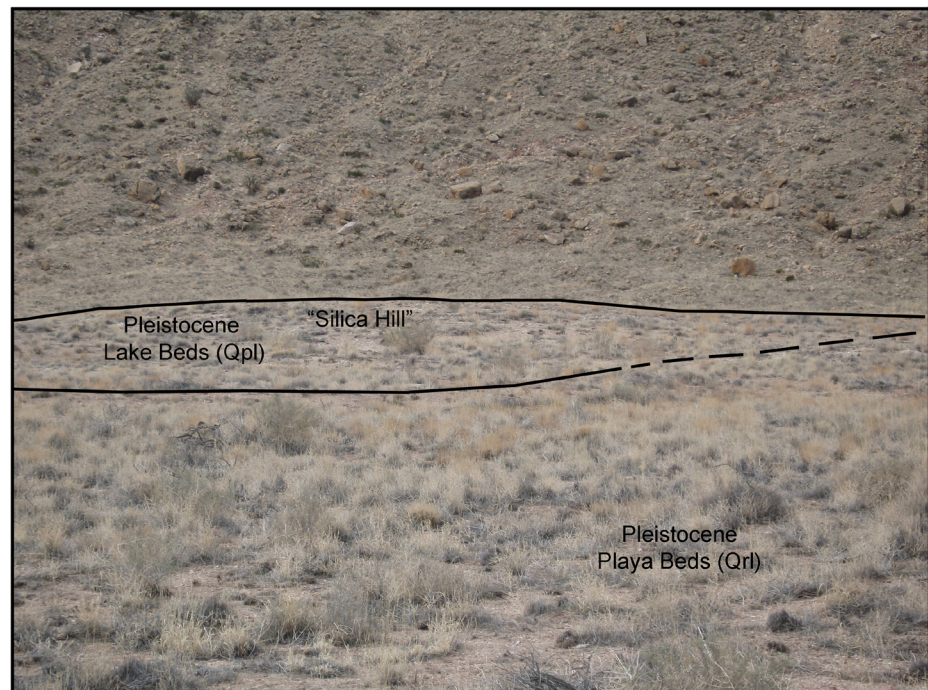




Fig. 19.8. Desiccation polygons or mud cracks occur on the crater floor, reflecting current arid conditions and intermittent rainfall. These features are found in playa sediment, new fine-grained alluvium, and remnants of drilling mud generated during mining operations. These recent, relatively soft-sediment features are similar to lithified features in the Triassic Moenkopi Fm in the upper crater walls (*e.g.*, Fig. 2.4).

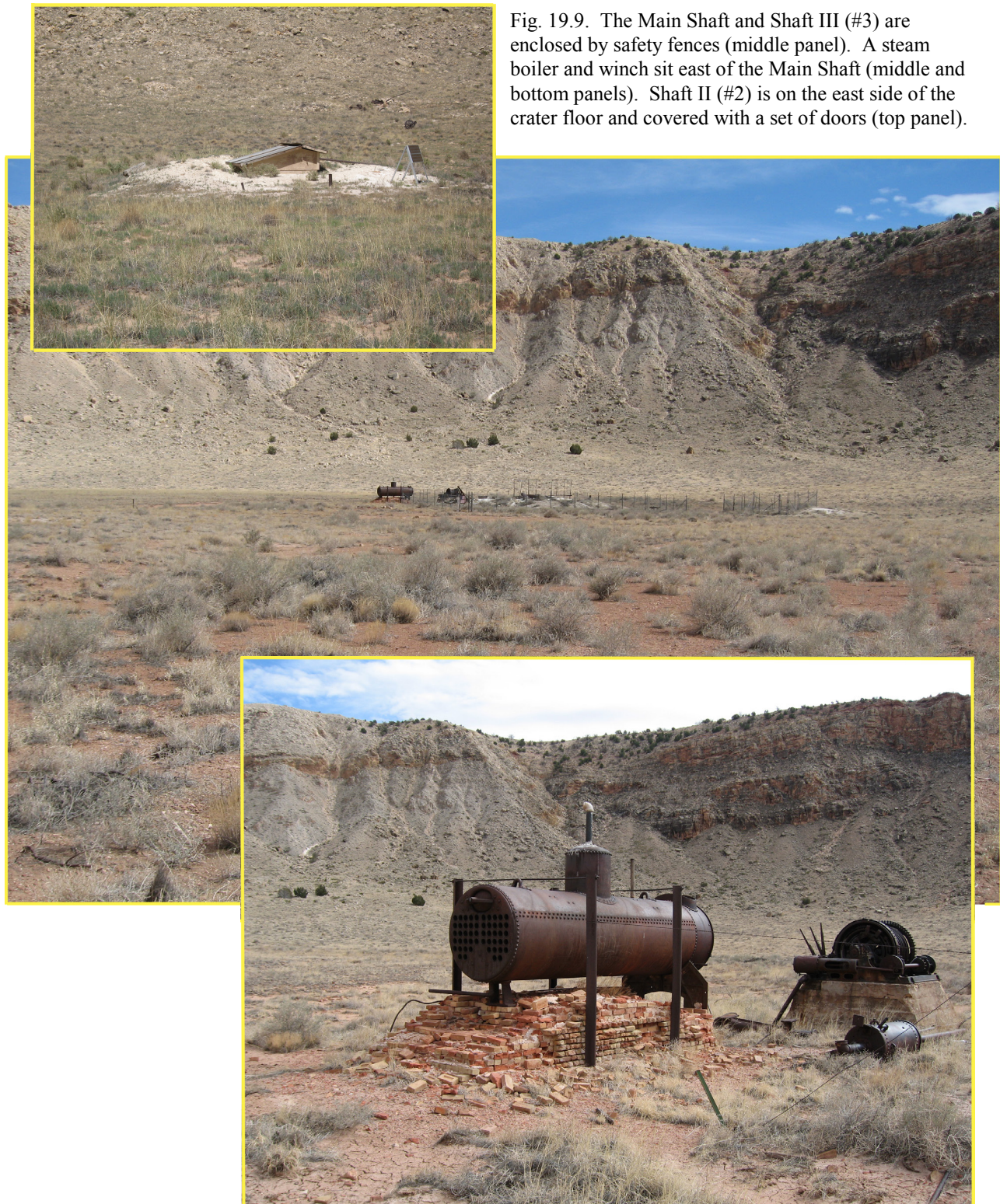


Fig. 19.9. The Main Shaft and Shaft III (#3) are enclosed by safety fences (middle panel). A steam boiler and winch sit east of the Main Shaft (middle and bottom panels). Shaft II (#2) is on the east side of the crater floor and covered with a set of doors (top panel).

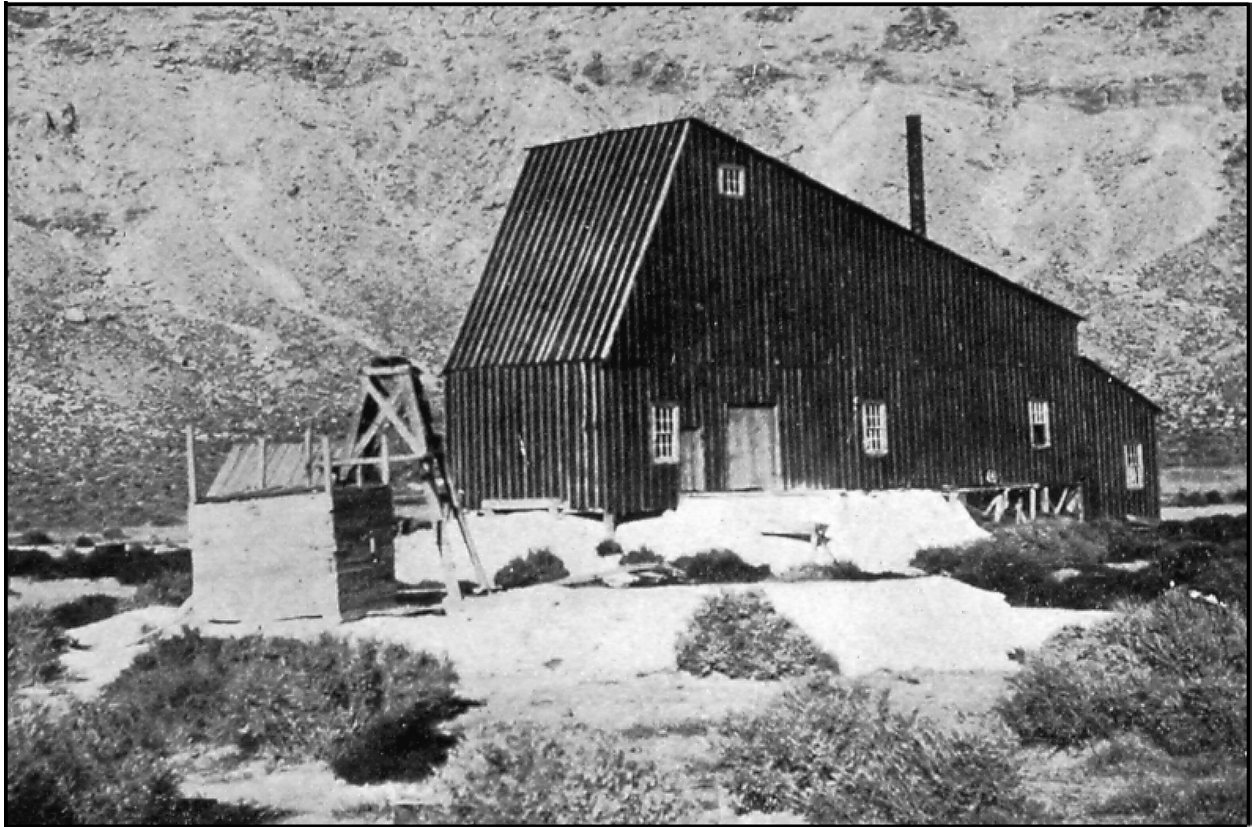


Fig. 19.10. Main shaft house in the center of the crater floor. The shaft is very wide so that it would be suitable for two compartments. Excavation in the shaft reached a depth of ~230 ft, which was ~20 ft beneath the water table. Pumps were installed, but the bottom of the shaft collapsed and the effort to descend farther was abandoned. (Bottom panel of Plate XI in Barringer, 1910.)

Fig. 19.11. A cave in the Toroweap Formation is visible from the trail while hiking out of the crater (right). Water flows from the rim of the crater down through vertical fractures in the crater wall (middle and bottom panels). Water is then flushed into the crater at the Kaibab-Toroweap contact and through the Toroweap, causing preferential erosion of Toroweap sand. This sequence is a potential analogue for some local hydrological and erosional features on Mars.



Note: This and other niches around the crater contain pack-rat middens. Please do not disturb the middens, because they will be analyzed to better determine the age of the crater and how climate has changed since the crater formed. The middens may also harbour the deadly Hantavirus Pulmonary Syndrome.

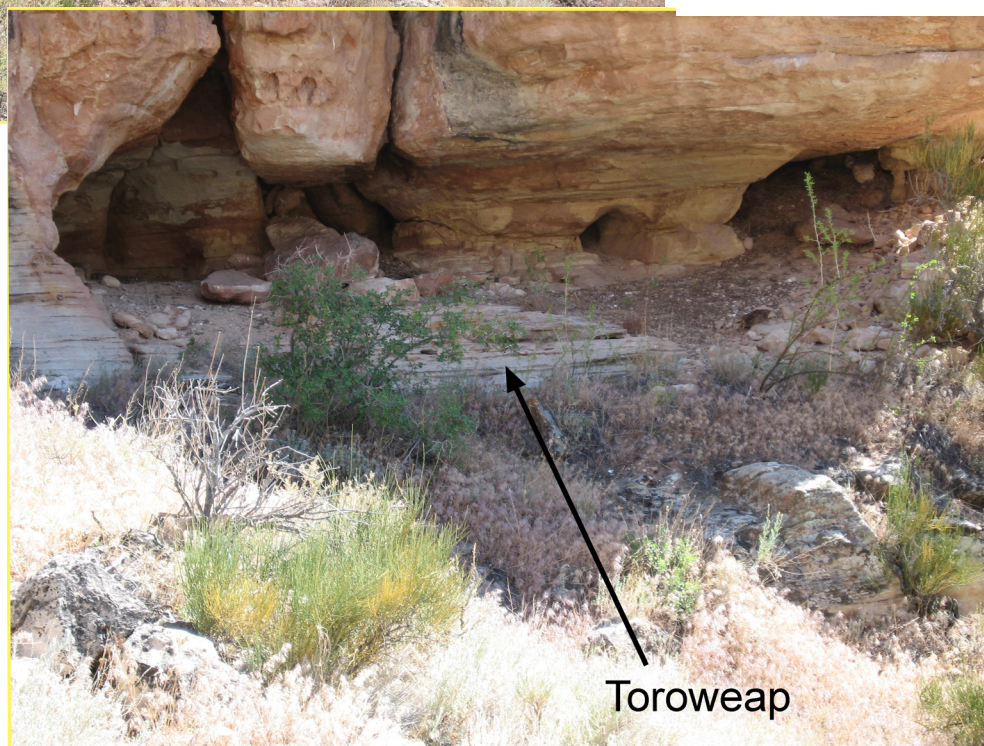




Fig. 19.12. Our route from the crater floor to the crater rim follows a trail that was developed by the Standard Iron Company during its 1903 to 1908 operations. The skeleton of a wooden slide (middle and bottom panels) also survives and is visible on the far side of a ravine that is cut along a tear fault. A winch sits at the top of the slide on the crater rim (top panel).

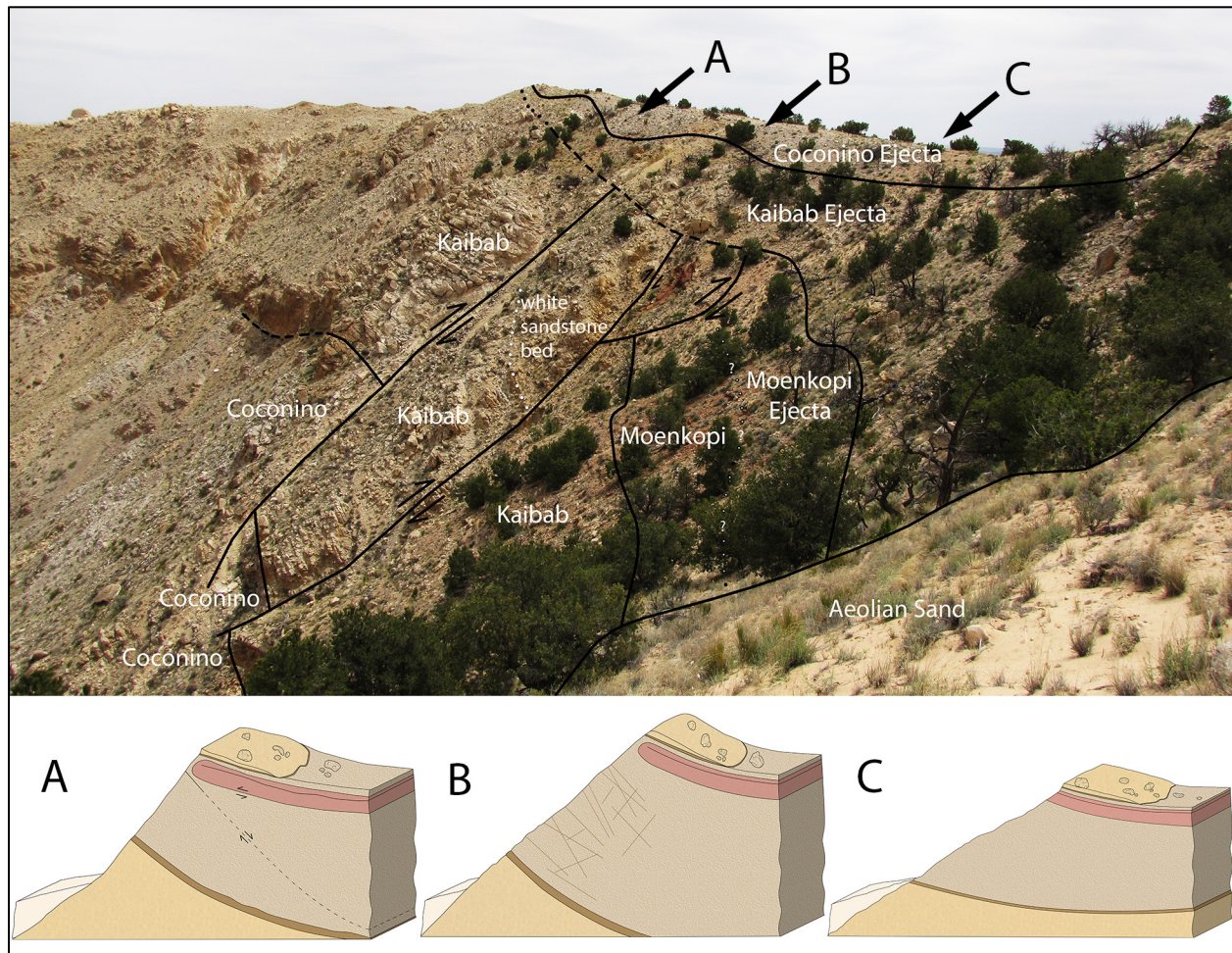


Fig. 19.13. The differential offsets along faults in the walls of the crater can be dramatic, as seen from the trail exiting the southeast side of the crater. The geology, originally mapped by Shoemaker, was recently remapped and measured (Denton and Kring, 2015). The geology in the image can be divided into three blocks: A, B, and C, separated by two right lateral faults. That is, Block A is uplifted higher than B, which is uplifted higher than C. Block B is caught between the two faults and differential motion along them lifted the eastern edge of the block ~5 m higher than the western edge, shattering strata throughout the block. The offset between blocks A and B was previously measured to be 45 m (Shoemaker and Kieffer, 1974). The offset between blocks B and C is about 7 m. The Coconino label on the image refers to both Coconino and Toroweap, although all units are visible in the schematic diagrams using the same color scheme as in Fig. 7.4. The strata in Block B, as measured at the Toroweap-Kaibab contact, were uplifted 78 m relative to their pre-impact positions. Additional faults affect the Kaibab (in Block A – see schematic) and Moenkopi (in Block C – see the image). See Denton and Kring (2015) for details. See also the perspective from Barringer Point shown in Fig. 18.17.

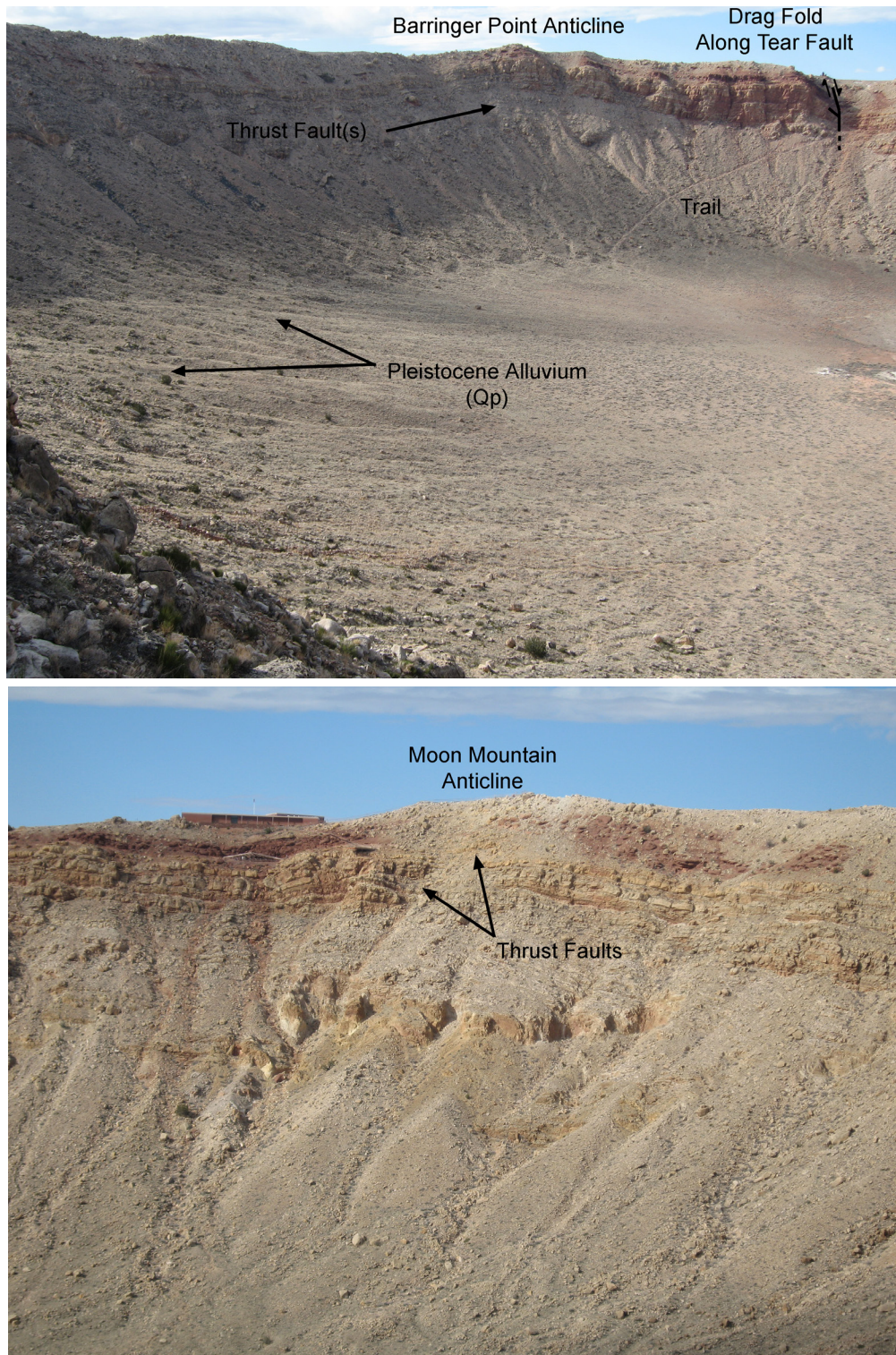


Fig. 19.14. Structural features associated with crater rim uplift are visible in distant crater walls. To the west-northwest (top panel) the Barringer Point anticline is visible; it is uplifted by one or more thrusts in the Beta Mbr of the Kaibab Fm. Moving clockwise around the crater rim, a complex tear fault is visible in the northwest “corner” of the crater. Drag along that fault is apparent to the left of the fault, near the trail we descended. Pleistocene alluvium that was shed from the crater walls is also visible in that same view. To the north, adjacent to the museum complex (bottom panel), the Moon Mountain anticline is visible. It is uplifted by thrust faults within the Alpha Mbr of the Kaibab Fm.



Fig. 19.15. The trail rises through Moenkopi (upper left). Slightly below trail level is the Kaibab-Moenkopi boundary (left center). Here, and at a few other locations around the crater, a breccia occurs at this boundary. Portions of the breccia are dominated by Kaibab clasts (lower right), although some portions contain Moenkopi clasts (upper right), including blocks with pre-existing desiccation cracks.



Fig. 19.16. Outcrop of breccia at the Kaibab-Moenkopi boundary. Clasts of dolomite are being etched by acidic water. The matrix is sandy and probably calcareous. The matrix appears to flow through a fracture separating a Kaibab cobble (upper center). Differential weathering of the sandy matrix and carbonate clasts accentuate the texture of the breccia. This outcrop is part of an extensive bed that can be traced along the north wall of the crater.

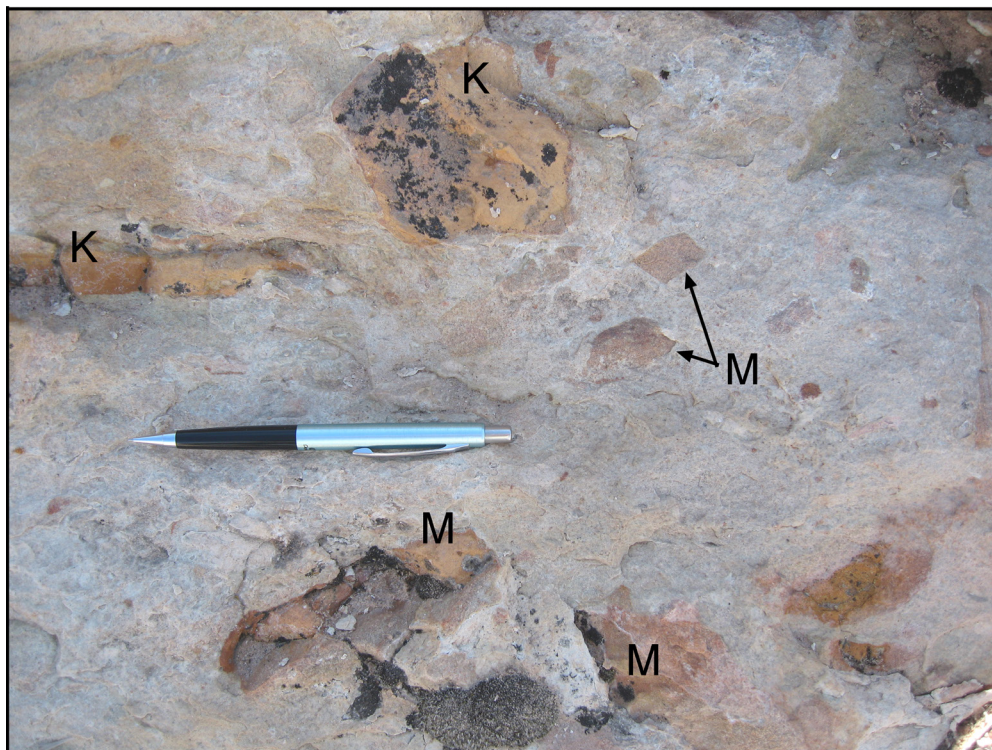


Fig. 19.17. Breccia along Kaibab-Moenkopi boundary that contains clasts from both units. Kaibab clasts are yellow and Moenkopi clasts are red. In case color reproduction is poor, they are labeled K and M, respectively. This outcrop is located in the southeast corner of the crater.

Fig. 19.18. Beds along the Kaibab-Moenkopi boundary have been compressed, forming folds whose limbs are sometimes sheared along small off-set faults. This outcrop is located in the southeast corner of the crater.





Fig. 19.19. Clasts or remnant beds within the breccia at the Kaibab-Moenkopi boundary have been fractured, displaced, and rotated. This outcrop is along the north wall of the crater.

Fig. 19.20. Large clast or remnant bed that has been fractured and displaced. Smaller clasts populate the breccia above and to the right of the large sheared clast. Intermediate-size clasts are at the top of the view (upper right). This outcrop is along the north wall of the crater.





Fig. 19.21. Most of the south rim of the crater is covered with debris from the Toroweap and Coconino formations. The eolian Coconino sandstone is being eroded to produce a second generation of aeolian sands that now blanket portions of the south rim. Most blocks appear to have fractured along cross-bed contacts, because there are very few blocks with any hint of cross-bedding. An exception is shown above.

❖ Bibliography

Note: This bibliography contains the sources used in the text above. To assist readers with other projects, it also includes a broader list of publications that have been involved in the developing story of the crater.

Abrahams, H.J., ed. (1983) *Heroic Efforts at Meteor Crater, Arizona: Selected Correspondence between Daniel Moreau Barringer and Elihu Thomson*. Associated University Press, East Brunswick, 322 p.

Ackermann, H.D. and Godson, R.H. (1966) P-wave velocity and attenuation summary, FY-66. In *Investigation of in situ physical properties of surface and subsurface site materials by engineering geophysical techniques*, annual report, fiscal year 1966, edited by J.S. Watkins. NASA Contractor Report (CR)-65502 and USGS Open-File Report 67-272, pp. 305-317.

Ackermann, H.D., Godson, R.H., and Watkins, J.S. (1975) A seismic refraction technique used for subsurface investigations at Meteor crater, Arizona. *Journal of Geophysical Research*, v. 80, pp. 765-775.

Adler, B., Whiteman, C.D., Hoch, S.W., Lehner, M., and Kalthoff, N. (2012) Warm-air intrusions in Arizona's Meteor Crater. *Journal of Applied Meteorology and Climatology*, v. 51, pp. 1010-1025.

Ai, H.-A. and Ahrens, T.J. (2004) Dynamic tensile strength of terrestrial rocks and application to impact cratering. *Meteoritics and Planetary Science*, v. 39, pp. 233-246.

Alexander, E.C. Jr. and Manuel, O.K. (1958) Isotopic anomalies of krypton and xenon in Canyon Diablo graphite. *Earth and Planetary Science Letters*, v. 2, pp. 220-224.

Altomare, C.M., Fagan, A.L., and Kring, D.A. (2014) Eolian deposits of pyroclastic volcanic debris in Meteor Crater. *Lunar and Planetary Science XLV*, Abstract #1448.

Amoroso, L. (2006) Age calibration of carbonate rind thickness in late Pleistocene soils for surficial deposit age estimation, Southwest USA. *Quaternary Research*, v. 65, pp. 172-178.

Anders, D., Kring, D.A., and Holzheid, A. (2010) Carbonate-rich material associated with Meteor Crater impact melt particles. *Lunar and Planetary Science XLI*, Abstract #1799.

Anders, E. and Lipschutz, M.E. (1966) Critique of paper by N.L. Carter and G.C. Kennedy, 'Origin of Diamonds in the Canyon Diablo and Novo Urei meteorites.' *Journal of Geophysical Research*, v. 71, pp. 643-674.

Artemieva, N.A. (2006) Size and velocity of Canyon Diablo meteorite - models comparison (abstract). *Meteoritics and Planetary Science*, v. 41, p. A17.

Artemieva, N. and Pierazzo, E. (2009) The Canyon Diablo impact event: Projectile motion through the atmosphere. *Meteoritics and Planetary Science*, v. 44, pp. 25-42.

Artemieva, N. and Pierazzo, E. (2011) The Canyon Diablo impact event: 2. Projectile fate and target

melting upon impact. *Meteoritics and Planetary Science*, v. 46, pp. 805-829.

Barnes, W.C. (1934) The "discovery" of Meteor crater. *Museum Northern Arizona* (Flagstaff). *Museum Notes*, v. 7, pp. 5-8.

Barringer, B. (1964) Daniel Moreau Barringer (1860-1929) and his crater (The beginning of the Crater Branch of Meteoritics). *Meteoritics*, v. 2, pp. 183-199.

Barringer, B. (1967) Historical notes on the Odessa Meteorite Crater. *Meteoritics*, v. 3, pp. 161-168.

Barringer, D.M. (1905) Coon Mountain and its crater. *Proceedings of the Academy of Natural Sciences of Philadelphia*, v. 57, pp. 861-886.

Barringer, D.M. (1910) Meteor Crater (formerly called Coon Mountain or Coon Butte) in northern central Arizona. Paper presented at the National Academy of Sciences, Princeton University, Nov. 16, 1909. 24 p. (plus 18 plates, and 3 maps).

Barringer, D.M. (1914) Further notes on Meteor Crater, Arizona. *American Journal of Science*, v. 39, pp. 482-483.

Barringer, D.M. (1924) Further notes on Meteor crater in northern central Arizona (No. 2). *Proceedings Academy of Natural Sciences of Philadelphia*, v. 76, pp. 275-278.

Barringer, D.M. (1958) From what direction did the meteorite come? *Footprints*, v. 30, no. 2, pp. 23-28.

Beatty, J.J. (1966) The great crater controversy. *Frontiers*, v. 30, pp. 112-117.

Bennett, J.H. and Manuel, O.K. (1967) On the origin of noble gas anomalies in Canyon Diablo graphite. *Earth and Planetary Science Letters* 3, 95-100.

Bills, D.J., Flynn, M.E., and Monroe, S. (2004) Hydrogeology of the Coconino Plateau and Adjacent Areas, Coconino and Yavapai Counties, Arizona. *USGS Scientific Investigations Report 2005-5222*, 116 p. plus plates.

Bingham, W.F. (1937) Summary of findings from exploration, geophysical survey, and test-drilling at Meteor crater, Arizona. *Pan-American Geologist*, v. 68, pp. 196-198.

Bjork, R.L. (1961) Analysis of the formation of Meteor crater, Arizona: A preliminary report. *Journal of Geophysical Research*, v. 66, pp. 3,379-3,387.

Blackwelder, E. (1932) The age of Meteor Crater. *Science*, v. 76, pp. 557-560.

Blau, P.J., Axon, H.J., and Goldstein, J.I. (1973) Investigation of the Canyon Diablo metallic spheroids and their relationship to the breakup of the Canyon Diablo meteorite. *Journal of Geophysical Research*, v. 78, pp. 363-374.

Boone, J.D. and Albritton, C.C. Jr. (1938) The impact of large meteorites. *Field and Laboratory*, v. 6, pp. 57-64.

- Borchers, B., Marrero, S., Balco, G., Caffee, M., Goehring, B., Lifton, N., Nishiizumi, K., Phillips, F., Schaefer, J., and Stone, J. (2016) Geological calibration of spallation production rates in the CRONUS-Earth project. *Quaternary Geochronology*, v. 31, pp. 188-198.
- Brereton, R.G. (1965) Aeromagnetic survey of Meteor crater, Arizona. *New York Academy Sciences, Annals*, v. 123, pp. 1175-1181.
- Brett, R. (1967) Metallic spherules in impactite and tektite glasses. *American Mineralogist*, v. 52, pp. 721-733.
- Brett, R.G. (1968) Opaque minerals in drill cuttings from Meteor Crater, Arizona. *U.S. Geological Survey Professional Paper 600-D*, D179-D180.
- Briley, D.J. and Moore, C.B. (1976) A checklist of published references to Barringer meteorite crater, Arizona, 1891-1970. *Center for Meteorite Studies, Arizona State University*, 71 p.
- Brown, F.M. (1933) The Age of Meteor Crater. *Science* 77, 239-240.
- Brown, D.E. and Lowe, C.H. (1980) Map of Biotic Communities of the Southwest. *U.S. Government Printing Office, Washington, DC*. (Also published as a supplementary map to *Biotic Communities: Southwestern United States and Northwestern Mexico*, edited by D.E. Brown, *University of Utah Press, Salt Lake City*, 1994).
- Bryan, J.B. (1978) Meteorite impact cratering on a digital computer: A simulation of the formation of Meteor (Barringer) Crater, Arizona. *Meteoritics*, v. 13, pp. 399-402.
- Bryan, J.B., Burton, D.E., Cunningham, M.E., and Lettis, L.A. Jr. (1978) A two-dimensional computer simulation of hypervelocity impact cratering: Some preliminary results for Meteor crater, Arizona. *Proceedings Lunar and Planetary Science Conference 9th*, pp. 3,931-3,964.
- Buchwald, V.F. (1975) *Handbook of iron meteorites*. *University of California Press, Berkeley*, v. 3, pp. 937-942.
- Buddhue, J.D. (1948) A sieve analysis of crushed sandstone from the Canyon Diablo, Arizona, meteorite crater. *Popular Astronomy*, v. 56, pp. 387-389.
- Bunch, T.E. and Cohen, A.J. (1964) Shock deformation of quartz from two meteorite craters. *Geological Society of America Bulletin*, v. 75, pp. 1,263-1,266.
- Busch, M.W., Giorgini, J.D., Ostro, S.J., Benner, L.A.M., Pravec, P., Kusnirak, P., Ireland, M.J., Scheeres, D.J., Broschart, S.B., Magri, C., Nolan, M.C., and Hine, A.A. (2007) Physical modeling of near-Earth asteroid (29075) 1950 DA. *Icarus*, v. 190, pp. 608-621.
- Carlson, R.H. and Roberts, W.A. (1963) Project Sedan: Mass Distribution and Throwout Studies. *U.S. Atomic Energy Commission, Report PNE-217F*, 143 p.
- Camp C.L., Colbert E.H., McKee E.D., and Welles S.P. (1947) A guide to the continental Triassic of northern Arizona. *Plateau*, v. 20, pp. 1-9.
- Carter, N.L. (1965) Basal quartz deformation lamellae--a criterion for recognition of impactites.

American Journal of Science, v. 263, pp. 786-806.

Carter, N.L. and Kennedy G.C. (1964) Origin of diamonds in the Canyon Diablo and Novo Urei meteorites. *Journal of Geophysical Research*, v. 69, pp. 2,403-2,421.

Carter, N.L. and Kennedy G.C. (1966) Origin of diamonds in the Canyon Diablo and Novo Urei meteorites — A reply. *Journal of Geophysical Research*, v. 71, pp. 663-672.

Cernok, A. and Kring, D.A. (2009) Were carbonate impact melts produced from the carbonate-rich target lithologies at Meteor Crater, Arizona? *Lunar and Planetary Science XL*, Abstract #1825.

Chamberlin, T.C. (1890) The method of multiple working hypotheses. *Science*, vol. XV, no. 366, pp. 92-96.

Chao, E.C.T. (1967) Impact metamorphism. In *Researches in Geochemistry*, v. 2, edited by P.H. Abelson, pp. 204-233. John Wiley and Sons, New York.

Chao, E.C.T., Shoemaker, E.M., and Madsen, B.M. (1960) First natural occurrence of coesite. *Science*, v. 132, pp. 220-222.

Chao, E.C.T., Fahey, J.J., Littler, J., and Milton, D.J. (1962) Stishovite, SiO₂, a very high pressure new mineral from Meteor crater, Arizona. *Journal of Geophysical Research*, v. 67, pp. 419-421.

Chao, E.C.T. (1966) Impact metamorphism. U.S. Geological Survey, Astrogeologic Studies Annual Progress Report, pp. 135-168.

Cherukuru, N.W., Calhoun, R., Lehner, M., Hoch, S.W., and Whiteman, C.D. (2015) Instrument configuration for dual-Doppler lidar coplanar scans: METCRAX II. *Journal of Applied Remote Sensing*, v. 9, 14 p., 096090, doi:10.1117/1.JRS.9.096090.

Clark, S.E. (2011) Analysis of Ejecta Deposits at Barringer Meteorite Crater, Northern Arizona. M.S. Thesis, Northern Arizona University, 40 p.

Collins, G.S., Mason, K.D., and Kring, D.A. (2016) Numerical modeling of Meteor Crater: Simple crater formation in a layered sedimentary target. 79th Annual Meeting of The Meteoritical Society, Abstract #6418.

Cook, C.S. (1964) Mass of the Canyon Diablo meteoroid. *Nature*, v. 204, p. 867.

Crocket, J.H. (1972) Some aspects of the geochemistry of Ru, OS, Ir and Pt in iron meteorites. *Geochimica et Cosmochimica Acta*, v. 36, pp. 517-535.

Crowson, H.L. (1971) A method for determining the residual meteoritical mass in the Barringer meteor crater. *Pure and Applied Geophysics*, v. 85, pp. 38-68.

Darton, N.H. (1910) A reconnaissance of parts of northwestern New Mexico and northern Arizona. USGS Bulletin 435, 88 p. and 17 pl. (including 3 folded maps).

Davis, N.F. (2016) *Images of America: Meteor Crater*. Arcadia Publishing, Charleston, 127 p.

Davis, O. and Kring, D.A. (2002) Preliminary analysis of the late Pleistocene lake sediments deposited in

Barringer Crater, Coconino County, Arizona (abstract). Abstract volume for the Annual Meeting of the Arizona-Nevada Academy of Sciences.

Davison, J.M. (1910) A contribution to the problem of Coon Butte. *Science*, v. 32, pp. 724-726.

Denton, C.A. and Kring, D.A. (2016) Differential vertical and radial displacement along faults in the crater wall during the formation of Meteor Crater, AZ. *Lunar and Planetary Science XLVII*, Abstract #1197.

Derby, O.A. (1895) Constituents of the Canyon Diablo Meteorite. *American Journal of Science*, v. 49, pp. 101-110.

Dietz, R.S. (1963) Astroblemes: Ancient meteorite-impact structures on the Earth. Middlehurst, B.M. and Kuiper, G.P., eds., *The Moon, Meteorites and Comets*, University of Chicago Press, Chicago, v. IV, pp. 285-300.

Dorninger, M., Whiteman, C.D., Bica, B., Eisenbach, S., Pospichal, B., and Steinacker, R., (2011) Meteorological events affecting cold-air ponds in a small basin. *Journal of Applied Meteorology and Climatology*, v. 50, pp. 2223-2234.

Duffield, W., Riggs, N., Kaufman, D., Champion, D., Fenton, C., Forman, S., McIntosh, W., Hereford, R., Plescia, J., and Ort, M. (2006) Multiple constraints on the age of Pleistocene lava dam across the Little Colorado River at Grand Falls, Arizona. *GSA Bulletin*, v. 118, pp. 421-429.

Durda, D.D. and Kring, D.A. (2015) Size-frequency and spatial distribution of ejecta blocks at Meteor Crater, AZ. *Lunar and Planetary Science XLVI*, Abstract #1487.

Elson, M.D. and Ort, M.H. (2003) Collaborative research at Sunset Crater Volcano. *Archaeology Southwest*, v. 17(1), pp.4-6.

Elston, W.E. (1990) How did impact processes on Earth and Moon become respectable in geological thought? *Earth Sciences History*, v. 9, pp. 82-87.

Elwood Madden, M.E., Kring, D.A., and Bodnar, R.J. (2006) Shock reequilibration of fluid inclusions in Coconino sandstone from Meteor Crater, Arizona. *Earth and Planetary Science Letters*, v. 241, pp. 32-46.

Eppler, D.T., Ehrlich, R., Nummedal, D., and Schultz, P.H. (1983) Sources of shape variation in lunar impact craters: Fourier shape analysis. *GSA Bulletin*, v. 94, pp. 274-291.

Fahey, J.J. (1964) Recovery of coesite and stishovite from Coconino sandstone of Meteor Crater, Arizona. *American Mineralogist*, v. 49, pp. 1643-1647.

Fairchild, H.L. (1907) Origin of Meteor Crater (Coon Butte), Arizona. *Geological Society of America Bulletin*, v. 18, pp. 493-504.

Fairchild, H.L. (1930) Nature and fate of the Meteor crater bolide. *Science*, v. 72, pp. 463-467.

Farrington, O.C. (1906) Analysis of 'iron shale' from Coon Mountain, Arizona. *American Journal of Science*, v. 22, pp. 303-309.

Fazio, A., Folco, L., D'Orazio M., Frezzotti, M. L., and Cordier, C. (2014) Shock metamorphism and impact melting in small impact crater on Earth: Evidence from Kamil crater, Egypt. *Meteoritics and Planetary Science*, v. 49, pp. 2175-2200.

Fechtig, H., Gault, D.E., Neukum, G., and Schneider, E. (1972) Laboratory simulation of lunar craters. *Naturwissenschaften*, v. 59, no. 4, pp. 151-157.

Fenton, C.R., Mark, D.F., Barfod, D.N., Niedermann, S., Goethals, M.M., and Stuart, F.M. (2013) $^{40}\text{Ar}/^{39}\text{Ar}$ dating of the SP and Bar Ten lava flows AZ, USA: Laying the foundation for the SPICE cosmogenic nuclide production-rate calibration project. *Quaternary Geochronology*, v. 18, pp. 158-172.

Fletcher, L.A. (1906) A search for a buried meteorite. *Nature*, v. 74, pp. 490-492.

Foote, A.E. (1891) Geological features of the meteoric locality in Arizona. *Academy of Natural Sciences Philadelphia Proceedings*, v. 40, p. 407.

Foote, A.E. (1892) A new locality for meteoric iron with a preliminary notice of discovery of diamonds in the iron. *Proc. American Association of Advanced Science*, v. 40, pp. 279-283.

Forester, R.M. (1987) Late Quaternary paleoclimate records from lacustrine ostracodes. In Ruddiman, W.F. and Wright, H.E. Jr. (eds.), *North America and Adjacent Oceans During the Last Glaciation*, v. K-3, pp. 261-276. The Geology of North America. Geological Society of America, Boulder.

Foster, G.E. (1953) Arizona's Meteorite Crater. Meteor Crater Publications, Winslow, Arizona, 28 pp.
Foster, G.E. (1957) The Barringer (Arizona) meteorite crater. Meteor Crater, Ariz., Published Privately, 31 p.

Foster, G.E. (1964) The Meteor Crater Story. Meteor Crater Enterprises, Inc., Winslow, Arizona, 32 pp.

Frandsen, A.D. (1967) Project Pre-Schooner II: Postshot geologic and engineering properties investigations. U.S. Army Engineer Nuclear Cratering Group, Final Report PNE-516, 63 pp.

Fu., P., Zhong, S., Whiteman, C.D., Horst, T., and Bian, X. (2010) An observational study of turbulence inside a closed basin. *Journal of Geophysical Research*, v. 115, 15 p., D23106, doi:10.1029/2010JD014345.

Gaither, T.A., Hagerty, J.J., and Gulilikson, A.L. (2016) Meteor Crater impact melt formation: Evidence for carbonate melting. *Lunar and Planetary Science XLVII*, Abstract #2113.

Garvie, L. A. J. (2017) Preliminary observations on nanoprecipitates in iron meteorites. *Lunar and Planetary Science XLVIII*, Abstract #1601.

Gaither, T.A., Hagerty, J.J., McHone, J.F., Newsom, H.E. (2012) Characterization of impact ejecta deposits from Meteor Crater, Arizona. *Lunar and Planetary Science XLIII*, Abstract #1601.

Gault, D.E., Shoemaker, G., and Moore, H. (1973) Spray ejected from the lunar surface by meteoroid impact. NASA TN- D-1767.

Gault, D.E. (1974) Impact crater. In *A Primer in Lunar Geology*, NASA TMX 62359, pp. 137-175.

- Gentieu, N.P. (1958) The biography of a crater. *Footprints*, v. 30, no. 2., pp. 3-14.
- Gilbert, G.K. (1896) The origin of hypotheses, illustrated by the discussion of a topographic problem. *Science*, v. 3, pp. 1-13 (plus 1 plate).
- Goderis, S., Kalleson, E., Tagle, R., Dypvik, H., Schmitt, R.-T., Erzinger, J., and Claeys, P. (2009) A non-magmatic iron projectile for the Gardnos impact event. *Chemical Geology*, v. 258, pp. 145-156.
- Goldstein, J.I., Yang, J., and Scott, E.R.D. (2014) Determining cooling rates of iron and stony-iron meteorites from measurements of Ni and Co at kamacite-taenite interfaces. *Geochimica et Cosmochimica Acta*, v. 140, pp. 297-320.
- Grady, M.M. (2000) *Catalogue of Meteorites* (Fifth edition). Cambridge University Press, Cambridge, 689 p. (plus CD-ROM).
- Grant, J.A. and Schultz, P.H. (1993) Erosion of ejecta at Meteor Crater, Arizona. *Journal of Geophysical Research*, v. 98, pp. 15,033-15047.
- Gray, G.W. (1977) Cobalt, iron, nickel, and grain size distribution; Meteor Crater, Arizona. M.S. Thesis, Arizona State University, 129 pages.
- Greenwood, W.R. and Morrison, D.A. (1969) Genetic significance of the morphology of some impact bombs from Meteor crater, Arizona. *Meteoritics*, v. 4, pp. 182-183.
- Grier, J.A., Swindle, T.D., Kring, D.A., and Melosh, H.J. (1999) Argon-40/argon-39 analyses of samples from the Gardnos impact structure, Norway. *Meteoritics and Planetary Science*, v. 34, pp. 803-807.
- Grieve, R.A.F. (1982) The record of impact on Earth: Implications for a major Cretaceous/Tertiary impact event. Geological Society of America, Special Paper 190, pp. 25-37.
- Grieve, R.A.F. (1991) Terrestrial impact: The record in the rocks. *Meteoritics*, v. 26, pp. 175-194.
- Grieve, R.A.F. and Garvin, J.B. (1984) A geometric model for excavation and modification at terrestrial simple impact craters. *Journal of Geophysical Research*, v. 89, pp. 11,561-11,572.
- Grieve, R.A.F., Garvin, J.B., Coderre, J.M., and Rupert, J. (1989) Test of a geometric model for the modification stage of simple impact crater development. *Meteoritics*, v. 24, pp. 83-88.
- Grieve R., Rupert J., Smith J., and Theriault A. (1995) The record of terrestrial impact cratering. *GSA Today*, v. 5(10), pp. 189 and 194-196.
- Hager, D. (1953) Crater Mound (Meteor crater), Arizona, a geologic feature. *American Association of Petroleum Geologists, Bulletin*, v. 37, pp. 821-857.
- Hager, D. (1954) Notes on Crater Mound in answer to some points raised by H.H. Nininger. *American Journal of Science*, v. 252, pp. 695-697.
- Haiden, T., Whiteman, C.D., Hoch, S.W., and Lehner, M. (2011) A mass flux model of nocturnal cold-air intrusions into a closed basin. *Journal of Applied Meteorology and Climatology*, v. 50, pp. 933-943.

Haines, D.V. (1966) Petrography of Meteor Crater Core 4, Meteor Crater, Arizona. In: Investigation of in situ physical properties of surface and subsurface site materials by engineering geophysical techniques, annual report, fiscal year 1966, edited by J.S. Watkins. NASA Contractor Report (CR)-65502 and USGS Open-File Report 67-272, pp. 171-194.

Hall, R.A. (1965) Secondary meteorites from the Arizona crater. *Meteoritics*, v. 2, pp. 337-348.

Hargraves, R.B. and Perkins W.E. (1969) Investigations of the effect of shock on natural remanent magnetism. *Journal of Geophysical Research*, v. 74, pp. 2,576-2,589.

Heymann, D. (1964) Origin of the Canyon Diablo No. 2 and No. 3 meteorites. *Nature*, v. 204, pp. 819-820.

Heymann, D., Lipschutz, M.E., Nielsen, B., and Anders, E. (1966) Canyon Diablo meteorite: Metallographic and mass spectrometric study of 56 fragments. *Journal of Geophysical Research*, v. 71, pp. 619-641.

Hilton, C., Bermingham, K. R., Ash, R. D., Piccoli, P. M., Kring, D. A., McCoy, T. J., and Walker, R. J. (2017) HSE abundances and Re-Os model age of a metallic vein in Canyon Diablo graphite. *Lunar and Planetary Science XLVIII*, Abstract #1671.

Hoch, S.W. and Whiteman, C.D. (2010) Topographic effects on the surface radiation balance in and around Arizona's Meteor Crater. *Journal of Applied Meteorology and Climatology*, v. 49, pp. 1114-1128.

Hoch, S.W., Whiteman, C.D., and Mayer, B. (2011) A systematic study of longwave radiative heating and cooling within valleys and basins using a three-dimensional radiative transfer model. *Journal of Applied Meteorology and Climatology*, v. 50, 2473-2489.

Hodge, P.W. and Wright, F.W. (1970) Meteoritic spherules in the soil surrounding terrestrial impact craters. *Nature*, v. 225, pp. 717-718.

Holliday, V.T., Kring, D.A., Mayer, J.H., and Goble, R.J. (2005) Age and effects of the Odessa meteorite impact, western Texas, USA. *Geology*, v. 33, pp. 945-948.

Hooten, J.A., Ort, M.H., and Elson, M.H. (2001) Origin of Cinders in Wupatki National Monument. Technical Report No. 2001-12, Desert Archeology, Tucson, 20 p.

Hörz, F., Ostertag, R., and Rainey, D A. (1983) Bunte breccia of the Ries: Continuous deposits of large impact craters. *Reviews of Geophysics and Space Physics*, v. 21, pp. 1667-1725.

Hörz, F., Mittlefehldt, D.W., See, T.H., and Galindo, C. (2002) Petrographic studies of the impact melts from Meteor Crater, Arizona, USA. *Meteoritics and Planetary Science*, v. 37, pp. 501-531.

Hörz, F., Archer, P.D. Jr., Hiles, P.B., Zolensky, M.E., and Evans, M. (2015) Devolatilization or melting of carbonates at Meteor Crater, AZ? *Meteoritics and Planetary Science*, v. 50, pages 1050-1070.

Hoyt, W.G. (1987) Coon Mountain Controversies: Meteor Crater and the Development of the Impact Theory. The University of Arizona Press, Tucson, 442 p.

- Huntoon, P.W. (2000) Variability of karstic permeability between unconfined and confined aquifers, Grand Canyon, Arizona. *Environmental and Engineering Geoscience*, v. VI(2), pp. 155-170.
- Ivanov, B.A. and Basilevsky, A.T. (1985) Meteorite craters (in Russian). *Priroda*, v. 10, pp. 23-35.
- Ives P.C., Levin B., Robinson R.D., and Rubin M. (1964) U. S. Geological Survey radiocarbon dates VII. *Radiocarbon*, v. 6, pp. 37-76.
- Jakosky, J.J., Wilson, C.H., and Daly, J.W. (1932) Geophysical examination of Meteor crater, Arizona. *American Institute of Mining, Metallurgical, and Petroleum Engineers, Transactions*, v. 97, pp. 63-98.
- Jakosky, J.J. (1932) Geophysical methods locate meteorite. *Engineering and Mining Journal-Press*, v. 133, pp. 392-393.
- Johnson G.W. (1960) Note on estimating the energies of the Arizona and Ungava meteorite craters. California Univ., Livermore, Lawrence Radiation Lab. Report UCRL-6227, 18 pp. (Report prepared for the U.S. Atomic Energy Commission)
- Kaputskina, I.G. and Fel'dman, V.I. (1988) Fractionation of meteoritic material in the impact process (in Russian). *Geokhimiya*, v. 11, pp. 1547-1557.
- Kargel, J.S. Coffin, P., Kraft, M., Lewis, J.S., Moore, C., Roddy, D., Shoemaker, E.M. and Wittke, J.H. (1996) Systematic collection and analysis of meteoritic materials from Meteor crater, Arizona (abstract). *Lunar and Planetary Science*, v. XXVII, pp. 645-646.
- Kelley, V.C. and Clinton, J.N. (1960) Fracture Systems and Tectonic Elements of the Colorado Plateau. University of New Mexico Publications in Geology, No. 6, University of New Mexico Press, Albuquerque, 104 p.
- Kelly, W.R., Holdworth, E., and Moore, C.B. (1974) The chemical composition of metallic spheroids and metallic particles within impactite from Barringer meteorite crater, Arizona. *Geochimica et Cosmochimica Acta*, v. 38, pp. 533-543.
- Kieffer, S.W. (1971) Shock metamorphism of the Coconino sandstone at Meteor crater, Arizona. *Journal of Geophysical Research*, v. 76, pp. 5449-5473.
- Kieffer, S.W. (1974) Shock metamorphism of the Coconino sandstone at Meteor Crater. In: *Guidebook to the Geology of Meteor Crater, Arizona*, edited by E.M. Shoemaker and S.W. Kieffer. Center for Meteorite Studies Publication No. 17, Arizona State University, pp. 12-19.
- Kieffer, S.W. (1976) Shock processes in porous quartzite: Transmission electron microscope observations and theory. *Contributions to Mineralogy and Petrology*, v. 59, pp. 41-93.
- Kieffer, S.W. and Simonds, C.H. (1980) The role of volatiles and lithology in the impact cratering process. *Reviews of Geophysics and Space Physics*, v. 18, pp. 143-181.
- Koeberl, C., Reimold, W.U., and Shirey, S.B. (1995) Siltan impact crater, South Africa: Geochemistry of target rocks, breccias, and impact glasses, and osmium isotope systematics. *Geochimica et Cosmochimica Acta*, v. 58, pp. 2893-2910.

- Koeberl, C., Reimold, W.U., and Shirey, S.B. (1998) The Aouelloul crater, Mauritania: On the problem of confirming the impact origin of a small crater. *Meteoritics and Planetary Science*, v. 33, pp. 513-517.
- Kofman, R. S., Herd C. D. K., and Froese, D. G. (2010) The Whitecourt meteorite impact crater, Alberta, Canada. *Meteoritics and Planetary Science*, v. 45, pp. 1429-1445.
- Kreins, E.R. (1953) Results of a systematic study of the ratio of meteorite to oxidite at the Barringer Meteorite Crater of Arizona. *Meteoritics*, v. 1, pp. 29-30.
- Kring, D.A. (1997) Air blast produced by the Meteor Crater impact event and a reconstruction of the affected environment. *Meteoritics and Planetary Science*, v. 32, pp. 517-530
- Kring, D.A. (1999) Calamity at Meteor Crater. *Sky and Telescope*, vol. 98, no. 5, pp. 48-53.
- Kring, D.A. (2003) Meteor Crater & An Asteroid's Impact on Floral Ecosystems; with sidebar 'Megafauna & Dietary Flora.' *Wildflower*, v. 19(4), pp. 16-17 and 29.
- Kring, D.A. (2005) Hypervelocity collisions into continental crust composed of sediments and an underlying crystalline basement: Comparing the Ries (~24 km) and Chicxulub (~180 km) impact craters. *Chemie der Erde*, v. 65, pp. 1-46.
- Kring, D.A. (2006) Blast from the Past. *Astronomy*, v. 34(8), pp. 46-51.
- Kring, D.A. (2007) Guidebook to the Geology of Barringer Meteorite Crater, Arizona (a.k.a. Meteor Crater). LPI Contribution No. 1355, Lunar and Planetary Institute, Houston, 150 p.
- Kring, D. A. (2007) The Chicxulub impact event and its environmental consequences at the Cretaceous-Tertiary boundary. *Palaeogeography, Palaeoclimatology, Palaeoecology*, v. 255, pp. 4-21.
- Kring, D.A. (2010) What can astronauts learn from terrestrial impact craters for operations on the Moon and Mars? *Nördlingen 2010: The Ries Crater, the Moon, and the Future of Human Space Exploration*, Abstract #7036.
- Kring, D.A. (2015) Botanical signature of tectonic fractures in the target rocks of Barringer Meteorite Crater, Arizona. *Lunar and Planetary Science XLVI*, Abstract #1036.
- Kring, D.A. (2016) Chicxulub Crater, twenty-five years later. *Lunar and Planetary Information Bulletin*, issue 144 (March 2016), pp. 2-8.
- Kring, D.A. and Andes, B.D. (2015) Cavernous openings in the target rocks and crater walls of Meteor Crater. *Second International Planetary Caves Conference*, Abstract #9025.
- Kring, D.A. and Boslough, M. (2014) Chelyabinsk: Portrait of an asteroid airburst. *Physics Today*, v. 67(8), pp. 32-37.
- Kring, D.A., Jull, A.J.T., McHargue, L.R., Bland, P.A., Hill, D.H., and Berry, F.J. (2001) Gold Basin meteorite strewn field, Mojave Desert, northwestern Arizona: Relic of a small late Pleistocene impact event. *Meteoritics and Planetary Science*, v. 36, pp. 1057-1066.

Kring, D.A., Balcerski, J., Blair, D.M., Chojnacki, M., Donohue, P.H., Drummond, S.A., Garber, J.M., Hopkins, M., Huber, M.S., Jaret, S.J., Losiak, A., Maier, A., Mithell, J., Ong, L., Ostrach, L.R., O'Sullivan, K.M., Potter, R.W.K., Robbins, S., Shankar, B., Shea, E.K., Singer, K.N., Sori, M., Sturm, S., Willmes, M., Zanetti, M., and Wittmann, A. (2011a) Asymmetrical distribution of impact ejected lithologies at Barringer Meteorite Crater (aka Meteor Crater). Lunar and Planetary Science XLII, Abstract #1746.

Kring, D.A., Balcerski, J., Blair, D.M., Chojnacki, M., Donohue, P.H., Drummond, S.A., Garber, J.M., Hopkins, M., Huber, M.S., Jaret, S.J., Losiak, A., Maier, A., Mithell, J., Ong, L., Ostrach, L.R., O'Sullivan, K.M., Potter, R.W.K., Robbins, S., Shankar, B., Shea, E.K., Singer, K.N., Sori, M., Sturm, S., Willmes, M., Zanetti, M., and Wittmann, A. (2011b) Fold hinge in overturned Coconino sandstone and its structural displacement during the formation of Barringer Meteorite Crater (aka Meteor Crater). Lunar and Planetary Science XLII, Abstract #1740.

Kring, D.A., Cole, S., Craft, K., Crites, S., Gaither, T., Jilly, C., Lemelin, M., Rosenburg, M., Seward, L., Song, E., Snape, J.F., Talpe, M., Thaisen, K., Veto, M., Wielicki, M., Williams, F., Worsham, E., and Garber, J. (2012) Extensional faulting of the overturned Coconino ejecta layer and emplacement of fallback breccia at Barringer Meteorite Crater (aka Meteor Crater). Lunar and Planetary Science XLIII, Abstract #1618.

Kring, D.A., Atwood-Stone, C., Boyd, A., Brown, J., Corley, L., Curran, N., Davis, C., Korman, K., Maine, A., McDonald, F., Montalvo, S., Nuno, R., Oezdemir, S., Rathbun, K., Rhodes, N., Susorney, H., Weiss, D., and Zanetti, M. (2015) Distribution of discontinuous Kaibab ejecta north of Meteor Crater, Arizona. Lunar and Planetary Science XLVI, Abstract #1186.

Krinov, E.L. (1966) The Arizona (Barringer) meteorite crater. Beynon, M.M., ed., *Giant Meteorites*, Pergamon Press, New York, pp. 78-124.

Ksanda, C.J. and Henderson, E.P. (1939) Identification of diamond in the Canyon Diablo iron. *American Mineralogist*, v. 24, pp. 677-680.

Kumar, P.S. and Kring, D.A. (2008) Impact fracturing and structural modification of sedimentary rocks at Meteor Crater, Arizona. *Journal of Geophysical Research*, v. 113, 12 p., E09009, doi:10.1029/2008JE003115.

Kumar, P.S., Head, J.W., and Kring, D.A. (2010) Erosional modification and gully formation at Meteor Crater, Arizona: Insights into crater degradation processes on Mars. *Icarus*, v. 208, pp. 608-620.

Kunz, G.F. and Huntington, E.P. (1939) On the diamond in the Canyon Diablo meteoric iron, and on the hardness of carborundum. *American Journal of Science*, v. 46, pp. 470-473.

LaPaz, L. (1953) The discovery and interpretation of nickel - iron granules associated with meteorite craters R.A.S.C. *Journal*, v. 47, pp. 191-194.

Lehner, M. and Whiteman, C.D. (2012) The thermally driven cross-basin circulation in idealized basins under varying wind conditions. *Journal of Applied Meteorology and Climatology*, v. 51, pp. 1026-1045.

Lehner, M., Whiteman, C.D., and Hoch, S.W. (2011) Diurnal cycle of thermally driven cross-basin winds in Arizona's Meteor Crater. *Journal of Applied Meteorology and Climatology*, v. 50, pp. 729-744.

Lehner, M., Whiteman, C.D., Hoch, S.W., Crosman, E.T., Jeglum, M.E., Cherukuru, N.W., Calhoun, R., Adler, B., Kalthoff, N., Rotunno, R., Horst, T.W., Semmer, S. Brown, W.O.J., Oncley, S.P., Vogt, R., Grudzielanek, A.M., Cermak, J., Fonteyne, J.N., Bernhofer, C., Pitacco, A., and Klein, P. (2016) The METCRAX II field experiment: A study of downslope windstorm-type flows in Arizona's Meteor Crater. *Bulletin of the American Meteorological Society*, v. 97, pp. 217-235.

Lehner, M., Rotunno, R., and Whiteman, C.D. (2016) Flow regimes over a basin induced by upstream katabatic flows – an idealized modeling study. *Journal of the Atmospheric Sciences*, v. 73, pp. 3821-3842.

Leonard, F.C. (1950) The name of the Barringer meteorite crater of Arizona. *Popular Astronomy*, v. 58, p. 469.

Leya, I., Wieler, R., Ma, P., Schnabel, C., and Herzog, G.F. (2002) Pre-atmospheric depths and thermal histories of Canyon Diablo spheroids. *Meteoritics and Planetary Science*, v. 37, pp. 1015-1025.

Lipschutz, M.E. and Anders, E. (1961a) The record in the meteorites, 4, Origin of diamonds in iron meteorites. *Geochimica et Cosmochimica Acta*, v. 24, pp. 83-105.

Lipschutz, M.E. and Anders, E. (1961b) On the mechanism of diamond formation. *Science*, v. 134, pp. 2095-2099.

Magie, W.F. (1910) Physical notes of Meteor Crater, Arizona. *Proceedings of the American Philosophical Society*, v. 49, p. 41.

Marrero, S., Phillips, F.M., Caffee, M.W., Smith, S.S., and Kring, D.A. (2010) Re-dating the Barringer Meteorite Crater (AZ) impact using cosmogenic chlorine-36 surface exposure method. 73rd Annual Meeting of The Meteoritical Society, Abstract #5150.

Mayer, B., Hoch, S.W., and Whiteman, C.D. (2010) Validating the MYSTIC three-dimensional radiative transfer model with observations from the complex topography of Arizona's Meteor Crater. *Atmospheric Chemistry and Physics Discussions*, v. 10, pp. 13373-13405.

Marvin, U.B. (1990) Impact and its revolutionary implications for geology. In: *Global Catastrophes in Earth History, An Interdisciplinary Conference on Impacts, Volcanism, and Mass Mortality*, V.L. Sharpton and P.D. Ward (eds.), Special Paper 247, Geological Society of America, Boulder, pp. 147-154.

McKee, E.D. (1934) The Coconino Sandstone – Its history and origin. *Contributions to Paleontology*, Carnegie Institution of Washington Publication 400, pp. 78-115.

McKee, E.D. (1938) The environment and history of the Toroweap and Kaibab Formations of northern Arizona and southern Utah. *Carnegie Institution of Washington Publication* 492, 221 p.

McKee, E.D. (1951) Triassic deposits of the Arizona-New Mexico border area. *New Mexico Geological Society Guidebook*, 2nd Field Conference, San Juan Basin, pp. 85-92.

McKee, E.D. (1954) Stratigraphy and history of the Moenkopi Formation of Triassic age. *Geological Society of America Memoir* 61, 133 p.

Mead, C.W., Littler, J., and Chao, E.C.T. (1965) Metallic spheroids from Meteor crater. *American*

Mineralogist, v. 50, pp. 667-681.

Melosh, H.J. and Collins, G.S. (2005) Meteor Crater formed by low-velocity impact. *Nature*, v. 434, p. 157.

Merrill, G.P. (1908) The Meteor Crater of Canyon Diablo, Arizona; its history, origin, and associated meteoric irons. *Smithsonian Miscellaneous Collections*, v. L, no. 1789, pp. 461-498 (with multiple plates).

Michlovich, E.S., Vogt, S., Masarik, J., Reedy, R.C., Elmore, D., and Lipschutz, M.E. (1994) Aluminum 26, ^{10}Be , and ^{36}Cl depth profiles in the Canyon Diablo iron meteorite. *Journal of Geophysical Research*, v. 99, pp. 23,187-23,194.

Moore, R.B. and Wolfe, E.W. (1987) Geologic Map of the East Part of the San Francisco Volcanic Field, Arizona. USGS Map MF-1960.

Moore, C.B., Birrell, P.J., and Lewis, C.F. (1967) Variations in the chemical and mineralogical composition of rim and plains specimens of the Canyon Diablo meteorite. *Geochimica et Cosmochimica Acta*, v. 31, pp. 1,885-1,892.

Newsom, H.E., Wright, S.P., Misra, S., and Hagerty, J.J. (2013) Comparison of simple impact craters: a case study of Meteor and Lonar Craters. In *Impact Cratering: Processes and Products*, Osinski, G.R. and Pierazzo, E. (eds.), Blackwell Publishing, Chichester, pp. 271-289.

Niermeyer, J.F. (1949) A new type of magnetometer survey of Barringer meteorite crater. *Popular Astronomy*, v. 57, pp. 1-5.

Nininger, H.H. (1949) Oxidation studies at Barringer Crater, Metal-center pellets and oxide droplets. *American Philosophical Society Yearbook*, pp. 126-130.

Nininger, H.H. (1951) Condensation globules at Meteor Crater. *Science*, v. 113, pp. 755-756.

Nininger, H.H. (1954) Impactite slag at Barringer crater. *American Journal of Science*, v. 252, pp. 277-290.

Nininger, H.H. (1956) Arizona's Meteorite Crater. American Meteorite Museum, Sedona, 232 p.

Nininger, H.H. (1957) A Comet Strikes the Earth. American Meteorite Museum, Sedona, 65 p.

Nishiizumi, K., Kohl, C.P., Shoemaker, E.M., Arnold, J.R., Klein, J., Fink, D., and Middleton, R. (1991) In situ ^{10}Be - ^{26}Al exposure ages at Meteor Crater, Arizona. *Geochimica et Cosmochimica Acta*, v. 55, pp. 2,699-2,703.

Noble, L.F. (1914) The Shinumo Quadrangle. U.S. Geological Survey Bulletin 549, 100 p.

Norwick, S.A. and Dexter, L.R., 2002, Rates of development of tafoni in the Moenkopi and Kaibab formations in Meteor Crater and on the Colorado Plateau, northeastern Arizona. *Earth Surface Processes and Landforms*, v. 27, pp. 11-26.

Oerter, E.J., Sharp, W.D., Oster, J.L., Ebeling, A., Valley, J.W., Korzdon, R., Orland, I.J., Hellstrom, J.,

Woodhead, J.D., Hergt, J.M., Chadwick, O.A., and Amundson, R., (2016) Pedothen carbonates reveal anomalous North American atmospheric circulation 70,000-55,000 years ago. *Proceedings of the National Academy of Sciences*, v. 113(4), pp. 919-924.

Öhman, T., Aittola, M., Kostama, V.-P., Raitala, J., and Kortenien, J. (2008) Polygonal impact craters in Argyre region, Mars: Implications for geology and cratering mechanics. *Meteoritics and Planetary Science*, v. 43, pp. 1605-1628.

Öpik, E.J. (1958) Meteor impact on solid surface. *Irish Astronomical Journal*, v. 5, pp. 14-33.

Öpik, E.P. (1936) Researches on the Physical Theory of Meteor Phenomena. I. Theory of the formation of meteor craters. *Publications of the Astronomical Observatory of the University of Tartu*, v. 28, pp. 3-12.

Ormö, J., Sturkell, E., Alwmark, C., and J. Melosh (2014) First known terrestrial impact of a binary asteroid from a main belt breakup event. *Scientific Reports*, v. 4, 5 p., 6724, doi: 10.1038/srep06724.

Ormö, J., Sturkell, E., Nölvak, J., Melero-Asensio, I., Frisk, Å., Wikström, T. (2014) The geology of the Målingen structure: A probable doublet to the Lockne marine-target impact crater, central Sweden. *Meteoritics and Planetary Science*, v. 29, pp. 313-327.

Ort, M.H., Elson, M.D., and Champion, D.E. (2002) A Paleomagnetic Dating Study of Sunset Crater Volcano. Technical Report No. 2002-16, Desert Archaeology, Inc., 16 p.

Osinski, G.R., Bunch, T.E., Flemming, R.L., Buitenhuis, E., and Wittke, J.H. (2015) Impact melt- and projectile-bearing ejecta at Barringer Crater, Arizona. *Earth and Planetary Science Letters*, v. 432, pp. 283-292.

Ostro, S.J., Campbell, D.B., Chandler, J.F., Hine, A.A., Hudson, R.S., Rosema, K.E., and Shapiro, I.I. (1991) Asteroid 1986 DA: Radar evidence for a metallic composition. *Science*, v. 252, pp. 1,401-1,404.

Palucis, M. and McEnulty, T., 2010, Meteor Crater, Az: A terrestrial analog to study gully formation on Mars – Mapping project report. The National Center for Airborne Laser Mapping, June 23, 2010, 8p.

Palucis, M.C., Dietrich, W.E., Howard, A., Nishiizumi, K., and Kring, D.A. (2012a) How much water is needed to make gullies on Mars: A conceptual model. *Lunar and Planetary Science XLIII*, Abstract #1499.

Palucis, M.C., Dietrich, W.E., Howard, A., Nishiizumi, K., and Kring, D.A. (2012b) Origin and evolution of gullies on crater walls by water: Estimating discharge rates and flow durations. *Third Conference on Early Mars*, Abstract #7088.

Palucis, M.C., Dietrich, W.E., Howard, A.D., Nishiizumi, K., Caffee, M.W., and Kring, D.A. (2015) Meteor Crater: An analog for using landforms to reconstruct past hydrologic conditions. *Annual Fall Meeting of the American Geophysical Union*, Abstract #P24A-07.

Peabody F.E. (1948) Reptile and amphibian trackways from the Lower Triassic Moenkopi Formation of Arizona and Utah. *University of California Publications, Bulletin of the Department of Geological Sciences*, v. 27, pp. 295-468.

- Phillips, F.M., Zreda, M.G., Smith, S.S., Elmore, D., Kubik, P.W., Dorn, R.I., and Roddy, D.J. (1991) Age and geomorphic history of Meteor Crater, Arizona, from cosmogenic ^{36}Cl and ^{14}C in rock varnish. *Geochimica et Cosmochimica Acta*, v. 55, pp. 2,695-2,698.
- Phillips, F.M., Zreda, M.G., and Flinsch, M.R. (1996) A reevaluation of cosmogenic ^{36}Cl production rates in terrestrial rocks. *Geophysical Research Letters*, v. 23, pp. 949-952.
- Pilon, J.A., Grieve, R.A.F., and Sharpton, V.L. (1991) The subsurface character of Meteor Crater, Arizona, as determined by ground-probing radar. *Journal of Geophysical Research*, v. 96, pp. 15,563-15,576.
- Pilon, J.A., Grieve, R.A.F., Sharpton, V.L., Coderre, J., and Kennedy, J. (1992) Reconnaissance ground penetrating radar survey of the interior of Meteor Crater, Arizona. Pilon, J.A., ed., *Geological Survey of Canada Paper 90-4, Ground Penetrating Radar*, Canada Communications Group, Ottawa, Canada, pp. 177-186.
- Plesko, C.S. (2013) Exploring the effects of pre-existing target faults on crater morphology. *Lunar and Planetary Science XLIV*, Abstract #2896.
- Poelchau, M.H., Kenkmann, T., and Kring, D.A. (2009) Rim uplift and crater shape in Meteor Crater: Effects of target heterogeneities and trajectory obliquity. *Journal of Geophysical Research*, v. 114, 14 p., E01006, doi:10.1029/2008JE003235.
- Ramsey, M.S. (2002) Ejecta distribution patterns at Meteor Crater, Arizona: On the applicability of lithologic end-member deconvolution for spaceborne thermal infrared data of Earth and Mars, *Journal of Geophysical Research*, v. 107, no. E9, 5059, doi: 10.1029/2001JE001827.
- Read, C.B. (1950, reprinted 1996) *Stratigraphy of the outcropping Permian rocks around the San Juan Basin*. New Mexico Geological Society Guidebook of the San Juan Basin, New Mexico and Colorado, 152 pp., edited by V.C. Kelley, E.C. Beaumont, and C. Silver, pp. 62-66.
- Regan, R.D. and Hinze, W.J. (1975) Gravity and magnetic investigations of Meteor crater, Arizona. *Journal of Geophysical Research*, v. 80, pp. 776-778.
- Regan, R.D. (1967) Technical letter: Astrogeology 29. Preliminary geophysical report on selected geologic test sites. United States Department of the Interior Geological Survey, pp. 1-22.
- Reger, R.D. and Batchelder G.L. (1971) Late Pleistocene molluscs and a minimum age of Meteor Crater, Arizona. *Journal of the Arizona Academy of Science*, v. 6, pp. 190-195.
- Reiche, P. (1938) An analysis of cross-lamination of the Coconino sandstone. *Journal of Geology*, v. 46, no. 7, pp. 905-932.
- Rinehart, J.S. (1957) A soil survey around the Barringer crater. *Sky and Telescope*, v. 16, pp. 366-369.
- Rinehart, J.S. (1958a) Distribution of meteoritic debris about the Arizona meteorite crater. *Smithsonian Contributions to Astrophysics*, v. 2, pp. 145-160.
- Rinehart, J.S. (1958b) Recent findings at the Arizona meteorite crater. *Footprints*, v. 30, no. 2, pp. 15-22.

- Roberts, W.A. (1965) Genetic stratigraphy of the Meteor crater outer lip. *Icarus*, v. 4, pp. 431-433.
- Roberts, W.A. (1968) Shock crater ejecta characteristics. In *Shock Metamorphism of Natural Materials*, B.M. French and N.M. Short (eds.), Mono Book Corp., Baltimore, MD, pp. 101-114.
- Roddy, D.J. (1977) Large-scale impact and explosion craters: Comparisons of morphological and structural analogs. In: *Impacts and Explosion Cratering*, D.J. Roddy, R.O. Pepin, and R.B. Merrill (eds.), Pergamon Press, New York, pp. 185-246.
- Roddy, D.J. (1978) Pre-impact geologic conditions, physical properties, energy calculations, meteorite and initial crater dimensions and orientations of joints, faults and walls at Meteor Crater, Arizona. *Proc. Lunar Planetary Science Conf. 9th*, pp. 3,891-3,930.
- Roddy, D.J. and Shoemaker, E.M. (1995) Meteor crater (Barringer meteorite crater), Arizona: Summary of impact conditions (abstract). *Meteoritics*, v. 30, pp. 567.
- Roddy, D.J., Boyce, J.M., Colton, G.W., and Dial A.L. Jr. (1975) Meteor Crater, Arizona, rim drilling and thickness, structural uplift, diameter, depth, volume, and mass-balance calculations. *Proc. Lunar Science Conf. 6th*, pp. 2,621-2,644.
- Roddy, D.J., Schuster, S.H., Dreyenhagen K.N., and Orphal, D.L. (1980) Computer code simulations of the formation of Meteor Crater, Arizona: Calculations MC-1 and MC-2. *Proc. Lunar Planetary Science Conf. 11th*, pp. 2,275-2,308.
- Rogers, A.F. (1928) Natural history of the silica minerals. *American Mineralogist*, v. 13, pp. 73-92.
- Rostoker, N. (1953) The formation of craters by high-speed particles. *Meteoritics*, v. 1, pp. 11-27.
- Roy, S. (2013) Near-surface Characterization via Seismic Surface-wave Inversion. Ph.D. Thesis, University of Houston.
- Roy, S., Stewart, R.R., and Kring, D.A. (2011) Seismic investigations at Barringer Crater, Arizona. *Lunar and Planetary Science XLII*, Abstract #1644.
- Ryabenko, V.A. and Val'ter, A.A. (1977) Meteorite explosion craters as an object of study in modern geology (in Russian). *Visnyk*, v. 1-6, pp. 7-16.
- Schaber, G.G. (1966) Radar Images: Meteor Crater, Arizona. USGS, NASA-CR-80742, 18 p.
- Schmidt, R.M. (1980) Meteor Crater: Energy of formation-implications of centrifuge scaling. *Proceedings Lunar and Planetary Science Conference 11th*, pp. 2,099-2,128.
- Schmieder, M., Chennaoui Aoudjehane, H., Buchner, E., and Tohver, E. (2015) Meteorite traces on a shatter cone surface from the Agoudal impact site, Morocco. *Geological Magazine*, v. 152, pp. 751-757.
- Schmieder, M., Boschi, S., Caudill, C., Chandnani, M., DiFrancesco, N.J., Hibbard, S.M., Hughson, K., Kinczyk, M., Martin, A.C., Martin, E., Martinot, M., McCarty, C.B., Powell, K.E., Sarafian, A., Schaub, D.R., Shirley, K., and D. A. Kring (2017) Mapping ejecta on the east and southeast side of Barringer Meteorite Crater (a.k.a. Meteor Crater), Arizona. *Lunar and Planetary Science XLVIII*, Abstract #2180.

Schnabel, C., Pierazzo, E., Xue, S., Herzog, G.F., Masarik, J., Cresswell, R.G., di Tada, M.L., Liu, K., and L.K. Fifield (1999) Shock melting of the Canyon Diablo impactor: constraints from nickel-59 contents and numerical modeling. *Science*, v. 285, pp. 85-88

Schuchert, C. (1918) On the Carboniferous of the Grand Canyon of Arizona. *American Journal of Science*, v. XLV (4th Series), pp. 347-434.

Schulte, P., Alegret, L., Arenillas, I., Arz, J.A., Barton, P.J., Bown, P.R., Bralower, T.J., Christeson, G.L., Claeys, P., Cockell, C.S., Collins, G.S., Deutsch, A., Goldin, T.J., Goto, K., Grajeles-Nishimura, J.M., Grieve, R.A.F., Gulick, S.P.S., Johnson, K.R., Kiessling, W., Koeberl, C., Kring, D.A., MacLeod, K.G., Matsui, T., Melosh, J., Montanari, A., Morgan, J.V., Neal, C.R., Nichols, D.J., Norris, R.D., Pierazzo, E., Ravizza, G., Rebolledo-Vieyra, M., Reimold, W.U., Robin, E., Salge, T., Speijer, R.P., Sweet, A.R., Urrutia-Fucugauchi, J., Vajda, V., Whalen, M.T., and Willumsen, P. (2010) The Chicxulub asteroid impact and mass extinction at the Cretaceous-Paleogene Boundary. *Science*, v. 327, pp. 1214-1218.

See, T.H., Hörz, F., Mittlefehldt, D.W., Varley, L., Mertzman, S., and Roddy, D. (2002) Major element analyses of the target rocks at Meteor Crater, Arizona. NASA Technical Memorandum (TM)-2002-210787, 31 p.

Settle, M. (1980) The role of fallback ejecta in the modification of impact craters. *Icarus*, v. 42, pp. 1-19.

Shipman, F.H. and Gregson, V.G., and Jones, A.H. (1971) A shock-wave study of Coconino sandstone. NASA Contractor Report (CR)-1842, 46 p.

Shoemaker, E.M. (1959) Impact mechanics at Meteor crater, Arizona. Prepared on half of the U.S. Atomic Energy Commission, USGS Open File Report 55-108, 55 p.

Shoemaker, E.M. (1960) Penetration mechanics of high velocity meteorites, illustrated by Meteor crater, Arizona. International Geological Congress, 21st, Copenhagen, pp. 418-434.

Shoemaker, E.M. (1963) Impact mechanics at Meteor crater, Arizona. In: *The Moon, Meteorites and Comets*, edited by Middlehurst, B.M. and Kuiper, G.P., University of Chicago Press, Chicago, v. IV, pp. 301-336.

Shoemaker, E.M., Gault, D.E., Moore, H.J., and Lugn, R.V. (1963) Hypervelocity impact of steel into Coconino Sandstone. *American Journal of Science*, v. 261, pp. 668-682.

Shoemaker, E.M., Batson, R.M., Holt, H.E., Morris, E.C., Rennilson, J.J., and Whitaker, E.A. (1967) Television observations from Surveyor V. Surveyor V Mission Report, Part 1, Science Results, Jet Propulsion Laboratory Technical Report 32-1246.

Shoemaker, E.M. (1983) Asteroid and comet bombardment of the Earth. *Annual Review of Earth and Planetary Sciences*, v. 11, pp. 461-494.

Shoemaker, E.M. (1987) Meteor Crater, Arizona. Geological Society of America Centennial Field Guide - Rocky Mountain Section, pp. 399-404.

Shoemaker, E.M. and Kieffer, S.W. (1974) Guidebook to the geology of Meteor crater, Arizona. Meteoritical Society, 37th Annual Meeting, Arizona State University Centre for Meteorite Studies,

Tempe, Arizona, 1974 (66 pp.) Reprinted in 1988.

Shoemaker, E.M., Gault, D.E., Moore, H.J., and Lugin, R.V. (1963) Hypervelocity impact of steel into Coconino sandstone. *American Journal of Science*, v. 261, pp. 668-682.

Short, N.M. (1964) Nuclear Explosion Craters, Astroblemes, and Cryptoexplosion Structures. University of California Ernest O. Lawrence Radiation Laboratory, UCRL-7787, 75 p.

Skinner, B.J. and Fahey, J.J. (1963) Observations on the inversion of stishovite to silica glass. *Journal of Geophysical Research*, v. 68, pp. 5,595-5,604.

Skrynnik, G.V. (1977) Meteorite craters on the Earth (in Russian). *Astronomicheskii Vestnik*, v. 11, pp. 198-210.

Smiley, T.L. (1958) The geology and dating of Sunset Crater, Flagstaff, Arizona. In *Guidebook of the Black Mesa Basin, Northeastern Arizona*, R.Y. Anderson and J.W. Harschbarger (eds.), New Mexico Geological Society, Ninth Field Conference, pp. 186-190.

Smith, M.D., Wolff, M.J., Lemmon, M.T., Spanovich, N., Banfield, D., Budney, C.J., Clancy, R.T., Ghosh, A., Landis, G.A., Smith, P., Whitney, B., Christensen, P.R., and Squyres, S.W. (2004) First atmospheric science results from the Mars Exploration Rovers Mini-TES. *Science*, v. 306, pp. 1750-1752.

Southgate, N. and F. Barringer (2002) *A Grand Obsession: Daniel Moreau Barringer and His Crater*. The Barringer Crater Company, Flagstaff, Arizona, 78 p.

Spencer, L.J. (1933) Meteorite craters as topographical features on the Earth's surface. *Geographical Journal* (London), v. 81, pp. 227-248.

Stöffler, D. (1972) Deformation and transformation of rock-forming minerals by natural and experimental shock processes: I. Behavior of minerals under shock compression. *Fortschr. Mineral.*, v. 49, pp. 50-113.

Stoek, P.J. (2007) *The International Atlas of Lunar Exploration*. Cambridge University Press, Cambridge, 440 p.

Sutton, S.R. (1985) Thermoluminescence measurements on shock-metamorphosed sandstone and dolomite from Meteor Crater, Arizona. 1. shock dependence of thermoluminescence properties. *Journal of Geophysical Research*, v. 90, pp. 3683-3689.

Sutton, S.R. (1985) Thermoluminescence measurements on shock-metamorphosed sandstone and dolomite from Meteor Crater, Arizona. 2. Thermoluminescence age of Meteor crater. *Journal of Geophysical Research*, v. 90, pp. 3,690-3,700.

Tagle, R., Schmitt, R.T., and Erzinger, J. (2009) Identification of the projectile component in the impact structures Rochechouart, France and Sääksjärvi, Finland: Implications for the impactor population for the Earth. *Geochimica et Cosmochimica Acta*, v. 73, pp. 4891-4906.

Tilghman, B.C. (1905) Coon Butte, Arizona. *Proceedings of the Academy of Natural Sciences of Philadelphia*, v. 57, pp. 887-914.

Turolski, A. (2012) Near-surface Geophysical Imaging of Complex Structures: Meteor Crater, AZ and Jemez Pueblo, NM. M.S. Thesis, University of Houston, 77 p.

Ulrich, G.E., Billingsley, G.H., Hereford, R., Wolfe, E.W., Nealey, L.D., and Sutton, R.L. (1984) Map showing the geology, structure, and uranium deposits of the Flagstaff $1^{\circ} \times 2^{\circ}$ quadrangle, Arizona. USGS Miscellaneous Investigations Series Map I-1446, scale 1:250,000.

Urey, H.C. (1956) Diamonds, meteorites, and the origin of the solar system. *Astrophysics Journal*, v. 124, pp. 623-637.

Val'ter, A.A. and Gurov, E.P. (1978) The system of mineralogical indicators in factors of shock metamorphism in granitoid rocks (in Russian). *Kosmicheskaya mineralogiya*, v. 11, pp. 92-102.

Vdovykin, G.P. (1973) The Canyon Diablo Meteorite. *Space Science Reviews*, v. 14, pp. 758-831.

Walters, L.A. (1966) In situ physical properties measurements. In Investigation of in situ physical properties of surface and subsurface site materials by engineering geophysical techniques, annual report, fiscal year 1966, edited by J.S. Watkins. NASA Contractor Report (CR)-65502 and USGS Open-File Report 67-272, pp. 7-24.

Wasson, J.T. (1967) Concentrations of Ni, Ga, and Ge in a series of Canyon Diablo and Odessa meteorite specimens. *Journal of Geophysical Research*, v. 72, pp. 721-730.

Wasson, J.T. (1968) Concentrations of nickel, gallium, germanium, and iridium in Canyon Diablo and other Arizona octahedrites. *Journal of Geophysical Research*, v. 73, 3,207-3,211.

Wasson, J.T. and Ouyan, X. (1990) Compositional range in the Canyon Diablo meteoroid. *Geochimica et Cosmochimica Acta*, v. 54, pp. 3,175-3,183.

Watkins, J.S., ed. (1966) Annual Report, Investigation of in situ physical properties of surface and subsurface site materials by engineering geophysical techniques. NASA Contract T-25091(G). Also catalogued as NASA Contractor Report (CR)-65502 and USGS Open-File Report 67-272. 373 p.

Watkins, J.S. and Walters, L.A. (1966) Laboratory physical property measurements on core and surface samples from six lunar analog test sites. In: Investigations of in situ physical properties of surface and subsurface site materials by engineering geophysical techniques, annual report, fiscal year 1966, edited by J.S. Watkins, NASA Contractor Report (CR)-65502 and USGS Open-File Report 67-272, pp. 259-267.

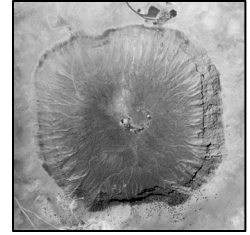
Watkins, J.S., Roach, C.H., and Christian, R.P. (1966) Correlation of physical properties – from laboratory measurements and from in situ measurements. In: Investigation of in situ physical properties of surface and subsurface site materials by engineering geophysical techniques, annual report, fiscal year 1966, edited by J.S. Watkins. NASA Contractor Report (CR)-65502 and USGS Open-File Report 67-272, pp. 25-35.

Welles, S.P. and Cosgriff, J. (1965) A revision of the Labyrinthodont family Capitosauridae. University of California Publications in Geological Sciences, v. 54, 148 p. (plus 1 plate).

Whiteman, C.D., Muschinski, A., Zhong, S., Fritts, D., Hoch, S.W., Hahnenberger, M., Yao, W.,

- Hohreiter, V., Behn, M., Cheon, Y., Clements, C.B., Horst, T.W., Brown, W.O.J., and Oncley, S.P. (2008) METCRAX 2006: Meteorological experiments in Arizona's Meteor Crater. *Bulletin of the American Meteorological Society*, v. 89, pp. 1665-1680.
- Whiteman, C.D., Hoch, S.W., Lehner, M., and Haiden, T. (2010) Nocturnal cold-air intrusions into a closed basin: Observational evidence and conceptual model. *Journal of Applied Meteorology and Climatology*, v. 49, pp. 1894-1905.
- Wier, G.W. and others (1989) Geologic Map of the Sedona 30' × 60' Quadrangle, Yavapai and Coconino Counties, Arizona. Scale 1:100,000, USGS Map I-1896.
- Worsham, E.A., Bermingham, K.R., and Walker, R.J. (2016) Siderophile element systematics of IAB complex iron meteorites: New insights into the formation of an enigmatic group. *Geochimica et Cosmochimica Acta*, v. 188, pp. 261-283.
- Wylie, C.C. (1943a) Calculations on the probable mass of the object which formed Meteor Crater. *Popular Astronomy*, v. 51, pp. 97-99.
- Wylie, C.C. (1943b) Second note on the probably mass of the object which formed Meteor Crater. *Popular Astronomy*, v. 51, pp. 158-161.
- Xue, S., Herzog, G.F., Hall, G.S., Klein, J., Middleton, R., and Juenemann, D. (1995) Stable nickel isotopes and cosmogenic beryllium-10 and aluminum-26 in metallic spheroids from Meteor crater, Arizona. *Meteoritics*, v. 30, pp. 303-310.

Field Notes



Field Notes

